BOTSWANA INTERNATIONAL UNIVERSITY OF SCIENCE & TECHNOLOGY

FACULTY OF SCIENCES
DEPARTMENT OF PHYSICS AND ASTRONOMY

GENERATION OF DISSIPATIVE AND NON-DISSIPATIVE MATTER-WAVE SOLITON TRAINS IN SPIN-ORBIT COUPLED BOSE-EINSTEIN CONDENSATES

BY

OTLAADISA PHELO

STUDENT ID: 13000730

BSc (Applied Science) (BIUST)

A Thesis to be Submitted to the Faculty of Sciences in Partial Fulfilment of the Requirements for the Award of the Degree of Master of Science in Physics of BIUST

Supervisor: **Professor Conrad Bertrand Tabi**
Department of Physics and Astronomy
Faculty of Sciences, BIUST
Email: tabic@biust.ac.bw

Co-supervisor: **Professor Timoléon Crépin Kofané**
Department of Physics and Astronomy
Faculty of Sciences, BIUST
Email: kofanet@biust.ac.bw

MARCH, 2022

Contents

CONTENTS i

DECLARATION iii

ACKNOWLEDGEMENTS iv

LIST OF FIGURES viii

LIST OF ABBREVIATIONS ix

LIST OF PUBLICATIONS x

ABSTRACT xi

GENERAL INTRODUCTION 1

THESIS OUTLINE 3

1 BOSE-EINSTEIN CONDENSATION (BEC) BASICS 4
1.1 Introduction . . . 4
1.2 Identical particles . . . 4
1.3 Bose-Einstein condensation in an ideal gas . . . 5
1.4 The Gross-Pitaevskii (GP) equation . . . 7
1.4.1 Single-component systems . . . 7
1.4.2 Two-component systems . . . 8
1.5 BEC experimental procedure . . . 9
1.5.1 Laser cooling . . . 9
1.5.2 Magnetic trapping . . . 10
1.5.3 Evaporative cooling . . . 10
1.6 Spin-orbit (SO) coupling in BECs . . . 10
1.6.1 SO coupling in one-dimensional (1D) ultracold atoms . . . 10
1.6.2 Synthetic SO coupling in cold atoms . . . 11
1.7 Solitons in BECs . . . 12
1.8 Modulational instability phenomenon in BECs . . . 13
1.9 Summary . . . 14

2 MODULATION INSTABILITY PROCESS IN HELICOIDAL SPIN-ORBIT COUPLED OPEN BOSE-EINSTEIN CONDENSATES 15
2.1 Introduction . . . 15
2.2 Theoretical model of an open two-component BECs in 1D . . . 16

2.2.1 A system of two-coupled 1D cubic GP equations 16
2.2.2 Derivation of a new vector form of the cubic Complex Ginzburg-Landau equations with helicoidal SO coupling 19
2.3 Linear stability analysis of the MI in two-component open BECs with helicoidal SO coupling 23
2.4 Discussion of MI process in open BECs with helicoidal SO coupling . . 24
2.5 Direct numerical simulations of the two coupled 1D cubic CGL equations with helicoidal SO coupling using the slipt-step Fourier transform method 28
2.6 Summary 33

3 MODULATION INSTABILITY OF TWO-DIMENSIONAL BOSE-EINSTEIN CONDENSATES WITH HELICOIDAL AND A MIXTURE OF RASHBA-DRESSELHAUS SPIN-ORBIT COUPLINGS 34
3.1 Introduction 34
3.2 Rashba-Dresselhaus SO coupling Hamiltonian 35
3.3 Basic set of equations 36
3.4 Linear stability analysis of a system of two coupled 2D cubic GP equations with helicoidal and a RD mixtures SO-couplings 40
3.5 MI gain analysis of two coupled 2D cubic GP equations with a mixture of RD SO couplings 41
3.5.1 Case 1: growth rate spectrum for $\beta_x = \beta_y = 0$ 41
3.5.2 Case 2: growth rate spectrum for $\beta_x = \beta_y = \beta$, with $(\beta x + \beta y) = \pi/2$ 43
3.6 Numerical results on wave train formation 48
3.6.1 MI patterns for the case $\beta_x = \beta_y = 0$ 49
3.6.2 MI patterns for the case $\beta_x = \beta_y = \beta$, and $(\beta x + \beta y) = \pi/2$ . . 50
3.7 Summary 52

GENERAL CONCLUSION 63

APPENDICES 65

BIBLIOGRAPHY 72

List of Publications 87

BOTSWANA INTERNATIONAL UNIVERSITY OF SCIENCE & TECHNOLOGY

POSTGRADUATE SCHOOL

Declaration Regarding the Work and Copyright

DECLARATION REGARDING THE WORK AND COPYRIGHT

Candidate : PHELO OTLAADISA

Student ID: 1300070

Thesis Titled: GENERATION OF DISSIPATIVE AND NON-DISSIPATIVE MATTER-WAVE SOLITON TRAINS IN SPIN-ORBIT COUPLED BOSE-EINSTEIN CONDENSATES

I, Phelo Otlaadisa, certify that the Thesis is all my own original work and that I have not obtained a degree in this University or elsewhere on the basis of any of this work.

This dissertation/thesis is copyright material protected under the Berne Convention, the Copyright and Neighbouring Rights Act, Act. No. 8 of 2000 and other international and national enactments, in that behalf, on intellectual property. It must not be reproduced by any means, in full or in part, except for short extracts in fair dealing; for researcher private study, critical scholarly review or discourse with an acknowledgement, without the written permission of the office of the Postgraduate School, on behalf of both the author and the BIUST.

Signed: P.O Date: 10/03/2022

Primary Supervisor (please write in caps or type) PROF CONRAD B. TABI

I, the Candidate's **Primary Supervisor**, hereby confirm that I have inspected the above titled thesis and, to the best of my knowledge, it is based on the original work of the candidate.

Signed: Date: 10/03/2022

ACKNOWLEDGEMENTS

I am indebted to many people who have helped me throughout my masters degree journey, I would like to thank some of those people here. Firstly, my heartfelt thanks go to my supervisor Professor Conrad B. Tabi, for his great counsel and high expectations.Thank you for giving me the chance to advance my academic journey. Thank you so very much for believing in me, I will forever be grateful.

Special thanks go to Professor Timeleon C. Kofane. He has a broad and deep understanding of many fields in physics as well as a gift for recalling very special details, all of which were invaluable as we discussed the physics in this thesis. I have benefited greatly from endless deliberations with him, and would like to thank him for putting up with my ignorance.

I would like to thank Karabo Kefilwe Ndebele, for her assistance throughout my research.

I really appreciate the love and support from my family and everyone who's been on my side. Cheers to you all.

Dedication

To the memory of my late grandparents, Mr Otlaadisa Mooketsi (1927-2014) and Mrs Dikeledi Otlaadisa (1937-2019), who invested a lot towards my education and has been the rock of stability throughout their lifetime.

To my mother, whose love sustains me still.

List of Figures

1.1 Distribution of elementary particles (bosons and fermions) in the quantum states [76]. 5
1.2 Formation of BEC [79] 7
1.3 Bright solitons and dark solitons in BEC [138]. 12
1.4 Evolution of a nonlinear wave train in the course of MI. Bottom: the corresponding evolution of wave spectrum [166]. 13

2.1 Panels $(\mathrm{aj})_{j=1,2,3,4}$ show the contour plots of the MI gain in the $(K, C_1)-$plane for: (a1)-(a2) $C_2 = C_3 = 2$, (a3)-(a4) $C_2 = C_3 = -2$. Panels $(\mathrm{bj})_{j=1,2,3,4}$ display the contour plot of the MI gain in the $(K, C_3)-$plane for (b1)-(b2) $C_1 = C_2 = 2$ and (b3)-(b4) $C_1 = C_2 = -2$, with $n_0 = 1$, $\alpha_0 = 1$ and $C_4 = 0.5$. 26
2.2 MI gain in the $(\alpha_0, \beta_0)-$plane for: $(\mathrm{aj})_{j=1,2,3,4}$ $C_3 > 0$ and $(\mathrm{bj})_{j=1,2,3,4}$ $C_3 < 0$. The coefficients C_1 and C_2 are taken such that in panels (a1)-(b1) $C_1 > 0$, $C_2 < 0$, (a2)-(b2) $C_1 = C_2 > 0$, (a3)-(b3) $C_1 = C_2 < 0$ and (a4)-(b4) $C_1 < 0$, $C_2 > 0$, with $n_0 = 1$ and $K = 1.5$. 27
2.3 The contour plots show the gain of MI in the $(K, \alpha_0)-$plane for: $(\mathrm{aj})_{j=1,2,3,4}$ $C_3 > 0$ and $(\mathrm{bj})_{j=1,2,3,4}$ $C_3 < 0$. The coefficients C_1 and C_2 are taken such that in panels (a1)-(b1) $C_1 > 0$, $C_2 < 0$, (a2)-(b2) $C_1 = C_2 > 0$, (a3)-(b3) $C_1 = C_2 < 0$ and (a4)-(b4) $C_1 < 0$, $C_2 > 0$, with $n_0 = 1$, $\beta_0 = 1$ and $C_4 = 0.5$, with $n_0 = 1$. 28
2.4 Spatiotemporal development of MI for $\alpha_0 = 0$, and β_0 taking the respective values : $(\mathrm{aj})_{j=1,2}$ $\beta_0 = 0$, $(\mathrm{bj})_{j=1,2}$ $\beta_0 = 1.5$ and $(\mathrm{cj})_{j=1,2}$ $\beta_0 = 2.5$, with the other parameter values being: $C_1 = C_2 = 5$, $C_3 = 2$, $C_4 = 0.5$, $K = 1.5$, $n_0 = 1$, $\Delta_0 = 0.01$. 30
2.5 Spatiotemporal development of MI for $\alpha_0 = 0.5$, and β_0 taking the respective values : $(\mathrm{aj})_{j=1,2}$ $\beta_0 = 0$, $(\mathrm{bj})_{j=1,2}$ $\beta_0 = 1.5$ and $(\mathrm{cj})_{j=1,2}$ $\beta_0 = 2.5$, with the other parameter values being: $C_1 = C_2 = 5$, $C_3 = 2$, $C_4 = 0.5$, $K = 1.5$, $n_0 = 1$, $\Delta_0 = 0.01$. 31
2.6 Spatiotemporal development of MI for $\beta_0 = -1.5$, and $C_3 = 2$, with α_0 taking the respective values : $(\mathrm{aj})_{j=1,2}$ $\alpha_0 = 0$, $(\mathrm{bj})_{j=1,2}$ $\alpha_0 = 0.25$ and $(\mathrm{cj})_{j=1,2}$ $\alpha_0 = 0.5$, with the other parameter values being: $C_1 = C_2 = 5$, $C_3 = 2$, $C_4 = 0.5$, $K = 1.5$, $n_0 = 1$, $\Delta_0 = 0.01$. 32
2.7 Spatiotemporal development of MI for $\beta_0 = -1.5$, and $C_3 = -2$, with α_0 taking the respective values : $(\mathrm{aj})_{j=1,2}$ $\alpha_0 = 0$, $(\mathrm{bj})_{j=1,2}$ $\alpha_0 = 0.25$ and $(\mathrm{cj})_{j=1,2}$ $\alpha_0 = 0.5$, with the other parameter values being: $C_1 = C_2 = 5$, $C_3 = 2$, $C_4 = 0.5$, $K = 1.5$, $n_0 = 1$, $\Delta_0 = 0.01$. 32

3.1 Distribution of the MI growth rate versus the interatomic coupling g for different values of the SO coupling strength when: (a) the RD SO coupling is absent, i.e., $\lambda_D = \lambda_R = 0$ and (b) in presence of the RD SO coupling, i.e., $\lambda_D = \lambda_R = 0.01$, with $g_{12} = 0.8$, $K_1 = K_2 = 1$ and $n_0 = 1$. 42
3.2 The panels show the growth rate of MI in the $(K_1, K_2)-$plane for $\alpha = 0$ (panels $(\text{aj})_{j=1,2,3}$) and $\alpha = 0.25$ (panel$(\text{bj})_{j=1,2,3}$). From left to right, the columns correspond to the different cases $\lambda_R = \lambda_D$, $\lambda_R > \lambda_D$ and $\lambda_R < \lambda_D$, respectively, with $g_{12} = 0.8$, and $n_0 = 1$. White regions correspond to zones of instability, while dark areas are where the CWs solutions are likely to remain stable under modulation. 42
3.3 Distribution of the MI growth rate versus the interatomic coupling g for different values of the SO coupling strength when: (a) the RD SO coupling is absent, i.e., $\lambda_D = \lambda_R = 0$ and (b) in presence of the RD SO coupling, i.e., $\lambda_D = \lambda_R = 0.01$, with $g_{12} = 0.8$, $K_1 = K_2 = 1$ and $n_0 = 1$. 44
3.4 Distribution of the MI growth rate versus the interatomic coupling g for different values of the SO coupling strength when: (a) the RD SO coupling is absent, i.e., $\lambda_D = \lambda_R = 0$ and (b) in presence of the RD SO coupling, i.e., $\lambda_D = \lambda_R = 0.01$, with $g_{12} = 0.8$, $K_1 = K_2 = 1$ and $n_0 = 1$. 45
3.5 The panels show the distribution of the growth rate of MI in the $(K_1, K_2)-$plane for $\lambda_R = \lambda_D = 0$ (panels $(\text{aj})_{j=1,2,3}$) and $\lambda_R = \lambda_D \neq 0$ (panel$(\text{bj})_{j=1,2,3}$). From left to right, the columns correspond to the different cases $\beta = 0.25$, $\beta = 0.5$ and $\beta = 1$, respectively, with $g_{12} = 0.8$, $\alpha = 0.25$ and $n_0 = 1$. White regions correspond to zones of instability, while dark areas are where the CWs solutions are likely to remain stable under modulation. 46
3.6 The panels show the growth rate of MI $(\alpha, \beta)-$plane for (a) $\lambda_R = \lambda_D = 0.01$, (b) $\lambda_R = 0.01$ and $\lambda_D = 0.02$ (c) $\lambda_R = 0.01$ and $\lambda_D = 0.04$, and (d) $\lambda_R = 0.04$ and $\lambda_D = 0.04$. 46
3.7 MI evolution in both condensates with increasing time in presence of both the SO coupling and the RD SO coupling. Fixing $\alpha = 0.1$, and $\lambda_R = \lambda_D = 0.01$, panels from (a) to (d) correspond to the respective instants $t = 25$, $t = 60$, $t = 100$ and $t = 170$. The other parameters are $K_1 = K_2 = 1.5$, $n_0 = 1$, $g_{11} = g_{22} = 0.5$ and $g_{12} = 0.6$. 47
3.8 MI evolution in both condensates with increasing time in presence of both the SO coupling and the RD SO coupling. Fixing $\alpha = 0.1$, and $\lambda_R > \lambda_D$, panels from (a) to (d) correspond to the respective instants $t = 25$, $t = 60$, $t = 100$ and $t = 170$. The other parameters are $K_1 = K_2 = 1.5$, $n_0 = 1$, $g_{11} = g_{22} = 0.5$ and $g_{12} = 0.6$. 48
3.9 MI evolution in both condensates with increasing time in presence of both the SO coupling and the RD SO coupling. Fixing $\alpha = 0.1$, and $\lambda_R < \lambda_D$, panels from (a) to (d) correspond to the respective instants $t = 25$, $t = 60$, $t = 100$ and $t = 170$. The other parameters are $K_1 = K_2 = 1.5$, $n_0 = 1$, $g_{11} = g_{22} = 0.5$ and $g_{12} = 0.6$. 53
3.10 The panels show cross sections of the density profiles of Fig. 3.9 at time $t = 100$, when $y = 10$. The cases $\lambda_R = \lambda_D$, $\lambda_R > \lambda_D$ and $\lambda_R < \lambda_D$ are summarized for both condensates. The other parameters are $K_1 = K_2 = 1.5$, $n_0 = 1$, $g_{11} = g_{22} = 0.5$, $g_{12} = 0.6$ and $\alpha = 0.1$. 54

3.11 The panels show cross sections of the density profiles of Fig. 3.9 for $\alpha = 0$ (solid blue line) and $\alpha = 0.1$ (dotted yellow line). Panels $(\mathrm{aj})_{j=1,2}$, $(\mathrm{bj})_{j=1,2}$ and $(\mathrm{cj})_{j=1,2}$ respectively correspond to instants $t = 20$, $t = 50$ and $t = 100$, with $y = 5$, $\lambda_R < \lambda_D$, $K_1 = K_2 = 1.5$, $n_0 = 1$, $g_{11} = g_{22} = 0.5$ and $g_{12} = 0.6$. 55
3.12 MI evolution in both condensates with increasing time in presence of both the SO coupling and the RD SO coupling. Fixing $\alpha = 0.1$, $\beta = 0.25$, and $\lambda_R = \lambda_D = 0.01$, panels from (a) to (d) correspond to the respective instants $t = 25$, $t = 60$, $t = 100$ and $t = 170$. The other parameters are $K_1 = K_2 = 1.5$, $n_0 = 1$, $g_{11} = g_{22} = 0.5$ and $g_{12} = 0.6$. . 56
3.13 MI evolution in both condensates with increasing time in presence of both the SO coupling and the RD SO coupling. Fixing $\alpha = 0.1$, $\beta = -0.25$, and $\lambda_R = \lambda_D = 0.01$, panels from (a) to (d) correspond to the respective instants $t = 25$, $t = 60$, $t = 100$ and $t = 170$. The other parameters are $K_1 = K_2 = 1.5$, $n_0 = 1$, $g_{11} = g_{22} = 0.5$ and $g_{12} = 0.6$. . 57
3.14 The panels show cross sections of the density profiles of Figs. 3.9 and 3.13 at time $t = 100$, when $y = 10$, $\alpha = 0$ (solid blue line), $\alpha = 0.1$ (dotted yellow line) and $\lambda_R = \lambda_D = 0.1$. The other parameters are $K_1 = K_2 = 1.5$, $n_0 = 1$, $g_{11} = g_{22} = 0.5$ and $g_{12} = 0.6$. 58
3.15 MI evolution in both condensates with increasing time in presence of both the SO coupling and the RD SO coupling. Fixing $\alpha = 0.1$, $\beta = 0.25$, and $\lambda_R > \lambda_D$, panels from (a) to (d) correspond to the respective instants $t = 25$, $t = 60$, $t = 100$ and $t = 170$. The other parameters are $K_1 = K_2 = 1.5$, $n_0 = 1$, $g_{11} = g_{22} = 0.5$ and $g_{12} = 0.6$. 59
3.16 The panels show cross sections of the density profiles of Fig. 3.15 when $y = 10$, $\alpha = 0$ (solid blue line), $\alpha = 0.1$ (dotted yellow line) and $\lambda_R > \lambda_D$. Panels $(\mathrm{aj})_{j=1,2}$, $(\mathrm{bj})_{j=1,2}$ and $(\mathrm{cj})_{j=1,2}$ respectively correspond to instants $t = 20$, $t = 50$ and $t = 100$, with $K_1 = K_2 = 1.5$, $n_0 = 1$, $g_{11} = g_{22} = 0.5$, $g_{12} = 0.6$ and $\alpha = 0.1$. 60
3.17 MI evolution in both condensates with increasing time in presence of both the SO coupling and the RD SO coupling. Fixing $\alpha = 0.1$, $\beta = 0.25$, and $\lambda_R < \lambda_D$, panels from (a) to (d) correspond to the respective instants $t = 25$, $t = 60$, $t = 100$ and $t = 170$. The other parameters are $K_1 = K_2 = 1.5$, $n_0 = 1$, $g_{11} = g_{22} = 0.5$ and $g_{12} = 0.6$. 61
3.18 The panels show cross sections of the density profiles of Fig. 3.17 when $y = 10$, $\alpha = 0$ (solid blue line), $\alpha = 0.1$ (dotted yellow line) and $\lambda_R < \lambda_D$. Panels $(\mathrm{aj})_{j=1,2}$, $(\mathrm{bj})_{j=1,2}$ and $(\mathrm{cj})_{j=1,2}$ respectively correspond to instants $t = 20$, $t = 50$ and $t = 100$, with $K_1 = K_2 = 1.5$, $n_0 = 1$, $g_{11} = g_{22} = 0.5$, $g_{12} = 0.6$ and $\alpha = 0.1$. 62

LIST OF ABBREVIATIONS

SO	Spin-orbit
BECs	Bose-Einstein Condensates
CGL	Complex Ginzburg-Landau
CW	Continuous wave
GP	Gross-Pitaevskii
Li	Lithium
MI	Modulation Instability
NLS	Nonlinear Schrödinger
RD	Rashba-Dresselhaus
Rb	Ribidium
Na	Sodium
SSFM	Split-step Fourier method
2D	Two dimensional

LIST OF PUBLICATIONS

This dissertation is based on the following papers::

1. **Phelo Otlaadisa**, Conrad Bertrand Tabi, and Timoléon Crépin Kofané, *"Modulation instability in helicoidal spin-orbit coupled open Bose-Einstein condensates"*, Phys. Rev. E 103, 052206 (2021).

2. Conrad Bertrand Tabi, **Phelo Otlaadisa**, and Timoléon Crépin Kofané, *"Modulation instability of two-dimensional Bose-Einstein condensates with helicoidal and a mixture of Rashba-Dresselhaus spin-orbit couplings"*, (Submitted to Physics Letters A).

ABSTRACT

The first experimental observation of spin-orbit (SO) coupling in Bose Einstein Condensates (BECs) provided an interesting new platform to explore a fascinating and growing field of research and lead to rich physical effects. In ultracold atomic systems,the synthetic SO coupling can be generated using two counter-propagating Raman lasers that couple two hyperfine ground states. Motivated by these experimental findings, some theoretical activities have been committed to the physics of SO-coupled BECs under different conditions. In this thesis, we explore the nonlinear dynamics induced by the modulational instability (MI) in dissipative and non-dissipative SO-coupled BECs in free space. The first chapter gives the general introduction of BEC and reviews of the basics and essential concepts used throughout the thesis: the Gross-Pitaevskii (GP) equation, SO coupling, solitons and MI process.
In the second chapter, our investigations start with the derivation of a new vector form of the cubic complex Ginzburg-Landau (CGL) equation describing the dynamics of dissipative solitons in the two-component helicoidal SO coupled open BECs. Employing standard linear stability analysis, we analyze theoretically the stability of continuous-wave solutions and obtain an expression for MI gain spectrum. Using direct simulations of the Fourier space, we numerically investigate the dynamics of the MI in the presence of helicoidal SO coupling. The validity of the analytical solutions obtained is confirmed by the numerical simulations.
In the third chapter, we report the dynamics of the MI process, exclusively studied in a two-component BEC with Rashba-Dresselhaus (RD) SO and helicoidal SO couplings. A generalized set of two-dimensional GP equations are derived. The tunability of the helicoidal gauge potential is exploited to separately address BECs dynamics in free space and a square lattice. The MI growth rate is derived for each case, and parametric analyses of MI show dependence of the instability to interatomic interaction strengths, the RD SO coupling, and helicoidal SO coupling, which combines the gauge amplitude and the helicoidal gauge potential. Direct numerical simulations are performed to confirm the analytical predictions. Trains of solitons are obtained, and their behaviors are debated when the RD SO parameters are varied under different combinations between the gauge amplitude and the helicoidal gauge potential. The latter gives a potential way to manipulate the trapping capacities of the proposed BEC models.

In conclusion, the results and discussions are presented. The scope for future work has also been suggested in detail.

Keywords: Two-component BECs, Modulational instability, Solitons, helicoidal coupling, Rashba coupling, Dresselhaus coupling, Gross-Pitaevskii equation, complex Ginzburg-Landau equation, split-step Fourier method.

GENERAL INTRODUCTION

Bose-Einstein Condensate is a macroscopic quantum state of matter in which a large percentage of particles collapses into their lowest energy level at temperatures very close to absolute zero. This form of matter was first predicted by Albert Einstein in 1925, inspired by Satyendra Nath Bose's insights about the Planck law for black-body radiation [1]. Einstein extended Bose's concept to an ideal gas of identical particles whose particle number is conserved, and in the same year, predicted that at extremely low temperatures, the particles would overlap, coalescing into an indistinguishable clump, known as a Bose-Einstein condensate [2]. Even though BEC was predicted in early 1900, its experimental achievement was not possible until 1995. Eric Cornell and Carl Wieman made the first discovery of Bose-Einstein condensate at the University of Colorado and National Institute of Standards and Technology –JILA lab, from a gas of rubidium-87 (^{87}Rb) atoms cooled to 170 nano-kelvins [3]. The observation of BEC in ultracold vapors of Sodium-23 (^{23}Na) [4] and Lithium-7 (^{7}Li) [5] atoms was later reported by groups in Massachusetts Institute of Technology (MIT) and Rice University in Houston, Texas, respectively. In these recent BEC observations, the atoms were enclosed in magnetic traps and cooled down to temperatures of the order of fractions of microkelvins. The first evidence for condensation was from time-of-flight measurements. Atoms were allowed to expand by turning off the confinement trap and then imaged with optical methods. A sharp peak in the momentum distribution of condensate density, below the critical temperature, has become the standard way to identify BEC in any kind of system. BECs were later observed in a variety of systems such as chromium atoms [6,7], excitons [8], microcavity exciton-polaritons [9,10], magnons [11], spin-polarized hydrogen atoms [12], and other alkali atoms.
The dynamical features of a BEC at very low temperatures can be modeled by a nonlinear Schrodinger(NLS) equation with an external potential, known as the Gross-Pitaevskii (GP) equation [13, 14]. The results obtained by solving the GP equation showed a correlation with most of the experiments. All the nonlinear phenomena observed in matter-wave condensates can be better explained with exact analytical solutions of the GP equation [15–18]. It is well known that the matter-wave dynamics of a BEC loaded in optical lattices, which can be effectively manipulated by external field, leads to a number of BEC applications, like atomic interferometry [19], quantum phase transitions [20], matter-wave amplification [21] and atom laser [22]. BECs have since been used to explore different properties in macroscopic quantum systems, including effects of the interatomic interactions. In the case of the BECs, the interatomic interactions introduce the nonlinearity in the GP equation, accounted for through an effective mean-field. Therefore, an intrinsic feature of the BEC dynamics is its nonlinearity, which is induced by interactions between atoms, even though the densities of the quantum bosonic gases are very low. The recent establishment of trapping techniques has led to the engineering of multicomponent condensates which are formed by trapping atoms in different internal states [23, 24].

Multicomponent condensates are made up of identical atoms with contrasting hyperfine states [23, 25] or different F-spin orientations [26, 27] or atomic-molecular BECs [28]. In multicomponent systems, additional types of interaction such as interspecies interactions can occur between different components of the condensates lead to new characteristics not observable in a single condensate. Among these characteristics, we have complex phase diagrams [27, 29–31], metastable states [32], vortex

transfer dynamics [30, 33], symmetry breaking instabilities [34, 35]. Extensive theoretical and experimental investigations have followed in the two-component BECs, whose dynamics are best described by the coupled GP equations, leading to the occurrence of extraordinary nonlinear structures, such as dark-bright complexes [36, 37], dark-dark solitons [38], bright-bright solitons [39], domain walls [40], vortex-antivortex dipoles [41], and skyrmions [42]. In fact, in binary BEC, dark-bright soliton complexes were predicted in theory [43] and observed in experiments in a repulsive ^{87} Rb BEC binary mixture, using a phase imprinting method [44]. In addition, it has been also demonstrated how the phase winding dynamics can be used to generate experimentally dark-bright solitons in a two-component BEC, where the single-particle dynamics can be explained by mapping the system to a two-component Bose-Hubbard model [45]. Most recently, multiple dark-bright solitons [36], as well as dark-dark solitons [37] were also created in a counterflow experiment [36]. The structure and the odd-even effect of the yrast spectrum in the two-component BEC has been studied using an analytical method [46].

One of the key issues of soliton wave theory is the universal MI phenomena, which is one of the most fundamental processes in nonlinear wave systems in nature. Modulation instability, is a ubiquitous mechanism for understanding the growth of a weakly modulated continuous wave in a nonlinear medium and leading to the generation of a train of pulses under the combined effects of nonlinearity and diffraction or dispersion in a spatially nonlinear field. Generally, MI occurs in the same regions of parameters as to where bright solitons are observed, and can be considered to initialize the formation of stable localized nonlinear excitations, or soliton trains, and is deeply studied in nonlinear optics [47], plasma physics [48], hydrodynamics [49], electrical transmission lines [50], biophysics [51, 52]. In the context of BEC, investigations show that the MI has been responsible for the dephasing and the localization of the condensate, which is vital in understanding the dynamic processes in the BEC systems, which include domain formation [53], generation and propagation of solitonic waves [54], quantum phase transitions [55], and so on. Moreover, there has been extensive research on the MI in BECs both experimentally and theoretically for single as well as two-component systems [56–65].

As in other physical systems [66], it was concluded that the single-component MI is feasible only for attractive interactions [67], and in such cases, the phase fluctuations caused by the MI leads to the formation of soliton trains [67]. However, the breakthrough work by Goldstein and Meystre [68] opens up the possibility of MI even for repulsive interactions in two-component BECs [53], similar to the result known in nonlinear optics [69], in the case when the cross-phase modulation is stronger than the self-phase modulation of each component. In such a case, the MI does not create trains of bright solitons, but rather creates domain walls that realize the phase separation in the immiscible binary BEC [70]. In addition, due to the production of the SO coupling in BEC, the dynamical instability of supercurrents, as a consequence of the violation of the Galilean invariance, was investigated [71, 72]. In particular, one may expect that the MI will lead to the generation of striped structures which realize the ground state in the SO-coupled BEC with the repulsive or attractive intrinsic nonlinearity. While the MI of two-component BECs with SO coupling in one- and two-dimension were recently explored [73, 74].

THESIS OUTLINE

- General objective:
  - To study the evolution of modulation instability phenomena and solitary structures, emerging from dissipative and non-dissipative SO-coupled BECs.
- Specific objectives:
  - To derive a new vector form cubic CGL equations describing the behavior of dissipative soliton trains in two-component helicoidal SO coupled open BECs.
  - Evaluate the effects of the repulsive and attractive intra-component, and inter-component interactions in two-component SO coupled open BECs based on the new vector form cubic CGL equations.
  - Evaluate the behaviors of the growth rate spectra under the combined effects of Rashba-Dresselhaus and helicoidal SO couplings.

This thesis is outlined as follows:

In Chapter 1, we give a detailed introduction to the model and phenomena that are studied in this thesis.

The second chapter describes the 1D coupled GP equations for the two-component helicoidal SO coupled dissipative BECs, from which the coupled cubic CGL equations are derived using the adiabatic elimination procedure. The stability of the condensate has been analyzed in detail for the system parameters such as SO coupling strength, helicoidal potential, intra-atomic and inter-atomic interactions. The analytical results of MI of plane wave solutions of the coupled cubic CGL equations obtained with the help of linear stability analysis have been confirmed numerically by direct simulation of the governing equation using the split-step Fourier method(SSFM).

In Chapter 3, we introduce the energy functional and derive a 2D coupled GP equation system which includes RD SO and helical SO couplings. We also show that the tunability of the helicoidal gauge potential allows the derivation of two distinct sets of GP equation systems, describing BECs in free space and in a square lattice, respectively. The analytical study of the linear stability analysis of CWs is addressed, where an analytical expression of the growth rates of MI is obtained, based on which the regions of instability are parametrically discussed. Some numerical simulations are presented, where predictions from the linear stability analysis are verified. One particularly insists on solitary wave formation in the condensates under the activation of MI, emphasizing the combined effects of a mixture of RD SO couplings and different combinations of the helicoidal gauge potential and the gauge amplitude.

Finally, we present a general conclusion and perspective for this general research topic.

Chapter 1

BOSE-EINSTEIN CONDENSATION (BEC) BASICS

1.1 Introduction

This chapter briefly examines the theory of Bose-Einstein condensation in ultracold gases. Starting with the non-interacting Bose-gas, we describe the quantum phase transition and identify its critical temperature T_c. We also discuss the GP equation which models the dynamics of BECs at ultra temperatures and give the experimental procedure for the production of BECs at the laboratories. Spin-orbit coupling, solitons, and modulation instability in BECs are also explained.

1.2 Identical particles

In classical mechanics, identical particles could be labeled solely based on their position and momentum coordinates at any given time. When these particles are observed during a collision, one can track each particle's trajectory and thus identify them at the end of the collision process. Conversely, in quantum mechanics, particles no longer have explicit trajectories. They lose their identity during collisions i.e. they start behaving more like waves and less like particles and begin to overlap. The resulting axiom is that all observables have to be invariant under the exchange of any two identical particles [75]. The particles are then said to be indistinguishable. At this point, the particles are governed by the wave function $\Psi(r,\, t)$, which gives the probability of finding a particle at position r in space-time t. The indistinguishability of particles introduce a complex phase rotation to the many-body wave function (where particles are labeled by their position r and spin α) as

$$\Psi...,\alpha_x,...,\alpha_y\ ,...(...,r_x,...,r_y,...,t) = e^{i\theta}\Psi...,\alpha_y,...,\alpha_x\ ,...(...,r_y,...,r_x,...,t). \tag{1.1}$$

When the complex phase, $e^{i\theta} = +1$, it gives symmetric wave functions with respect to the label exchange. This corresponds to one of the two major classes of identical particles: bosons, which share quantum states and have a whole number spin. If the complex phase, $e^{i\theta} = -1$, the wave function is anti-symmetric, meaning that particles under observation are fermions. Thus, no sharing of quantum states as described by Pauli's exclusion principle is observed and those fermions have half-integer spin. These symmetric properties of the wave function have some striking effects on the behavior of the particles.

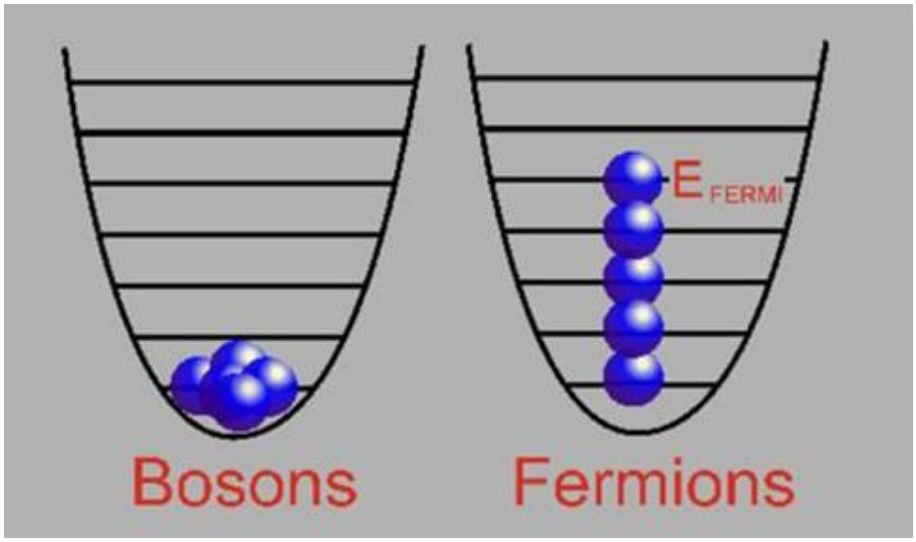


Figure 1.1: Distribution of elementary particles (bosons and fermions) in the quantum states [76].

1.3 Bose-Einstein condensation in an ideal gas

We consider a gas of N non-interacting bosons with mass m in a box of volume V at thermal equilibrium T. The average occupation number of particles in a single quantum level k follows the Bose–Einstein distribution [13, 14]

$$f(\mathcal{E}_i) = \frac{1}{e^{\beta(\mathcal{E}_i-\mu)} - 1}, \tag{1.2}$$

where $\beta = \dfrac{1}{k_B T}$, k_B is the Boltzmann's constant, $\mathcal{E}_i$ is the energy of a single-particle state i, and μ is the chemical potential, accounting for the energy needed to add a particle to the system at a constant volume and entropy. It is determined from the condition

$$\sum_i f(\mathcal{E}_i) = N, \tag{1.3}$$

where N is the total number of bosons in the system. Assuming that f is an infinitesimal function of the total energy $\mathcal{E}$, we can approximate the summation of Eq. (1.3) by an integral

$$N = \int g(\mathcal{E}) f(\mathcal{E}) d\mathcal{E}, \tag{1.4}$$

where $g(\mathcal{E})$ is the density of states of the system, representing the number of quantum levels in the range $[\mathcal{E}, \mathcal{E} + d\mathcal{E}]$.
From Eq. (1.2), we can deduce that the chemical potential should be less than the single particle ground state energy $\mathcal{E}_0$, otherwise this state would have a negative occupation number. When the μ approaches $\mathcal{E}_0$ from smaller values, the ground state population N_0 increases macroscopically, forming a BEC. The total number of particles can then be written as

$$N = N_0 + \int g(\mathcal{E}) f(\mathcal{E}) d\mathcal{E}. \tag{1.5}$$

For a uniform d-dimensional system with a size L the energy density of states for a free particle with a mass m, is given by [77]

$$g^{(d)}(\mathcal{E}) = \Omega_d \left(\frac{L}{2\pi}\right)^d \frac{1}{2}\left(\frac{2m}{\hbar^2}\right)^{\frac{d}{2}} \mathcal{E}^{\frac{d}{2}-1}, \tag{1.6}$$

where

$$\Omega_d = \begin{cases} 4\pi & (d=3) \\ 2\pi & (d=2) \\ 1 & (d=1). \end{cases}$$

Assuming our system is in 3D, the density of states simplifies to

$$g^{(3)}(\mathcal{E}) = \frac{V}{4\pi^2}\left(\frac{2m}{\hbar^2}\right)^{\frac{3}{2}} \sqrt{\mathcal{E}}. \tag{1.7}$$

Substituting Eq. (1.7) into Eq. (1.5), we get

$$N = N_0 + \frac{V}{4\pi^2}\left(\frac{2m}{\hbar^2}\right)^{\frac{3}{2}} \int_0^\infty \sqrt{\mathcal{E}} \frac{d\mathcal{E}}{e^{\beta(\mathcal{E}_i-\mu)}-1}, \tag{1.8}$$

with the second term being the number of particles in the excited states N^{ex}. It represents the thermal component of gas at temperature T and chemical potential μ. For a finite temperature T and a large volume V, N^{ex} has a smooth behavior as a function of μ and reaches its maximum asymptotically at $\mu = \epsilon_0 = 0$. If we evaluate the integral in Eq. (1.8), we obtain

$$N^{\text{ex}}_{\text{max}} = V\left(\frac{mK_BT}{2\pi\hbar^2}\right)^{\frac{3}{2}} \zeta\left(\frac{3}{2}\right), \tag{1.9}$$

where $\zeta\left(\frac{3}{2}\right) \approx 2.612$ is the Riemann zeta function [77].
If $N^{\text{ex}}_{\text{max}} < N$, the system exhibits BEC. As the system is cooled, there will be a critical temperature T_C (step by step derivation shown in appendix A), at which $N^{\text{ex}}_{\text{max}} = N$, given by

$$T_C = \left(\frac{2\pi\hbar^2}{mK_B}\right)\left(\frac{N}{2.612V}\right)^{\frac{2}{3}}. \tag{1.10}$$

Let

$$n = \frac{N}{V} = 2.612\frac{1}{\lambda^3_{T_C}}, \tag{1.11}$$

with $\lambda_{T_C} = \sqrt{\dfrac{2\pi\hbar^2}{mK_BT_C}}$ being the thermal de Broglie wavelength. This means, below the critical temperature, the thermal de Broglie wavelength is comparable to the mean interparticle distance $n^{-\frac{1}{3}}$ (n is the particle density). The onset of BEC becomes

$$n\lambda^3_{T_C} \leq 2.612, \tag{1.12}$$

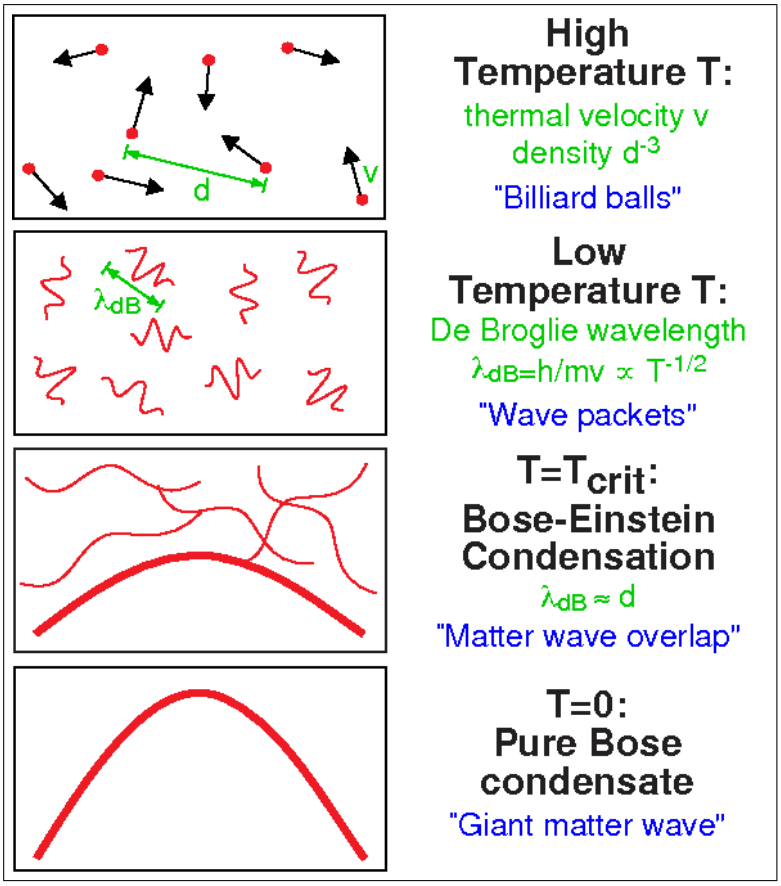


Figure 1.2: Formation of BEC [79]

i.e. the condensation takes place when the de Broglie wave packets of the particles begin to overlap significantly. To determine the variation of the condensate with the temperature we take the ratio of Eq. (1.8) and Eq. (1.9)

$$\frac{N_0}{N} = 1 - \left(\frac{T}{T_C}\right)^{\frac{3}{2}}. \tag{1.13}$$

Figure 1.2 shows the evolution of the condensate at temperature T.

1.4 The Gross-Pitaevskii (GP) equation

1.4.1 Single-component systems

BEC was firstly studied for non-interacting bosons, for which the many-body wave function is a product of single-particle wave functions. But the real bosonic atoms interact with each other, and the presence of interactions between the atoms depletes the condensate fraction. The elementary model that best describes BEC in an interacting Bose gas is based on the Bogoliubov approximation of lowest-order mean-field theory and second quantization [80]. According to this approach, the dynamical behavior of a BEC at very low temperatures is best described by a nonlinear Schrödinger equation

with an external potential, the Gross-Pitaevskii(GP) equation [13, 14]

$$i\hbar\frac{\partial\psi(r,t)}{\partial t} = -\frac{\hbar^2}{2m}\nabla^2\psi(r,t) + U(r,t)\psi(r,t) + \frac{4\pi\hbar}{m}a_s(r,t)|\psi(r,t)|^2\psi(r,t), \qquad (1.14)$$

where $\psi(r,t)$ is a wave function for a single-particle, $r = (x,y,z)$ and t represent spatial and temporal coordinates respectively, m is the atomic mass, $U(r,t)$ is the external potential that acts on the individual atoms, ∇^2 is the Laplace operator with respect to r, and a_s is the scattering wavelength which determines the strength of collisions between the atoms: $a_s > 0$ and $a_s < 0$ correspond to repulsive and attractive interactions, respectively. The strength and sign of a_s in BEC experiments can be modified by the Feshbach resonance management technique [81]. Moreover, the wave function is subject to the normalization condition, which is determined by the total number, N, of atoms in the condensate:

$$\int |\psi(r,t)|^2 dr = N. \qquad (1.15)$$

In the mean-field approximation, the interatomic collisions of BECs in the GP equation are taken into account through the cubic term. Therefore, an intrinsic feature of BEC dynamics is its nonlinearity, which is due to interactions between atoms. This nonlinearity has resulted in the observation of many important excitations in the BECs such as dark solitons [82], representing holes in the otherwise homogeneous atomic distributions, bright solitons [82], characterized by a spatially localized atomic density distribution, compactons [83], and nonlinear periodic waves [84]. In addition, gray solitons [85], gap matter solitons [86], vortices [33], vortex lattices [87], Faraday waves [88], Bloch oscillations of BECs, Landau-Zener tunneling [89], superfluid to Mott-insulator phase transition [90], and compression of a condensate [91], have been observed theoretically as well as experimentally.

1.4.2 Two-component systems

Experimental implementation of single-component BECs led to advances in trapping techniques, allowing atomic clouds to be simultaneously confined to different hyperfine spin states, thus forming a multi-component BEC. The first such experiment was performed in a mixture of two magnetically trapped hyperfine states of ^{87}Rb [23], the *pseudo-spinor* condensates. Subsequently, experiments in optically trapped ^{23}Na [24], were able to produce multi-component condensates for varying Zeeman sublevels of the same hyperfine level, the *spinor* condensates. Regarding the modeling of multi-component BECs, we proceed from the single-component GP equation to the corresponding system of coupled GP equations

$$i\hbar\frac{\partial}{\partial t}\psi_i(r,t) = -\frac{\hbar^2}{2m_i}\nabla^2\psi_i(r,t) + U_i(r,t)\psi_i(r,t) + (g_{ii}|\psi_i(r,t)|^2 + g_{ij}|\psi_j(r,t)|^2)\psi_i(r,t). \qquad (1.16)$$

Here, $\psi_i(r,t), i = 1,2$ represents the BEC wave functions of the two components, for which we can define densities $n_i = |\psi_i(r,t)|^2$ analogous to the single component case. The interaction parameters g_{ii} and g_{ij} are proportional to the scattering length for intra- (g_{11}, g_{22}) and inter-component (g_{12},g_{21}) interactions respectively: $g_{ii} = 4\pi\hbar a_s^{(ii)}/m_i$ and $g_{ij} = g_{ji} = 4\pi\hbar a_s^{(ij)}/m_i$, $j = 1,2$. The trapping potentials $U_i(r,t)$ are

induced by the same external field and may be different. Masses are different for BEC mixtures made of different atoms and equal for mixtures of the same atomic species. When the interactions are repulsive, the scattering lengths in Eq. (1.16) are positive, that is, $a_s^{(11)} > 0$, $a_s^{(22)} > 0$, and $a_s^{(12)} > 0$. The immiscibility condition of the two components and the onset of the separation between them is given by [92]

$$a_s^{(11)} a_s^{(22)} < (a_s^{(12)})^2. \tag{1.17}$$

This indicates that the repulsion between atoms in the mixture is stronger than the repulsion in each constituent atom. Condition (1.17) relates to infinite space, while the pressure of the trapping potential makes the binary BEC more miscible and shifts the critical point, $a_s^{(11)} a_s^{(22)} = (a_s^{(12)})^2$ to bigger values of positive $a_s^{(12)}$ [93]. Immiscible two-component condensates, in a trap, form domain walls separating the two components [94]. Such domain walls were observed in experiments [95]. Those binary mixtures of BECs may contain two different hyperfine states of identical atoms, such as ^{87}Rb [23,25] and ^{23}Na [26], or can be created in a heteronuclear mixture of ^{41}K and ^{87}Rb [96, 97], Na–Rb [32, 98], Cs–Rb [99], Li–Rb [100], ^{41}K–^{87}Rb [97], ^{7}Li and ^{133}Cs [101]. Besides BEC, GP equation can also be used in modeling of nonlinear optics, superconductors, and super fluids [102].

1.5 BEC experimental procedure

Here, we discuss the steps involved in the formation of a BEC in the laboratory. There are three important steps involved: laser cooling, magnetic trapping, and evaporative cooling. There are particular details which differ between experiments, but they follow a similar outline.

1.5.1 Laser cooling

The idea of laser cooling was separately proposed in 1975 by Theodor W. Hansch and Arthur L. Schawlow of Stanford University for gas of atoms and by David Wineland and Hans G. Dehmelt of the University of Washington for trapped ions [103]. Laser cooling is a technique where particles are cooled down by decreasing their speed using laser light [104]. Atoms are initially laser-cooled using six laser beams arranged as three orthogonal pairs of counter-propagating beams. The atoms absorb the photons from the beams and jump up to higher energy levels. When the photons are emitted from the atoms, they gain momentum, producing a speed reduction. On the contrary, the absorption of photons produces acceleration in the atoms. This means there is no gain in momentum in the spontaneous emission process. Here, is where the Doppler effect is used. The laser frequency is adjusted such that only the atoms, moving towards the laser beam see the blue shift and are partially absorbed. This cooled down the atom and therefore decreasing the temperature of the atomic cloud. The laser cooling mechanism stops when the velocity gains by atoms, as it emits a photon, compensates for the loss of velocity due to the scattering process. There are many other techniques that can be used for laser cooling, such as the gray molasses, cavity meditated cooling and the Zeeman slower, just to name a few.

1.5.2 Magnetic trapping

Though laser cooling can bring the atomic sample to very low temperatures, atoms can escape out of the laser regions due to random motions, after pre-cooling, atoms are transmitted into a magneto-optical trap. The trap combines with optical molasses (3D laser cooling), with an appropriate external magnetic field which induces a spatial force that pushes back atoms to the middle of the trapping potential. This process enables to maintain atoms in the external trap. There are different trapping potentials that can be realized to produce BECs.

1.5.3 Evaporative cooling

This is the last step in BEC. In evaporative cooling, energetic particles are allowed to leave the trap, carrying away more than their share of thermal energy, hence decreasing the temperature of the system. This allows the atomic sample to be cooled by many orders of magnitude, mitigating the loss of atoms by an overall increase in phase space density.

1.6 Spin-orbit (SO) coupling in BECs

One of the major motivations for this research is the study of spin-orbit coupling. SO coupling leads to many interesting concepts in a broad range of quantum systems from nuclear physics, condensed matter physics to atomic physics. For instance, in condensed matter systems, SO coupling can lead to quantum spin Hall states or topological insulators, which have potential applications in quantum devices. Recently, SO coupling has been artificially created in ultracold dilute atomic Bose and Fermi gases with the aid of synthetic gauge fields. SO coupling have been proved to be an ideal process for examining the relationship between quantum many-body systems under Abelian and non-Abelian gauge fields in ultracold gases. In this section we give a general introduction of SO coupling.

1.6.1 SO coupling in one-dimensional (1D) ultracold atoms

SO coupling is an interaction of particles that depends on the values and mutual orientations of the particles' orbital and spin angular momenta, and that leads to the fine-structure splitting of the system's energy levels. SO coupling is a relativistic effect. Formally, it is obtained if the energy of particles, moving rapidly in an external field is found with an accuracy of v^2/c^2, where v is the speed of the particle and c is the speed of light [105]. The SO effect happens naturally in a hydrogen atom. To understand this, we can imagine a semiclassical atom with an electron in a quantized orbit. We consider the frame of reference where the electron is stationary, that is, the frame of reference moves with the electron. In such a case, the nucleus will appear as orbiting the electron, and it will produce a positive current loop, that, in turn, creates a magnetic field $\overrightarrow{B}$. The electron has an intrinsic angular momentum, or spin, which creates the electron's spin magnetic moment $\overrightarrow{\mu_s}$. This means that the $\overrightarrow{\mu_s}$ will feel a torque due to the $\overrightarrow{B}$, created by the orbit of the nucleus. This torque will tend to rotate the magnetic moment and thus change the energy of the electron: $\Delta H = -\overrightarrow{\mu_s}.\overrightarrow{B}$. The energy difference between the states is the splitting in the spectral lines. To see how the

orbital and spin angular momentum interact, we need to relate the effective magnetic field to the motion of the electron. The orbital angular momentum of the electron in a semi-classical sense gives the orbiting speed of the electron and thus the strength of the effective magnetic field. This is how the orbital angular momentum and the spin of the electron become coupled together, by the Zeeman splitting from the effective magnetic field [106]

$$\Delta H_L = \frac{g_s \mu_B}{\hbar m_e e c^2} \frac{1}{r} \frac{\partial U(r)}{\partial r} \overrightarrow{L} \cdot \overrightarrow{S}, \tag{1.18}$$

where $g_s \approx 2$ is the electron-spin g-factor, μ_B is the Bohr magneton, $\hbar$ the Planck's constant, m_e electron mass, U the potential energy of the electron, and e the elementary charge. $\overrightarrow{S}$ represents the spin angular-momentum vector, while $\overrightarrow{L} = \overrightarrow{r} \times \overrightarrow{p}$ is the angular momentum of a particle, with $\overrightarrow{r}$ being the particle's position vector and its momentum vector $\overrightarrow{p}$.

Implementation of the interaction which includes both spin and motional degrees of freedom is interesting by itself, as it allows access to new quantum phases which define different orderings of the SO coupled system and different macroscopic behaviors [107].The idea of SO coupling is very general and can refer to many situations from different fields of physics: from the fine and hyperfine splitting in atomic and nuclear physics [108–110], to topological insulators and quantum spin Hall effect in condensed matter physics [111, 112], or Rashba [113, 114] and Dresselhaus [115] SO interactions in semiconductors.

1.6.2 Synthetic SO coupling in cold atoms

Ultracold gases are versatile playgrounds to realize, explore, and discover various physical models and phenomena, but usually have a neutral charge. However, magnetic phenomena are of a particular interest in quantum mechanics. They appear, for example, in spin Hall effects [116, 117], SO coupling [114, 115], Aharonov-Bohm effect, Hofstadter butterfly physics, and topological insulators [118–120], when a charged particle interacts with a magnetic field. To better understand these effects, in situations where particle statistics and interactions are important, synthetic gauge fields are used to investigate the coupling of electromagnetic fields with neutrally charged particles. Synthetic gauge fields couple an atom's internal degree of freedom with an external degree of freedom, and use external control of the spin state to control the dressed quasi-momentum energy minimum. In non-relativistic quantum mechanics, the SO coupling is induced from the non-relativistic limit of the Dirac equation. It emerges as a magnetic field seen by the moving electron (Lorentz transform of electromagnetic field) coupling the spin in dipole form (to the leading order of non-relativistic limit). The magnetic field depends on the motion of the electron. If we study the motion in terms of Hamiltonian formalism, the electromagnetic coupling enters through vector potential A and scalar potential V. If A is constant, $\overrightarrow{B} = \nabla \times A = 0$, therefore no SO coupling is present. This feature is no longer valid in non-Abelian cases. Even if A is constant, $\overrightarrow{B} = \nabla \times A + \frac{1}{i\hbar} A \times A = \frac{1}{i\hbar} A \times A$ does not vanish in general. For neutral atoms, coupling between the motional degree of freedom and atom's spin does not happen naturally like for charged particles. However, the effective SO coupling can be emulated with the help of external fields. This led to many experimental pursuits, aiming to engineer SO coupled systems with ultracold atomic set-ups. The first step in that direction was done by Spielman's group [121]. They engineered a SO coupling

in a neutral BEC by dressing two atomic hyperfine states with a pair of propagating lasers. After that, in 2012, SO coupled Fermi gases were produced using a pair of Raman beams [122, 123].

1.7 Solitons in BECs

Nonlinear models are widely used in the scientific community to understand the fundamentals of nature. There are so many nonlinear models which have been developed thus far. In physics, the most celebrated NLS equation manifests in optical fibres [124–126] and with an appropriate potential as a GP equation in BECs [13]. The Korteweg and deVries (KdV), sine-Gordon and Boussinesq equations routinely appear in hydrodynamics and plasma physics [128]. The integrability of these equations leads to extremely interesting properties for their soliton solutions. Solitons can be observed in space and time as localized wave-packets or pulse trains which results from the balance between dispersion and nonlinearity. Solitary waves were first described in a water channel by John Scott Russell in 1845 [129, 130] and 1895, Korteweg and de-Vries derived the first mathematical equation for solitons, the so-called KdV equation, which describes wave propagation in shallow water channels [131]. Through theoretical predictions and their subsequent experimental corroborations, solitons have been observed in different fields such as fluid mechanics [132, 133], plasma physics [132, 134], nonlinear optics [126, 135, 136] and BECs [137]. As mentioned in Sec. 1.4, the GP equation has become a fundamental theoretical tool in describing the dynamics of BECs. The GP equation is a nonlinear equation with counteractive dispersion and nonlinear terms, which gives rise to topological excitations known as matter-wave solitons. In this section, we describe the two forms of matter-wave solitons in BECs, the bright solitons, and dark solitons (fig. 1.3). The form of solitons in BEC is de-

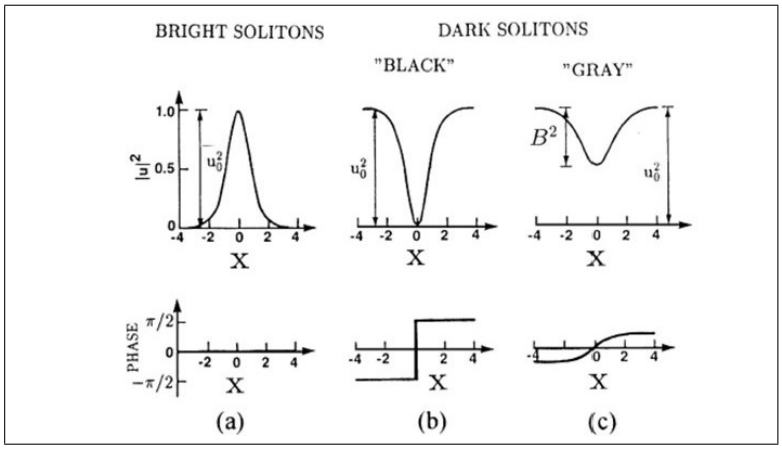


Figure 1.3: Bright solitons and dark solitons in BEC [138].

termined by the sign of the scattering length a_s [127]. If a_s is negative, solitons are characterized by a peak in associated wave amplitude. These solitons are known as bright solitons [139–141]. In the atomic BEC with intrinsic self-attraction, the production of one-dimensional matter-wave bright solitons in cigar-shaped configurations was achieved in condensates of ^{7}Li [142–144] and ^{85}Rb [145, 146]. Collisions between moving quasi-1D solitons also admit accurate experimental implementation [147] and theoretical analysis [147,148]. The positive a_s, gives the BEC the effective self-repulsive

nonlinearity. This type of the inherent interaction gives rise to dark solitons identified by a minimum local density, and a sharp phase slope of the wavefunction at the position of the minimum [149–151]. The dark matter-wave solitons are further categorized into black solitons and gray solitons. The black solitons occur when the local density minimum of dark soliton is zero, while, gray soliton appears at the local density minimum of dark soliton greater than zero [152–154]. Dark matter-wave solitons have been observed in a ^{23}Na condensate [155] and in cigar-shaped ^{87}Rb [155–157]. The dynamics of single-soliton states [155,156], and multiple dark solitons [137,158,159] have been investigated, both experimentally and theoretically. Later, stable dark-bright soliton complexes in binary BEC were predicted in theory [36] and observed in experiments [160,161] as well. In more recent works, multiple dark-bright solitons [37,162], as well as dark-dark solitons [163,164] were also experimentally created. In addition, in the same setting of the self-repulsive nonlinearity, not only dark solitons but also bright solitons are possible too, in particular, if, instead of the usual parabolic trap, a periodic (optical lattice) potential [165] is used to confine the condensate, then gap solitons can be formed.

1.8 Modulational instability phenomenon in BECs

MI is one of the most ubiquitous processes that is observed in most nonlinear physical systems. The effect of MI is the result of interaction between a strong carrier harmonic wave at a frequency ω and small sidebands $\omega \pm \Omega$ [166]. The generation of the sidebands in the spectrum is due to weak perturbation to a waveform (fig. 1.4), imposed by nonlinearity and dispersive effects as a result, the continuous wave disintegrates during propagation [167–169], giving rise to a train of spatially or temporally separated solitary waves [167–171].

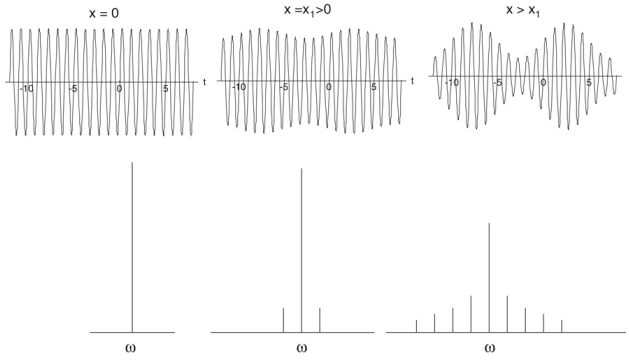


Figure 1.4: Evolution of a nonlinear wave train in the course of MI. Bottom: the corresponding evolution of wave spectrum [166].

MI was realized in numerous physical situations including water wave hydrodynamics, electrodynamics, nonlinear optics, plasma, and convection theory. It is a coherent medium for studying some other nonlinear phenomena such as envelope solitons [172–178], envelope shocks [179], and freak (or rogue) waves [180, 181]. This approach is essentially a linear stability analysis of the stationary CW solution to the NLS equation. The linearized equation for the perturbation is valid only when the perturbation is weak. The CW solution of the NLS equation becomes unstable towards the generation of a chain of bright solitons. In the same way, the train of BEC

bright matter-wave solitons can be generated in the context of BEC described by GP equation, under certain conditions of MI [182, 183]. Thus, the MI process deals with the stability of the CW solution and pattern formation in a system of BECs [184, 185].

1.9 Summary

We have dealt with generalities on BECs in this chapter. At first, we have described both non-interacting and interacting particles boson gases. We have presented an overview of experimental procedures that lead to the observation of BECs. We also described the soliton formation, spin-orbit coupling, and modulation instability in BECs, which will be studied in detail in the next chapter.

Chapter 2

MODULATION INSTABILITY PROCESS IN HELICOIDAL SPIN-ORBIT COUPLED OPEN BOSE-EINSTEIN CONDENSATES

2.1 Introduction

In many cold atom experiments, the condensates are confined in harmonic traps without external disturbances. Therefore, the center of mass of the system swings around the midpoint of the trap in simple harmonic motion without dissipation. Such systems are said to be isolated quantum systems. In isolated systems, the dynamics of the system are completely independent of those of the environment. Thus, the observables associated with this system, at its creation, remain conserved over the evolution of the system. In any quantum system, there is a membrane or a boundary separating the system from its surroundings. For closed systems, this boundary is impermeable, which means there is no information exchange between the system and the environment. However, in quantum mechanics, the narrative of closed systems seems to be an approximation. In reality, quantum systems must be considered as open systems, since any microscopic system is subject to interactions with many external factors. This coupling has little or no effect on the system, and can lead to energy dissipation or quantum decoherence in the system, hence the need for a simple system best describing the evolution of the system and environment. In open systems, the boundary is no longer impermeable, and thus, there is free flow of information between the system and the environment. These systems are referred to as dissipative. Dissipative systems are most common in nature and are nowadays attracting a great deal of attention in nonlinear medium studies. Very recently, monitored dissipation has proven to be a useful tool for probing quantum systems in ultra-cold setup [186]. Moreover, dissipation has been manipulated as a measurement tool for examining quantum effects in ultra-cold atoms and various other systems [187]. Dissipation is used as a ubiquitous mechanism in quantum state preparation [188, 189], entanglement generation [190], and quantum information processing [191]. BECs behave quite differently when in contact with an external environment (reservoir). When in contact with a reservoir, BEC is subject to particle and heat exchange. The reservoir can be made of a thermal bath or non-condensate atoms. Therefore, in such open BEC systems, atom losses and

dissipation are unavoidable phenomena when interactions between the condensed and uncondensed atoms are taken into account, which significantly affect the dynamics of the system. The linear coupling between the reservoir and condensate atoms inside the traps corresponds to the energy exchange between the system and reservoir through the creation and absorption of bath quanta or condensate atoms in the traps. While, in the system, dissipation is induced by the reservoir fluctuation in agreement with the fluctuation-dissipation theorem [192]. The dissipation is balanced by a transfer from the uncondensed trapped atoms into the condensate atoms. Those on their turn are refilled by continuous pumping processes [193]. In the meantime, dissipation in a double-well BEC coupled to a thermal bath was found to cause macroscopic quantum self-trapping state to decay away [194].

In addition to that localized particle, dissipation was also found to restore BEC coherence [195]. Furthermore, the real-time dynamics of open quantum spin-1/2 or hardcore boson systems on a spatial lattice, described by a Markovian quantum master equation has also been investigated [196]. On the other hand, experimentally, grand canonical conditions in the condensed phase have been realized in a photon BEC coupled to a dyeing medium [197], where thermalization of the photon gas is achieved by absorption and re-emission processes on dye molecules [198].

In this chapter, we investigate analytically and numerically the MI phenomena and solitary structures, emerging from SO coupled dissipative BEC. In general, the self-modulation of waves in the BEC dynamics in an atomic trap are governed by the GP equation [199]. Moreover, in the case of SO coupled to the dissipative BECs, an atomic BEC is attached to a source of uncondensed atoms and a sink. It has been shown that the idealized description in terms of a GP equation breaks down for this dissipative dynamics of open BECs [200].

2.2 Theoretical model of an open two-component BECs in 1D

In this section, we start with describing a single-particle Hamiltonian of an inhomogeneous 1D two-component BECs. Then, a coupled GP equations describing the evolution of the condensate wave functions of the two-component helicoidal SO-coupled BECs evenly distributed between the two pseudospin states is defined. We add dissipative terms to the coupled GP equations and coupled the resulting equations with rate equation coupling between condensed and uncondensed atoms. Consequently, we apply an adiabatic elimination procedure and show that the two-component helicoidal SO-coupled dissipative BECs obeys coupled cubic CGL equations in a complex field.

2.2.1 A system of two-coupled 1D cubic GP equations

We consider a 1D inhomogeneous spatial two-component BECs with helicoidal SO coupling. The single-particle Hamiltonian H_0 of the system takes the form [201]

$$H_0 = \frac{[p + \alpha \mathbf{A}(x)]^2}{2} + \frac{\Delta \sigma_z}{2}, \tag{2.1}$$

where $p = -i\partial/\partial x$ is the linear momentum operator, $\mathbf{A}(x)$ is the gauge potential varying space, α is the potential amplitude, Δ is the Zeeman splitting, and we choose

the units such that $m = \hbar = 1$. The Hamiltonian contains the Pauli spin matrix

$$\sigma_z = \begin{pmatrix} 1 & 0 \\ 0 & -1 \end{pmatrix}. \tag{2.2}$$

If we consider the intra-atomic and inter-atomic interactions in the BECs, in the Hartree approximation, then the dimensionless GP equation describing a spinor order parameter $\mathbf{\Psi} = (\mathbf{\Psi_1}, \mathbf{\Psi_2})^{\mathbf{T}}$ (T stands for the transpose) solves the GP equation

$$i\frac{\partial \mathbf{\Psi}}{\partial t} = \frac{1}{2}\left[\frac{1}{i}\frac{\partial}{\partial x} + \alpha A(x)\right]^2 \mathbf{\Psi} + \frac{\Delta\sigma_3}{2}\mathbf{\Psi} + G\mathbf{\Psi}, \tag{2.3}$$

where the spatial variable x, time t, density $|\mathbf{\Psi}|^{\mathbf{2}}$, and energy are expressed in normalized units $a_\perp$, $w_\perp^{-1}$, $a_\perp^{-1}$, and $\hbar w_\perp$, respectively. $G = \mathrm{diag}(g_1|\psi_1|^2 + g_{12}|\psi_2|^2, g_2|\psi_2|^2 + g_{12}|\psi_1|^2)$ indicates the strengths of the two-body intraspecie interactions $g_{11} = 2a_{11}/a_\perp$, $g_{22} = 2a_{22}/a_\perp$ and the strength of the two-body inter-species interactions $g_{12} = 2a_{12}/a_\perp$ and $g_{21} = 2a_{21}/a_\perp$. Here $a_\perp = \sqrt{\hbar/(mw_\perp)}$, is the transverse characteristic length, $w_\perp$ is the transverse trap frequency, m is the atomic mass, and $\hbar$ is the Planck constant. Finally, the a_{11}, a_{22}, and a_{12} are the s-wave scattering lengths that can be adjusted by optical [202], and magnetic [203] Feshbach resonance techniques in the experiment. The strength of SO coupling can be controlled experimentally using different techniques is considered to be helicoidal with the period π/β, i.e. $\mathbf{A}(x) = \sigma\mathbf{n}(x)$, where $\mathbf{n}(x) = (\cos(2\beta x), \sin(2\beta x), 0)$ and $\sigma = (\sigma_1, \sigma_2, \sigma_3)$. β is the frequency of rotation, the positive and negative values of β are defined for the right-handed mode and left-handed mode, respectively [204–206].

The point translational symmetry of the helicoidal structure of the vector potential which shifts by the period π/β, is converted to a continuous translational symmetry by switching the rotating frame for the gauge field $A(x)$ using gauge transformation [201]

$$\Psi = e^{-i(\alpha^2+\beta^2)t/2} e^{-i\sigma_3\beta x}\Psi. \tag{2.4}$$

Then, the point translation symmetry of Eq. (2.3) becomes a continuous translational symmetry of the condensate wave functions of a closed two-component helicoidal SO-coupled BECs equally distributed between the two pseudospin states, loaded in a 1D setting. In the mean-field theory, the macroscopic wave functions of such a system obey the following coupled 1D cubic GP equations in the absence of an external trapping potential term [207]

$$i\frac{\partial\psi_1}{\partial t} = -\frac{1}{2}\frac{\partial^2\psi_1}{\partial x^2} + i\beta\frac{\partial\psi_1}{\partial x} - i\alpha\frac{\partial\psi_2}{\partial x} + \frac{\Delta}{2}\psi_1 + \left(g_{11}|\psi_1|^2 + g_{12}|\psi_2|^2\right)\psi_1, \tag{2.5}$$

$$i\frac{\partial\psi_2}{\partial t} = -\frac{1}{2}\frac{\partial^2\psi_2}{\partial x^2} - i\beta\frac{\partial\psi_2}{\partial x} - i\alpha\frac{\partial\psi_1}{\partial x} - \frac{\Delta}{2}\psi_2 + \left(g_{22}|\psi_2|^2 + g_{21}|\psi_1|^2\right)\psi_2. \tag{2.6}$$

Here, ψ_1 and ψ_2 are the two-component BECs pseudo-spin states, respectively, β is the helicoidal gauge potential, α represents the SO coupling. The wave functions are normalized as $N = \int(|\psi(x,t)|^2 dx, |)$, while $\mathcal{N}$ is the sum of numbers N_1 and N_2 of atoms of j-th component is

$$N = N_1 + N_2 = \int \left(|\psi_1|^2 + |\psi_2|^2\right) dx, \tag{2.7}$$

which is the dynamical invariant of the lossless system. The GP equation, in the present form, cannot best explain the growth of or the loss of atoms out of a condensate. To describe the dynamics of condensate with its surroundings, we couple it to an eternal reservoir following the atom-laser scheme. There are three different procedures toward a theoretical description of a continuous-wave atom laser. The first one is based on rate equations [208, 209]. The second one derives a quantum mechanical master equation [210, 211]. The third one, which we consider for this work, uses a classical treatment of the electromagnetic field [212], which was adequate to describe many features of the laser. Furthermore, as done by Kneer et al. [212], we introduce two additional loss and gain terms in the coupled cubic GP equations. The loss terms,

$$H_{\text{loss}}\psi_1 = -\frac{i}{2}\gamma_c\psi_1, \tag{2.8}$$

and

$$H_{\text{loss}}\psi_2 = -\frac{i}{2}\gamma_c\psi_2, \tag{2.9}$$

which are due to coupling the atom wave out of the resonator, lead to an exponential decay of the number of atoms in the condensates ψ_1 and ψ_2, respectively, with γ_c being the condensed atoms escape rate from the BEC. On the other hand, the gain terms,

$$H_{\text{gain}}\psi_1 = \frac{i}{2}\Gamma n_u\psi_1, \tag{2.10}$$

and

$$H_{\text{gain}}\psi_2 = \frac{i}{2}\Gamma n_u\psi_2, \tag{2.11}$$

leading to an increase of atoms in the condensates, whereas Γ is the rate constant coupling the condensate fields ψ_1 and ψ_2, with the number of atoms outside the condensates n_u, respectively. When we add the loss and the gain terms in the GP equations (2.5) and (2.6), we get generalized GP equations

$$i\frac{\partial\psi_1}{\partial t} = -\frac{1}{2}\frac{\partial^2\psi_1}{\partial x^2} + i\beta\frac{\partial\psi_1}{\partial x} - i\alpha\frac{\partial\psi_2}{\partial x} + \frac{\Delta}{2}\psi_1 + \left(g_{11}|\psi_1|^2 + g_{12}|\psi_2|^2\right)\psi_1 - \frac{i}{2}\gamma_c\psi_1 + \frac{i}{2}\Gamma n_u\psi_1, \tag{2.12}$$

$$i\frac{\partial\psi_2}{\partial t} = -\frac{1}{2}\frac{\partial^2\psi_2}{\partial x^2} - i\beta\frac{\partial\psi_2}{\partial x} - i\alpha\frac{\partial\psi_1}{\partial x} - \frac{\Delta}{2}\psi_2 + \left(g_{22}|\psi_2|^2 + g_{12}|\psi_1|^2\right)\psi_2 - \frac{i}{2}\gamma_c\psi_2 + \frac{i}{2}\Gamma n_u\psi_2. \tag{2.13}$$

In addition, for the number of uncondensed atoms n_u, we assume the rate equation [200]

$$\frac{dn_u}{dt} = R(x) - \gamma_u n_u - \Gamma n_u n_c. \tag{2.14}$$

Here, we have modeled the rate equation by referring to a local coupling [200] instead of the overall atomic population over the whole trap volume [212].

The physical interpretation of the rate equation (2.14) can be given as follows. The first term indicates that uncondensed atoms have been generated from an unbounded reservoir of atoms with a rate $R(x)$. On the other hand, the term $-\gamma_u n_u$ takes into account that atoms can escape from our system without being trapped in the condensed state, and γ_u is the rate of losses due to atoms leaving the trap. The last term for the rate equation in Eq. (2.14), $-\Gamma n_u n_c$, which is equivalent to the number of atoms n_u in the condensate, describes the transition of atoms into the condensate. Finally, $n_c = |\psi_1|^2 + |\psi_2|^2$ is the local density of the condensed phase.

2.2.2 Derivation of a new vector form of the cubic Complex Ginzburg-Landau equations with helicoidal SO coupling

In the above subsection, we have generalized a system of coupled 1D cubic GP equations governing the dynamics of the two-component condensed atoms with helicoidal coupling by including gain and loss, which in turn has been coupled to the rate equation governing the number of uncondensed atoms [212]. In the case of one-component BEC without helicoidal coupling, a general model of an atom laser, comprising of a pump and loss term in the GP equation has been presented. As a result, it has been shown that there exists a threshold for the pump above which the mean matter field assumes a nonvanishing value in the steady-state. Oscillations around the stationary solution, even in the presence of a loss term, have been found in the transient regime [212]. In addition, to improve the model, it should be pointed out, however, that, the physical grounds for an additional space-dependent diffusive process has been provided [200]. Using the same approach as in Ref. [200], under the same conditions, we show that the dissipative two-component BECs with helicoidal coupling obey a system of coupled 1D cubic CGL equations. When condensates are immersed in a dissipative environment and subject to thermal noise, the uncondensed phase n_u undergoes diffusion processes, and is described by including diffusion in Eq. (2.14) as follows

$$\frac{\partial n_u}{\partial t} = R(x) - \gamma_u n_u - \Gamma n_u(|\psi_1|^2 + |\psi_2|^2) + D_x \frac{\partial^2 n_u}{\partial x^2}. \tag{2.15}$$

In that case, the fluctuation-dissipation theorem must hold [200], so the corresponding diffusion constant in real space is

$$D_x = \frac{1}{\gamma_u}\frac{k_B T}{m}, \tag{2.16}$$

where m is the mass of the atoms, T, the temperature and k_B, the Boltzmann constant. It is also noteworthy that a mean field theory of the dynamics of a non-equilibrium BEC of exciton-polaritons in a semiconductor microactivity has been used and the Goldstone mode of a spatially homogeneous system has been found to be diffusive based on generalized GP equations including loss and amplification terms, and coupled to an equation for the density of reservoir polaritons, and where the spatial diffusion rate of reservoir polaritons have been also taken into account [213]. For further nonlinear analysis, space Fourier transform is applied on the physical variables of Eq. (2.15) as

follows

$$\begin{aligned}\mathcal{F}(k) &= \int_{-\infty}^{+\infty} \frac{\partial n_u(x,t)}{\partial t} e^{-ikx} \partial x \\ &= \int_{-\infty}^{+\infty} \left(R(x) - \gamma_u n_u(x,t) + D_x \frac{\partial^2 n_u(x,t)}{\partial x^2} \right) e^{-ikx} dx \\ &- \int_{-\infty}^{+\infty} \left(\Gamma n_u(x,t)(|\psi_1(x,t)|^2 + |\psi_2(x,t)|^2) \right) e^{-ikx} dx. \end{aligned} \tag{2.17}$$

The linear terms $R(x,t)$, $\gamma_u n_u(x,t)$ and $D_x \frac{\partial^2 n_u(x,t)}{\partial x^2}$ are trivial, whereas the nonlinear term $\Gamma n_u(x,t)(|\psi_1(x,t)|^2 + |\psi_2(x,t)|^2)$ gives a convolution integral. We consider only the $k = 0$ component in the nonlinear term which is just a perturbation. Then, its Fourier transform is resolved using Plancherel's theorem (Parseval's identity)

$$\begin{aligned}\mathcal{F}n_c &= \int_{-\infty}^{+\infty} \left(|\psi_1(x)|^2 + |\psi_2(x)|^2 \right) dx, \\ &= \int_{-\infty}^{+\infty} \left(a|\psi_1(k)|^2 + b|\psi_2(k)|^2 \right) dk, \end{aligned} \tag{2.18}$$

where $a = b = 1$, (i.e. a and b are constants), and has a Fourier transform $2\pi\delta(k)$. The above equation simplifies to

$$\mathcal{F}n_c = \int_{-\infty}^{+\infty} \left(|\psi_1|^2 + |\psi_2|^2 \right) \delta(k) dk, \tag{2.19}$$

that is

$$\mathcal{F}n_c = \left(|\psi_1|_0^2 + |\psi_2|_0^2 \right) \delta(k). \tag{2.20}$$

Where the distribution $\delta(x)$ denotes the Dirac delta function. Consequently, we obtain the needed space Fourier transform for Eq. (2.15), which reads

$$\frac{d\tilde{n}_u}{dt} = \tilde{R} - (\gamma_u + D_x k^2)\tilde{n}_u - \Gamma \tilde{n}_u (|\psi_1|_0^2 + |\psi_2|_0^2)\delta(k), \tag{2.21}$$

where $\tilde{n}_u(k) = \mathcal{F}n_u(x,t)$, $\tilde{R}(k) = \mathcal{F}R(x)$, $-k^2\tilde{n}_u = \mathcal{F}\frac{\partial^2 n_u(x,t)}{\partial x^2}$. In deriving Eq. (2.21), we have considered only the $k = 0$ component in the nonlinear terms which is just a perturbation [201]. This gives the stationary solution of the rate equation (2.21)

$$\tilde{n}_u = \frac{\dfrac{\tilde{R}}{\gamma_u}}{1 + \dfrac{D_x}{\gamma_u} k^2 + \dfrac{\Gamma}{\gamma_u}(|\psi_1|_0^2 + |\psi_2|_0^2)\delta(k)}. \tag{2.22}$$

For long wavelength perturbations and far from saturation, the two additional terms in the denominator are less than one. So, we can then expand Eq. (2.22) as

$$\tilde{n}_u = \frac{\tilde{R}}{\gamma_u} \left(1 - \frac{D_x}{\gamma_u} k^2 - \frac{\Gamma}{\gamma_u}(|\psi_1|_0^2 + |\psi_2|_0^2)\delta(k) \right). \tag{2.23}$$

Taking the inverse Fourier transform of the obtained Eq. (2.23), we have an operator relation as

$$n_u = \frac{R}{\gamma_u}\left[1 + \frac{D_x}{\gamma_u}\cdot\frac{\partial^2}{\partial x^2} - \frac{\Gamma}{\gamma_u}(|\psi_1|^2 + |\psi_2|^2)\right]. \tag{2.24}$$

The adiabatic elimination approach involves of taking the stationary solution (2.24) and replacing into Eq. (2.12) and Eq. (2.13).

By doing this, we derive a two coupled GP equation for ψ_1 and ψ_2 with complex coefficients to capture the dynamics of a BECs subject to dissipative losses and compensating external drive which reads as

$$i\frac{\partial\psi_1}{\partial t} = \left(i\frac{RD_r\Gamma}{2\gamma_u^2} - \frac{1}{2}\right)\frac{\partial\psi_1^2}{\partial x^2} + i\beta\frac{\partial\psi_1}{\partial x} - i\alpha\frac{\partial\psi_2}{\partial x} + \left(\frac{\Delta}{2} - \frac{i}{2}\gamma_c + i\frac{R\Gamma}{2\gamma_u}\right)\psi_1$$

$$+ \left(g_1 - i\frac{R\Gamma^2}{2\gamma_u^2}\right)|\psi_1|^2\psi_1 + \left(g_{12} - i\frac{R\Gamma^2}{2\gamma_u^2}\right)|\psi_2|^2\psi_1, \tag{2.25}$$

$$i\frac{\partial\psi_2}{\partial t} = \left(i\frac{RD_r\Gamma}{2\gamma_u^2} - \frac{1}{2}\right)\frac{\partial\psi_2^2}{\partial x^2} - i\beta\frac{\partial\psi_2}{\partial x} - i\alpha\frac{\partial\psi_1}{\partial x} + \left(-\frac{\Delta}{2} - \frac{i}{2}\gamma_c + i\frac{R\Gamma}{2\gamma_u}\right)\psi_2$$

$$+ \left(g_2 - i\frac{R\Gamma^2}{2\gamma_u^2}\right)|\psi_2|^2\psi_2 + \left(g_{12} - i\frac{R\Gamma^2}{2\gamma_u^2}\right)|\psi_1|^2\psi_2. \tag{2.26}$$

Next, we introduce the spatial and temporal dimensionless quantities in Eqs. (2.25) and (2.26)

$$\tau = \gamma_c t, \tag{2.27}$$

is the dimensionless time, while

$$X = \frac{x}{l_0}, \tag{2.28}$$

is the dimensionless space coordinate, with

$$l_0 = \left(\frac{\bar{R}D_x\Gamma}{2\gamma_u^2\gamma_c}\right)^{\frac{1}{2}} = 3\times10^{-6}m \tag{2.29}$$

being the characteristic length of the dissipative dynamics, and the dimensionless wave functions

$$|\tilde{\psi_j}|^2 = \frac{\bar{R}\Gamma^2}{2\gamma_u^2\gamma_c}|\psi_j|^2. \tag{2.30}$$

As mentioned before [200], the threshold condition (gain = losses) is satisfied for $R = \bar{R}$, where $\frac{\bar{R}\Gamma}{\gamma_u} = \gamma_c$. Next, we introduce in Eqs. (2.25) and (2.26) appropriate units for the measurements of time and spatial coordinates. After such transformations, the

considered system is reduced to the system of two coupled 1D rescaled cubic CGL equations with helicoidal coupling

$$i\frac{\partial\psi_1}{\partial\tau} = (i\epsilon + \Delta_0)\,\psi_1 + (1+iC_4)\,\frac{\partial^2\psi_1}{\partial X^2} + i\beta_0\frac{\partial\psi_1}{\partial X} - i\alpha_0\frac{\partial\psi_2}{\partial X} - (1+iC_1)\,|\psi_1|^2\psi_1 - (1+iC_3)\,|\psi_2|^2\psi_1, \quad (2.31)$$

$$i\frac{\partial\psi_2}{\partial\tau} = (i\epsilon - \Delta_0)\,\psi_2 + (1+iC_4)\,\frac{\partial^2\psi_2}{\partial X^2} - i\beta_0\frac{\partial\psi_2}{\partial X} - i\alpha_0\frac{\partial\psi_1}{\partial X} - (1+iC_2)\,|\psi_2|^2\psi_2 - (1+iC_3)\,|\psi_1|^2\psi_2. \quad (2.32)$$

In the above dimensionless system,

$$\epsilon = \frac{1}{2}\left(\frac{R\Gamma}{\gamma_u\gamma_c} - 1\right) = \frac{1}{2}\left(\frac{R}{\bar{R}} - 1\right), \;\; C_1 = \frac{2g_{11}\gamma_u^2}{R\Gamma^2}, \;\; C_2 = \frac{2g_{22}\gamma_u^2}{R\Gamma^2},$$
$$C_3 = \frac{2g_{12}\gamma_u^2}{R\Gamma^2}, \;\; C_4 = \frac{\gamma_u^2}{RD_x\Gamma}, \;\; \beta_0 = \frac{\beta}{l_0\gamma_c}, \;\; \alpha_0 = \frac{\alpha}{l_0\gamma_c}, \;\; \Delta_0 = \frac{\Delta}{2\gamma_c}, \quad (2.33)$$

are the other significant parameters. The equations (2.31) and (2.32) are the new coupled or vector form of the cubic CGL equation in the presence of helicoidal SO coupling in dissipative BECs. Coupled cubic CGL equations have attracted interest. Several authors [213–219] have derived the vector cubic CGL equation in the absence of spin-orbit coupling in a large variety of subfields. In this case, the vector cubic CGL equation appeared in the context of laser physics, which offer very interesting opportunities for examining the spatiotemporal phenomena due to the vector nature of the composite amplitude of the electric field. The vector degrees of freedom are associated with the polarization of laser light. On the other hand, laser systems are made up of various components. An accurate model will take into consideration consecutive sets of propagation equations. The possibility of vectorial topological defects which are not predictable by the scalar theory has been analyzed [213]. The vector cubic CGL equation has been derived as an amplitude description of an atomic transition between spin sublevels, where the interactions between the polarization state of light and transverse effects results in unprecedented states of laser light such as standing waves, with a spatially periodic linear polarization, or coexisting traveling waves with different wavenumbers and circular polarizations [215].

The vector cubic CGL equation has been studied in detail as a general model for the superposition of two counterpropagating waves with the same frequency in nonlinear electrical transmission lines [216] and as a model for electrically coupled Hindmarsh-Rose neuronal model with power-law long-range dispersive interactions [217]. In optics, the vector cubic CGL equation serves as models of dual-core erbium-doped optical fibers, the dopant being used to induce the linear gain in one core [82, 219]. Exact solitary pulse solutions, that include space- or time-dependent wave numbers, have been derived analytically, for specific variable coefficients of the nonlinear gain/loss terms, by a modified Hirota bilinear method [220]. Different types of pattern development are there in the dynamic states of the one-spatial dimension (localized structures) [221] and of the two-spatial dimensions (topological defects) [222–225] for the vectorial cubic CGL equation. Examples are the synchronization properties of spatiotemporally chaotic states [222], the identification of a transition from a glass to a

gas phase [223], and the formation and annihilation processes leading to the different types of defects [224]. Moreover, processes of creation and annihilation of different types of vector defects, as well as transition between different regimes of space-time dynamics have been described [225].

For a finite geometry, predictions of confined states, temporally modulated confined states and other dynamic states have been discussed, with applications to a phenomenological description of oscillatory convection in binary fluid convection [226]. The vector cubic-quintic CGL equation has also been studied. Various categories of solitary waves describing the evolution of progressive bright-bright, front-front, dark-dark, and other groups of solitary waves have been found [227]. The evolution and the stability of the vector dissipative optical light bullets [228] and the MI gain regions [229] have been investigated in the (2+1)-dimensional vectorial cubic–quintic equations.

2.3 Linear stability analysis of the MI in two-component open BECs with helicoidal SO coupling

In this section, we explore instabilities of a propagating CW or quasi-CW state in the form of a miscible binary condensate with uniform densities n_{10}, n_{20} and the chemical potential μ of both components, which is described by Eqs. (2.31) and (2.32). To analyze the MI of the considered system, we use the standard linear stability analysis. The steady-state solutions of a system of two coupled 1D cubic CGL equations with helicoidal coupling (2.31) and (2.32), corresponding to the CW state, is written as

$$\psi_j = e^{-i\mu\tau}\sqrt{n_{j0}}, \quad j = 1, 2, \tag{2.34}$$

and Eq. (2.34) shows that the densities, Zeeman splitting, interactions, and chemical potential are determined by algebraic equation

$$\Delta_d \quad = \quad (-1)^{3-j}\left(\mu + n_{3-j,0} - n_{j0}\right) \quad + \quad i(-1)^{3-j}\left(C_j n_{j0} + C_3 n_{3-j,0} - \epsilon\right). \tag{2.35}$$

To analyze the MI of CW wave solutions, in the helicoidal SO-coupled BECs, we perturb the state (2.34) by introducing

$$\psi_j = e^{-i\mu\tau}(\sqrt{n_{j0}} + \delta\psi_j), \tag{2.36}$$

where $\delta\psi_j$ are the small perturbations, with $|\delta\psi_j| \ll \sqrt{n_{j0}}$ being the complex fields which obey the following linearized equations

$$i\frac{\partial(\delta\psi_1)}{\partial\tau} = (1 + iC_4)\frac{\partial^2(\delta\psi_1)}{\partial X^2} + i\beta_0\frac{\partial(\delta\psi_1)}{\partial X} - i\alpha_0\frac{\partial(\delta\psi_2)}{\partial X}$$

$$- (1 + iC_1)n_{10}(\delta\psi_1^* + \delta\psi_1) - (1 + iC_3)\sqrt{n_{10}n_{20}}(\delta\psi_2^* + \delta\psi_2), \tag{2.37}$$

$$i\frac{\partial(\delta\psi_2)}{\partial\tau} = (1+iC_4)\frac{\partial^2(\delta\psi_2)}{\partial X^2} - i\beta_0\frac{\partial(\delta\psi_2)}{\partial X} - i\alpha_0\frac{\partial(\delta\psi_)}{\partial X}$$

$$-(1+iC_2)n_{20}(\delta\psi_2^* + \delta\psi_2) - (1+iC_3)\sqrt{n_{10}n_{20}}(\delta\psi_1^* + \delta\psi_1), \quad (2.38)$$

where $\delta\psi_j^*$ are the complex conjugates of the perturbed fields $\delta\psi_j$. Now, we assume the following ansatzes for the perturbed fields

$$\delta\psi_j(X,\tau) = \zeta_j e^{i(KX-\Omega\tau)} + \eta_j^* e^{-i(KX-\Omega\tau)}, \quad (2.39)$$

where K is the wave number, Ω is a complex modulation frequency, ζ_j, and η_j are constant complex amplitudes, respectively. The substitution of Eq. (2.39) into Eqs. (2.37) and (2.38) gives the linear homogeneous system of equations in terms of ζ_1, ζ_2, η_1 and η_2

$$\begin{aligned}
n_{11}\zeta_1 + n_{12}\zeta_2 + n_{13}\eta_1 + n_{14}\eta_2 &= 0,\\
n_{21}\zeta_1 + n_{22}\zeta_2 + n_{23}\eta_1 + n_{24}\eta_2 &= 0,\\
n_{31}\zeta_1 + n_{32}\zeta_2 + n_{33}\eta_1 + n_{34}\eta_2 &= 0,\\
n_{41}\zeta_1 + n_{42}\zeta_2 + n_{43}\eta_1 + n_{44}\eta_2 &= 0,
\end{aligned} \quad (2.40)$$

with:

$$\begin{aligned}
n_{11} &= K\beta_0 + K^2(1+iC_4) + (1+iC_1)n_0 + \Omega,\\
n_{12} &= (1+iC_3)n_0 - K\alpha_0,\\
n_{13} &= (1+iC_1)n_0,\\
n_{14} &= (1+iC_3)n_0,\\
n_{22} &= K^2(1+iC_4) + (1+iC_2)n_0 - K\beta_0 + \Omega,\\
n_{24} &= (1+iC_2)n_0,\\
n_{31} &= (1-iC_1)n_0,\\
n_{32} &= (1-iC_3)n_0,\\
n_{33} &= K^2(1-iC_4) + (1-iC_1)n_0 - K\beta_0 - \Omega,\\
n_{34} &= (1-iC_3)n_0 + K\alpha_0,\\
n_{42} &= (1-iC_2)n_0,\\
n_{44} &= K^2(1-iC_4) + (1-iC_2)n_0 + K\beta_0 - \Omega,
\end{aligned} \quad (2.41)$$

where $n_{10} = n_{20} = n_0$.

2.4 Discussion of MI process in open BECs with helicoidal SO coupling

A nontrivial solution of a system of four equations, requires that $\mathrm{Det}(n=0)$, where $\mathbf{n}$ $(\zeta_1, \zeta_2, \eta_1, \eta_2)$ is a 4×4 complex matrix, and the dispersion relation of the system for Ω becomes

$$\Omega^4 + P_3\Omega^3 + P_2\Omega^2 + P_1\Omega + P_0 = 0, \quad (2.42)$$

where
$P_3 = n_{11} + n_{22} - n_{33} - n_{44}$,
$P_2 = n_{11}n_{22} - n_{11}n_{44} - n_{22}n_{33} - n_{22}n_{44} + n_{33}n_{44} - n_{34}^2 + n_{14}n_{32} + n_{42}n_{24} - n_{11}n_{33} + n_{14}n_{32} - n_{12}^2 + n_{13}n_{31}$,
$P_1 = n_{22}n_{33}n_{44} - n_{22}n_{34}^2 - n_{11}n_{34}^2 + n_{11}n_{33}n_{44} - n_{11}n_{22}n_{44} + n_{11}n_{14}n_{32} - n_{14}n_{32}n_{44} + n_{14}n_{34}n_{42} + n_{11}n_{42}n_{24} + n_{24}n_{32}n_{34} - n_{24}n_{33}n_{42} - n_{11}n_{22}n_{33} + n_{33}n_{12}^2 + n_{12}^2n_{44} - n_{12}n_{14}n_{31} - n_{13}n_{12}n_{32} - n_{14}n_{12}n_{42} + n_{14}n_{31}n_{34} - n_{14}n_{32}n_{33} + n_{13}n_{22}n_{31} - n_{13}n_{31}n_{44} + n_{13}n_{32}n_{34} - n_{12}n_{24}n_{32} + n_{13}n_{14}n_{31} + n_{14}n_{22}n_{32}$,
$P_0 = n_{11}n_{24}n_{34}n_{32} - n_{11}n_{24}n_{33}n_{42} - n_{11}n_{14}n_{32}n_{44} + n_{11}n_{14}n_{34}n_{42} + n_{11}n_{22}n_{44}n_{33} - n_{11}n_{22}n_{34}^2 - n_{12}n_{31}n_{24}n_{34} + n_{12}n_{24}n_{32}n_{33} - n_{44}n_{33}n_{12}^2 + n_{12}^2n_{34}^2 + n_{14}n_{31}n_{12}n_{44} - n_{12}n_{14}n_{32}n_{34} + n_{13}n_{24}n_{31}n_{42} - n_{13}n_{24}n_{32}^2 + n_{13}n_{44}n_{12}n_{32} - n_{13}n_{12}n_{42}n_{34} - n_{13}n_{22}n_{31}n_{44} + n_{13}n_{22}n_{32}n_{34} - n_{14}n_{12}n_{34}n_{32} + n_{14}n_{12}n_{42}n_{33} + n_{14}n_{31}n_{34}n_{22} - n_{14}n_{32}n_{33}n_{22} - n_{14}^2n_{31}n_{42} + n_{14}^2n_{32}^2$.
The four solutions given by Eq. (2.42) are

$$\Omega_{1,2} = -\frac{P_3}{4} - \frac{1}{2}\sqrt{\frac{1}{4}P_3^2 - \frac{2}{3}P_2 + \Lambda} \pm \frac{1}{2}\sqrt{\frac{2}{3}P_2 - \frac{1}{4}P_3^2 - \Lambda - 2P_2 + \frac{3}{4}P_3^2 + \frac{P_3^3 - 4P_3P_2 + 8P_0}{4\sqrt{\frac{1}{4}P_3^2 - \frac{2}{3}P_2 + \Lambda}}}, \quad (2.43)$$

$$\Omega_{3,4} = -\frac{P_3}{4} + \frac{1}{2}\sqrt{\frac{1}{4}P_3^2 - \frac{2}{3}P_2 + \Lambda} \pm \frac{1}{2}\sqrt{\frac{2}{3}P_2 - \frac{1}{4}P_3^2 - \Lambda - 2P_2 + \frac{3}{4}P_3^2 - \frac{P_3^3 - 4P_3P_2 + 8P_0}{4\sqrt{\frac{1}{4}P_3^2 - \frac{2}{3}P_2 + \Lambda}}}, \quad (2.44)$$

where

$$\Lambda = \frac{1}{3}\left(\sqrt[3]{\frac{\Delta_1 + \sqrt{\Delta_1^2 - 4\Delta_0^3}}{2}} + \frac{\Delta_0}{\sqrt[3]{\frac{\Delta_1 + \sqrt{\Delta_1^2 - 4\Delta_0^3}}{2}}}\right) \quad (2.45)$$

and $\Delta_0 = P_2^2 + 12P_0$, $\Delta_1 = 2P_2^3 + 27P_1^2 - 72P_2P_0$. From Eqs. (2.43) and (2.44), the value of the Ω depends on the signs and magnitudes of the terms involved and can be positive, negative, or complex. The CW state is stable when Ω real, otherwise, MI takes place. The instability growth rate is defined as $\zeta(\Omega) = |\mathrm{Im}(\Omega)|_{\max}$. From the elements of Eq. (2.40), it is obvious that the growth rate is strongly dependent on system parameters, but does not depend on the coefficients $(\Delta_d + i\epsilon)$ and $(-\Delta_d + i\epsilon)$, which do not influence the MI spectrum. Also, for the rest of calculations, we consider two BEC components with equal densities $n_{01} = n_{02} = n_0$.
In Fig. 2.1, panels $(\mathrm{aj})_{j=1,2,3,4}$ and $(\mathrm{bj})_{j=1,2,3,4}$ depict the effect of the intra (C_1) and intercomponent (C_3) interactions, respectively, in presence and absence of the helicoidal gauge potential β_0. Figures 2.1 (a1) and (a2), where the intra (C_2) and intercomponent (C_3) are repulsive, i.e. $C_2 = C_3 > 0$, the maximum growth rate of MI is expected for $C_1 > 0$, for $\beta_0 = 0$. However, for $\beta_0 = 4$, there is an emergence of MI side bands, while most of the instability zones appear under intracomponent attraction, i.e. $C_1 < 0$. A reverse situation is ostensible in Figs. 2.1 (a3) and (a4) for which the intra (C_2) and

intercomponent (C_3) interactions are attractive ($C_2 = C_3 < 0$). For $\beta_0 = 0$, the MI may likely take place in the zone $C_1 < 0$, while there is MI explosion in the instability domain, with $C_1 > 0$ being likely available for the CW to disintegrate into solitonic objects. Figs. 2.1 $(\text{bj})_{j=1,2,3,4}$ show the MI growth rate in the (K, C_3)-plane. We should stress once more that $C_3 > 0$ and $C_3 < 0$ imply repulsive and attractive intercomponent interactions, respectively. Figures 2.1 (b1)-(b2) correspond to $C_1 = C_2 > 0$ and Figs. 2.1 (b3)-(b4) give results for $C_1 = C_2 < 0$. In general, the MI development is highly affected by the atomic interactions and the presence of the helicoidal gauge potential brings about MI growth rate explosion, which implies that different zones of instability are available and may lead to a broad range of dynamical behaviors. It is worth noting that for the above results, we have fixed the value of the SO coupling strength as $\alpha_0 = 1$, which does not reflect its impact on the appearance of MI.

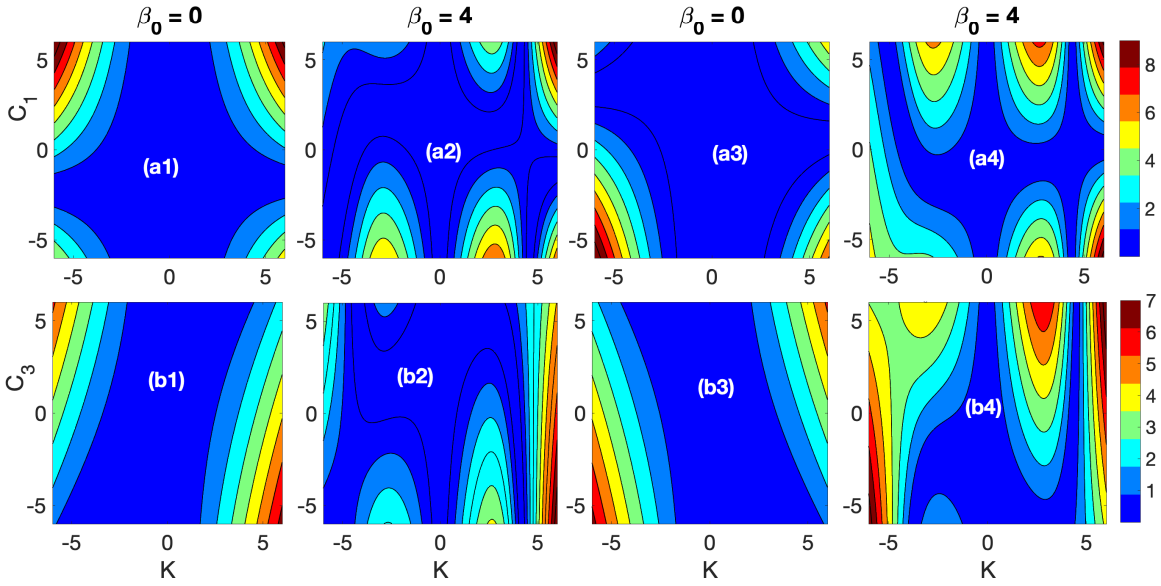


Figure 2.1: Panels $(\text{aj})_{j=1,2,3,4}$ show the contour plots of the MI gain in the $(K, C_1)-$plane for: (a1)-(a2) $C_2 = C_3 = 2$, (a3)-(a4) $C_2 = C_3 = -2$. Panels $(\text{bj})_{j=1,2,3,4}$ display the contour plot of the MI gain in the $(K, C_3)-$plane for (b1)-(b2) $C_1 = C_2 = 2$ and (b3)-(b4) $C_1 = C_2 = -2$, with $n_0 = 1$, $\alpha_0 = 1$ and $C_4 = 0.5$.

This explains why in Fig. 2.2, the growth rate is represented in the $(\alpha_0, \beta_0)-$plane both under repulsive and attractive intercomponent couplings. Panels $(\text{aj})_{j=1,2,3,4}$ of Fig. 2.2 depict the case $C_3 > 0$, and one plays on the signs of the intracomponent interaction parameters C_1 and C_2. As a whole, asymmetric patterns of the MI growth rate are obtained for $C_1 = C_2 > 0$ and $C_1 = C_2 < 0$, i.e. when both components are intrinsically repulsive or attractive. Nevertheless, symmetric lobes of MI appear when C_1 and C_2 are of different signs. The same behaviors are obvious in Fig. 2.2 $(\text{bj})_{j=1,2,3,4}$, where $C_3 < 0$, except that for $(C_1 > 0;\ C_2 < 0)$ and $(C_1 < 0;\ C_2 > 0)$, only high values of α_0 and β_0 are likely to cause instability. Also, for $C_1 = C_2 > 0$ and $C_1 = C_2 < 0$, regions of MI are switched between $\alpha_0 > 0$ and $\alpha_0 < 0$, while such a context tends to enhance only one region of instability. To be noted it is also the fact that the intensity of the MI growth rate is greater when intercomponent interaction effects are attractive.

Figure 2.3 shows the behaviors of the MI growth rate in the plane (K, α_0) when

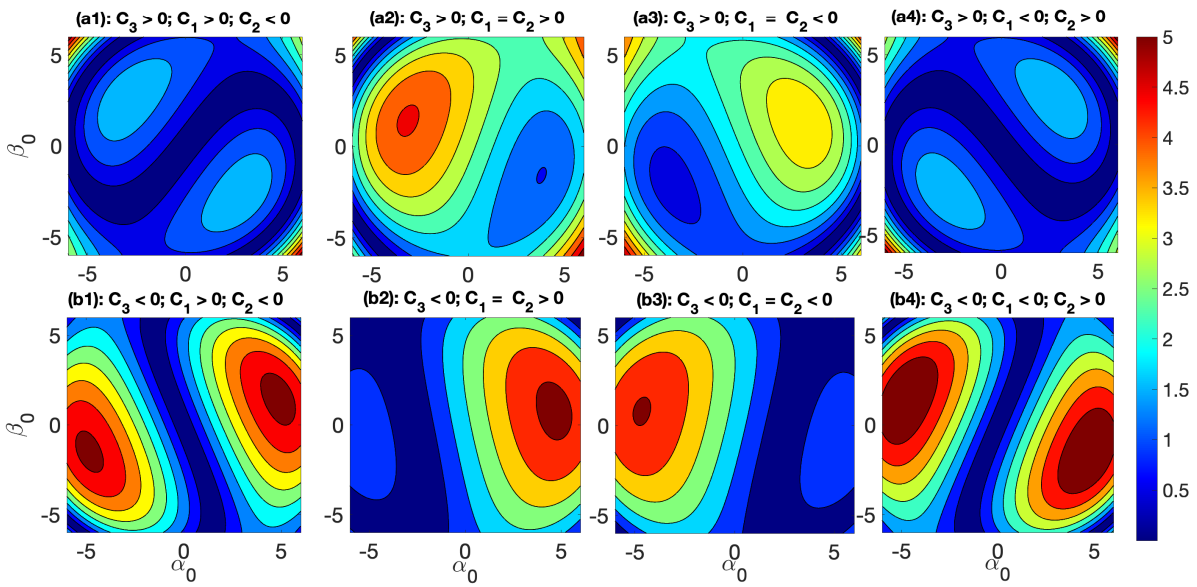


Figure 2.2: MI gain in the $(\alpha_0, \beta_0)-$plane for: $(\text{aj})_{j=1,2,3,4}$ $C_3 > 0$ and $(\text{bj})_{j=1,2,3,4}$ $C_3 < 0$. The coefficients C_1 and C_2 are taken such that in panels (a1)-(b1) $C_1 > 0$, $C_2 < 0$, (a2)-(b2) $C_1 = C_2 > 0$, (a3)-(b3) $C_1 = C_2 < 0$ and (a4)-(b4) $C_1 < 0$, $C_2 > 0$, with $n_0 = 1$ and $K = 1.5$.

$C_3 > 0$ (panels $(\text{aj})_{j=1,2,3,4}$) and when $C_3 < 0$ (panels $(\text{bj})_{j=1,2,3,4}$). In the first case, i.e. under repulsive intercomponent, opposite signs of the intracomponent (C_1 and C_2) interactions give rise to symmetric lobes of instability with maximum growth rate appearing for $\alpha_0 < 0$ ($C_1 > 0$; $C_2 < 0$) and $\alpha_0 > 0$ ($C_1 < 0$; $C_2 > 0$), which are respectively depicted in Figs. 2.3(a1) and (a4). For the rest, asymmetric growth rate spectra appear both when the two components are simultaneously repulsive (see Fig. 2.3(a2)) and attractive (see Fig. 2.3(a3)), with additional windows of instability. Along the same line, when $C_3 < 0$, we have the features of panels $(\text{bj})_{j=1,2,3,4}$ in Fig. 2.3, where changes in the signs of C_1 and C_2 modify the maximum MI growth rate zones. When $(C_1 > 0; C_2 < 0)$ and $(C_1 < 0; C_2 > 0)$, there are two symmetric lobes of instability with the maximum growth rate being respectively situated in the areas $\alpha_0 > 0$ (see Fig. 2.3(b1)) and $\alpha_0 < 0$ (see Fig. 2.3(b4)). This also includes additional windows of instability around $\alpha_0 = 0$ that change interval of K where the CW is supposed to disintegrate. Interestingly, such coherent figures of MI growth rate become asymmetric when the intracomponent interactions are both repulsive (see Fig. 2.3(b2)) and attractive (see Fig. 2.3(b3)). Particularly, the growth rate maximum shifts to the area $K > 0$ for $C_1 = C_2 > 0$, and to the zone $K < 0$ for $C_1 = C_2 < 0$, while the instability tends to disappear in the other regions for K and α_0, the SOC parameter. Remarkably, the sign of the multicomponent coupling parameter has some important consequences on the intensity of the MI growth rate and on its distribution. The proposed model includes two BEC components. In that note, the above analysis shows that the two types of intercomponent interactions can contribute to the emergence of MI. Most of the models that have been proposed until now, not only consider the NLS equations, but also avoid the difficulty brought by the dissipative effects and the resultant coupled cubic CGL equations.

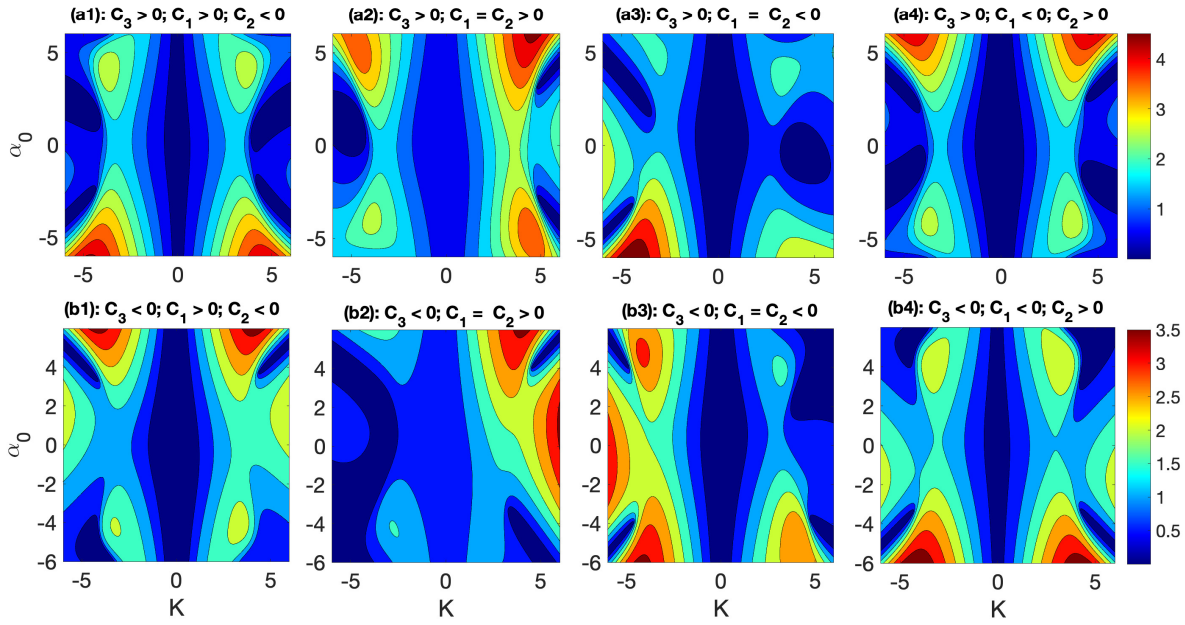


Figure 2.3: The contour plots show the gain of MI in the $(K, \alpha_0)-$plane for: $(\mathrm{aj})_{j=1,2,3,4}$ $C_3 > 0$ and $(\mathrm{bj})_{j=1,2,3,4}$ $C_3 < 0$. The coefficients C_1 and C_2 are taken such that in panels (a1)-(b1) $C_1 > 0$, $C_2 < 0$, (a2)-(b2) $C_1 = C_2 > 0$, (a3)-(b3) $C_1 = C_2 < 0$ and (a4)-(b4) $C_1 < 0$, $C_2 > 0$, with $n_0 = 1$, $\beta_0 = 1$ and $C_4 = 0.5$, with $n_0 = 1$.

2.5 Direct numerical simulations of the two coupled 1D cubic CGL equations with helicoidal SO coupling using the slipt-step Fourier transform method

Linear stability analysis can determine the instability zones in parameter space and predict quantitatively how the amplitude of modulation sideband evolves at the onset of instability. However, such analysis is based on the linearization of the perturbed plane wave solution around the unperturbed carrier wave, which is valid only when the amplitude of perturbation is small in comparison with that of the carrier wave. The linear approximation does not actually give some information about the long time dynamical features of the system as the amplitude of unstable sideband grows exponentially. Therefore, in order to check the validity of our analytical predictions and to investigate the longtime evolution of MI, we have carried out numerical investigations of MI on the vector cubic CGL Eqs. (2.31) and (2.32) using the SSFM, with initial conditions

$$\psi_1(X, 0) = \psi_2(X, 0) = n_0 + \varepsilon \cos(KX), \tag{2.46}$$

where the perturbation wavenumber K takes values from the instability regions of Figs. 2.1-2.3, $n_0 = 1$ and $\varepsilon = 0.001$, so that $\varepsilon \ll n_0$. The manifestation of MI is detected through the amplitude maxima, while one gives importance to the combined effects of the SO coupling, the intercomponent interaction parameter and the helicoidal gauge potential. Different combinations of the intracomponent interaction values have been used in a single CGL equation by Arecchi et al. [200]. They, however, found that for ^{87}Rb, with $C_1 = 0.52$ and $C_2 = 2.05$, instability could not develop, since such parameters were in the stability region. Nevertheless, instability was found for ^{7}Li,

for which $C_1 = 0.04$ and $C_2 = -0.51$. Beyond the above one-component cases, we believe that other set of parameters can be investigated to meet the necessary criteria for instability to develop in two-component BECs with non-identical atomic species, such as $^{41}\mathrm{K}-{}^{87}\mathrm{Rb}$ and $^{7}\mathrm{Li}-{}^{133}\mathrm{Cs}$. The choice of suitable parameter values, especially when SO coupling and helicoidal gauge potential are involved, will be guided by the predictions from the linear stability analysis.

In Fig. 2.4 we consider repulsive intercomponent interactions ($C_3 > 0$), and address the effect of the helicoidal gauge potential without the SOC, i.e. $\alpha_0 = 0$. Interestingly, when both the SOC and the helicoidal gauge potential are switched off, wave patterns are initiated but vanish with time increasing for both components. However, with increasing the value of the helicoidal gauge potential β_0, there appear localized oscillations in the two condensates with a slight temporal CW background (see panels $(\mathrm{aj})_{j=1,2}$ in Fig. 2.4). This particular aspect is consistent with our linear stability analysis of MI, since the obtained patterns have the shape of solitonic objects, which emerge as the consequence of the constructive interplay between dispersive and nonlinear effects. One fact to be noted here is that as β_0 increases, the delay in the occurrence of MI decreases. This is confirmed by Fig. 2.4$(\mathrm{cj})_{j=1,2}$, where the patterns are also more localized in amplitude, with $|\psi_2|^2 > |\psi_1|^2$.

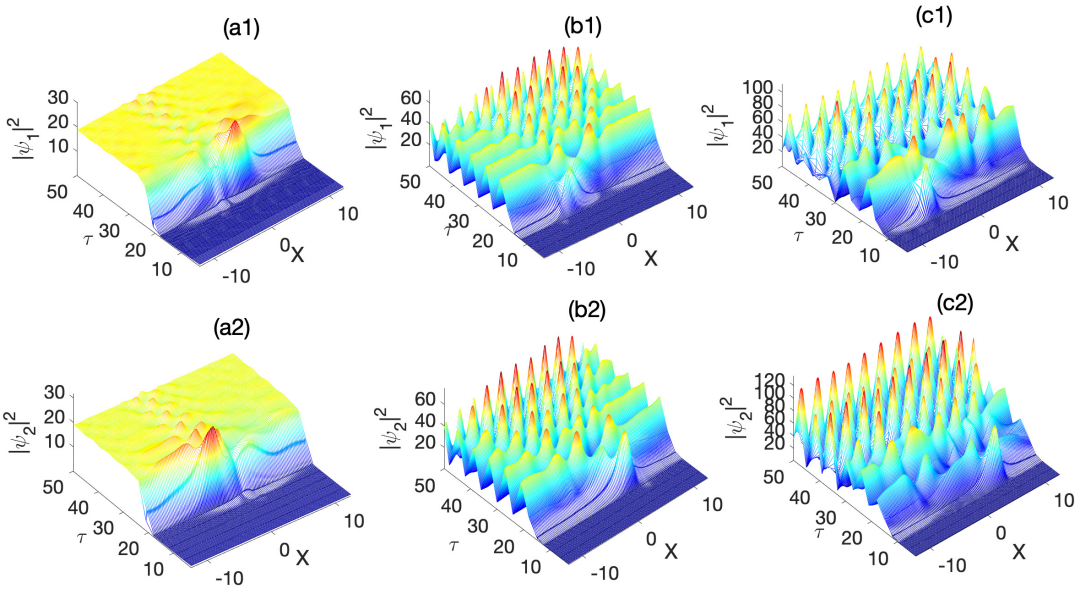


Figure 2.4: Spatiotemporal development of MI for $\alpha_0 = 0$, and β_0 taking the respective values : $(\text{aj})_{j=1,2}$ $\beta_0 = 0$, $(\text{bj})_{j=1,2}$ $\beta_0 = 1.5$ and $(\text{cj})_{j=1,2}$ $\beta_0 = 2.5$, with the other parameter values being: $C_1 = C_2 = 5$, $C_3 = 2$, $C_4 = 0.5$, $K = 1.5$, $n_0 = 1$, $\Delta_0 = 0.01$.

The patterns of Fig. 2.5 show spatiotemporal evolution of MI in presence of the SO coupling, when the helicoidal gauge potential respectively takes the values $\beta_0 = 0$ (panels $(\text{aj})_{j=1,2}$ in Fig. 2.5), $\beta_0 = 1.5$ (panels $(\text{bj})_{j=1,2}$ in Fig. 2.5) and $\beta_0 = 2.5$ (panels $(\text{cj})_{j=1,2}$ in Fig. 2.5). It is illustrated that even in absence of the helicoidal gauge potential, the stability of the CW is strongly affected. In fact, from the structure of Eqs. (2.31) and (2.32), the helicoidal gauge potential is inherent to individual components and have been actually considered by a few number of authors. Recently for example, Saha et al. [230] studied dilute superfluidity of spin-1 bosons and insisted on suitable balance between antiferromagnetic interactions and SO coupling as the condition for superfluid spin-liquid phase to appear in coupled BECs. Along the same line, Chen et al. [231], who considered only Raman and SO couplings, showed that the SO coupling contributes efficiently to the occurrence of the instability, regardless of the nature of the intercomponent coupling. Moreover, in the context of the coupled NLS equations, it was further shown by Li et al. [201] that the helicoidal gauge potential can be used as an efficient tool to control MI in BECs. This is illustrated further in panels $(\text{bj})_{j=1,2}$ and $(\text{cj})_{j=1,2}$ of Fig. 2.5, where β_0 takes the respective values 1.5 and 2.5. additionally, like in Fig. 2.4, the time required for the effective onset of instability decreases with the increase in β_0, a fact that could not be predicted by the linear stability analysis. In the meantime, the reader should be aware that as the presence of the term in β_0 bring about helicity, the later can be left-handed ($\beta_0 > 0$) or right-handed ($\beta_0 < 0$). It should also be emphasized that the results presented in Figs. 2.4 and 2.5 considered only the left-handed character of the helicoidal gauge potential. In Fig. 2.2 particularly, we have seen that a suitable choice of the values of α_0 and β_0 can lead to the instability of the CW, both under repulsive and attractive intercomponent interactions, with coefficient C_3. It is worth reminding that some theoretical and numerical investigations have revealed that patterns formation via the activation of MI was exclusively possible in attractive single-component BECs [232–234]. However, it was also found that when more than two wave fields are involved, the coupling between

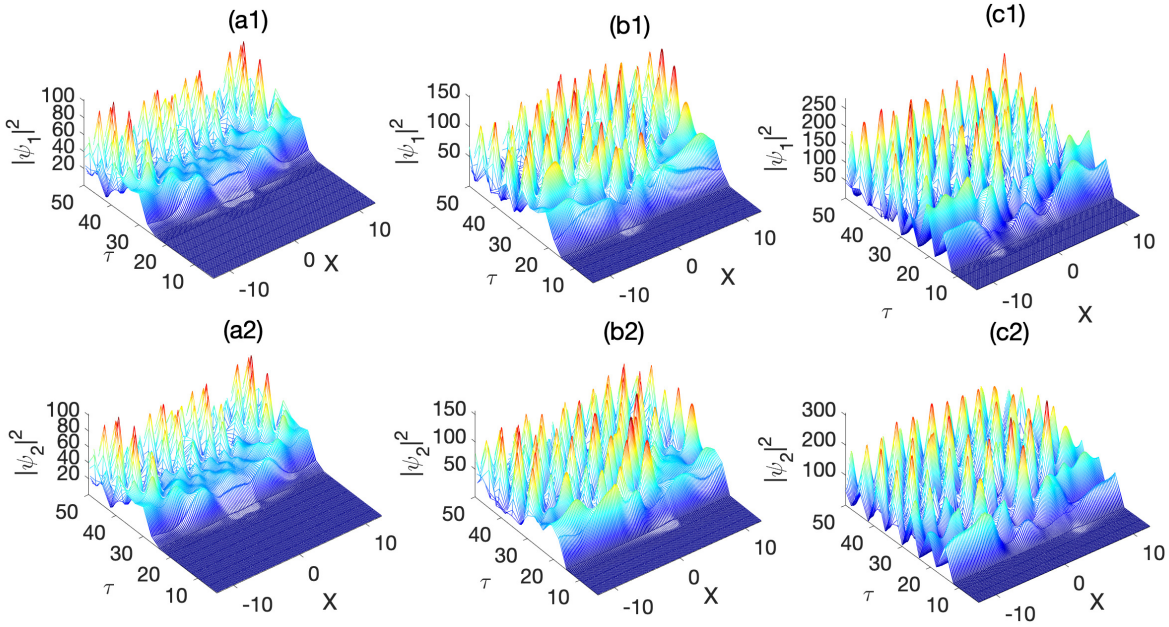


Figure 2.5: Spatiotemporal development of MI for $\alpha_0 = 0.5$, and β_0 taking the respective values : $(\mathrm{aj})_{j=1,2}$ $\beta_0 = 0$, $(\mathrm{bj})_{j=1,2}$ $\beta_0 = 1.5$ and $(\mathrm{cj})_{j=1,2}$ $\beta_0 = 2.5$, with the other parameter values being: $C_1 = C_2 = 5$, $C_3 = 2$, $C_4 = 0.5$, $K = 1.5$, $n_0 = 1$, $\Delta_0 = 0.01$.

multicomponent waves can lead to MI development, even under exclusively repulsive BECs [68, 235–237].

In order to explore the concomitant effect of C_3 and negative β_0, we represent in Fig. 2.6, the spatiotemporal manifestation of MI when $\beta_0 < 0$ and $C_3 > 0$, with α_0 taking different values. In panels $(\mathrm{aj})_{j=1,2}$ of Fig. 2.6, for which $\alpha_0 = 0$, slight localized patterns appear, but the MI phenomenon really develops when $\alpha_0 = 0.25$ and 0.5 as depicted in panels $(\mathrm{bj})_{j=1,2}$ on Fig. 2.6 and $(\mathrm{cj})_{j=1,2}$. Obviously, there is an increase in the density of the two components, but for $\alpha_0 = 0.5$, the amplitude of the component ψ_2 decreases progressively with time, likely due to the dissipative character of the proposed model, while the component ψ_1 tends to develop quasi-coherent structures as time evolves. To further explore the impact of negative β_0, we consider in Fig. 2.7, the context where the two components undergo attractive interactions, i.e. $C_3 < 0$. As predicted by the MI growth rate, there is, in general, pattern formation and the ostensible spectrum of behaviors reinforces the idea that spatiotemporal patterns in our context may show features not present without SO coupling. This was already addressed by Xu et al. [238], who showed that SO coupling may dictate the shape of exact bright soliton solutions and lead to the formation of multihump solitons, and their recombination to a single bright solitons. Albeit it is not exactly the case, we notice from panels $(\mathrm{cj})_{j=1,2}$ in Fig. 2.7 that over long time propagation, the train of patterns tends to recombine to single structures when time increases. This implies that switching between repulsive and attractive intercomponent couplings induces a radical modification on the solitonic patterns that emerge and which gives credit to our linear stability analysis and the proposed coupled cubic CGL equations.

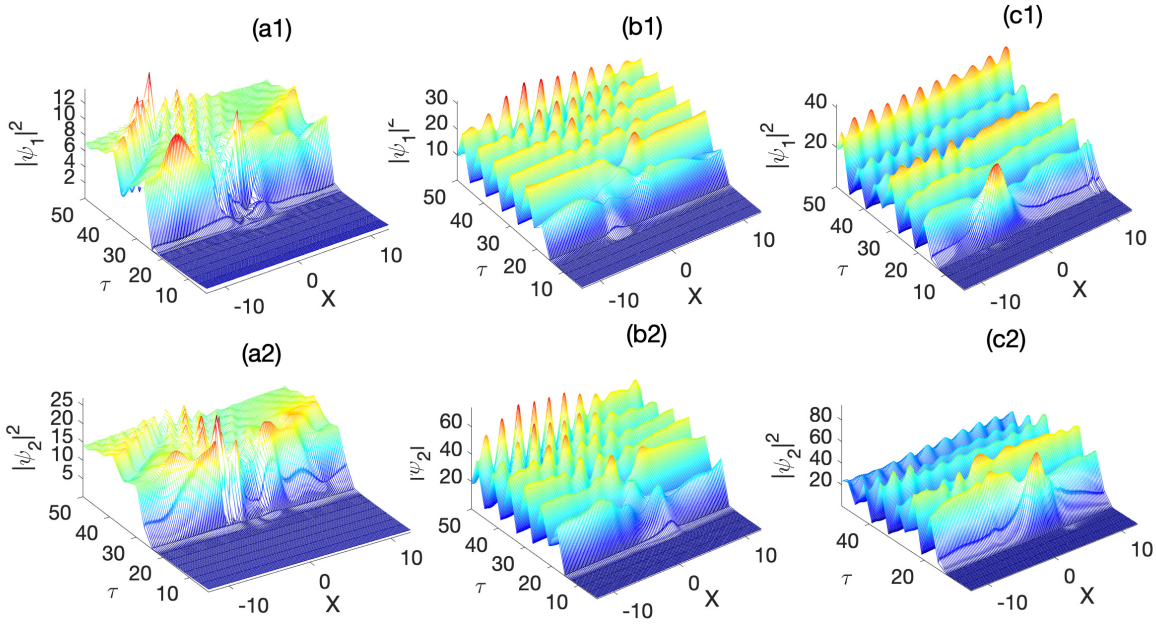


Figure 2.6: Spatiotemporal development of MI for $\beta_0 = -1.5$, and $C_3 = 2$, with α_0 taking the respective values : $(\mathrm{aj})_{j=1,2}$ $\alpha_0 = 0$, $(\mathrm{bj})_{j=1,2}$ $\alpha_0 = 0.25$ and $(\mathrm{cj})_{j=1,2}$ $\alpha_0 = 0.5$, with the other parameter values being: $C_1 = C_2 = 5$, $C_3 = 2$, $C_4 = 0.5$, $K = 1.5$, $n_0 = 1$, $\Delta_0 = 0.01$.

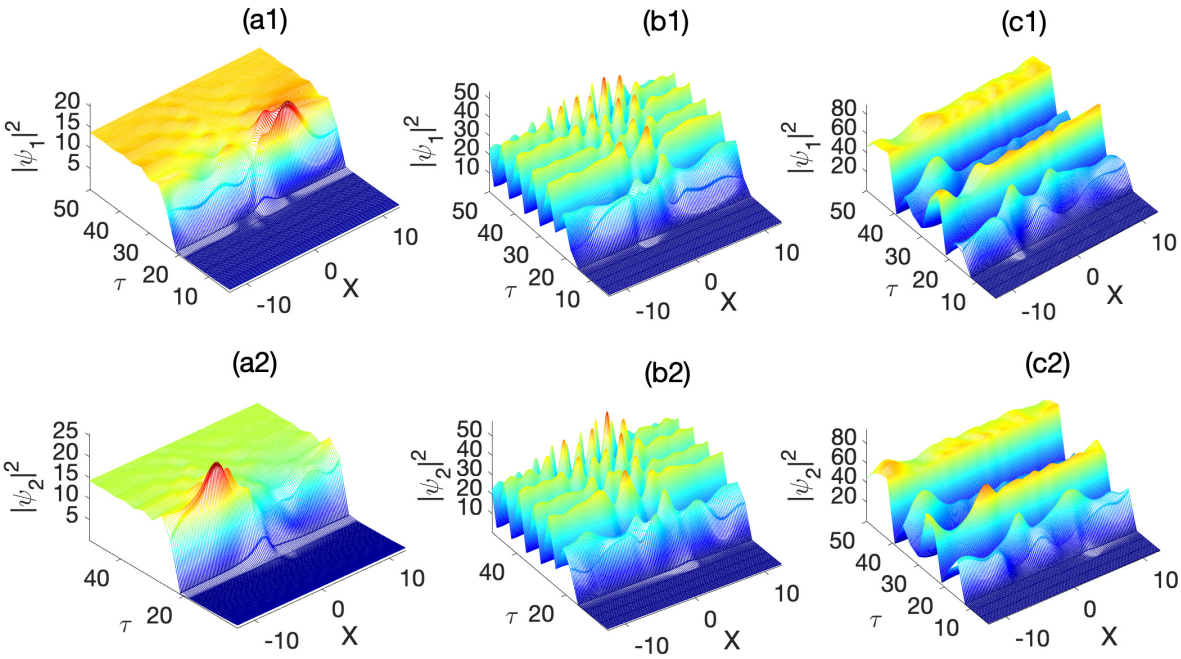


Figure 2.7: Spatiotemporal development of MI for $\beta_0 = -1.5$, and $C_3 = -2$, with α_0 taking the respective values : $(\mathrm{aj})_{j=1,2}$ $\alpha_0 = 0$, $(\mathrm{bj})_{j=1,2}$ $\alpha_0 = 0.25$ and $(\mathrm{cj})_{j=1,2}$ $\alpha_0 = 0.5$, with the other parameter values being: $C_1 = C_2 = 5$, $C_3 = 2$, $C_4 = 0.5$, $K = 1.5$, $n_0 = 1$, $\Delta_0 = 0.01$.

2.6 Summary

The theory of MI has been addressed both analytically and numerically, along with its response to the simultaneous effects of the SO coupling, the helicoidal gauge potential, and the intercomponent interactions. Analytically, a nonlinear dispersion relation has been derived in the form of a fourth-order polynomial alongside the MI growth rate. Comprehensively, the possible compositions of signs of intra-component and inter-component interactions have been discussed, both in repulsive and attractive contexts. Our analysis illustrates that SO coupling, and the intrinsic helical gauge potential, inevitably contribute to the CW disintegration, regardless of the nature of the interaction strength. This is manifested by the appearance of new instability sidebands, thereby enhancing the MI. We performed direct numerical simulations to reinforce our analytical predictions, and the results are unanimous with analytical predictions. Nonlinear and longtime spatiotemporal wave patterns of the underlying set of coupled cubic CGL equations exist and are, as a whole, robust for a wide range of the involved physical specifications. In the process, SO coupling and helicoidal gauge potential may be used as tunable knobs to generate and control complicated nonlinear dynamical processes and the resulting localized long-lived excitations, both in left-handed and right-handed helicoidal dissipative two-component BECs.

Chapter 3

MODULATION INSTABILITY OF TWO-DIMENSIONAL BOSE-EINSTEIN CONDENSATES WITH HELICOIDAL AND A MIXTURE OF RASHBA-DRESSELHAUS SPIN-ORBIT COUPLINGS

3.1 Introduction

Ultracold atomic gases are easily and very efficiently controlled by external magnetic and optical fields. As a result, ultracold gases can be used in advanced studies of condensed-matter and high-energy physics phenomena. However, due to the charge neutrality of the constituent atoms, no Lorentz force acts on these systems in the presence of an electromagnetic field. This makes these systems less reliable in the simulation of phenomena resulting from the coupling between a matter field and a gauge field. Therefore, in recent years scientists have been enthusiastically engaged in studying different ways to produce effective gauge potentials for ultracold atoms [239–244]. One way to generate such a synthetic gauge field is by coupling the atoms with spatially varying laser fields [245,246]. This offers a great advantage since it can be used to generate artificial Abelian gauge, which provides analogs of conventional magnetic fields, one can in principle produce non-Abelian gauge fields [239,247], and the resulting field is adjusted using the laser beams [248]. Among the simplest such non-Abelian fields are artificially induced SO couplings of the linear momentum, $\mathbf{p}$ of a particle to its spin σ in cold atom systems [249]. Different synthetic SO couplings can be engineered by two counter-propagating Raman lasers that couple two hyperfine ground states, and most experimental parameters can be controlled by optical or magnetic means [67, 250]. SO coupled cold atoms lead to exotic substantial effects, such as the fractional quantum spin-Hall effect [117, 251], topological insulators [118–120], GaAs quantum wells [252, 253], Majorana [254, 255] and so on.
A special case of SO coupling is the Rashba-Dresselhaus coupling, which is actively

studied due to its significance in spintronics [256–258]. In RD coupling, the vector potential is proportional to the spin-1/2 operator of a particle within a plane. In Ref. [259], it was proposed that RD-type SO coupling could be generalized for spins greater than 1/2 in cold atomic gases using the N-pod setup, where N laser beams are used to couple N internal atomic ground states to a standard auxiliary state. A tetrapod setup ($N = 4$) was suggested to generate RD-type coupling, where the vector potential is proportional to a spin-1 operator within a plane. The RD coupling has been shown to generate nontrivial structures in spin-1/2, spin-1, and spin-2 BECs [260–267]. In the homogeneous RD-coupled BECs, the solutions of the single-particle Hamiltonian are plane waves.

These solutions provide insight into the stationary states of a trapped system, which might be approximated by superpositions of different numbers of degenerate single-particle solutions. In Ref. [260], it had been stated that the ground state of the trapped RD coupled condensate has two possible phases in the spin-1 case, namely, the plane-wave and also the standing-wave phases. In the plane-wave phase, the ground state of the condensate will be approximated by a single plane wave, whereas in the standing wave phase, each spinor component consists of two counterpropagating coherent plane waves forming a standing-wave.

In this chapter, we first introduce the general Hamiltonian for RD coupled system and we go on to address the nonlinear dynamics of solitary wave formation induced by MI in a mixture of two-component atomic-gas BECs in 2D free space. We introduce a system of two dimensional coupled GP equations with the inclusion of Rashba and Dresselhaus couplings. Only a few studies were devoted on 2D SO coupled BECs of mixed RD type and Rabi couplings [268–270]. In fact, it has been reported that 2D solitons are completely unstable in the case of a balanced Rashba and Dresselhaus mixture [271]. Moreover, for any mixing degree of RD SO couplings, stable solitons can be created in the dipolar BECs [272]. We solve the corresponding GP equations and analyze plane wave stability by means of linear stability analysis and obtain a linearized coupled 2D cubic GP equations under the joint effects of a mixture of RD SO couplings. The analytic expression of growth of MI gain is discussed for different combinations of intra- and inter-component interactions strength. Furthermore, we perform direct numerical integration of the initial coupled 2D cubic GP equations with RD SO couplings.

3.2 Rashba-Dresselhaus SO coupling Hamiltonian

The Rashba-Dresselhaus SO coupling is a certain type of non-Abelian gauge field, originally developed in the context of two-dimensional semiconductors [113, 115]. The Rashba SO coupling and the Dresselhaus SO coupling both couple the momentum $\mathbf{p}$ and the spin σ, but their origins are different. The Rashba SO coupling is the result of the inversion asymmetry of the confining potential (or the structure), whereas the Dresselhaus SO coupling is the result of the inversion asymmetry of the bulk [273,274]. The overall spin-orbit coupling is the result of an interplay between the Rashba and the Dresselhaus SO couplings. The Rashba SO coupling is given by the Hamiltonian

$$H_R = \alpha(P_x\sigma_y - Py\sigma_x), \tag{3.1}$$

and the Dresselhaus SO coupling is

$$H_D = \beta(P_x\sigma_x - Py\sigma_y), \tag{3.2}$$

where α and β are respective coupling strengths. The general Rashba-Dresselhaus coupling Hamiltonian is defined as

$$H_{RD} = \frac{\hbar^2 k}{m} p_x\sigma_x + \eta_{soc}\frac{\hbar^2 k}{m} p_y\sigma_y. \tag{3.3}$$

The parameter k represents the overall strength of the RD SO coupling, while η_{soc} characterize the anisotropy/isotropy of the SO coupling in the x-y plane which can be experimentally controlled by coupling lasers with different amplitudes in the x-y plane. As a definition, the pure Rashba case corresponds to an isotropic SO coupling with $\eta_{soc} = 1$. Otherwise for $0 \leq \eta_{soc} < 1$ the anisotropic coupling is called Rashba-Dresselhaus. These two types of interactions have recently received much attention because of their potential role in the generation and manipulation of polarized spin currents, the spin filters [275], spin accumulation [276], and spin optics [277].

3.3 Basic set of equations

In the SO-coupled BEC, research shows that the symmetric properties of MI disintegrates in the presence of the helical gauge potential, changing the distribution of the MI region and the gain of MI in the parameter space. Also, as the helical gauge potential increases, the MI gain increases for the repulsive atomic interaction case, and when the helical gauge potential decreases, the MI gain decreases for the attractive atomic interaction case [278]. Furthermore, when the miscibility condition due to interatomic interactions is met, both the primary and secondary instability bands lead to spontaneous MI growth [237]. Meanwhile, under the action of the SO coupling, the binary BEC is subject to the MI, which implies that the ground state of the system is likely represented by a striped phase [279]. A study of MI in two-dimensional SO-coupled BECs of pseudo-spin components has been presented, and SO coupling contributes to instability regardless of the nature of intra- and inter-component interaction strengths [280]. It has shown that the SO coupling and Rabi coupled Bose-Bose mixture modify the MI growth rate leading to multiple domains of instability [281].

In order to study the dynamical evolution of the two component helicoidal and a mixture of RD SO coupled BECs under the mean-field approximation, a two-component BEC model is proposed and includes the helicoidal and a mixture of RD SO couplings. Within the mean-field formulation, the two pseudospin states are described by an energy functional given by

$$\mathcal{E} = \int_{-\infty}^{+\infty}\int_{-\infty}^{+\infty} (\mathcal{E}_0 + \mathcal{E}_{int})\, dxdy \tag{3.4}$$

where

$$\mathcal{E}_0 = \frac{1}{2}\left(\Psi^* H_0 \Psi\right), \tag{3.5}$$

where $\Psi = (\Psi_1, \Psi_2)^T$ (T stands for the transpose) is the condensate wavefunction, Ψ_1 and Ψ_2 are associated with the pseudo-spin components. The interaction Hamiltonian

$\mathcal{E}_{int}$ takes the common contact form of the scattering interaction of the $s-$wave [282]. The model Hamiltonian H_0 assumes the form

$$H_0 = H_{HSO} + H_Z + H_{RSO} + H_{DSO}, \tag{3.6}$$

where H_{HSO}, H_Z, H_{RSO}, and H_{DSO} are the helicoidal SO coupling Hamiltonian, Zeeman Hamiltonian, Rashba Hamiltonian, and Dresselhaus Hamiltonian, respectively. The single-particle Hamiltonian of the system can be written as [283]

$$H_{HSO} = \frac{1}{2}\left[(\sigma_0 p_x + \alpha(\vec{\sigma}\cdot\vec{n}))^2 + (\sigma_0 p_y + \alpha(\vec{\sigma}\cdot\vec{m}))^2\right], \tag{3.7}$$

where $p_x = -i\partial/\partial x$ and $p_y = -i\partial/\partial y$ are the momentum operators, $\sigma = (\sigma_x, \sigma_y, \sigma_z)$ is the vector Pauli matrices, σ_0 is the identity matrix, α is the strength of helicoidal SO coupling, and the position-dependent unit vectors $\vec{n}$ and $\vec{m}$ determine the SO coupling direction. For the sake of simplicity, we consider a helicoidal SO coupling with the periods π/β_x and π/β_y, respectively, given by

$$\begin{aligned}\vec{n} &= (\cos(2\beta_x x + 2\beta_y y), 0, \sin(2\beta_x x + 2\beta_y y)),\\ \vec{m} &= (-\sin(2\beta_x x + 2\beta_y y), 0, \cos(2\beta_x x + 2\beta_y y)),\end{aligned} \tag{3.8}$$

where β_x and β_y are the frequencies of rotation in the $x-$ and $y-$directions. The positive and negative values of β_x and β_y are refer to the right- and left-handed modes, respectively [284–286]. We should note that the components of a non-Abelian spin-dependent gauge field could also be done, for instance, by relating the position-dependent unit vectors to a more generalized coordinate-dependent phase parametrization [283]. This question will be addressed in a future work. Next, the Zeeman Hamiltonian is given by

$$H_Z = \frac{\Delta\sigma_z}{2}, \tag{3.9}$$

where Δ is the strength of Zeeman splitting. Originally, the Rashba effect was studied as a phenomenon due to spin splitting by an applied electric field in 3D electron gas systems. The Rashba Hamiltonian originating from SO coupling is given as

$$H_{RSO} = \lambda_R(\vec{\sigma}\wedge\vec{p})\cdot\hat{e}_z, \tag{3.10}$$

where λ_R is the strength of Rashba SO coupling, $\hat{e}_z$ is the unit vector directed along the symmetry axis. In this study, the 2D Rashba SO coupling Hamiltonian reduces to

$$H_{RSO} = \lambda_R(\sigma_x p_y - \sigma_y p_x). \tag{3.11}$$

The Dresselhaus Hamiltonian originating from SO coupling is given as

$$H_{DSO} = \lambda_{3D}(\vec{\sigma}\cdot\vec{K}), \tag{3.12}$$

where λ_{3D} is the 3D strength of Dresselhaus SO coupling, $K_z = p_z(p_x^2 - p_y^2)$, and K_x and K_y can be obtained from K_z by cyclic permutations, leading to $K_x = p_x(p_y^2 - p_z^2)$ and $K_y = p_y(p_z^2 - p_x^2)$, respectively. Here, the 2D Dresselhaus SO coupling Hamiltonian reduces to

$$H_{DSO} = \lambda_D(\sigma_x p_x - \sigma_y p_y), \tag{3.13}$$

where λ_D is the 2D strength of Dresselhaus SO coupling. It should be noted that the Rashba and Dresselhaus SO coupling strengths are intrinsic properties of materials that are largely dependent on their specificity, with restrained growth adjustability in the laboratory. Indeed, the Rashba Hamiltonian is typical of hexagonal A_2B_6 crystals, while the Dresselhaus Hamiltonian is typical of cubic A_3B_5 crystals. Recently SO couplings with equal Rashba and Dresselhaus strengths have been demonstrated in a neutral atomic BEC by dressing two atomic spin states with a pair of Raman lasers, which create a momentum-sensitive coupling between two internal atomic states [121]. The interaction Hamiltonian is given by

$$\mathcal{E}_{int} = \frac{1}{2}\left(g_{11}|\Psi_1|^4 + g_{22}|\Psi_2|^4 + 2g_{12}|\Psi_1|^2|\Psi_2|^2\right), \tag{3.14}$$

where $g_{11} = 2a_{11}/a_\perp$ and $g_{22} = 2a_{22}/a_\perp$ are the two-body intraspecie interactions coefficients, while $g_{12} = 2a_{12}/a_\perp$ and $g_{21} = 2a_{21}/a_\perp$ are the two-body inter-species interaction coefficients. Here, $a_\perp = \sqrt{\hbar/(mw_\perp)}$ denotes the transverse characteristic length, with $w_\perp$ being the transverse trap frequency, m is the atomic mass and $\hbar$ is the Planck constant, a_{11}, a_{22}, and a_{12} are the scattering lengths of the $s-$wave, experimentally adjustable via optical [255], and magnetic [249] Feshbach resonance techniques. The BEC dynamics in the mean-field approximation is governed by $i\hbar\frac{\partial\Psi_j}{\partial t} = \frac{\delta\mathcal{E}}{\delta\Psi_j^*}$, $(j = 1, 2)$, from which the following equations are obtained (see appendix B1)

$$\begin{aligned}
i\frac{\partial\Psi_1}{\partial t} &= -\frac{1}{2}\left(\frac{\partial^2}{\partial x^2} + \frac{\partial^2}{\partial y^2}\right)\Psi_1 + i\beta_x\frac{\partial\Psi_1}{\partial x} + i\beta_y\frac{\partial\Psi_2}{\partial y} + \alpha(\beta_x - \beta_y)(\Psi_2\cos(2\beta_x x + 2\beta_y y) \\
&\quad - \Psi_1\sin(2\beta_x x + 2\beta_y y)) - i\alpha\left(\sin(2\beta_x x + 2\beta_y y)\frac{\partial\Psi_1}{\partial x} + \cos(2\beta_x x + 2\beta_y y)\frac{\partial\Psi_1}{\partial y}\right) \\
&\quad - i\alpha\left(\cos(2\beta_x x + 2\beta_y y)\frac{\partial\Psi_2}{\partial x} - \sin(2\beta_x x + 2\beta_y y)\frac{\partial\Psi_2}{\partial y}\right) - i(\lambda_R + i\lambda_D)\frac{\partial\Psi_2}{\partial y} \\
&\quad - \beta_y(\lambda_R + i\lambda_D)\Psi_1 + i\beta_x(\lambda_R - i\lambda_D)\Psi_2 + (\lambda_R - i\lambda_D)\frac{\partial\Psi_2}{\partial x} + \frac{\Delta}{2}\Psi_1 \\
&\quad + (g_{11}|\Psi_1|^2 + g_{12}|\Psi_2|^2)\Psi_1,
\end{aligned} \tag{3.15a}$$

$$\begin{aligned}
i\frac{\partial\Psi_2}{\partial t} &= -\frac{1}{2}\left(\frac{\partial^2}{\partial x^2} + \frac{\partial^2}{\partial y^2}\right)\Psi_2 - i\beta_x\frac{\partial\Psi_2}{\partial x} + i\beta_y\frac{\partial\Psi_1}{\partial y} - \alpha(\beta_x - \beta_y)(\Psi_1\cos(2\beta_x x + 2\beta_y y) \\
&\quad + \Psi_2\sin(2\beta_x x + 2\beta_y y)) - i\alpha\left(\cos(2\beta_x x + 2\beta_y y)\frac{\partial\Psi_1}{\partial x} - \sin(2\beta_x x + 2\beta_y y)\frac{\partial\Psi_1}{\partial y}\right) \\
&\quad + i\alpha\left(\sin(2\beta_x x + 2\beta_y y)\frac{\partial\Psi_2}{\partial x} - \cos(2\beta_x x + 2\beta_y y)\frac{\partial\Psi_2}{\partial y}\right) - (\lambda_R - i\lambda_D)\frac{\partial\Psi_1}{\partial x} \\
&\quad - \beta_y(\lambda_R - i\lambda_D)\Psi_2 + i\beta_x(\lambda_R - i\lambda_D)\Psi_1 - i(\lambda_R + i\lambda_D)\frac{\partial\Psi_1}{\partial y} - \frac{\Delta}{2}\Psi_2 \\
&\quad + (g_{22}|\Psi_2|^2 + g_{21}|\Psi_1|^2)\Psi_2.
\end{aligned} \tag{3.15b}$$

As it is obvious, some coefficients of the above set of GP equations are dependent of space, which take us away form the main objective of this work. In order to obtain the free space equation, there are specific values to be taken by β_x and β_y. In doing so, we will consider the two cases $\beta_x = \beta_y = 0$ and $\beta_x = \beta_y = \beta$, with $(\beta x + \beta y) = \pi/2$. The

cases $\beta_x = \beta_y = 0$ pictures a system where the helicoidal gauge potential is switched off, leaving the system with, among other terms, the SO coupling parameter α and the RD SO coupling terms supported by λ_R and λ_D, respectively. The corresponding set of equations then writes

$$i\frac{\partial\psi_1}{\partial t} = -\frac{1}{2}\left(\frac{\partial^2}{\partial x^2}+\frac{\partial^2}{\partial y^2}\right)\psi_1 - i\alpha\frac{\partial\psi_1}{\partial y} - i\alpha\frac{\partial\psi_2}{\partial x} + \frac{\Delta}{2}\psi_1 + (g_{11}|\psi_1|^2 + g_{12}|\psi_2|^2)\psi_1 + \lambda_R\left(\frac{\partial\psi_2}{\partial x} - i\frac{\partial\psi_2}{\partial y}\right) - i\lambda_D\left(\frac{\partial\psi_2}{\partial x} + i\frac{\partial\psi_2}{\partial y}\right), \tag{3.16a}$$

$$i\frac{\partial\psi_2}{\partial t} = -\frac{1}{2}\left(\frac{\partial^2}{\partial x^2}+\frac{\partial^2}{\partial y^2}\right)\psi_2 - i\alpha\frac{\partial\psi_1}{\partial x} - i\alpha\frac{\partial\psi_2}{\partial y} - \frac{\Delta}{2}\psi_2 + (g_{22}|\psi_2|^2 + g_{21}|\psi_1|^2)\psi_2 - \lambda_R\left(\frac{\partial\psi_1}{\partial x} + i\frac{\partial\psi_1}{\partial y}\right) + i\lambda_D\left(\frac{\partial\psi_1}{\partial x} - i\frac{\partial\psi_1}{\partial y}\right). \tag{3.16b}$$

The other case, i.e. $\beta_x = \beta_y = \beta$, with $(\beta x + \beta y) = \frac{\pi}{2}$, which corresponds to a case of square lattice cell with equal $x-$ and $y-$ periods, includes all the effects brought by the helicoidal SO coupling and the RD SO coupling, leading to the set of GP equations

$$i\frac{\partial\psi_1}{\partial t} = -\frac{1}{2}\left(\frac{\partial^2}{\partial x^2}+\frac{\partial^2}{\partial y^2}\right)\psi_1 + i\beta\frac{\partial\psi_1}{\partial x} + i\beta\frac{\partial\psi_2}{\partial y} + i\alpha\frac{\partial\psi_1}{\partial y} + i\alpha\frac{\partial\psi_2}{\partial x} - \beta\psi_1(\lambda_R + i\lambda_D) + \beta\psi_2(\lambda_D + i\lambda_R) + \lambda_R\left(\frac{\partial\psi_2}{\partial x} - i\frac{\partial\psi_2}{\partial y}\right) - i\lambda_D\left(\frac{\partial\psi_2}{\partial x} + i\frac{\partial\psi_2}{\partial y}\right) + \frac{\Delta}{2}\psi_1 + \left(g_{11}|\psi_1|^2 + g_{12}|\psi_2|^2\right)\psi_1, \tag{3.17a}$$

$$i\frac{\partial\psi_2}{\partial t} = -\frac{1}{2}\left(\frac{\partial^2}{\partial x^2}+\frac{\partial^2}{\partial y^2}\right)\psi_2 - i\beta\frac{\partial\psi_2}{\partial x} + i\beta\frac{\partial\psi_1}{\partial y} + i\alpha\frac{\partial\psi_1}{\partial x} + i\alpha\frac{\partial\psi_2}{\partial y} - \beta\psi_2(\lambda_R - i\lambda_D) + \beta\psi_1(\lambda_D + i\lambda_R) - \lambda_R\left(\frac{\partial\psi_1}{\partial x} + i\frac{\partial\psi_1}{\partial y}\right) - i\lambda_D\left(\frac{\partial\psi_1}{\partial x} - i\frac{\partial\psi_1}{\partial y}\right) - \frac{\Delta}{2}\psi_2 + \left(g_{22}|\psi_2|^2 + g_{21}|\psi_1|^2\right)\psi_2. \tag{3.17b}$$

We should also stress that in order to get the system of Eqs.(3.15), we have introduced the following gauge transformations

$$\Psi_j = e^{-i\alpha^2 t}e^{-i(\beta_x^2+\beta_y^2)t/2}e^{-i(\sigma_z\beta_x x+\sigma_x\beta_y y)}\psi_j,\ j = 1, 2, \tag{3.18}$$

to switch to the rotating frame for the chosen gauge field. In doing so, the point translation symmetry transforms into a continuous translational symmetry of the derived equation. Finally, the spatial variables x and y, time t, density $(|\psi_1|^2 + |\psi_2|^2)$, and energy are given in the normalized units $a_\perp$, $w_\perp^{-1}$, $a_\perp^{-1}$, and $\hbar w_\perp$, respectively. The wave functions are normalized as $N_j = \int(|\psi_j|^2 dxdy)$, $(j = 1, 2,)$, while the total number of atoms of the jth component is $N = N_1 + N_2 = \int\int(|\psi_1|^2 + |\psi_2|^2)\,dxdy$, which is a dynamical invariant of non-dissipative BEC systems. In what follows, we address comprehensively the instability of CWs solutions, taking advantages of the above two cases.

3.4 Linear stability analysis of a system of two coupled 2D cubic GP equations with helicoidal and a RD mixtures SO-couplings

According to the general theory of MI, the above systems admit CW solutions $\psi_j = e^{-i\mu t}\sqrt{n_{j0}}, \quad j = 1, 2,$, where μ is the common chemical potential of both components, with uniform densities $n_{10} = n_{20} = n_0$. By replacing such solutions into the generic GP equations, a linear dispersion relation is found between the chemical potential, the Zeeman splitting energy, the density n_0 and the interatomic interaction parameters g_{11}, g_{22} and g_{12}. In general, the stability of the CW solutions is checked by introducing small perturbations so that $\psi_j = e^{-i\mu t}(\sqrt{n_{j0}} + \delta\psi_j)$, $j = 1, 2$, where the perturbed fields $\delta\psi_j$ are taken in the form

$$\delta\psi_j = \zeta_j \cos(K_1 x + K_2 y - \Omega t) + i\eta_j \sin(K_1 x + K_2 y - \Omega t), \tag{3.19}$$

where K_1 and K_2 are the perturbation wavenumbers in the x and y direction, respectively; Ω is a complex modulation frequency, ζ_j, and η_j are constant complex amplitudes. Linearizing the above perturbed solutions around the unperturbed ones leads to a linear homogeneous system of equations in terms of ζ_1, ζ_2, η_1 and η_2 of the form

$$M \times (\zeta_1, \zeta_2, \eta_1, \eta_2)^T = 0, \tag{3.20}$$

where M is the system's matrix written as

$$M = \begin{pmatrix} m_{11} & m_{12} & m_{13} & m_{14} \\ m_{21} & m_{22} & m_{23} & m_{24} \\ m_{31} & m_{32} & m_{33} & m_{34} \\ m_{41} & m_{42} & m_{43} & m_{44} \end{pmatrix}, \tag{3.21}$$

with the elements m_{ij} of the matrix depending not only on the perturbation frequency Ω and the wavenumbers K_1 and K_2, but also on the other parameters including the SO coupling strengths and the interatomic interaction parameters. Interestingly, for system (3.21) to admit non-trial solution, the determinant of its matrix should be null, which leads to a general nonlinear dispersion relations of the form

$$\Omega^4 + P_3\Omega^3 + P_2\Omega^2 + P_1\Omega + P_0 = 0, \tag{3.22}$$

where general expressions for the coefficients P_j $(j = 1, 2, 3)$ are given in the appendix B2. Eq.(3.22) can be solved analytically to obtain the solutions

$$\begin{aligned}
\Omega_{1,2} &= -\frac{P_3}{4} - \frac{1}{2}\sqrt{\frac{1}{4}P_3^2 - \frac{2}{3}P_2 + \Lambda} \\
&\quad \pm \frac{1}{2}\left(\sqrt{\frac{2}{3}P_2 - \frac{1}{4}P_3^2 - \Lambda - 2P_2 + \frac{3}{4}P_3^2 + \frac{P_3^3 - 4P_3P_2 + 8P_0}{4\sqrt{\frac{1}{4}P_3^2 - \frac{2}{3}P_2 + \Lambda}}}\right), \\
\Omega_{3,4} &= -\frac{P_3}{4} + \frac{1}{2}\sqrt{\frac{1}{4}P_3^2 - \frac{2}{3}P_2 + \Lambda} \\
&\quad \pm \frac{1}{2}\left(\sqrt{\frac{2}{3}P_2 - \frac{1}{4}P_3^2 - \Lambda - 2P_2 + \frac{3}{4}P_3^2 - \frac{P_3^3 - 4P_3P_2 + 8P_0}{4\sqrt{\frac{1}{4}P_3^2 - \frac{2}{3}P_2 + \Lambda}}}\right),
\end{aligned} \tag{3.23}$$

where $\Lambda = \frac{1}{3}\left(\sqrt[3]{\frac{\Delta_2+\sqrt{\Delta_2^2-4\Delta_1^3}}{2}} + \frac{\Delta_1}{\sqrt[3]{\frac{\Delta_2+\sqrt{\Delta_2^2-4\Delta_1^3}}{2}}}\right)$, with $\Delta_1 = P_2^2 - 3P_3P_1 + 12P_0$, and $\Delta_2 = 2P_2^3 - 9P_3P_2P_1 + 27P_3^2P_0 + 27P_1^2 - 72P_2P_0$. Depending on system parameters, solutions (3.23) can be positive, negative or even complex. Nevertheless, the stability of the CW is due to real, negative or positive, values of Ω. In general, complex solutions of Eq.(3.21) are written as $\Omega = \Omega_r + i\Omega_i$, so that $e^{-i\Omega t} = e^{-i\Omega_r t} \times e^{\Omega_i t}$. The latter implies that MI will take for a non-zero imaginary part of the perturbation frequency, which allows to extract necessary information on the occurence of the instability using the maximum MI growth rate

$$\zeta(\Omega) = \{|\mathrm{Im}(\Omega)|\}_{\max}. \tag{3.24}$$

3.5 MI gain analysis of two coupled 2D cubic GP equations with a mixture of RD SO couplings

3.5.1 Case 1: growth rate spectrum for $\beta_x = \beta_y = 0$

This case corresponds to the modified GP equations (3.16). Following the above-described procedure of linear stability analysis, the Zeeman splitting, the interatomic interactions and chemical potential are linked by the dispersion relation (matrix elements are given in appendix B3)

$$\frac{\Delta}{2} = (-1)^j \left(g_{jj}n_{j0} + g_{12}n_{3-j,0} - \mu\right). \tag{3.25}$$

In order to proceed, we consider $g_{11} = g_{22} = g$ and we, first of all, discuss the values of g and g_{12} that may give rise to instability. The corresponding results are displayed in Fig. 3.1, where the MI growth rate is plotted against the intracomponent coupling strength g. Fixing $g_{12} = 0.8$, we first consider in Fig. 3.1(a) the case where $\lambda_R = \lambda_D = 0$, which implies that the RD SO coupling is switched off. The selected values of α give rise to regions of g where the MI growth rate is positive. Such regions are highly affected by the values of the gauge amplitude. For example, $\alpha = 0.1$ gives rise to values of $\zeta \neq 0$ only in the area $g < 0$, while the maximum pick is situated at $g = -0.5$. This means that for that value of α, only attractive intercomponent interactions support MI and suitably balance with repulsive intercomponent coupling. With increasing α, the instability interval gets expanded and includes some positive values of g. Progressively, the maximum growth rate ζ shifts towards positive values of g, while instability finally relies on values of $g > 0$, exclusively, for $\alpha = 1$.

In order to explore the competition between the gauge amplitude and the RD SO coupling parameters, we fix in Fig. 3.1 (b) $\lambda_R = \lambda_D = 0.01$, with g_{12} keeping the same value and α changing as in Fig. 3.1(a). The same scenario is apparent, except that minor instability regions emerge, with g taking positive and negative values. Interestingly, for the case $\alpha = 1$, there is a singularity that admits instability on both sides, except that the maximum growth rate of instability is situated in the area $g > 0$. This shows that the investigated instability is likely to take place when intracomponent interactions are repulsive. In the same context, it would be interesting to mention that the features depicted in Fig. 3.1 represent both miscibility and immiscibility cases.

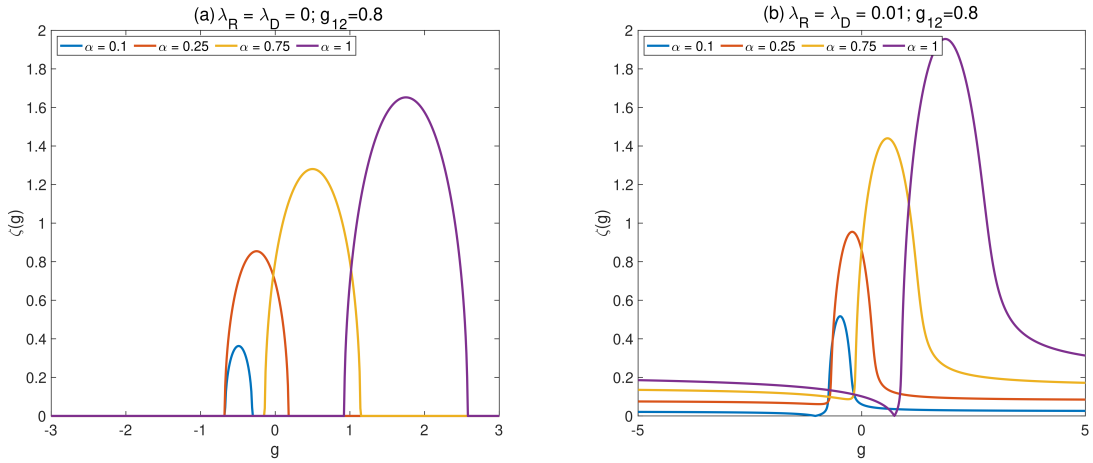


Figure 3.1: Distribution of the MI growth rate versus the interatomic coupling g for different values of the SO coupling strength when: (a) the RD SO coupling is absent, i.e., $\lambda_D = \lambda_R = 0$ and (b) in presence of the RD SO coupling, i.e., $\lambda_D = \lambda_R = 0.01$, with $g_{12} = 0.8$, $K_1 = K_2 = 1$ and $n_0 = 1$.

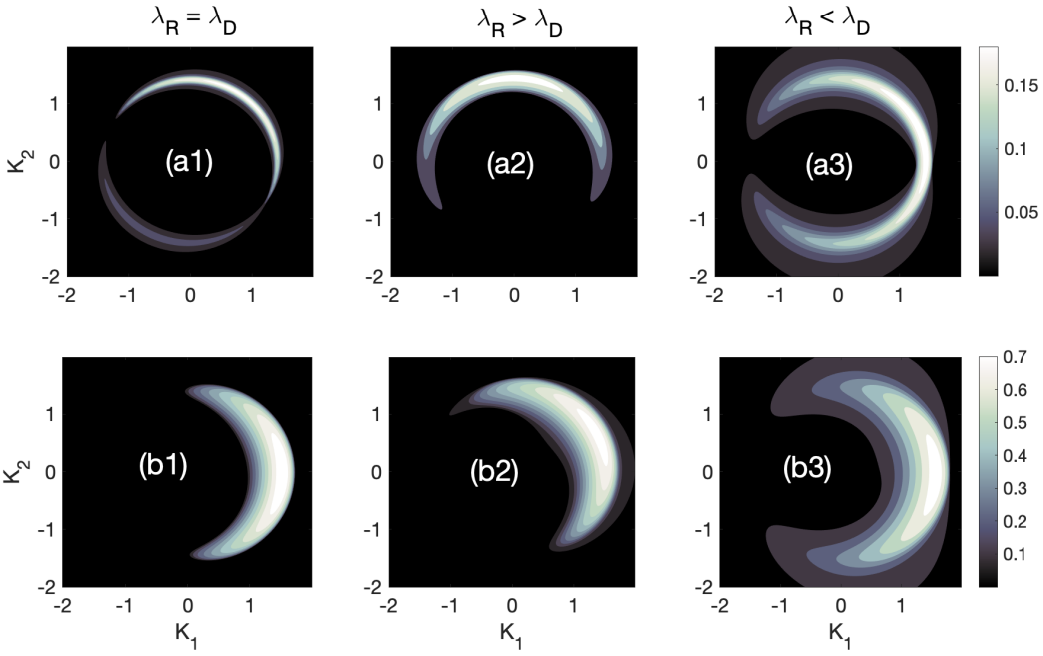


Figure 3.2: The panels show the growth rate of MI in the $(K_1, K_2)-$plane for $\alpha = 0$ (panels $(\mathrm{aj})_{j=1,2,3}$) and $\alpha = 0.25$ (panel$(\mathrm{bj})_{j=1,2,3}$). From left to right, the columns correspond to the different cases $\lambda_R = \lambda_D$, $\lambda_R > \lambda_D$ and $\lambda_R < \lambda_D$, respectively, with $g_{12} = 0.8$, and $n_0 = 1$. White regions correspond to zones of instability, while dark areas are where the CWs solutions are likely to remain stable under modulation.

In panels of Fig. 3.2, based on the predictions form Fig. 3.1, the MI growth rate distribution is represented against the wavenumbers K_1 and K_2, where panels $(\mathrm{aj})_{j=1,2,3}$ correspond to the case $\alpha = 0$ and panels $(\mathrm{bj})_{j=1,2,3}$ display the MI growth rate spectrum for $\alpha = 0.25$. The different cases $\lambda_R = \lambda_D$, $\lambda_R > \lambda_D$ and $\lambda_R < \lambda_D$ are treated for each of the values of the gauge amplitude α. For example, in panel (a1), in the absence

of the gauge amplitude and $\lambda_R = \lambda_D$, the MI is characterized by asymmetric white regions with a crescent shape. When $\lambda_R > \lambda_D$, there remains an extended reduced cylinder, while the maximum growth rate takes place in positive zones of K_2 with corresponding values of K_1 being found in positive and negative areas as depicted in Fig. 3.2(a2). Interestingly, the detected partially circular growth rate zone gets expanded and rotates around $K_1 = K_2 = 0$. As it is confirmed by Fig. 3.2(a3), the region of instability is extended by a hallow of instability around the bright main cylindrical zone, which gives more chance to instability to occur when K_1 and K_2 are both positive or negative. For the rest of the regions that are dark, the plane wave is supposed to remain unstable under modulation. Remarkably, the features displayed by the growth rate distribution of panels $(\mathrm{bj})_{j=1,2,3}$ in Fig. 3.2 show a strong impact of the presence of the gauge amplitude. Even though this case does not include the helicoidal term, the instability zone display meniscus, which is mainly situated in the positive area of the perturbation wavenumber K_1, with values of K_2 being positive or negative as witnessed in Fig. 3.2(b1), where $\lambda_R = \lambda_D$, one can also notice a rotation around $K_1 = K_2 = 0$ due to the presence of gauge amplitude. There is a delocalization of such zones of instability under the condition $\lambda_R > \lambda_D$ [see Fig. 3.2(b2)], while the MI growth rate distribution in the $(K_1, K_2)-$plane gets further expanded. Like in the case of Fig. 3.2(a3), the instability zone enlarges and gives rise to the emergence of an apparent hallow of instability points.

3.5.2 Case 2: growth rate spectrum for $\beta_x = \beta_y = \beta$, with $(\beta x + \beta y) = \pi/2$

This other particular case corresponds to the set of GP equations (3.17) and includes strong competition between the helicoidal and the RD SO couplings. To remind, the first case, for which $\beta_x = \beta_y = 0$ was switching off the effect of the helicoidal gauge potential, therefore reducing the presence of the helicoidal SO coupling to only the gauge amplitude. Therefore, in the present context, and based on the linear stability analysis with uniform densities, the Zeeman splitting energy, the chemical potential, and the interatomic coupling parameters are linked via the linear dispersion relation

$$\begin{aligned}\frac{\Delta}{2} &= (-1)^j \left(g_{jj} n_{j0} + g_{12} n_{3-j,0} - \mu\right) - (-1)^j \beta\lambda_R \\ &\quad + i\beta\lambda_D - (-1)^{3-j}\beta\lambda_D + (-1)^j i\beta\lambda_R, \quad j = 1, 2.\end{aligned} \tag{3.26}$$

Moreover, the reader should be aware that the coefficient of the nonlinear dispersion relation (3.22) will be affected by the presence of terms supported by the presence of the helicoidal gauge potential β, as witnessed by the matrix elements given in appendix B4.

When $\lambda_D = \lambda_R = 0$, the RD SO coupling is absent, and one recovers the two-dimensional system proposed by Kartashov [287] and studied recently by Li et al. [278]. Such a system takes advantage of the presence of the helicoidal SO coupling and includes a strong impact from the interatomic interactions. In order to find suitable values for g and g_{12} capable of giving rise to instability in this context, we have plotted the MI growth rate versus g in Fig. 3.3. There, panel (a) corresponds to $\alpha = 0$ and panel (b) to $\alpha = 0.25$. When the gauge amplitude is switched of, i.e., $\alpha = 0$, $\beta = 0.25$ instability is announced in areas where $g < 0$, around, and including, the point $g = -0.5$. That exclusive repulsive effect of the intracomponent interaction is

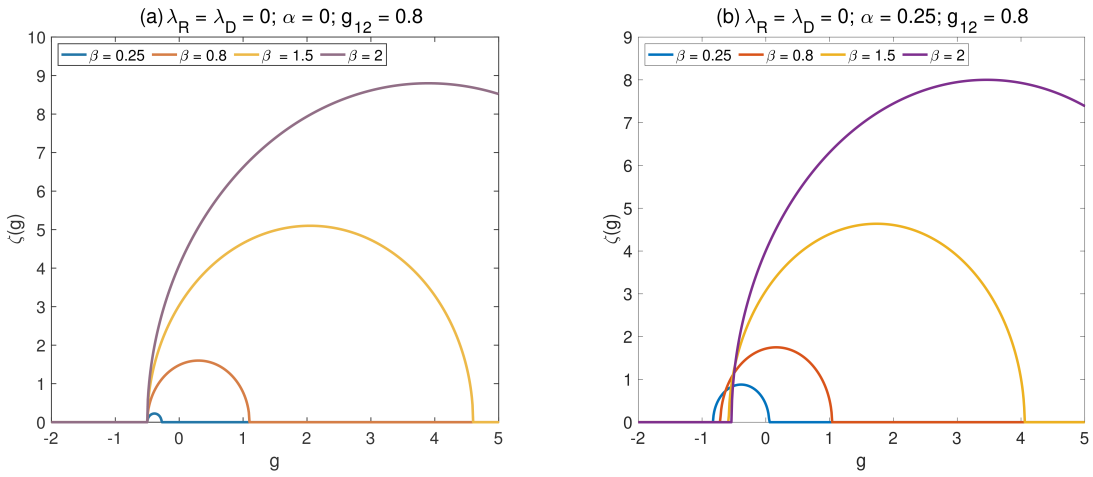


Figure 3.3: Distribution of the MI growth rate versus the interatomic coupling g for different values of the SO coupling strength when: (a) the RD SO coupling is absent, i.e., $\lambda_D = \lambda_R = 0$ and (b) in presence of the RD SO coupling, i.e., $\lambda_D = \lambda_R = 0.01$, with $g_{12} = 0.8$, $K_1 = K_2 = 1$ and $n_0 = 1$.

broken when β increases, therefore extending the MI growth rate spectrum towards positive values of g. The phenomenon becomes more pronounced as the helicoidal gauge potential increases, leading to a marginal instability zone appearing in the whole area $g > g_{cr}$, with $g_{cr} < -0.5$ being the lower values taken by g. The same spectrum of behaviors is ostensible in Fig. 3.3(b), where the gauge amplitude $\alpha \neq 0$, with β taking the same values as in Fig. 3.3(a). We should, however, stress that the MI growth rate corresponding to $\beta = 0.25$ is more localized than the one in Fig. 3.3(a) and covers a large interval of g that supports instability. With increasing the helicoidal gauge potential, the zone of instability gets slightly delocalized and expands more and more with increasing β.

The most interesting case, which deserves to be regarded with emphasis, is realized when $\lambda_D = \lambda_R \neq 0$, in the presence of the gauge amplitude α and the helicoidal gauge potential β. When α and β take non-zero values, they constitute the helicoidal SO coupling [287]. The competition between the two types of SO coupling on the values of g supporting instability is summarized in Fig. 3.4, where the growth rate of instability is displayed for different values of the helicoidal gauge potential β. Fig. 3.4(a) shows the MI growth rate distribution when the gauge amplitude α is zero. There are intervals of g where ζ is non-zero, which get expanded with increasing the helicoidal gauge potential β from 0.25 to 2. Interestingly, minor zones of instability appear from where some possible values of g can be extracted to obtain instability. Fully considering the helicoidal SO coupling, ζ is shown in Fig. 3.4(b), where $\alpha = 0.25$. The main behavior that appears here is the enlargement of the instability zone with increasing β. Also, the interval of g where instability is expected is well delimited and includes as a whole positive and negative values of the intracomponent interaction parameter.

The spectrum of Figs. 3.3 and 3.4 gave us information on values of some key parameters, like the interatomic coupling parameters, to be used for instability to manifest itself. Taking advantage of that, the growth rate of MI is plotted in Fig. 3.5, in the plane of the perturbation wavenumbers K_1 and K_2. Fixing $\alpha = 0.25$ $g = -0.4$ and $g = 0.8$, the panels $(\mathrm{aj})_{j=1,2,3}$ of Fig. 3.5 show the growth rate spectrum for $\lambda_R = \lambda_D = 0$, while panels, from left to right correspond respectively to $\beta = 0.25$, $\beta = 0.5$ and $\beta = 1$.

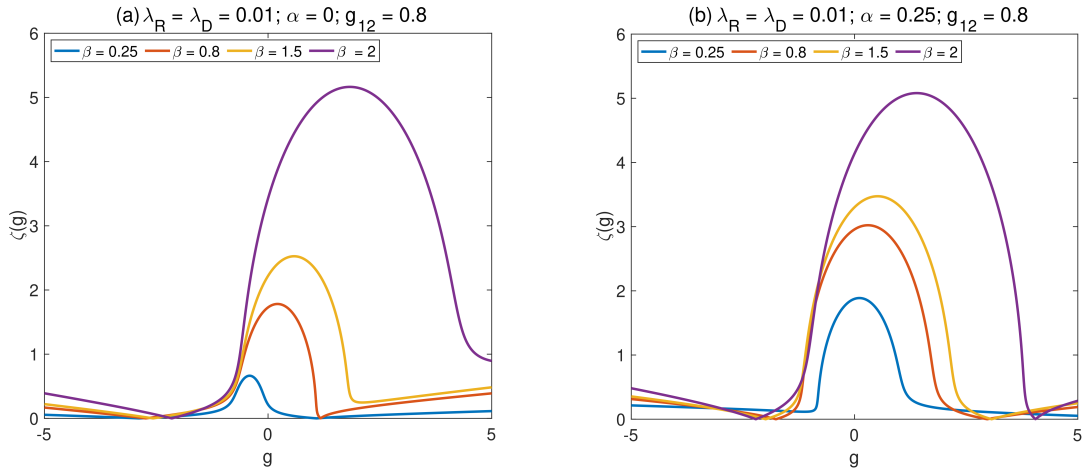


Figure 3.4: Distribution of the MI growth rate versus the interatomic coupling g for different values of the SO coupling strength when: (a) the RD SO coupling is absent, i.e., $\lambda_D = \lambda_R = 0$ and (b) in presence of the RD SO coupling, i.e., $\lambda_D = \lambda_R = 0.01$, with $g_{12} = 0.8$, $K_1 = K_2 = 1$ and $n_0 = 1$.

Initially, instability is supported by a set of asymmetric breast, with maximum mainly situated in the area $K_2 > 0$, while minor and major objects belong, respectively, to areas $K_1 > 0$ and $K_1 < 0$. With increasing the helicoidal gauge potential β to 0.5, the instability zones get expanded, therefore covering wider areas where unstable patterns could be expected. This fact is confirmed by the last figure of instability in this series, where the breasts are amplified, with hallows of points visible in the negative part of the wavenumber K_2, which might give rise to instability. We should stress that by switching off the RD SO coupling, the system at hand just feels the effect of the helicoidal SO coupling. Otherwise, the model comprises two submodels that can constitute individual studies, especially when generalized to three-dimensional formulations. For instance, bringing back the RD SO coupling by imposing $\lambda_R = \lambda_D \neq 0$, one gets the instability figures of panels $(\text{bj})_{j=1,2,3}$ in Fig. 3.5, where β, the helicoidal gauge potential, changes in the same manner. Evidently, the competition between the helicoidal SO coupling and the RD SO-coupling modifies the figure of instability. For example, instead of the two breasts of instability obtained in panels $(\text{aj})_{j=1,2,3}$ of Fig. 3.5, the instability develops under four lobes, distributed in positive and negative zones of K_1 and K_2. In this context, the intensity of the MI growth rate gets amplified as β increases, leading to four expanded regions of instability.

To conclude our linear stability analysis, we represent in Fig. 3.6 the MI growth rate distribution versus α and β. Fixing $g_{12} = 0.8$ and $g = 1.2$, different combinations of λ_D and λ_R are used to assess the competitive impact between the helicoidal and the RD SO coupling on the MI growth rate behavior. For $\lambda_R = \lambda_D = 0.01$, instability is supported by an asymmetric cylinder with a hole of stability around, and including, the point $(\alpha, \beta) = (0, 0)$. Interestingly, the maximum instability growth rate is shared between some of the areas $\beta > 0$ and $\beta < 0$. Precision should be made that when $\beta > 0$ the coupling is said to be the left-handed, and right-handed when $\beta < 0$. With increasing the Dresselhaus SO-coupling parameter λ_D to 0.02, one obtains the features of Fig. 3.6(b), where the zone of maximum instability tends to shift to the $\beta < 0$, and $\alpha < 0$, zones into a broken cylindrical MI growth rate. This is more visible

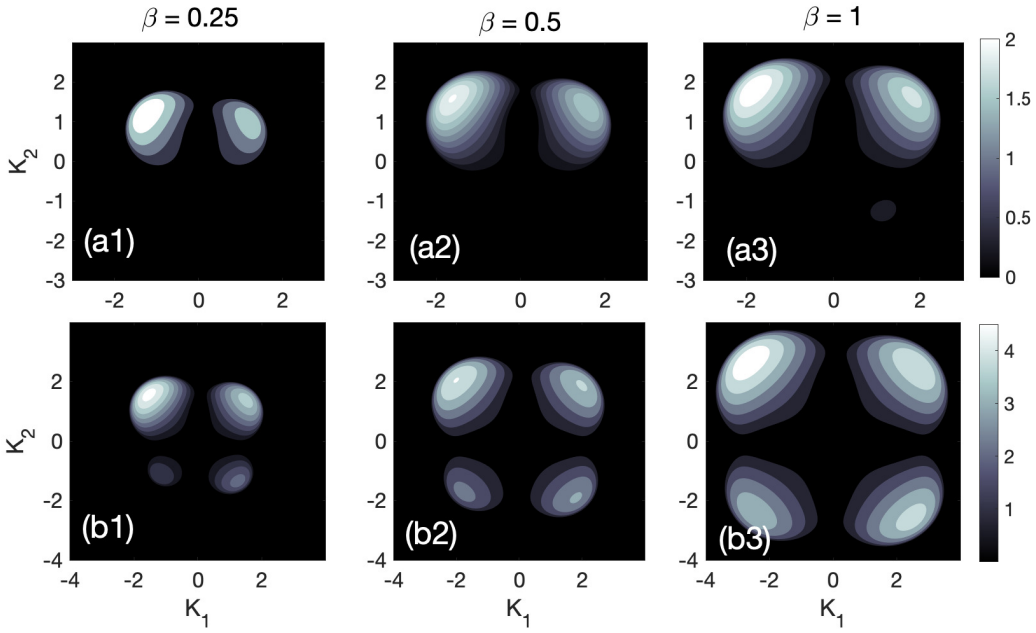


Figure 3.5: The panels show the distribution of the growth rate of MI in the $(K_1, K_2)-$plane for $\lambda_R = \lambda_D = 0$ (panels $(\text{aj})_{j=1,2,3}$) and $\lambda_R = \lambda_D \neq 0$ $(\text{panel(bj)}_{j=1,2,3})$. From left to right, the columns correspond to the different cases $\beta = 0.25$, $\beta = 0.5$ and $\beta = 1$, respectively, with $g_{12} = 0.8$, $\alpha = 0.25$ and $n_0 = 1$. White regions correspond to zones of instability, while dark areas are where the CWs solutions are likely to remain stable under modulation.

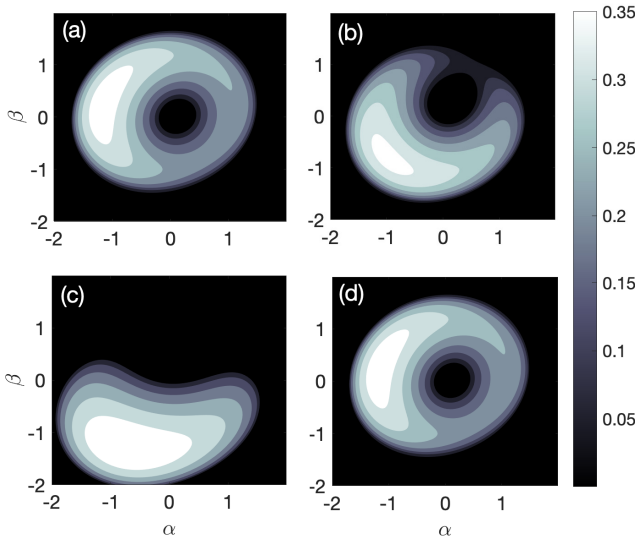


Figure 3.6: The panels show the growth rate of MI $(\alpha, \beta)-$plane for (a) $\lambda_R = \lambda_D = 0.01$, (b) $\lambda_R = 0.01$ and $\lambda_D = 0.02$ (c) $\lambda_R = 0.01$ and $\lambda_D = 0.04$, and (d) $\lambda_R = 0.04$ and $\lambda_D = 0.04$.

in Fig. 3.6(c), where the cylindrical structure of the MI growth rate is completely broken, with the maximum growth rate taking place exclusively for right-handed SO

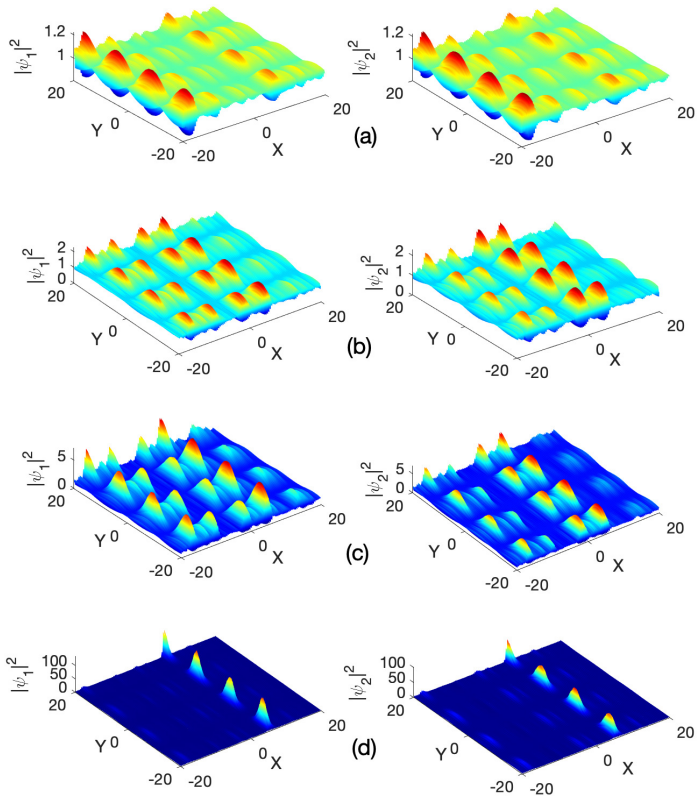


Figure 3.7: MI evolution in both condensates with increasing time in presence of both the SO coupling and the RD SO coupling. Fixing $\alpha = 0.1$, and $\lambda_R = \lambda_D = 0.01$, panels from (a) to (d) correspond to the respective instants $t = 25$, $t = 60$, $t = 100$ and $t = 170$. The other parameters are $K_1 = K_2 = 1.5$, $n_0 = 1$, $g_{11} = g_{22} = 0.5$ and $g_{12} = 0.6$.

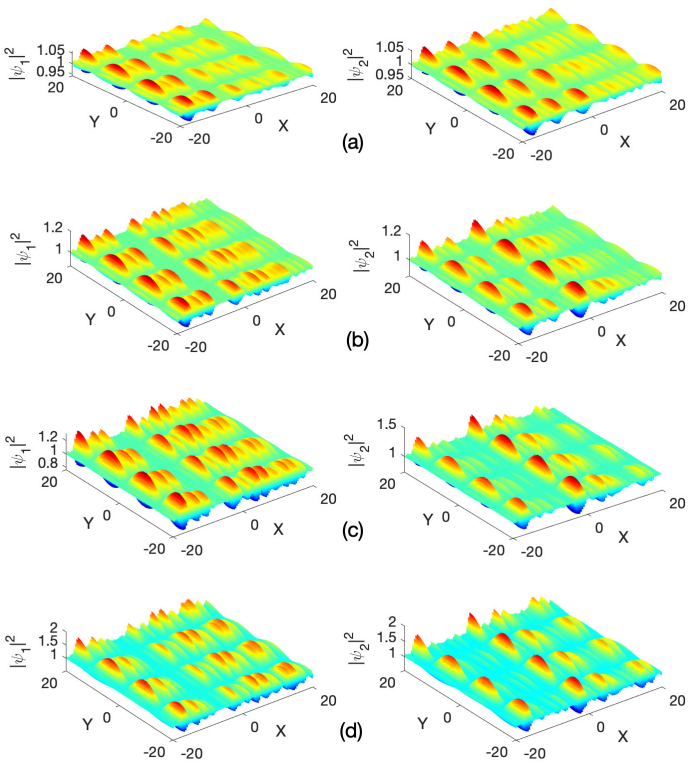


Figure 3.8: MI evolution in both condensates with increasing time in presence of both the SO coupling and the RD SO coupling. Fixing $\alpha = 0.1$, and $\lambda_R > \lambda_D$, panels from (a) to (d) correspond to the respective instants $t = 25$, $t = 60$, $t = 100$ and $t = 170$. The other parameters are $K_1 = K_2 = 1.5$, $n_0 = 1$, $g_{11} = g_{22} = 0.5$ and $g_{12} = 0.6$.

coupling, with $\lambda_D = 0.02$ and $\lambda_R = 0.01$. Interestingly, the initial MI spectrum of Fig. 3.6(a) is recovered when increasing λ_R to 0.04 as shown in Fig. 3.6(d). This implies that the Rashba SO coupling, in this particular context, has the reverse effect of the Dresselhaus SO-coupling. To remind, MI in BEC has been given considerable importance over a long period of time, owing to its fundamental and applied interest in various aspects [288]. In particular, MI has been found to be relevant in understanding the formation and propagation of solitonic waves and also apparent in explaining the domain formation and quantum phase transition. Overall, the above linear stability analysis shows that the MI growth rate ζ is very sensitive to the variation of the competing SO parameters, which offers different figures of instability, to be confirmed numerically in the next section.

3.6 Numerical results on wave train formation

The linear stability analysis performed in Sec. 3.4 relies on linearizing the perturbed CWs around the unperturbed solutions. Therefore, only the onset of MI can be predicted, while no information about the longtime spatiotemporal evolution of the instability growth can be obtained, which requires their confrontation with direct numerical simulations on Eqs. (3.16) and (3.17). This is achieved using the SSFM using the initial

conditions:

$$\begin{aligned}\psi_1(x,y,0) &= \psi_2(x,y,0)\\ &= n_0 + \varepsilon\cos(K_1 x + K_2 y),\end{aligned} \tag{3.27}$$

where the perturbation wavenumbers $K = K_1 = K_2$ have been chosen based on the growth rate spectra of Figs. 3.1a-3.3, with $n_0 = 1$ and $\varepsilon = 0.001$, so that $\varepsilon \ll n_0$. The features of MI are discussed in terms of the amplitude maxima, while one pays particular attention to the simultaneous effects brought by the helicoidal and the RD SO couplings. Different combinations of such parameters values are used according to the predictions of the linear stability analysis. However, we should stress that according to the derivation of the model at hand, we have the two possibilities discussed in the linear stability part. Precision should be made that instability features show some differences, while the two systems may share some instability regions. For this chapter, numerical results for each of the cases are treated separately.

3.6.1 MI patterns for the case $\beta_x = \beta_y = 0$

This particular case refers to Eqs. (3.16) and results from numerical simulations are recorded in Figs. 3.7-3.9. The model does not consider the effect of β, the helicoidal gauge potential, so competitive effects will be brought out only by the gauge amplitude α, λ_R and λ_D. In such a context, the CW solutions disintegrate into trains of objects that have solitonic forms. This is a confirmation of our linear stability analysis, which once more confirms MI to be a direct mechanism leading to soliton formation under a suitable balance between nonlinearity and dispersion as shown in Fig. 3.7, where the different panels correspond to different instants. For $\alpha = 0.25$ and $\lambda_R = \lambda_D = 0.1$. unstable patterns appear in the form of breathing wave trains with a plane wave background which disappears with time increasing and progressively turns into sets of bell-shape solitons as depicted in Fig. 3.7(c) and (d) when $t = 170$. In general, the density of both condensates has the same shape, except that wave propagation seems to take place in opposite x-directions. The scenario appears in Fig. 3.8, where we have imposed $\lambda_R > \lambda_D$, with left and right columns corresponding respectively to the densities $|\psi_1|^2$ and $|\psi_2|^2$. Under such conditions, there is soliton formation in the two components, with the instability evolving erratically along the x-axis and coherently along the y-axis. This particular behavior reveals the presence of the gauge amplitude, which is not balanced by the helicoidal gauge potential in model Eqs. (3.16). While the wave amplitude increases with time in both components, instability tends to be quenched in the second condensate along the increasing x-direction. At the same time, patterns persist with an increasing frequency in the first component. At time $t = 170$, the erratic behavior along the x-direction of the formed patterns becomes more apparent with more patterns for $|\psi_1|^2$ than $|\psi_2|^2$. This is indeed contrary to what was obtained in Fig. 3.7(c), where only one train of solitons remained along the y-axis at the same instant. This also shows a wave propagation that evolves in the x-direction. More interestingly, when $\lambda_R < \lambda_D$, we obtain the features depicted in Fig. 3.9, where the CW disintegrates into a train of wave objects, therefore sustaining the presence of instability. Here, with increasing time, the number of pulse-like patterns increases in the x-direction, in an erratic way, while they evolve periodically on the y-axis. As in the previous case, their intensity increases, and they become more localized. At time $t = 100$ and position $y = 10$, the cross-sections of the above-discussed densities are

depicted in Fig. 3.10. Remarkably, the outcome of MI is the emergence of trains of solitons with pulse shape. It is also clearly visible that the RD changes bring about different behavior in the emerging trains, which is in accordance with the results of Figs. 3.7-3.9. Along the same line, the panels of Fig. 3.11 show the cross-sections of the density profiles for different values of the gauge amplitude α. For two values of α, the obtained train of solitons show the robustness of such entities in the proposed model and concord predictions from the linear stability analysis, where even the value $\alpha = 0$ was predicted to support the occurrence of MI.

3.6.2 MI patterns for the case $\beta_x = \beta_y = \beta$, and $(\beta x + \beta y) = \pi/2$

This case considers the gauge amplitude and the helicoidal gauge potential and the combined effects that bring about the helicoidal SO coupling. Therefore, this part fully brings together the latter and the effect of the RD SO coupling. The results showing the MI evolution in such a model are presented in Fig. 3.12-3.18. In fact, Fig. 3.12 shows results for $\alpha \neq 0$ and $\beta \neq 0$, with $\lambda_R = \lambda_D = 0.1$, which indeed show the emergence of train of wave, periodic along the x-axis, but erratic with Y increasing. This is contrary to what was observed in the previous case and clearly pictures the impact of the helicoidal gauge potential on the MI process. However, unstable patterns are more distributed for $|\psi_2|^2$ than for $|\psi_1|^2$, which support a certain energy concentration, knowing that the initial state was the same. At this point, the presence of β gives the possibility to characterize patterns for right- and left-handed helicoidal SO couplings, respectively obtained for $\beta < 0$ and $\beta > 0$. Obviously, the features of Fig. 3.12 correspond to the left-handed coupling context. Further calculations, especially for the right-handed SO coupling, are recorded in Fig. 3.13, where trains of solitons are generated for $\beta < 0$. In Fig. 3.14, wave patterns due to right-handed and left-handed helicoidal SO couplings are compared. It is clear that not only β affects the occurrence of MI, but it also sustains the robustness of the soliton-like objects in the proposed model. The formation of peaks solitary peaks in BEC systems has been debated in several contributions. That phenomenon was described by Hai et al. [289], where they showed that breathing wave packets can display some deformation while propagating. Although this was shown on a single BEC, and based on Strecker's et al. experiment [290], the width and frequency of the wave train oscillation may be affected, therefore delocalizing the center of the soliton, with the direct result being what is displayed in Fig. 3.14. Although the calculations made in the present work are a result of the activation of the MI, it remains that such structures are inherent to BECs, especially when a suitable balance between nonlinear and dispersive effects is found, as interestingly demonstrated by Salanish et al. [291] in a one-component BEC of ^{7}Li.

The effect of λ_R and λ_D cannot also be neglected in this context, as the cross terms between the two condensates modulate the balance between nonlinearity and dispersion, which brings about new behaviors. This can be more effective when $\lambda_R > \lambda_D$ as shown in Fig. 3.15, where $\alpha = 0.1$ and $\beta = 0.25$. Initially, the distribution of wave patterns is high for $|\psi_1|$, but during propagation, there is energy transfer through the coupling, which increases pattern distribution in favor of $|\psi_2|$. With time, of course, the MI persists, which justifies a strong disturbance of the CW stability by the Rashba SO coupling term. Still, propagation takes place in the $y-$direction. The numerical results recorded in Fig. 3.16 further show how the balance between λ_R and λ_D in-

fluences the MI progression both under left- and right-handed SO coupling. At time $t = 20$, strong density disturbance generates envelope solitons in both compounds. With time increasing, the breather soliton expands, and the number of oscillations increases, probably due to multiple collisions among the emerging solitons. However, the effect of the sign β manifests itself by intermittent alternations between in- and out-of-phase oscillations. Being in the presence of a mixture of open BECs, the oscillations, after a certain time, extend to the boundaries, as supported by Fig. 3.16$(\mathrm{bj})_{1=1,2}$, where the train is made of ordinary and composite solitons. Compared to the extended breathing modes of Fig. 3.11$(\mathrm{aj})_{j=1,2}$, its clear that the structures of Fig. 3.16$(\mathrm{aj})_{j=1,2}$ are more confined, which supports the presence of a virtual potential. Of course, a real experiment predicts any matter-wave state to be created in a trapping potential. Actually, the two-component model of the BEC that combines the SO-Rashba coupling and attractive cubic interactions supports semi-vortices and mixed modes, which get self-trapped in the common isotropic harmonic-oscillator trapping potential and remain robust even when the potential gets quenched [292]. This otherwise reveals the independent tunability of the Rashba SO coupling and the harmonic-oscillator trap. Even in the absence of trapping potentials, other seminal contributions have indicated that in exciton-polariton condensates with dissipation due to a narrow external pump beam, the formation of strongly localized stationary solutions, also known as quasi-compactons [293], may take place. Indeed, the models are modified by the presence of the RD terms, which may explain the observed behaviors in a certain way. We may then expect the numerical structures form model (3.17) also to be apparently trapped. This means that the helicoidal SO coupling should be complete through the presence of α and β for the trapping effect to be strong. Otherwise, the gauge amplitude alone, mixed with the RD SO coupling, cannot trap the soliton trains that expand from the onset, even though over a long time, nonlinear structures emerge. This is also true for the case $\lambda_R > \lambda_D$ depicted in Fig. 3.17, where the final instant $t = 170$ displays patterns whose amplitude increases with y. More interestingly, the cross-section of both components oscillations, depicted in Fig. 3.18 show an increase in the number of peaks. This shows the real effect of a dominating Dresselhaus SO coupling parameter λ_D. Also, when the system is switched from left- to right-handed helicoidal SO coupling, the last stage shows dominating peaks belonging to the condensate ψ_1.

When the helicoidal gauge potential is well-tuned, the combination of the two effects of RD SO-coupling may bring about new classes of patterns as already debated in several contributions dealing with vortices and more exotic topological excitations in rotating two-and three-dimensional SO-coupled BECs. In such contexts, it was shown that RD SO coupling may lead to a broad range of quantum phases among which plane wave phase [294], bright soliton phase [295, 296], dark soliton phase [297], stripe phase [294, 298, 299], topological superfluid phase [215], polarized and unpolarized phases [300], just to name a few. Most of such excitation phases may be observed via the activation of MI, but the difficulty still remains in manipulating the large number of parameters involved. This explains why we restricted ourselves to repulsive intra- and intercomponent interactions, and more importantly, the way they compete with other parameters like the helicoidal gauge potential and the subsequent Rashba and Dresselhaus SO-coupling parameters.

3.7 Summary

In this chapter, we performed a systematic and detailed investigation of the combined effects of helicoidal and RD SO coupling. The tunability of the helicoidal SO coupling allows getting two distinct GP models, which include RD SO coupling. The analysis of MI is carried out in both systems separately, and one finds new distribution behaviors of the growth rate spectra under the combined effects of the two types of SO coupling. In the first case, BECs oscillate in free space, and such dynamics involves only the gauge amplitude α, coupled to the RD SO coupling. In contrast, the second case, related to a square lattice, involves both the full helicoidal SO coupling and the RD coupling. In the free space, the strong influence of the gauge amplitude can take place and give rise to extended oscillating patterns. More confined and coherent structures characterize MI in the square lattice approximation, which reveals the trapping behavior of the helicoidal SO coupling. This is further supported by the emergence of breathing-like solitons extending progressively to the domain edges as time increases. Such dynamics are addressed for $\lambda_R = \lambda_D$, $\lambda_R > \lambda_D$ and $\lambda_R < \lambda_D$, which impose distinct behaviors to the emergent modulated matter waves. In free space, however, the change in the gauge amplitude α, together with the above combinations between λ_R and λ_D, does not allow to confine the emerging solitons, which corroborates the fact that RD SO coupling does not provide any trapping mechanism [271]. The latter is indeed recovered by applying the helicoidal SO coupling. It was, for example, shown by Liu et al. [301] that another mechanism to stabilize 2D and 3D solitons under simultaneous Rashba and Dresselhaus SO coupling was through the application of long-range anisotropic attractive dipole-dipole interactions. Anisotropic vector solitons were generated, and their collision confirmed the trapping effect of the dipole-dipole interactions. A new direction to the present study may be the generation of soliton via wave collision and their stabilization through the helicoidal SO coupling.

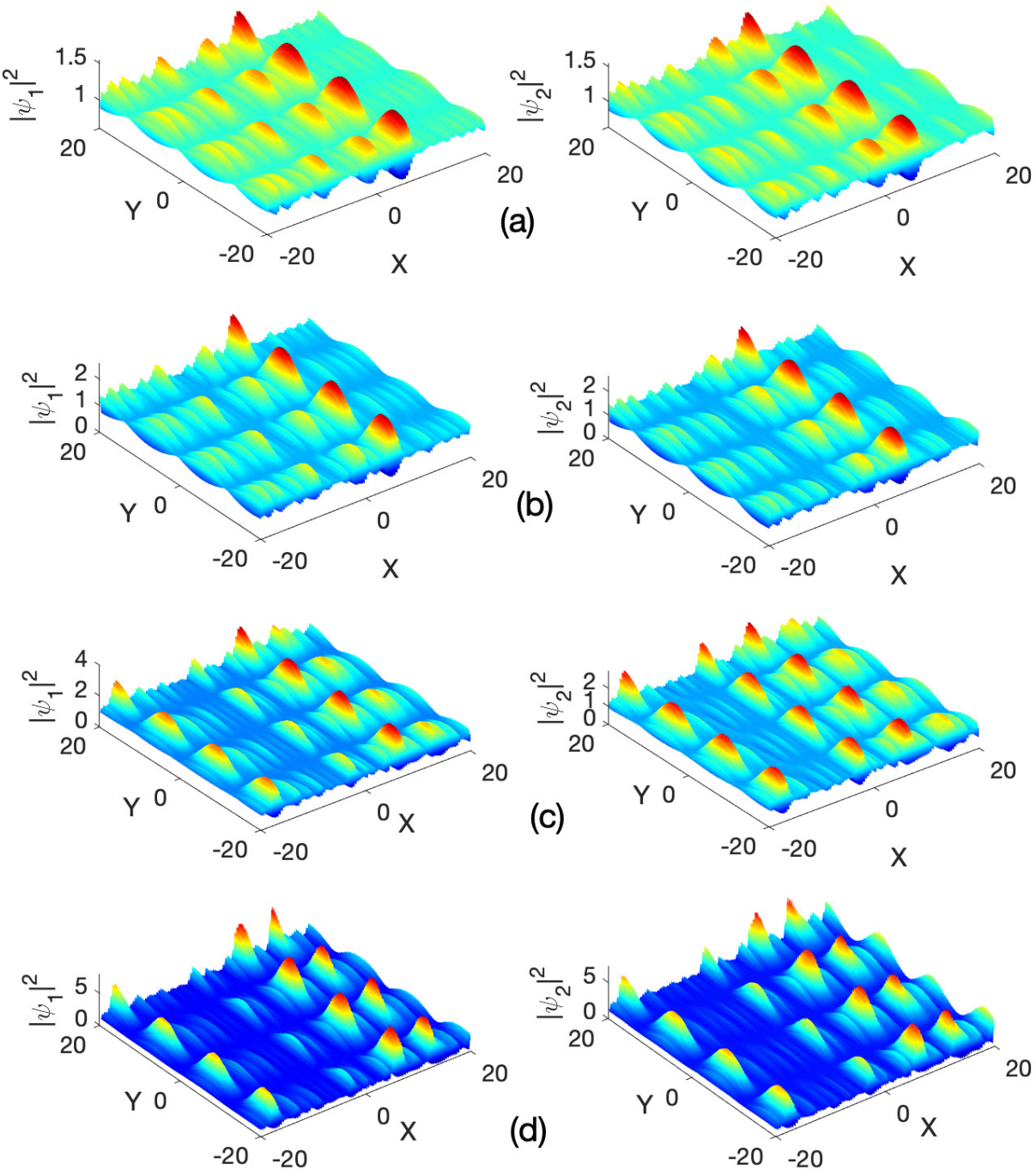


Figure 3.9: MI evolution in both condensates with increasing time in presence of both the SO coupling and the RD SO coupling. Fixing $\alpha = 0.1$, and $\lambda_R < \lambda_D$, panels from (a) to (d) correspond to the respective instants $t = 25$, $t = 60$, $t = 100$ and $t = 170$. The other parameters are $K_1 = K_2 = 1.5$, $n_0 = 1$, $g_{11} = g_{22} = 0.5$ and $g_{12} = 0.6$.

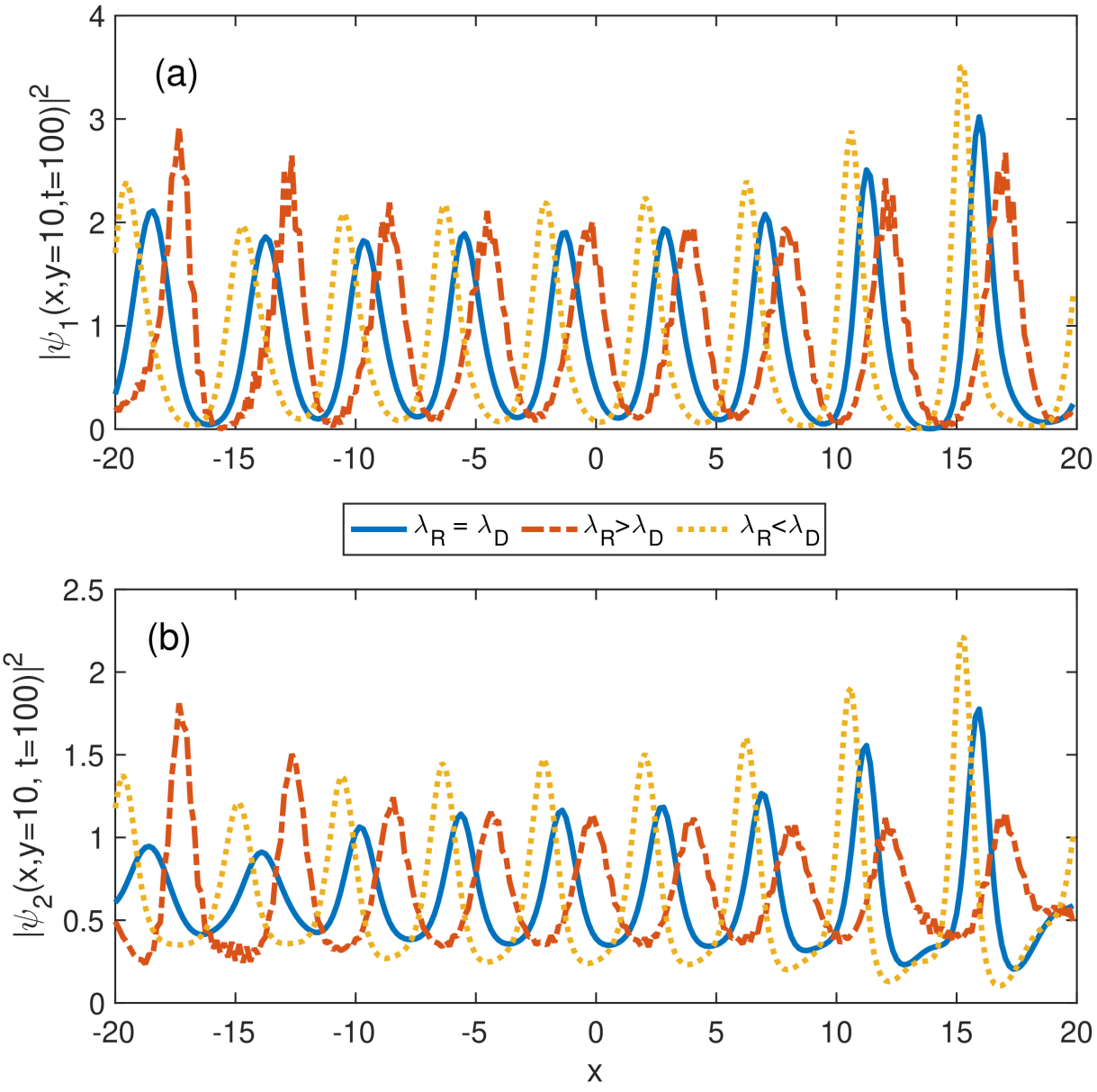


Figure 3.10: The panels show cross sections of the density profiles of Fig. 3.9 at time $t = 100$, when $y = 10$. The cases $\lambda_R = \lambda_D$, $\lambda_R > \lambda_D$ and $\lambda_R < \lambda_D$ are summarized for both condensates. The other parameters are $K_1 = K_2 = 1.5$, $n_0 = 1$, $g_{11} = g_{22} = 0.5$, $g_{12} = 0.6$ and $\alpha = 0.1$.

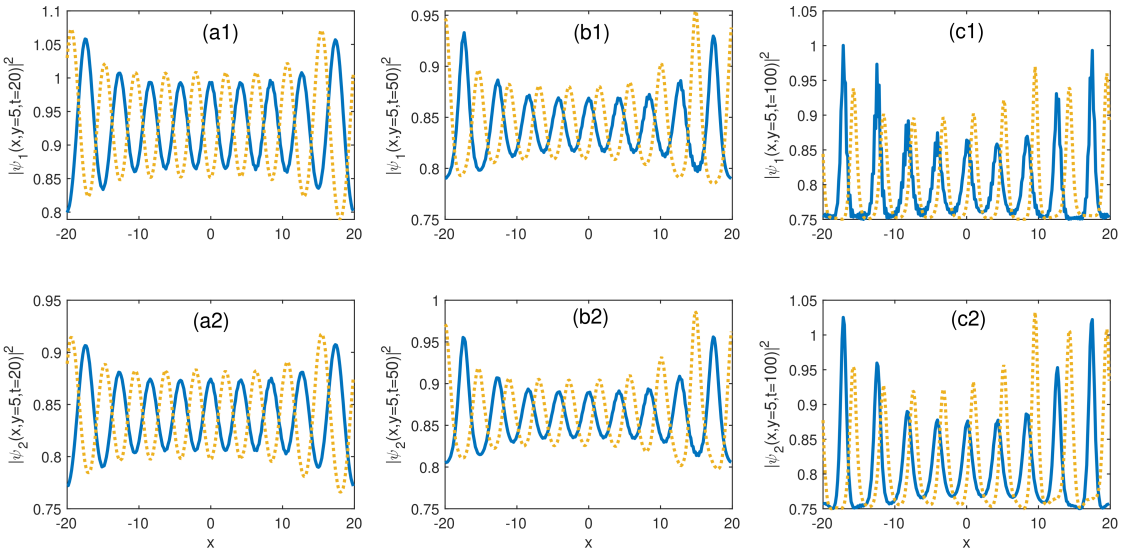


Figure 3.11: The panels show cross sections of the density profiles of Fig. 3.9 for $\alpha = 0$ (solid blue line) and $\alpha = 0.1$ (dotted yellow line). Panels $(\text{aj})_{j=1,2}$, $(\text{bj})_{j=1,2}$ and $(\text{cj})_{j=1,2}$ respectively correspond to instants $t = 20$, $t = 50$ and $t = 100$, with $y = 5$, $\lambda_R < \lambda_D$, $K_1 = K_2 = 1.5$, $n_0 = 1$, $g_{11} = g_{22} = 0.5$ and $g_{12} = 0.6$.

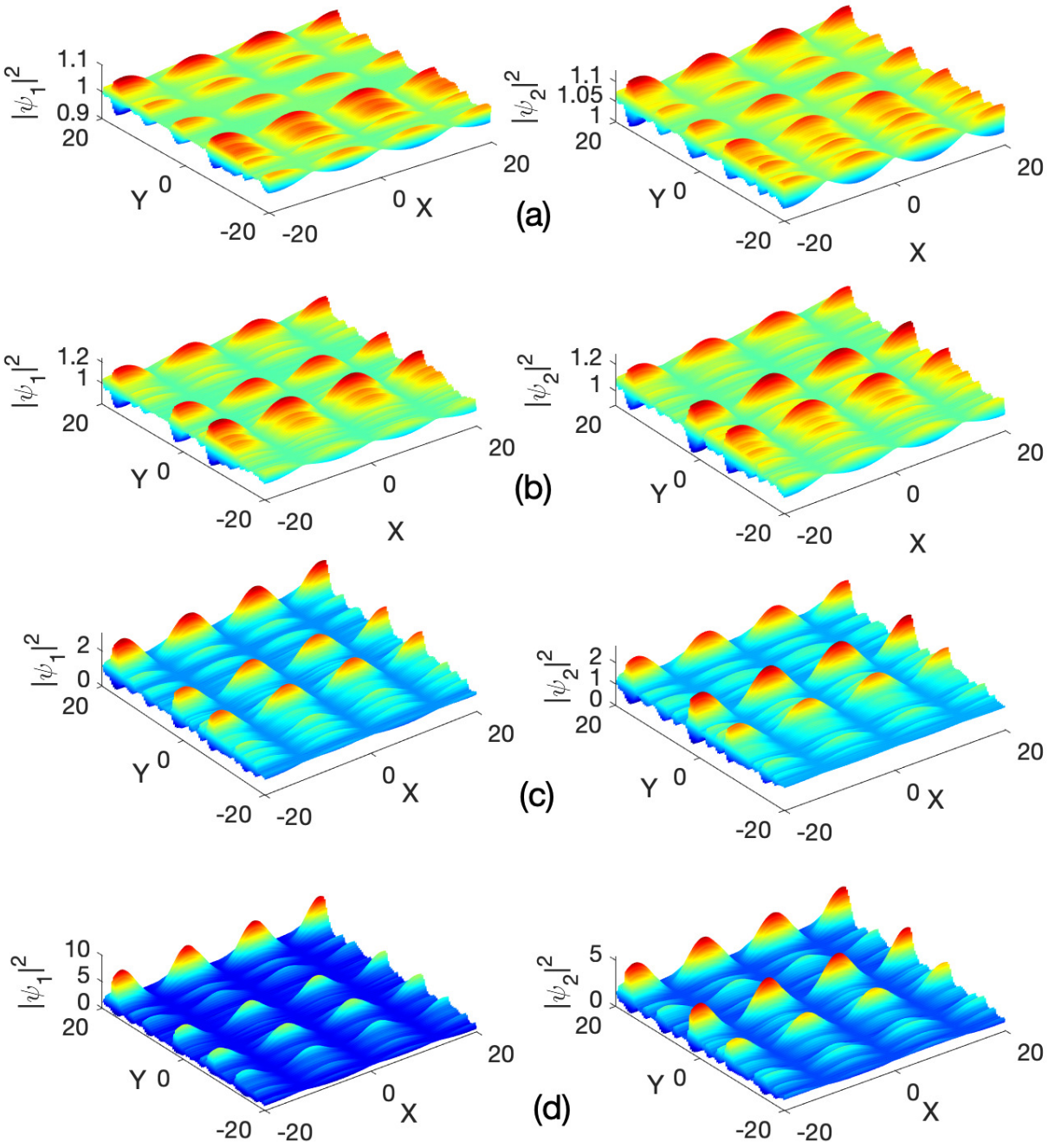


Figure 3.12: MI evolution in both condensates with increasing time in presence of both the SO coupling and the RD SO coupling. Fixing $\alpha = 0.1$, $\beta = 0.25$, and $\lambda_R = \lambda_D = 0.01$, panels from (a) to (d) correspond to the respective instants $t = 25$, $t = 60$, $t = 100$ and $t = 170$. The other parameters are $K_1 = K_2 = 1.5$, $n_0 = 1$, $g_{11} = g_{22} = 0.5$ and $g_{12} = 0.6$.

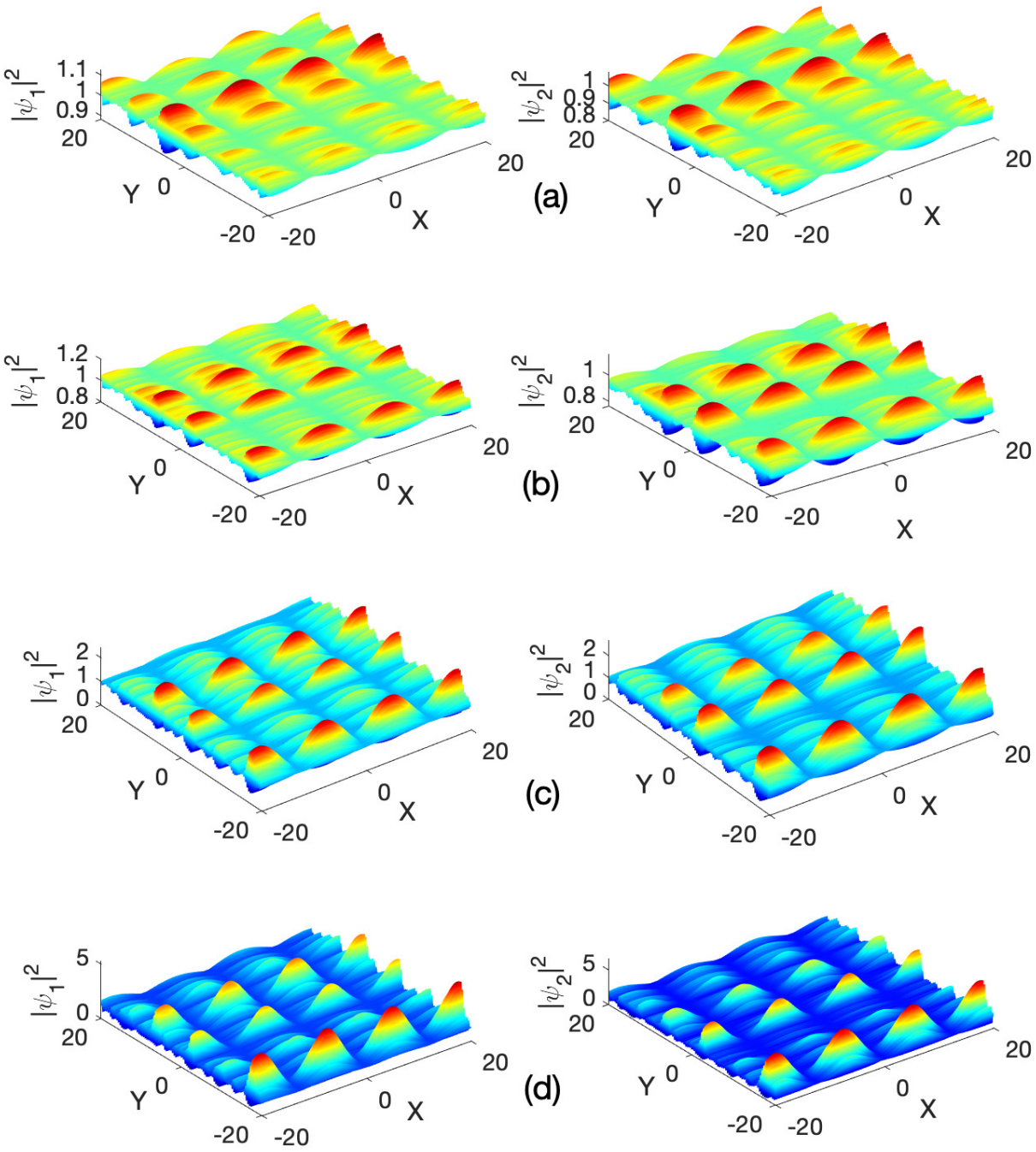


Figure 3.13: MI evolution in both condensates with increasing time in presence of both the SO coupling and the RD SO coupling. Fixing $\alpha = 0.1$, $\beta = -0.25$, and $\lambda_R = \lambda_D = 0.01$, panels from (a) to (d) correspond to the respective instants $t = 25$, $t = 60$, $t = 100$ and $t = 170$. The other parameters are $K_1 = K_2 = 1.5$, $n_0 = 1$, $g_{11} = g_{22} = 0.5$ and $g_{12} = 0.6$.

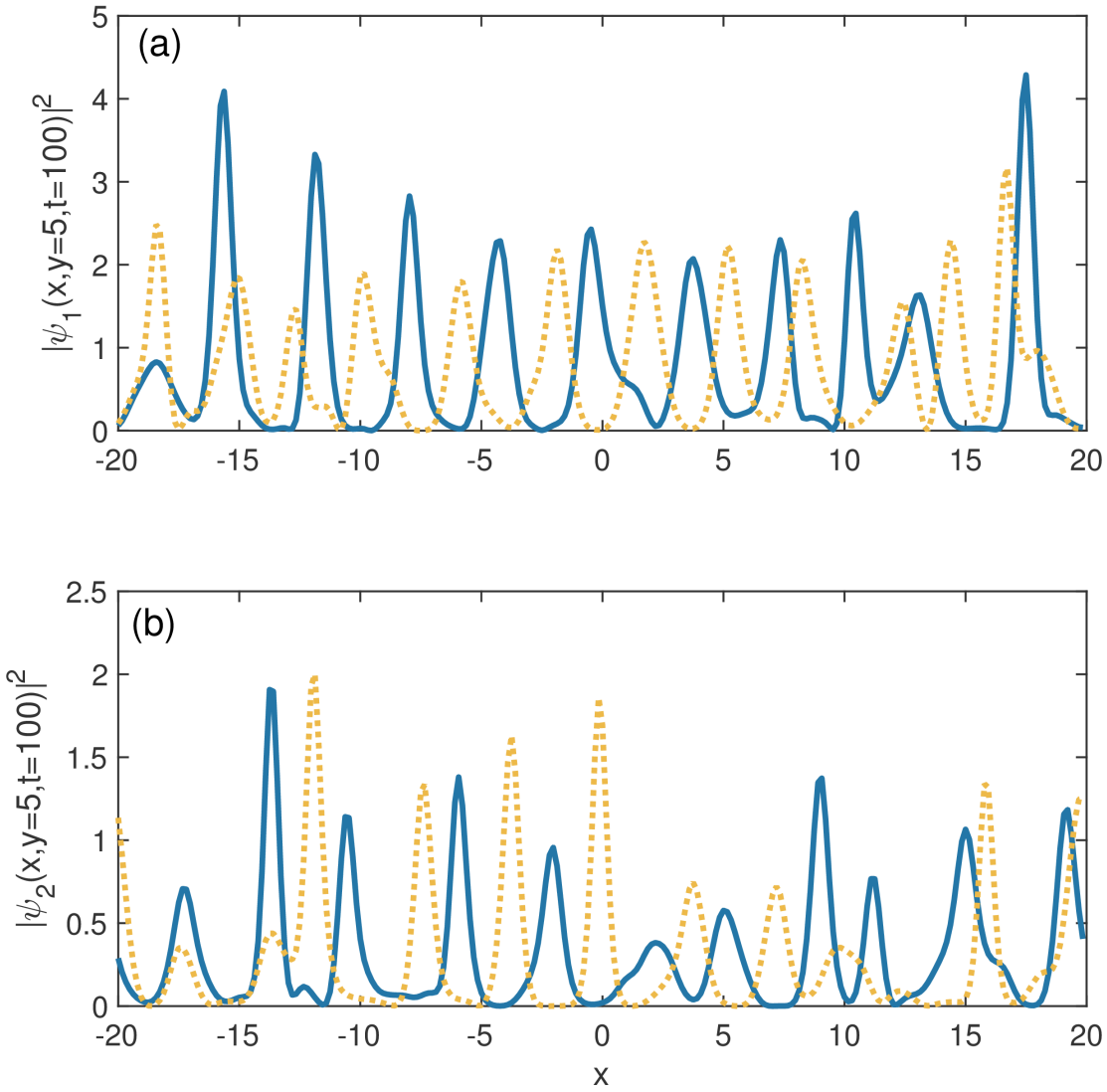


Figure 3.14: The panels show cross sections of the density profiles of Figs. 3.9 and 3.13 at time $t = 100$, when $y = 10$, $\alpha = 0$ (solid blue line), $\alpha = 0.1$ (dotted yellow line) and $\lambda_R = \lambda_D = 0.1$. The other parameters are $K_1 = K_2 = 1.5$, $n_0 = 1$, $g_{11} = g_{22} = 0.5$ and $g_{12} = 0.6$.

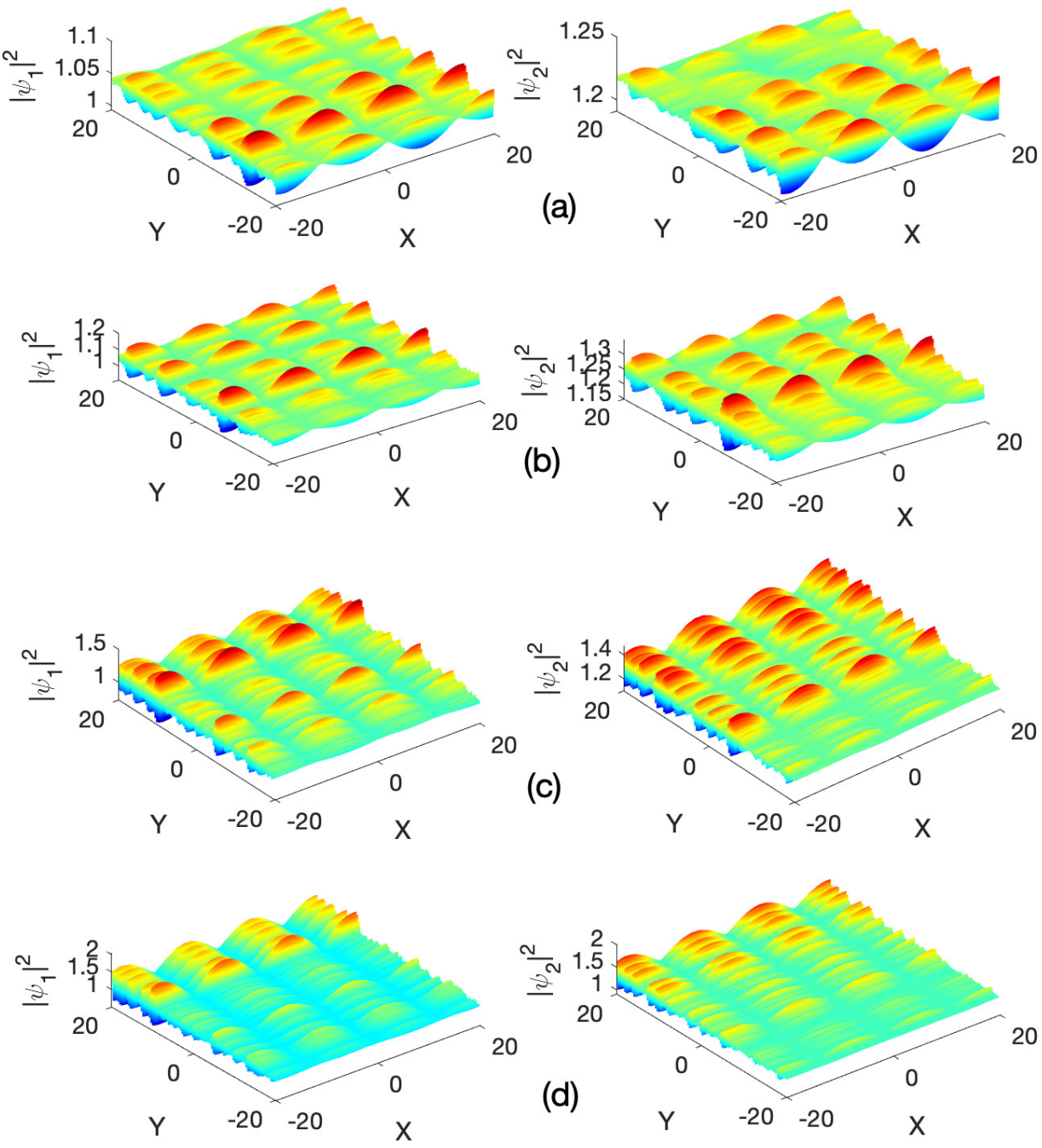


Figure 3.15: MI evolution in both condensates with increasing time in presence of both the SO coupling and the RD SO coupling. Fixing $\alpha = 0.1$, $\beta = 0.25$, and $\lambda_R > \lambda_D$, panels from (a) to (d) correspond to the respective instants $t = 25$, $t = 60$, $t = 100$ and $t = 170$. The other parameters are $K_1 = K_2 = 1.5$, $n_0 = 1$, $g_{11} = g_{22} = 0.5$ and $g_{12} = 0.6$.

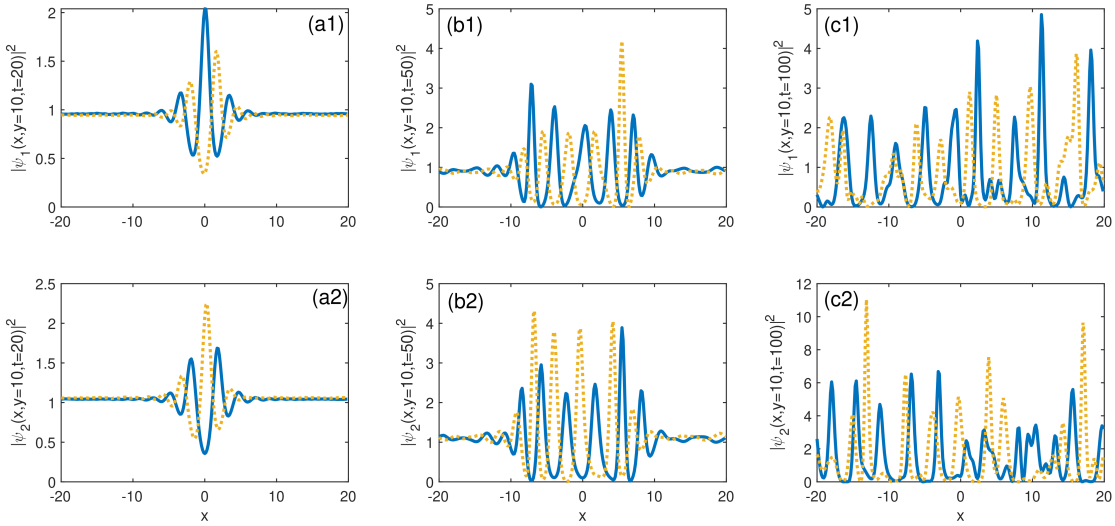


Figure 3.16: The panels show cross sections of the density profiles of Fig. 3.15 when $y = 10$, $\alpha = 0$ (solid blue line), $\alpha = 0.1$ (dotted yellow line) and $\lambda_R > \lambda_D$. Panels $(\mathrm{aj})_{j=1,2}$, $(\mathrm{bj})_{j=1,2}$ and $(\mathrm{cj})_{j=1,2}$ respectively correspond to instants $t = 20$, $t = 50$ and $t = 100$, with $K_1 = K_2 = 1.5$, $n_0 = 1$, $g_{11} = g_{22} = 0.5$, $g_{12} = 0.6$ and $\alpha = 0.1$.

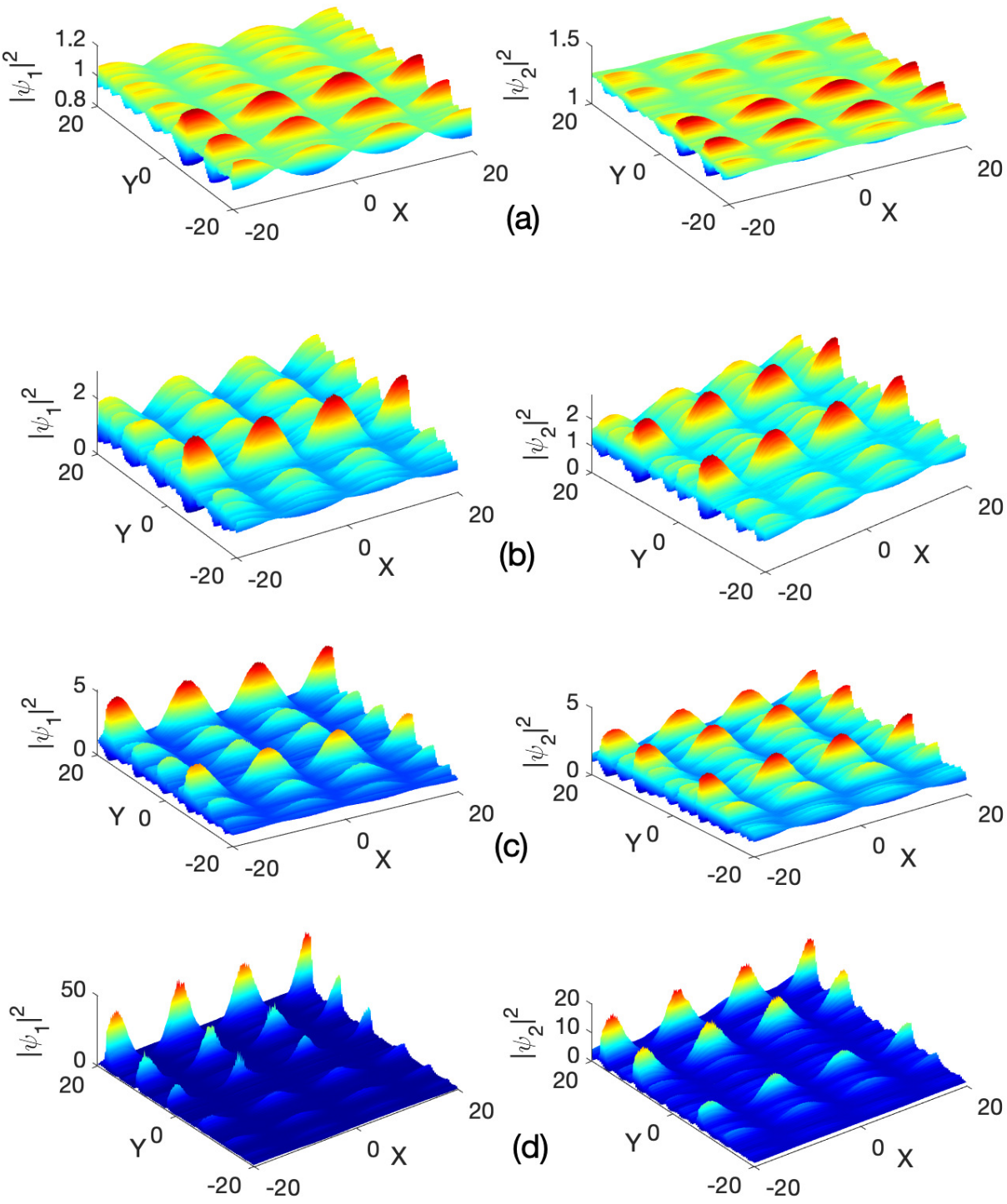


Figure 3.17: MI evolution in both condensates with increasing time in presence of both the SO coupling and the RD SO coupling. Fixing $\alpha = 0.1$, $\beta = 0.25$, and $\lambda_R < \lambda_D$, panels from (a) to (d) correspond to the respective instants $t = 25$, $t = 60$, $t = 100$ and $t = 170$. The other parameters are $K_1 = K_2 = 1.5$, $n_0 = 1$, $g_{11} = g_{22} = 0.5$ and $g_{12} = 0.6$.

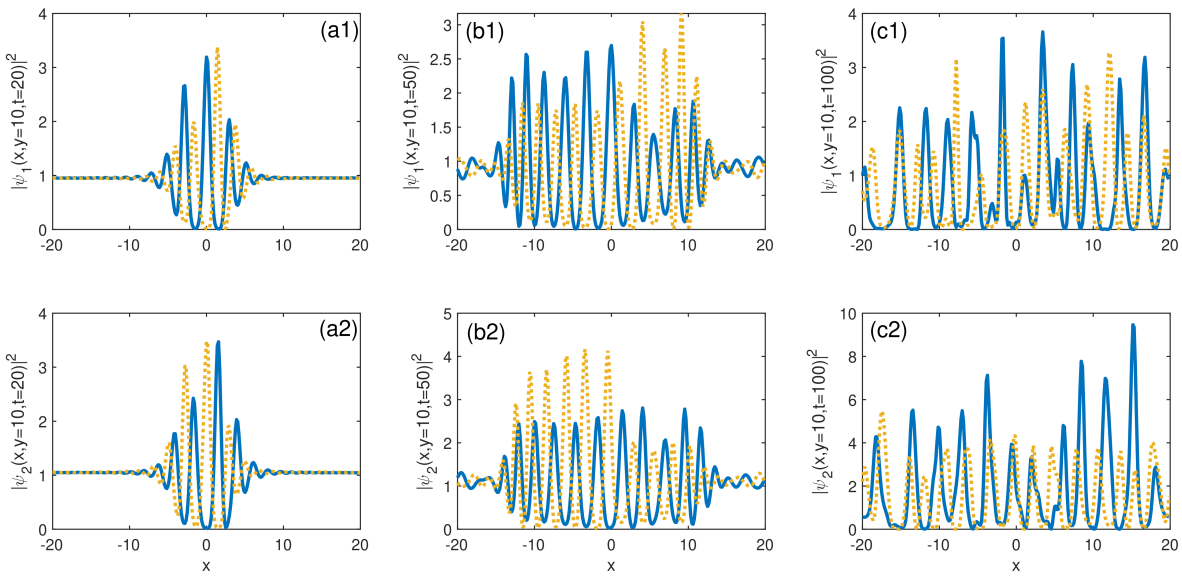


Figure 3.18: The panels show cross sections of the density profiles of Fig. 3.17 when $y = 10$, $\alpha = 0$ (solid blue line), $\alpha = 0.1$ (dotted yellow line) and $\lambda_R < \lambda_D$. Panels $(\text{aj})_{j=1,2}$, $(\text{bj})_{j=1,2}$ and $(\text{cj})_{j=1,2}$ respectively correspond to instants $t = 20$, $t = 50$ and $t = 100$, with $K_1 = K_2 = 1.5$, $n_0 = 1$, $g_{11} = g_{22} = 0.5$, $g_{12} = 0.6$ and $\alpha = 0.1$.

GENERAL CONCLUSION

The overall objective of this research was to assess the MI phenomenon and solitary structures, emerging from dissipative and non-dissipative BECs under the combined effect of helicoidal gauge potential and SO couplings. In the first chapter, we have given the general introduction underlying the concept of BECs related to our thesis work. The thesis is summed up as follows:

In the second chapter, we derived a coupled cubic CGL equations for two-component helicoidal SO-coupled dissipative BECs from a coupled GP equations governing the dynamics of the condensate wave functions of the two-component helicoidal SO-coupled BECs, evenly distributed between the two pseudospin states, under dissipative effects together with rate equation coupling condensed and uncondensed atoms. The theory of MI has been addressed both analytically and numerically, along with its response to the simultaneous effects of the SO coupling, the helicoidal gauge potential and the inter-component interactions. Analytically, a nonlinear dispersion relation has been derived in the form of a fourth-order polynomial alongside with the MI growth rate. Comprehensively, the possible combinations of signs of intra- and intercomponent interactions have been discussed, both in the repulsive and attractive contexts. Our analysis illustrates that SO coupling, and the intrinsic helicoidal potential, inevitably contributes to the CW disintegration, regardless of the nature of the interaction strength. This is manifested by the appearance of new instability sidebands, thereby enhancing the MI. Analytical predictions were corroborated by direct numerical simulations, which have shown that nonlinear and longtime spatiotemporal wave patterns of the underlying set of coupled cubic CGL equations exist and are, as a whole, robust for a wide variety of the involved physical parameters. In the process, SOC and helicoidal gauge potential may be used as tunable knobs to generate and control complicated nonlinear dynamical processes and the resulting localized long-lived excitations, both in left-handed and right-handed helicoidal dissipative two-component BECs.

In the third chapter, we have investigated the combined effects of helicoidal and RD SO coupling. The tunability of the helicoidal SO coupling allows getting two distinct GP models, which include RD SO coupling. The analysis of MI is carried out in both systems separately, and one finds new distribution behaviors of the growth rate spectra under the combined effects of the two types of SO coupling. In the first case, BECs oscillate in free space, and such dynamics involves only the gauge amplitude α, coupled to the RD SO coupling. In contrast, the second case, related to a square lattice, involves both the full helicoidal SO coupling and the RD coupling. In the free space, the strong influence of the gauge amplitude can take place and give rise to extended oscillating patterns. More confined and coherent structures characterize MI in the square lattice approximation, which reveals the trapping behavior of the helicoidal SO coupling. This is further supported by the emergence of breathing-like solitons extending progressively to the domain edges as time increases. Such dynamics

are addressed for $\lambda_R = \lambda_D$, $\lambda_R > \lambda_D$ and $\lambda_R < \lambda_D$, which impose distinct behaviors to the emergent modulated matter waves. In free space, however, the change in the gauge amplitude α, together with the above combinations between λ_R and λ_D, does not allow to confine the emerging solitons, which corroborates the fact that RD SO coupling does not provide any trapping mechanism [271]. The latter is indeed recovered by applying the helicoidal SO coupling. It was, for example, shown by Liu et al. [272] that another mechanism to stabilize 2D and 3D solitons under simultaneous Rashba and Dresselhaus SO coupling was through the application of long-range anisotropic attractive dipole-dipole interactions. Anisotropic vector solitons were generated, and their collision confirmed the trapping effect of the dipole-dipole interactions. A new direction to the present study may be the generation of soliton via wave collision and their stabilization through the helicoidal SO coupling.

Evidently, the present contribution not only opens a new route for the investigation of several interesting physical aspects of dissipative multicomponent condensates, but also reveals the richness in the complex dynamics exhibited by the SO-coupled BECs, as inspired by the recent theoretical and experimental results on dynamical instabilities [302, 303]. It is also a promising starting point to study the behavior of the proposed system under the coupled effects the SO coupling and multi-body interatomic interactions in higher dimensions. Finally, we believe that a powerful tool in probing novel dynamical behaviors will be provided by further studies on SO-coupled dissipative BECs, and shed more light on the suitable system parameter values to be used.

Interesting extensions of this thesis may be:

- Examine the Rayleigh-Taylor instability in two-species Bose-Einstein condensates with SO couplings.
- Explore the form of rogue wave solutions of 2D coupled Gross-Pitaevskii equations with variable coefficients and with SO couplings that describe atomic Bose–Einstein condensates in different experimentally relevant settings.
- Investigate the property of matter-wave solitons in Bose–Einstein condensates with helicoidal and Rasha-Dresselhaus SO couplings by multiscale perturbation method.
- Investigate the modulational instability phenomenon in Bose–Einstein condensates under local two- and three-body interactions with helicoidal and Rasha-Dresselhaus SO couplings.
- Investigate the modulational instability phenomenon of rotating SO coupled Bose–Einstein condensates in a toroidal trap with helicoidal and Rasha-Dresselhaus SO couplings.
- Investigate, via a variational approach, the dynamics and properties of nonlinear matter waves in a trapped BEC with helicoidal and Rasha-Dresselhaus SO couplings, subject to a PT -symmetric linear potential, with the trap in the form of a super-Gaussian potential.

APPENDICES

Appendix A: Critical temperature (1.10)

To find the critical temperature relation, we start off with 1.8

$$N = \frac{V}{4\pi^2}\left(\frac{2m}{\hbar^2}\right)^{3/2}\int_0^\infty \sqrt{\epsilon}\frac{d\epsilon}{e^{\beta\epsilon}-1}.$$

Let $x = \beta\epsilon$, and evaluate the energy integral using the relation $\frac{1}{e^{-x}-1} = \sum_{n=1}^{\infty} e^{-nx}$ then the integral part of N becomes

$$\sum_{n=1}^{\infty}\int_0^\infty e^{-nx}\sqrt{\epsilon}d\epsilon,$$

if $x = \beta\epsilon$ then $\epsilon = \sqrt{\frac{x}{\beta}}\cdot\frac{dx}{d\epsilon} = \beta$ and $d\epsilon = \frac{1}{\beta}dx$. substitute the new variables

$$\sum_{n=1}^{\infty}\int_0^\infty x^{1/2}\beta^{-1/2}e^{-nx}\frac{1}{\beta}dx,$$

$$\beta^{-3/2}\sum_{n=1}^{\infty}\int_0^\infty x^{1/2}e^{-nx}dx,$$

let $t = nx$, $\sqrt{x} = \sqrt{\frac{t}{n}}\cdot\frac{dt}{dx} = n$, $dx = \frac{1}{n}dt$, write the integral in terms of the new variable t

$$\beta^{-3/2}\sum_{n=1}^{\infty}\int_0^\infty n^{-1/2}e^{-t}\sqrt{t}dt.$$

Simplifying further we obtain

$$\beta^{-3/2}\sum_{n=1}^{\infty}n^{-3/2}\int_0^\infty e^{-t}\sqrt{t}dt.$$

Let the Riemann zeta function be $\zeta(\frac{3}{2}) = \sum_{n=1}^{\infty} n^{-3/2}$ and the gamma function be $\Gamma(\frac{3}{2}) = \int_0^\infty e^{-t}\sqrt{t}dt$, so that

$$\beta^{-3/2}\sum_{n=1}^{\infty}n^{-3/2}\int_0^\infty e^{-t}\sqrt{t}dt = \beta^{-3/2}\zeta(\frac{3}{2})\Gamma(\frac{3}{2}),$$

$\beta = \frac{1}{K_BT}$, $\zeta(\frac{3}{2}) = 2.612$ and $\Gamma(\frac{3}{2}) = \Gamma(\frac{1}{2}+1) = \frac{1}{2}\Gamma(\frac{1}{2}) = \frac{1}{2}\cdot\sqrt{\pi}$. Then the total number of particles become

$$N = \frac{V}{4\pi^2}\left(\frac{2m}{\hbar^2}\right)^{3/2}\left(\frac{1}{K_BT}\right)^{-3/2}\frac{\sqrt{\pi}}{2}2.612,$$

at $T = T_c$ this simplifies to

$$N = V\left(\frac{mK_BT_c}{2\pi\hbar^2}\right)^{3/2} 2.612.$$

The critical temperature T_c is obtained as

$$T_c = \frac{2\pi\hbar^2}{mK_B}\left(\frac{N}{2.612V}\right)^{2/3}.$$

Appendix B

B1. Two-dimensional GP equations derivation

Within the mean-field formulation, the two pseudospin states are described by an energy functional given by

$$\mathcal{E} = \int_{-\infty}^{+\infty}\int_{-\infty}^{+\infty}(\mathcal{E}_0 + \mathcal{E}_{int})\,dxdy \tag{3.28}$$

where

$$\mathcal{E}_0 = \frac{1}{2}\left(\Psi^* H_0 \Psi\right), \tag{3.29}$$

where $\Psi = (\Psi_1, \Psi_2)^T$ (T stands for the transpose) is the condensate wavefunction, Ψ_1 and Ψ_2 are associated with the pseudo-spin components. The interaction Hamiltonian $\mathcal{E}_{int}$ takes the common contact form of the scattering interaction of the $s-$wave [282]. The model Hamiltonian H_0 assumes the form

$$H_0 = H_{HSO} + H_Z + H_{RSO} + H_{DSO}, \tag{3.30}$$

where H_{HSO}, H_Z, H_{RSO}, and H_{DSO} are the helicoidal SO coupling Hamiltonian, Zeeman Hamiltonian, Rashba Hamiltonian, and Dresselhaus Hamiltonian, respectively. The single-particle Hamiltonian of the system can be written as [283]

$$H_{HSO} = \frac{1}{2}\left[(\sigma_0 p_x + \alpha(\vec{\sigma}\cdot\vec{n}))^2 + (\sigma_0 p_y + \alpha(\vec{\sigma}\cdot\vec{m}))^2\right], \tag{3.31}$$

where $p_x = -i\partial/\partial x$ and $p_y = -i\partial/\partial y$ are the momentum operators, α is the strength of helicoidal SO coupling, and the position-dependent unit vectors $\vec{n}$ and $\vec{m}$ determine the SO coupling direction, $\sigma = (\sigma_x, \sigma_y, \sigma_z)$ is the vector Pauli matrices, σ_0 is the identity matrix

$$\sigma_x = \begin{pmatrix}0 & 1\\ 1 & 0\end{pmatrix}, \sigma_y = \begin{pmatrix}0 & -i\\ i & 0\end{pmatrix}, \sigma_z = \begin{pmatrix}1 & 0\\ 0 & -1\end{pmatrix} \sigma_0 = \begin{pmatrix}1 & 0\\ 0 & 1\end{pmatrix}. \tag{3.32}$$

For the sake of simplicity, we consider a helicoidal SO coupling with the periods π/β_x and π/β_y, respectively, given by

$$\begin{aligned}\vec{n} &= (\cos(2\beta_x x + 2\beta_y y), 0, \sin(2\beta_x x + 2\beta_y y)),\\ \vec{m} &= (-\sin(2\beta_x x + 2\beta_y y), 0, \cos(2\beta_x x + 2\beta_y y)),\end{aligned} \tag{3.33}$$

where β_x and β_y are the frequencies of rotation in the $x-$ and $y-$directions. The positive and negative values of β_x and β_y are refer to the right- and left-handed modes, respectively [284–286]. The 2D spinor BEC in the prescence of SOC can be writtens as

$$i\frac{\partial\vec{\Psi}}{\partial t}=\frac{1}{2}\left[\left(-i\sigma_0\frac{\partial}{\partial x}+\alpha(\vec{\sigma}\cdot\vec{n})\right)^2\left(-i\sigma_0\frac{\partial}{\partial y}+\alpha(\vec{\sigma}\cdot\vec{m})\right)^2\right]\vec{\Psi}. \tag{3.34}$$

Let's say

$$T_1\vec{\Psi}=\frac{1}{2}\left(-i\sigma_0\frac{\partial}{\partial x}+\alpha(\vec{\sigma}\cdot\vec{n})\right)^2\vec{\Psi}, \tag{3.35a}$$

$$T_2\vec{\Psi}=\left(-i\sigma_0\frac{\partial}{\partial y}+\alpha(\vec{\sigma}\cdot\vec{m})\right)^2\vec{\Psi}. \tag{3.35b}$$

We recall that we considered the following gauge transformation Eq. (**??**)

$$\Psi_j=e^{-i\alpha^2t}e^{-i(\beta_x^2+\beta_y^2)t/2}e^{-i(\sigma_z\beta_x x+\sigma_x\beta_y y)}\vec{\psi_j}, \tag{3.36}$$

Substituiting Eqs. (3.32),(3.33) and (3.36)into Eq. (3.35) we get

$$\begin{aligned}T_1\vec{\Psi}=i\beta_x&\begin{pmatrix}\dfrac{\partial\psi_1}{\partial x}\\-\dfrac{\partial\psi_2}{\partial x}\end{pmatrix}+\frac{\beta_x^2}{2}\begin{pmatrix}\psi_1\\\psi_2\end{pmatrix}-\frac{1}{2}\begin{pmatrix}\dfrac{\partial^2\psi_1}{\partial x^2}\\\dfrac{\partial^2\psi_2}{\partial x^2}\end{pmatrix}+\frac{\alpha^2}{2}\begin{pmatrix}\psi_1\\\psi_2\end{pmatrix}\\&-\alpha\beta_x\begin{pmatrix}(sin(2\beta_x x+2\beta_y y)\Psi_1-cos(2\beta_x x+2\beta_y y)\Psi_2)\\(cos(2\beta_x x+2\beta_y y)\Psi_1+sin(2\beta_x x+2\beta_y y)\Psi_2)\end{pmatrix}\\&-i\alpha\begin{pmatrix}\left(sin(2\beta_x x+2\beta_y y)\dfrac{\partial\psi_1}{\partial x}+cos(2\beta_x x+2\beta_y y)\dfrac{\partial\psi_2}{\partial x}\right)\\\left(cos(2\beta_x x+2\beta_y y)\dfrac{\partial\psi_1}{\partial x}-sin(2\beta_x x+2\beta_y y)\dfrac{\partial\psi_2}{\partial x}\right)\end{pmatrix}\end{aligned} \tag{3.37a}$$

$$\begin{aligned}T_2\vec{\Psi}=i\beta_y&\begin{pmatrix}\dfrac{\partial\psi_2}{\partial y}\\-\dfrac{\partial\psi_1}{\partial y}\end{pmatrix}+\frac{\beta_y^2}{2}\begin{pmatrix}\psi_1\\\psi_2\end{pmatrix}-\frac{1}{2}\begin{pmatrix}\dfrac{\partial^2\psi_1}{\partial y^2}\\\dfrac{\partial^2\psi_2}{\partial y^2}\end{pmatrix}+\frac{\alpha^2}{2}\begin{pmatrix}\psi_1\\\psi_2\end{pmatrix}\\&-\alpha\beta_y\begin{pmatrix}(-sin(2\beta_x x+2\beta_y y)\Psi_1+cos(2\beta_x x+2\beta_y y)\Psi_2)\\(-cos(2\beta_x x+2\beta_y y)\Psi_1-sin(2\beta_x x+2\beta_y y)\Psi_2)\end{pmatrix}\\&-i\alpha\begin{pmatrix}\left(cos(2\beta_x x+2\beta_y y)\dfrac{\partial\psi_1}{\partial y}-sin(2\beta_x x+2\beta_y y)\dfrac{\partial\psi_2}{\partial y}\right)\\\left(-sin(2\beta_x x+2\beta_y y)\dfrac{\partial\psi_1}{\partial y}-cos(2\beta_x x+2\beta_y y)\dfrac{\partial\psi_2}{\partial y}\right)\end{pmatrix}\end{aligned} \tag{3.37b}$$

Next, the Zeeman Hamiltonian is given by

$$H_Z=\frac{\Delta\sigma_z}{2}, \tag{3.38}$$

where Δ is the strength of Zeeman splitting. We consider the last two terms

$$\begin{aligned}\frac{\Delta\sigma_z}{2}\vec{\Psi} &= \frac{\Delta}{2}\begin{pmatrix}1 & 0\\ 0 & -1\end{pmatrix}\begin{pmatrix}\Psi_1\\ \Psi_2\end{pmatrix}\\ &= \frac{\Delta}{2}\begin{pmatrix}1\times\Psi_1+0\times\Psi_2\\ 0\times\Psi_1-1\times\Psi_2\end{pmatrix}\\ &= \frac{\Delta}{2}\begin{pmatrix}\Psi_1\\ -\Psi_2\end{pmatrix}\end{aligned} \tag{3.39}$$

Originally, the Rashba effect was studied as a phenomenon due to spin splitting by an applied electric field in 3D electron gas systems. The Rashba Hamiltonian originating from SO coupling is given as

$$H_{RSO} = \lambda_R(\vec{\sigma}\wedge\vec{p})\cdot\hat{e}_z, \tag{3.40}$$

where λ_R is the strength of Rashba SO coupling, $\hat{e}_z$ is the unit vector directed along the symmetry axis

$$\begin{aligned}H_{RSO} &= \lambda_R\begin{pmatrix}\sigma_x & \sigma_y & \sigma_z\\ p_x & p_y & 0\end{pmatrix}\cdot\hat{e}_z\\ &= \lambda_R\left(\vec{i}(\sigma_y 0-\sigma_z p_y)-\vec{j}(\sigma_x 0-\sigma_z p_x)+\vec{k}(\sigma_x\cdot p_y-\sigma_y\cdot p_x)\right)\cdot\hat{e}_z\\ &= \lambda_R\left(-\vec{i}\sigma_z p_y+\vec{j}\sigma_z p_x+\vec{k}(\sigma_x p_y-\sigma_y p_x)\right)(o\vec{i}+0\vec{j}+1\vec{k})\\ &= \lambda_R\left((-\vec{i}\sigma_z p_y\cdot o\vec{i})+(\vec{j}\sigma_z p_x\cdot 0\vec{j})+\vec{k}(\sigma_x p_y-\sigma_y p_x)\cdot 1\vec{k}\right),\end{aligned} \tag{3.41}$$

the 2D Rashba SO coupling Hamiltonian reduces to

$$H_{RSO} = \lambda_R\left(\sigma_x p_y-\sigma_y p_x\right). \tag{3.42}$$

Since $p_x = -i\frac{\partial}{\partial x}$ and $p_y = -i\frac{\partial}{\partial y}$, then

$$\begin{aligned}H_{RSO} &= \lambda_R\left(\sigma_x p_y-\sigma_y p_x\right)\\ &= \lambda_R\left(\sigma_x(-i\frac{\partial}{\partial y})\right)-\sigma_y\left(-i\frac{\partial}{\partial x}\right)\\ &= i\lambda_R(-\sigma_x\frac{\partial}{\partial y}+\sigma_y\frac{\partial}{\partial x}).\end{aligned} \tag{3.43}$$

Finally

$$H_{RSO} = -i\lambda_R\left(\sigma_x\frac{\partial}{\partial y}-\sigma_y\frac{\partial}{\partial x}\right). \tag{3.44}$$

substituting the gauge transformation Eq. (**??**) into Eq. (3.44) we get

$$H_{RSO}\vec{\Psi} = -i\lambda_R\left(i\beta_y\begin{pmatrix}\psi_1\\ \psi_2\end{pmatrix}+\begin{pmatrix}\frac{\partial\psi_2}{\partial y}\\ \frac{\partial\psi_1}{\partial y}\end{pmatrix}+i\beta_x\begin{pmatrix}i\psi_2\\ i\psi_1\end{pmatrix}-\begin{pmatrix}-i\frac{\partial\psi_2}{\partial x}\\ i\frac{\partial\psi_1}{\partial x}\end{pmatrix}\right) \tag{3.45}$$

The Dresselhaus Hamiltonian originating from SO coupling is given as

$$H_{DSO} = \lambda_{3D}(\vec{\sigma} \cdot \vec{K}), \tag{3.46}$$

where λ_{3D} is the 3D strength of Dresselhaus SO coupling, $K_z = p_z(p_x^2 - p_y^2)$, and K_x and K_y can be obtained from K_z by cyclic permutations, leading to $K_x = p_x(p_y^2 - p_z^2)$ and $K_y = p_y(p_z^2 - p_x^2)$, respectively. Here, the 2D Dresselhaus SO coupling Hamiltonian reduces to

$$H_{DSO} = \lambda_D(\sigma_x p_x - \sigma_y p_y), \tag{3.47}$$

where λ_D is the 2D strength of Dresselhaus SO coupling. substituting the gauge transformation Eq. (**??**) into Eq. (3.47) we get

$$H_{DSO}\vec{\Psi} = \lambda_D \left(beta_x \begin{pmatrix} \psi_2 \\ \psi_1 \end{pmatrix} + \begin{pmatrix} -i\dfrac{\partial \psi_2}{\partial x} \\ -i\dfrac{\partial \psi_1}{\partial x} \end{pmatrix} + i\beta_y \begin{pmatrix} -\psi_1 \\ \psi_2 \end{pmatrix} + \begin{pmatrix} \dfrac{\partial \psi_2}{\partial y} \\ -\dfrac{\partial \psi_1}{\partial y} \end{pmatrix} \right) \tag{3.48}$$

The interaction Hamiltonian is given by

$$\mathcal{E}_{int} = \frac{1}{2}\left(g_{11}|\Psi_1|^4 + g_{22}|\Psi_2|^4 + 2g_{12}|\Psi_1|^2|\Psi_2|^2\right), \tag{3.49}$$

where $g_{11} = 2a_{11}/a_\perp$ and $g_{22} = 2a_{22}/a_\perp$ are the two-body intraspecie interactions coefficients, while $g_{12} = 2a_{12}/a_\perp$ and $g_{21} = 2a_{21}/a_\perp$ are the two-body inter-species interaction coefficients. Here, $a_\perp = \sqrt{\hbar/(mw_\perp)}$ denotes the transverse characteristic length, with $w_\perp$ being the transverse trap frequency, m is the atomic mass and $\hbar$ is the Planck constant, a_{11}, a_{22}, and a_{12} are the scattering lengths of the $s-$wave.

$$\begin{aligned} G &= diag\left(g_{11}|\Psi_1|^2 + g_{12}|\Psi_2|^2, g_{22}|\Psi_2|^2 + g_{21}|\Psi_1|^2\right) \\ &= \begin{pmatrix} g_{11}|\Psi_1|^2 + g_{12}|\Psi_2|^2 & 0 \\ 0 & g_{22}|\Psi_2|^2 + g_{21}|\Psi_1|^2 \end{pmatrix}, \end{aligned} \tag{3.50}$$

so,

$$\begin{aligned} G\vec{\Psi} &= diag\left(g_{11}|\Psi_1|^2 + g_{12}|\Psi_2|^2, g_{22}|\Psi_2|^2 + g_{21}|\Psi_1|^2\right) \\ &= \begin{pmatrix} g_{11}|\Psi_1|^2 + g_{12}|\Psi_2|^2 & 0 \\ 0 & g_{22}|\Psi_2|^2 + g_{21}|\Psi_1|^2 \end{pmatrix} \begin{pmatrix} \Psi_1 \\ \Psi_2 \end{pmatrix} \\ &= \begin{pmatrix} (g_{11}|\Psi_1|^2 + g_{12}|\Psi_2|^2) \times \Psi_1 + 0 \times \Psi_2 \\ 0 \times \Psi_1 + (g_{22}|\Psi_2|^2 + g_{21}|\Psi_1|^2) \times \Psi_2 \end{pmatrix} \\ &= \begin{pmatrix} (g_{11}|\Psi_1|^2 + g_{12}|\Psi_2|^2) \times \Psi_1 \\ (g_{22}|\Psi_2|^2 + g_{21}|\Psi_1|^2) \times \Psi_2 \end{pmatrix} \end{aligned} \tag{3.51}$$

The BEC dynamics in the mean-field approximation is governed by $i\hbar\frac{\partial \Psi_j}{\partial t} = \frac{\delta \mathcal{E}}{\delta \Psi_j^*}$, $(j = 1, 2)$, from which we obtained Eq. (3.15)

B2. Coefficients P_j $(j = 0, 1, 2, 3)$ of the dispersion relation (3.22)

The coefficients of dispersion relation. (3.22) in Chapter 3 are given by

$$
\begin{aligned}
P_3 &= m_{11} + m_{22} - m_{33} - m_{44},\\
P_2 &= m_{11}n_{22} - m_{11}m_{44} - m_{22}m_{33} - m_{22}m_{44} + m_{33}m_{44} - m_{34}m_{43} + m_{14}m_{41} + m_{42}m_{24} - m_{11}m_{33}\\
&\quad + m_{23}m_{32} - m_{12}m_{21} + m_{13}m_{31},\\
P_1 &= m_{22}m_{33}m_{44} - m_{22}m_{34}m_{43} - m_{11}m_{34}m_{43} + m_{11}m_{33}m_{44} - m_{11}m_{22}m_{44} + m_{11}m_{23}m_{32}\\
&\quad + m_{23}m_{34}m_{42} + m_{11}m_{42}m_{24} + m_{24}m_{32}m_{43} - m_{24}m_{33}m_{42} - m_{11}m_{22}m_{33} + m_{33}m_{12}m_{21}\\
&\quad - m_{13}m_{12}m_{32} - m_{14}m_{21}m_{42} + m_{14}m_{31}m_{43} - m_{14}m_{41}m_{33} + m_{13}m_{22}m_{31}\\
&\quad - m_{13}m_{31}m_{44} + m_{13}m_{34}m_{41} - m_{12}m_{24}m_{41} + m_{13}m_{14}m_{31}\\
&\quad + m_{14}m_{22}m_{41} - m_{23}m_{32}m_{44} + m_{12}m_{21}m_{44} - m_{12}m_{23}m_{31},\\
P_0 &= m_{11}m_{24}m_{32}m_{43} - m_{11}m_{24}m_{33}m_{42} - m_{11}m_{23}m_{32}m_{44} + m_{11}m_{23}m_{34}m_{42} + m_{11}m_{22}m_{44}m_{33}\\
&\quad - m_{12}m_{31}m_{24}m_{43} + m_{12}m_{24}m_{33}m_{41} - m_{44}m_{33}m_{12}m_{21} + m_{12}m_{21}m_{34}m_{43} + m_{12}m_{23}m_{31}m_{44}\\
&\quad + m_{13}m_{24}m_{31}m_{42} - m_{13}m_{24}m_{32}m_{41} + m_{13}m_{21}m_{32}m_{44} - m_{13}m_{21}m_{34}m_{42} - m_{13}m_{22}m_{31}m_{44}\\
&\quad - m_{14}m_{21}m_{32}m_{43} + m_{14}m_{21}m_{33}m_{42} + m_{14}m_{22}m_{31}m_{43} - m_{14}m_{22}m_{33}m_{41} - m_{14}m_{23}m_{31}m_{42}\\
&\quad - m_{11}m_{22}m_{34}m_{43} - m_{12}m_{23}m_{34}m_{41} + m_{13}m_{22}m_{34}m_{41} + m_{14}m_{23}m_{32}m_{41}.
\end{aligned}
\tag{3.52}
$$

B3. Matrix (3.21) elements for the case $\beta_x = \beta_y = 0$

Appendix B4 shows the elements of matrix for the case$\beta_x = \beta_y = 0$

$$
\begin{aligned}
&m_{11} = \Omega - \alpha K_2, \;\; m_{12} = -K_1\alpha - (iK_1 + K_2)\lambda_R - \lambda_D(K_1 + iK_2),\\
&m_{13} = -\frac{1}{2}(K_1^2 + K_2^2), \;\; m_{14} = 0, \;\; m_{21} = \lambda_R(iK_1 - K_2) + \lambda_D(K_1 - iK_2) - K_1\alpha,\\
&m_{22} = \Omega - \alpha K_2, \;\; m_{23} = 0, \;\; m_{24} = -\frac{1}{2}(K_1^2 + K_2^2), \;\; m_{31} = \frac{1}{2}(K_1^2 + K_1^2) + 2g_{11}n_0,\\
&m_{32} = 2g_{12}n_0, \;\; m_{33} = -\Omega + \alpha K_2, \;\; m_{34} = K_1\alpha + \lambda_R(K_2 + iK_1) + \lambda_D(K_1 + iK_2),\\
&m_{41} = 2g_{12}n_0, \;\; m_{42} = \frac{1}{2}(K_1^2 + K_2^2) + 2g_{22}n_0, \;\; m_{43} = k_1\alpha + \lambda_R(K_2 - iK_1) + \lambda_D(iK_2 - K_1),\\
&m_{44} = -\Omega + \alpha K_2.
\end{aligned}
\tag{3.53}
$$

B4. Matrix (3.21) elements for the case $\beta_x = \beta_y = \beta$, with $(\beta x + \beta y) = \pi/2$

Appendix B5 shows the elements of matrix for the case$\beta_x = \beta_y = \beta$

$$
\begin{aligned}
&m_{11} = \Omega + (\beta K_1 + \alpha K_2), \;\; m_{12} = K_1\alpha + K_2\beta - (iK_1 + K_2)\lambda_R - \lambda_D(K_1 + iK_2),\\
&m_{13} = -\frac{1}{2}(K_1^2 + K_2^2) + \beta(\lambda_D + i\lambda_R), \;\; m_{14} = -\beta(\lambda_D + i\lambda_R),\\
&m_{21} = (\beta K_2 + \alpha K_1) + \lambda_R(iK_1 - K_2) + \lambda_D(K_1 - iK_2), \;\; m_{22} = \Omega + (\alpha K_2 + \beta K_1),\\
&m_{23} = -\beta(\lambda_D + i\lambda_R),\\
&m_{24} = -\frac{1}{2}(K_1^2 + K_2^2) + \beta(\lambda_D + i\lambda_R), \;\; m_{31} = \frac{1}{2}(K_1^2 + K_1^2) + 2g_{11}n_0 - \beta(\lambda_D + i\lambda_R),\\
&m_{32} = 2g_{12}n_0 + \beta(\lambda_D + i\lambda_R), \;\; m_{33} = -\Omega - (\beta K_1 + \alpha K_2),\\
&m_{34} = \lambda_R(K_2 + iK_1) + \lambda_D(K_1 + iK_2) - (K_1\alpha + K_2\beta),\\
&m_{41} = 2g_{12}n_0 + \beta(\lambda_D + i\lambda_R), \;\; m_{42} = \frac{1}{2}(K_1^2 + K_2^2) + 2g_{22}n_0 - \beta(\lambda_D + i\lambda_R),\\
&m_{43} = \lambda_R(K_2 - iK_1) + \lambda_D(iK_2 - K_1) - (\beta K_2 + K_1\alpha), \;\; m_{44} = -\Omega + (\beta K_1 - \alpha K_2).
\end{aligned}
\tag{3.54}
$$

Bibliography

[1] W. Ketterle, C. Townsend, S. Stringari, Physics World **29**, (1997).

[2] D. Bennett, *Properties of the Bose Einstein Condensate* sciencing.com, https://sciencing.com/properties-bose-einstein-condensate-8737764.html. 12 April 2021.

[3] M. H. Anderson, J. R. Ensher, M. R. Matthews, C. E. Wieman and E. A. Cornell, Science **269**, 198 (1995).

[4] K. B. Davis, M.-O. Mewes, M. R. Andrews, N. J. van Druten, D. S. Durfee, D. M. Kurn, W. Ketterle, Phys. Rev. Lett. **75**, 3969 (1995).

[5] C. C. Bradley, C. A. Sackett, R. G. Hulet, Phys. Rev. Lett. **78**, 985 (1997).

[6] A. Griesmaier, J. Werner, S. Hensler, J. Stuhler and T. Pfau, Phys. Rev. Lett **94**, 160401 (2005).

[7] Q. Beaufils, R. Chicireanu, T. Zanon, B. Laburthe-Tolra, E. Marechal, L. Vernac, J.-C. Keller and O. Gorceix, Phys. Rev. A **77**, 061601 (2008).

[8] L. V. Butov, C. W. Lai, A. L. Ivanov, A. C. Gossard and D. S. Chemla, Nature **417**, 47 (2002).

[9] H. Deng, G. Welhs, C. Santori, J. Bloch and Y. Yamamoto, Science **298**, 199 (2002).

[10] J. Kasprzak, M. Richard, S. Kundermann, A. Baas, P. Jeambrun, J. M. J. Keeling, F. M. Marchetti, M. H. Szymanska, R. Andre, J. L. Staehli, V. Savona, P. B. Littlewood, B. Deveaud and L. S. Dang, Nature **443**, 409 (2006).

[11] S. O. Demokritov, V. E. Demidov, O. Dzyapko, G. A. Melkov, A. A. Serga, B. Hillebrands and A. N. Slavin, Nature **443**, 430 (2006).

[12] D. G. Fried, T. C. Killian, L. Willmann, D. Landhuis, S. C. Moss, D. Kleppner, and T. J. Greytak, Phys. Rev. Lett. **81**, 3811 (1998).

[13] C. J. Pethick and H. Smith, *Bose-Einstein Condensation in Dilute Gases* (Cambridge University Press, Cambridge, 2002).

[14] L. P. Pitaevskii and A. Stringari, *Bose-Einstein Condensation* (Clarendon Press, Oxford, 2003).

[15] V. K. Kuetche, T. B. Bouetou, T. C. Kofane, A. B. Moubissi, and K. Porsezian, Phys. Rev. A **82**, 053619 (2010).

[16] A. Mohamadou, E. Wamba, D. Lissouck, and T. C. Kofane, Phys. Rev. E **85**, 046605 (2012).

[17] D. B. Belobo, G. H. Ben-Bolie, and T. C. Kofane, Phys. Rev. E **89**, 042913 (2014).

[18] D. B. Belobo, G. H. Ben-Bolie, and T. C. Kofane, Phys. Rev. E **91**, 042902 (2015).

[19] B. P. Anderson, K. Dholakia, and E. M. Wright, Phys. Rev. A **67**, 033601 (2003).

[20] R. Kanamoto, H. Saito, and M. Ueda, Phys. Rev. A **67**, 013608 (2003).

[21] S. Inouye, T. Pfau, S. Gupta, A. P. Chikkatur, A. Gorlitz, D. E. Pritchard, and W. Ketterle, Nature **402**, 641 (1999).

[22] E. W. Hagley, L. Deng, M. Kozuma, J. Wen, K. Helmerson, S. L. Rolston, and W. D. Phillips, Science **283**, 1706 (1999).

[23] C. J. Myatt, E. A. Burt, R. W. Ghrist, E. A. Cornell, and C. E. Wieman, Phys. Rev. Lett. **78**, 586 (1997).

[24] J. Stenger, S. Inouye, D. M. Stamper-Kurn, H.-J. Miesner, A. P. Chikkatur, and W. Ketterle, Nature (London) **396**, 345 (1998).

[25] D. S. Hall, M. R. Matthews, J. R. Ensher, C. E. Wieman, and E. A. Cornell, Phys. Rev. Lett. **81**, 1539 (1998).

[26] D. M. Stamper-Kurn, M. R. Andrews, A. P. Chikkatur, S. Inouye, H.-J. Miesner, J. Stenger, and W. Ketterle, Phys. Rev. Lett. **80**, 2072 (1998).

[27] J. Stenger, S. Inouye, A. P. Chikkatur, D. M. Stamper-Kurn, D. E. Pritchard, and W. Ketterle, Phys. Rev. Lett. **82**, 4569 (1999).

[28] R. Wynar, R. S. Freeland, D. J. Han, C. Ryu, and D. J. Heinzen , Science **287**, 1016 (2000).

[29] T.-L. Ho and V. B. Shenoy, Phys. Rev. Lett. **77**, 3276 (1996).

[30] P. Ohberg and S. Stenholm, Phys. Rev. A **57**, 1272 (1998).

[31] E. Timmermans, Phys. Rev. Lett. **81**, 5718 (1998).

[32] H. Pu and N. P. Bigelow, Phys. Rev. Lett. **80**, 1134 (1998).

[33] M. R. Matthews, B. P. Anderson, P. C. Haljan, D. S. Hall, C. E. Wieman, and E. A. Cornell, Phys. Rev. Lett. **83**, 2498 (1999).

[34] J. J. Garcia-Ripoll and V. M. Perez-Garcia, Phys. Rev. Lett. **84**, 4264 (2000).

[35] B. D. Esry and C. H. Greene, Phys. Rev. A **59**, 1457 (1999).

[36] T. Busch and J. R. Anglin, Phys. Rev. Lett. **87**, 010401 (2001).

[37] C. Hamner, J. J. Chang, P. Engels, and M. A. Hoefer, Phys. Rev. Lett. **106**, 065302 (2011).

[38] P. Ohberg and L. Santos, Phys. Rev. Lett. **86**, 2918 (2001).

[39] L. Salasnich and B. A. Malomed, Phys. Rev. A **74**, 053610 (2006).

[40] K. Kasamatsu and M. Tsubota, Phys. Rev. Lett. **93**, 100402 (2004).

[41] D. V. Freilich, D. M. Bianchi, A. M. Kaufman, T. K. Langin, and D. S. Hall, Science **329**, 1182 (2010).

[42] T. Kawakami, T. Mizushima, M. Nitta, and K. Machida, Phys. Rev. Lett. **109**, 015301 (2012).

[43] S. Stellmer, C. Becker, P. Soltan-Panahi, E.M. Richter, S. Dorscher, M. Baumert, J. Kronjager, K. Bongs, and K. Sengstock, Phys. Rev. Lett. **101**, 120406 (2008).

[44] H. G. Luo and W. M. Liu, Phys. Rev. A **84**, 053631 (2011).

[45] C. Hamner, Y. Zhang, J. J. Chang, C. Zhang, and P. Engels, Phys. Rev. Lett. **111**, 264101 (2013).

[46] B.-H. Xie, H. Jing, S. Jin, and M.-L. Ge, Phys. Rev. A **65**, 055601 (2002).

[47] K. K. Ndebele, C. B. Tabi, and T. C. Kofane, J. Opt. Soc. Am. B. **32**, A214 (2020).

[48] C. B. Tabi, C. S. Panguetna, T. G. Motsumi, and T. C. Kofane, Phys. Scr. **95**, 075211 (2020).

[49] T. B. Benjamin and J. E. Feir, J. Fluid Mech. **27**, 417 (1967).

[50] P. Marquie, J. M. Bilbault, and M. Remoissenet, Phys. Rev. E **49**, 828 (1994).

[51] C. B. Tabi , A. S. Eteme , and T. C. Kofane, Nonlinear Dyn. **100**, 3799 (2020).

[52] N. R. Zaoro, C. B. Tabi, A. S. Eteme, and T. C. Kofane, Phys. Let. A **384**, 126133 (2020).

[53] K. Kasamatsu and M. Tsubota, Phys. Rev. Lett. **93**, 100402 (2004).

[54] P. G. Kevrekidis, R. Carretero-Gonzalez, G. Theocharis, D. J. Frantzeskakis, and B. A. Malomed, Phys. Rev. A **68**, 035602 (2003).

[55] A. Smerzi, A. Trombettoni, P. G. Kevrekidis, and A. R. Bishop, Phys. Rev. Lett. **89**, 170402 (2002).

[56] G. Theocharis, Z. Rapti, P. G. Kevrekidis, D. J. Frantzeskakis, and V. V. Konotop, Phys. Rev. A **67**, 063610 (2003).

[57] L. Li, Z. Li, B. A. Malomed, D. Mihalache, and W. M. Liu, Phys. Rev. A **72**, 033611 (2005).

[58] E. V. Doktorov, V. M. Rothos, and Y. S. Kivshar, Phys. Rev. A **76**, 013626 (2007).

[59] E. Wamba, A. Mohamadou, and T. C. Kofane, Phys. Rev. E **77**, 046216 (2008).

[60] J. K. Xue, G. Q. Li, A. X. Zhang, and P. Peng, Phys. Rev. E **77**, 016606 (2008).

[61] B. B. Baizakov, A. Bouketir, A. Messikh, and B. A. Umarov, Phys. Rev. E **79**, 046605 (2009).

[62] A. Mohamadou, E. Wamba, S. Y. Doka, T. B. Ekogo, and T. C. Kofane, Phys. Rev. A **84**, 023602 (2011).

[63] E. Kengne, A. Lakhssassi, W. M. Lui, and R. Vaillancourt, Phys. Rev. E **87**, 022914 (2013).

[64] E. Kengne and W. M. Lui, Phys. Rev. E **98**, 012204 (2018).

[65] D. Zanga, S. I. Fewo, C. B. Tabi, and T. C. Kofane, Commun. Nonlinear Sci. Numer. Simulat. **80**, 104993 (2020).

[66] G. P. Agrawal, *Nonlinear Fiber Optics*, 5th ed. (Academic, San Diego, 2013).

[67] J. Higbie and D. M. Stamper-Kurn, Phys. Rev. Lett. **88**, 090401 (2002).

[68] E. V. Goldstein and P. Meystre, Phys. Rev. A **55**, 2935 (1997).

[69] M. Yu, C. J. McKinstrie, and G. P. Agrawal, Phys. Rev. E **48**, 2178 (1993).

[70] N. P. Robins, W. Zhang, E. A. Ostrovskaya, and Y. S. Kivshar, Phys. Rev. A **64**, 021601 (2001).

[71] T. Ozawa, L. P. Pitaevskii, and S. Stringari, Phys. Rev. A **87**, 063610 (2013).

[72] S. Gautam and S. K. Adhikari, Phys. Rev. A **90**, 043619 (2014).

[73] I. A. Bhat, T. Mithun, B. A. Malomed, and K. Porsezian, Phys. Rev. A **92**, 063606 (2015).

[74] S. Bhuvaneswari, K. Nithyanandan, P. Muruganandam, and K. Porsezian, J. Phys. B: At. Mol. Opt. Phys. **49**, 245301 (2016).

[75] S. Wuster ,*Classical and Quantum Field Theory of Bose Einstein Condensates*, (2007).

[76] `http://2.bp.blogspot.com/-kwqEBZtDpW8/TvVOxo3zP7I/AAAAAAAAArw/ID940BXQ_i4/s1600/BoFe.jpg`

[77] K. Huang, *Statistical Mechanics*, John Wiely and Sons, New York, (1987).

[78] D. V. Schroeder, *Introduction to Thermal physics*, Pearson Education Limited, Essex, (2014).

[79] D. Durfee and W. Ketterle, Optics express, **28**, 299 (1998).

[80] N. N. Bogoliubov, J. Phys. **11**, 23 (1947).

[81] B. A. Malomed, *Soliton Management in Periodic Systems*, (2006).

[82] I. Bloch, J. Dalibard, and W. Zwerger, Rev. Mod. Phys. **80**, 885 (2008).

[83] F. K. Abdullaev, P. G. Kevrekidis, and M. Salerno, Phys. Rev. Lett. **105**, 113901 (2010).

[84] F. K Abdullaev, V. V. Konotop, M. Salerno, and A. V. Yulin, Phys. Rev. E **82**, 056606 (2010).

[85] I. Shomroni, E. Lahoud, S. Levy, and J. Steinhauer, Nature Phys. **5**, 193 (2009).

[86] F. K. Abdullaev, A. A. Abdumalikov, and R. M. Galimzyanov, Phys. Lett. A **367**, 149 (2007).

[87] P. Engels, I. Coddington, P. C. Haljan, and E. A. Cornell, Phys. Rev. Lett. **89**, 100403 (2002).

[88] K. Staliunas, S. Longhi, and G. J. de Valcarcel, Phys. Rev. Lett. **89**, 210406 (2002).

[89] F. K. Abdullaev and M. Salerno, Phys. Rev. A **72**, 033617 (2005).

[90] M. Greiner, O. Mandel, T. Esslinger, T. W. Hansch, and I. Bloch, Nature **415**, 39 (2002).

[91] L. Fallani, F. S. Cataliotti, J. Catani, C. Fort, M. Modugno, M. Zawada, and M. Inguscio, Phys. Rev. Lett. **91**, 240405 (2003).

[92] V. P. Mineev, Zh. Eksp. Teor. Fiz. **67**, 263 (1974) [Sov. Phys. JETP 40 132 (1974)].

[93] L. Wen, W. M. Liu, Y. Cai, J. M. Zhang, and J. Hu, Phys. Rev. A **85**, 043602 (2012).

[94] G. Parker, and N. P. Proukakis, Phys. Rev. A **87**, 013625 (2013).

[95] N. Gemelke, X. Zhang, C.-L. Hung, and C. Chin, Nature **460**, 995 (2009).

[96] G. Modugno, G. Ferrari, G. Roati, R. J. Brecha, A. Simoni, and M. Inguscio, Science **294**, 1320 (2001).

[97] G. Modugno, M. Modugno, F. Riboli, G. Roati, and M. Inguscio, Phys. Rev. Lett. **89**, 190404 (2002).

[98] H. Pu and N. P. Bigelow, Phys. Rev. Lett. **80**, 1130 (1998).

[99] M. J. Jamieson, H. Sarbazi-Azad, H. Ouerdane, G.-H. Jeung, Y. S. Lee, and W. C. Lee, J. Phys. B **36**, 1085 (2003).

[100] D. Schumayer and B. Apagyi, Phys. Rev. A **69**, 043620 (2004).

[101] M. Mudrich, S. Kraft, K. Singer, R. Grimm, A. Mosk, and M. Weidemuller, Phys. Rev. Lett. **88**, 253001 (2002).

[102] S. De Palo, C. Castellani, C. Di Castro, and B. K. Chakraverty, Phys. Rev. B **60**, 564 (1999).

[103] W. D. Phillips, Reviews of Modern Physics, **70**, 721 (1998).

[104] S. Chu, Science, **253**, 861 (1991).

[105] Spin-Orbit Coupling. (n.d.) The Great Soviet Encyclopedia, 3rd Edition. (1970-1979). Retrieved January 6 2021 from https://encyclopedia2.thefreedictionary.com/Spin-Orbit+Coupling

[106] E. M Lifshitz and L. D. Landau, *Course of Theoretical Physics, Quantum Mechanics*, Pergamon Press Co., New York, USA, (1977).

[107] C. Qu, K. Sun, and C. Zhang, Phys. Rev. A, **91**, 053630(2015).

[108] L. D. Landau and L. M. Lifshitz, *Quantum Mechanics Non-Relativistic Theory*, Third Edition: Volume 3. Butterworth-Heinemann, January (1981).

[109] P. J. Siemens and A. S. Jensen, *Elements of Nuclei: Many-Body Physics with the Strong Interaction*, Allan Wylde, (1993).

[110] S. Weinberg, *Lectures on Quantum Mechanics*, Cambridge University Press, (2013).

[111] M. Z. Hasan and C. L. Kane, Rev.Mod.Phys. **82**, 3045 (2010).

[112] B. A. Bernevig and T. L. Hughes, *Topological Insulators and Topological Superconductors*, Princeton University Press, (2013).

[113] E. I. Rashba, Fizika Tverdogo Tela **2**, 1224 (1960). [Sov. Phys. Solid State 2, 1109 (1960)].

[114] Y. A. Bychkov and E. I. Rashba, Journal of Physics C: Solid State Physics, **17**, 6039 (1984).

[115] G. Dresselhaus, Phys. Rev **100**, 580 (1955).

[116] M. Kato, X.-F. Zhang, and H. Saito, Phys. Rev. A **95**,043605 (2017).

[117] M. Konig, S. Wiedmann, C. Brüne, A. Roth, H. Buhmann, Laurens W. Molenkamp, X.-L. Qi, and S.-C. Zhang, Science **318**, 76 (2007).

[118] C. L. Kane and E. J.Mele. Z2. Phys. Rev. Lett. **95**, 146802 (2005).

[119] B. A. Bernevig, T. L. Hughes, and S.-C. Zhang, Science **314**, 1757 (2006).

[120] D. Hsieh, D. Qian, L. Wray, Y. Xia, Y. S. Hor, R. J. Cava, and M. Z. Hasan, Nature **452**, 970 (2008).

[121] Y. J. Lin, K. Jimenez-Garcia, and I. B. Spielman, Nature **471**, 83 (2011).

[122] L. W. Cheuk, A. T. Sommer, Z. Hadzibabic, T. Yefsah, W. S. Bakr and M. W. Zwierlein, Phys. Rev. Lett. **109**, 095302 (2012).

[123] P.-J. Wang, Z.-Q. Yu, Z. Fu, J. Miao, L. Huang, S. Chai, H. Zhai and J. Zhang, Phys. Rev. Lett. **109**, 095301 (2012).

[124] A. Hasegawa, *Optical Solitons in Fibers*, Springer-Verlag, New York, (1990).

[125] F. Abdullaev, S. Darmanyan, and P. Khabibullaev, *Optical Solitons* , Springer-Verlag, Berlin, (1993).

[126] G. P. Agrawal, *Applications of Nonlinear Fiber Optics*, Academic Press, San Diego, CA, (2001).

[127] C.J. Pethick and H. Smith, "Bose-Einstein Condensation in Dilute Gases" (Cambridge University Press, Cambridge, 2002).

[128] A. Scott, *Nonlinear Science: emergence and dynamics of coherent structures*, Oxford University Press, Oxford, (1999).

[129] M.J. Ablowitz and H. Segur, *Solitons and the Inverse Scattering Transform*, SIAM, Philadelphia, (1981).

[130] P.G. Drazin and R.S. Johnson, *Solitons: An Introduction*, Cambridge University Press, Cambridge, U.K., (1989).

[131] D.J. Korteweg and C. de Vries, Philos. Mag. **39**, 422 (1898).

[132] T. Taniuti and H. Washimi, Phys. Rev. Lett. **21**, 209 (1968).

[133] E. A. Kuznetsov and A. M. Rubenchik, Physics Reports (Review Section of Physics Letters) **142**, 103 (1986).

[134] N. J. Zabusky and M. D. Kruskal, Phys. Rev. Lett. **15**, 240 (1965).

[135] H.Hasegawa and Y. Kodama, Solitons in Optical Communications (Oxford University Press, New York, 1995).

[136] H.A. Haus and W. S. Wong, Rev. Mod. Phys. **68**, 423 (1996).

[137] D. J. Frantzeskakis, J. Phys. A: Math. Theor. **43**, 213001 (2010).

[138] W. J. Tomlinson, R. J. Hawkins, A. M. Weiner, J. P. Heritage, and R. N. Thurston, Journal of the Optical. Society of America B-Optical Physics, (1989).

[139] V. M. Perez-Garcia, H. Michinel, and H. Herrero, Phys. Rev. A **57**, 3837 (1998).

[140] S. K. Adhikari, New J. Phys. **5**, 137 (2003).

[141] L. D. Carr, M. A. Leung, W. P. Reinhardt, J. Phys. B **33**, 3983 (2000).

[142] K. E. Strecker, G. B. Partridge, A. G. Truscott, and R. G. Hulet, Nature **417**, 150 (2002).

[143] . L. Khaykovich, F. Schreck, G. Ferrari, T. Bourdel, J. Cubizolles, L. D. Carr, Y. Castin, and C. Salomon, Science **296**, 1290 (2002).

[144] K. E. Strecker, G. B. Partridge, A. G. Truscott, and R. G. Hulet, New J. Phys. **5**, 73 (2003).

[145] S. L. Cornish, S. T. Thompson, and C. E. Wieman, Phys. Rev. Lett. **96**, 170401 (2006).

[146] A. L. Marchant, T. P. Billam, T. P. Wiles, M. M. H. Yu, S. A. Gardiner, and L. Cornish, Nature Communications **4**, 1865 (2013).

[147] J. H. V. Nguyen, P. Dyke, D. Luo, B. A. Malomed, and R. G. Hulet, Nature Physics **10**, 918 (2014).

[148] N. G. Parker, A. M. Martin, S. L. Cornish, and C. S. Adams, J. Phys. B **41**, 045303 (2008).

[149] S. A. Morgan, R.J. Ballagh, and K. Burnett, Phys. Rev. A **55**, 4338 (1997).

[150] A. E. Muryshev, H. B. van Linden van den Heuvell, and G. V. Shlyapnikov, Phys. Rev. A **60**, 2665 (1999).

[151] S.K. Adhikari, J. Low Temp. Phys. **143**, 267 (2006).

[152] T. Busch and J.R. Anglin, Phys. Rev. Lett. **84**, 2298 (2000).

[153] D.J. Frantzeskakis, G. Theocharis, F. K. Diakonos, P. Schmelcher, and Y. S. Kivshar, Phys. Rev. A **66**, 053608 (2002).

[154] J. Dziarmaga, Z.P. Karkuszewski, and K. Sacha, J. Phys. B **36**, 1217 (2003).

[155] J. Denschlag, J. E. Simsarian, D. L. Feder, Charles W. Clark, L. A. Collins, J. Cubizolles, L. Deng, E. W. Hagley, K. Helmerson, W. P. Reinhardt, S. L. Rolston, B. I. Schneider, and W. D. Phillips, Science **287**, 97 (2000).

[156] S. Burger, K. Bongs, S. Dettmer, W. Ertmer, K. Sengstock, A. Sanpera, G.V. Shlyapnikov, and M. Lewenstein, Phys. Rev. Lett. **83**, 5198 (1999).

[157] B. P. Anderson, P. C. Haljan, C. A. Regal, D. L. Feder, L. A. Collins, C. W. Clark, and E. A. Cornell, Phys. Rev. Lett. **86**, 2926 (2001).

[158] A. Weller, J. P. Ronzheimer, C. Gross, J. Esteve, M. K. Oberthaler, D. J. Frantzeskakis, G. Theocharis, and P. G. Kevrekidis, Phys. Rev. Lett. **101**, 130401 (2008).

[159] G. Theocharis, A. Weller, J. P. Ronzheimer, C. Gross, M. K. Oberthaler, P. G. Kevrekidis, Phys. Rev. A **81**, 063604 (2010).

[160] C. Becker, S. Stellmer, P. Soltan-Panahi, S. Dorscher, M. Baumert, E.-M. Richter, J. Kronjager, K. Bongs, and K. Senhstock, Nature Physics **4**, 496 (2008).

[161] S. Middelkamp, J. J. Chang, C. Hamner, R. Carretero-Gonzalez, P. G. Kevrekidis, V. Achilleos, D. J. Frantzeskakis, P. Schmelcher, and P. Engels, Phys. Lett. A **375**, 642 (2011).

[162] D. Yan, J. J. Chang, C. Hamner, P. G. Kevrekidis, P. Engels, V. Achilleos, D. J. Frantzeskakis, R. Carretero-Gonzalez, and P. Schmelcher,Phys. Rev. A **84**, 053630 (2011).

[163] M. A. Hoefer, J. J. Chang, C. Hamner, and P. Engels, Phys. Rev. A **84**, 041605 (2011).

[164] D. Yan, J. J. Chang, C. Hamner, M. Hoefer, P. G. Kevrekidis, P. Engels, V. Achilleos, D. J. Frantzeskakis, and J. Cuevas, J. Phys. B: At. Mol. Opt. Phys. **45**, 115301 (2012).

[165] O. Morsch and M. Oberthaler, Rev. Mod. Phys. **78**, 179 (2006).

[166] V. E. Zakharov and L. A. Ostrovsky, Physica D: Nonlinear Phenomena **238** 540 (2009).

[167] V. I. Bespalov and V. I. Talanov, JETP Lett. 3, **307** (1966).

[168] V. I. Karpman, JETP Lett. **6**, 277 (1967).

[169] A. Hasegawa and W. F. Brinkman, J. Quant. Electron. **16**, 694 (1980).

[170] M. D. Iturbe-Castillo, M. Torres-Cisneros, J. J. Snchez-Mondragn, S. Chvez-Cerda, S. I. Stepanov, V. A. Vysloukh, and G. E. Torres-Cisneros, Opt. Lett. **20**, 1853 (1995).

[171] M. I. Carvalho, S. R. Singh, and D. N. Christodoulides, Opt. Commun. **126**, 167 (1996).

[172] S. Sultana and I. Kourakis, Plasma Phys. Controlled Fusion **53**, 045003 (2011).

[173] J. Borhanian, I. Kourakis, and S. Sobhanian, Phys. Lett. A **373**, 3667 (2009).

[174] V. Saxena, A. Sen, and P. Kaw, Phys. Rev. E **80**, 016406 (2009).

[175] V. Saxena and I. Kourakis, Eur. Phys. Lett. **100**, 15002 (2012).

[176] G. Sanchez-Arriaga, E. Siminos, V. Saxena, and I. Kourakis, Phys. Rev. E **91**, 033102 (2015).

[177] V. Saxena, A. Das, A. Sen, and P. Kaw, Phys. Plasmas **13**, 032309 (2006).

[178] V. Saxena, A. Das, S. Sengupta, P. Kaw, and A. Sen, Phys. Plasmas **14**, 072307 (2007).

[179] S. Sultana and I. Kourakis, Eur. Phys. J. D **66**, 100 (2012).

[180] M. McKerr, I. Kourakis, and F. Haas, Plasma Phys. Controlled Fusion **56**, 035007 (2010).

[181] G. P. Veldes, J. Borhanian, M. McKerr, V. Saxena, D. J. Frantzeskakis, and I. Kourakis, J. Opt. **15**, 064003 (2013).

[182] L.D. Carr and J. Brand, Phys. Rev. Lett. **92**, 040401 (2004).

[183] L. Salasnich, A. Parola, and L. Reatto, Phys. Rev. Lett. **91**, 080405 (2003).

[184] A. Trombettoni, P. G. Kevrekidis, H. E. Nistazakis, and D. J. Frantzeskakis, J. Phys. B: At. Mol. Opt. Phys. **39**, 231 (2006).

[185] V. V. Konotop and M. Salerno, Phys. Rev. A **65**, 021602 (2002).

[186] C. Gmachl, F. Capasso, D. L. Sivco and A. Y. Cho, Rep. Prog. Phys. **64**, 1533 (2001).

[187] G. Barontini, R. Labouvie, F. Stubenrauch, A. Vogler, V. Guarrera, and H. Ott, Phys. Rev. Lett. **110**, 035302 (2013).

[188] S. Diehl, A. Micheli, A. Kantian, B. Kraus, H. P. Buchler, and P. Zoller, Nature Phys. **4**, 878 (2008).

[189] B. Kraus, H. P. Buchler, S. Diehl, A. Kantian, A. Micheli, and P. Zoller, Phys. Rev. A **78**, 042307 (2008).

[190] H. Krauter, C. A. Muschik, K. Jensen, W. Wasilewski, J. M. Petersen, J. I. Cirac, and E. S. Polzik, Phys. Rev. Lett. **107**, 080503 (2011).

[191] F. Verstraete, M. M. Wolf, and J. I. Cirac, Nature Phys. **5**, 633 (2009).

[192] M. O. Scully, M. S. Zubairy, *Quantum Optics*, (Cambridge University Press, UK, 1997).

[193] I. Bloch, T. W. Hansch, T. Esslinger, Phys. Rev. Lett. **82**, 3003 (1999).

[194] J. Ruostekoski and D. F. Walls, Phys. Rev. A **58**, 50 (1998).

[195] D. Witthaut, F. Trimborn, H. Hennig, G. Kordas, T. Giesel, and S. Wimberger, Phys. Rev. A **83**, 063608 (2011).

[196] S. Caspar, F. Hebenstreit, D. Mesterhazy, and U. J. Wiese, New J. Phys. **18**, 073015 (2016).

[197] J. Marelic and R. A. Nyman, Phys. Rev. A **91**, 033813 (2015).

[198] P. Kirton and J. Keeling, Phys. Rev. Lett. **111**, 100404 (2013).

[199] L. P. Pitaevskii,Zh. Eksp. Teor. Fiz. **40**, 646 (1961) [Sov. Phys. JETP **13**, 451 (1961)].

[200] F. T. Arecchi, J. Bragard, and L. M. Castellano, Opt. Commun. **179**, 156 (1999).

[201] Y. V. Kartashov and V. V. Konotop, Phys. Rev. Lett. **118**, 190401 (2017).

[202] S. Blatt, T. L. Nicholson, B. J. Bloom, J. R. Williams, J. W. Thomsen, P. S. Julienne, and J. Ye, Phys. Rev. Lett. **107**, 073202 (2011).

[203] S. Inouye, M. R. Andrews, J. Stenger, H.-J. Miesner, D. M. Stamper-Kurn, and W. Ketterle, Nature (London) **392**, 151 (1998).

[204] M. C. Rechtsman, J. M. Zeuner, Y. Plotnik, Y. Lumer, D. Podolsky, F. Dreisow, S. Nolte, M. Segev, and A. Szameit, Nature (London) **496**, 196 (2013).

[205] S. V. Samsonov, A. D. R. Phelps, V. L. Bratman, G. Burt, G. G. Denisov, A. W. Cross, K. Ronald, W. He, and H. Yin, Phys. Rev. Lett. **92**, 118301 (2004).

[206] G. Burt, S. V. Samsonov, K. Ronald, G. G. Denisov, A. R. Young, V. L. Bratman, A. D. R. Phelps, A. W. Cross, I. V. Konoplev, W. He, J. Thomson, and C. G. Whyte, Phys. Rev. E **70**, 046402 (2004).

[207] X. -X. Li, R. -J. Cheng, A. -X. Zhang, and J. -K. Xue, Phys. Rev. E **100**, 032220 (2019).

[208] R. J. C. Spreeuw, T. Pfau, U. Janicke, and M. Wilkens, Europhys. Lett. **32**, 469 (1995).

[209] G. M. Moy, J. J. Hope, and C. M. Savage, Phys. Rev. A **55**, 3631 (1997).

[210] H. M. Wiseman and M. J. Collett, Phys. Lett. A **202**, 246 (1995).

[211] C. Borde, Phys. Lett. A **204**, 217 (1995).

[212] B. Kneer, T. Wong, K. Vogel, W. P. Schleich, and D. Walls, Phys. Rev. A **58**, 4841 (1998).

[213] M. Wouters and I. Carusotto, Phys. Rev. Lett. **99**, 140402 (2007).

[214] L. M. Pismen, Phys. Rev. Lett. **72**, 2557 (1994).

[215] M. S. Miguel, Phys. Rev. Lett. **75**, 425 (1995).

[216] F. Ndzana, A. Mohamadou, and T. C. Kofane, Chaos **18**, 043121 (2008).

[217] A. S. Eteme, C. B. Tabi, and A. Mohamadou, Chaos, Solitons and Fractals **104**, 813 (2017).

[218] J. Atai and B. A. Malomed, Phys. Rev. E **54**, 4371 (1996).

[219] H. Sakaguchi and B. A. Malomed, Physica D **147**, 273 (2000).

[220] O. S. Pak, C. K. Lam, K. Nakkeeran, B. Malomed, K. W. Chow, and K. Senthilnathan, J. Phys. Soc. Jpn **78**, 084001 (2009).

[221] A. Amengual, E. Hernandez-Garcia, R. Montagne, M. San Miguel, Phys. Rev. Lett. **78**, 4379 (1997).

[222] E. Hernandez-Garcia, M. Hoyuelos, P. Colet, M. San Miguel, R. Montagne, Int. J. Bif. Chaos **9**, 2257 (1999).

[223] M. Hoyuelos, E. Hernandez-Garcia, P. Colet, M. San Miguel, Comp. Phys. Comm. **121**, 414 (1999).

[224] E. Hernandez-Garcia, M. Hoyuelos, P. Colet, M. San Miguel, Phys. Rev. Lett. **85**, 744 (2000).

[225] Miguel Hoyuelos, Emilio Hernandez-Garcia, Pere Colet, Maxi San Miguel, Physica D **174**, 176 (2003).

[226] M. C. Cross, Phys. Rev. A **38** (1988) 3593.

[227] G. A. Zakeri and E. Yomba, J. Phys. Soc. Jpn **82**, 084002 (2013).

[228] A. Djazet, C. B. Tabi, S. I. Fewo, and T. C. Kofane, Appl. Phys. B **126**, 74 (2020).

[229] G. A. Zakeri and E. Yomba, Phys. Rev. E **91**, 062904 (2015).

[230] S. Saha, E. J. König , J. Lee, and J. H. Pixley, Phys. Rev. Res. **2**, 013252 (2020).

[231] L. Chen, Y. Zhang, and H. Pu, Phys. Rev. A **102**, 023317 (2020).

[232] H. Saito, and M. Ueda, Phys. Rev. Lett. **86**, 1406 (2001).

[233] A. M. Kamchatnov, A. Gammal, F. K. Abdullaev, and R. A. Kraenkel, Phys. Lett. A **319**, 406 (2003).

[234] L.D. Carr and J. Brand, Phys. Rev. Lett.**92**, 040401 (2004).

[235] D. B. Belobo, G. H. Ben-Bolie, T. B. Ekogo, and T. C. Kofane, Int. Mod. Phys. B **52**, 1415 (2013).

[236] S. Bhuvaneswari, K. Nithyanandan, P. Muruganandam, and K. Porsezian, J. Phys. B: At. Mol. Opt. Phys. **49**, 245301 (2016)

[237] T. Mithun, and K. Kasamatsu, J. Phys. B: At. Mol. Opt. Phys. **52**, 045301 (2019).

[238] Y. Xu, Y. Zhang, and C. Zhang, Phys. Rev. A **92**, 013633 (2015)

[239] K. Osterloh, M. Baig, L. Santos, P. Zoller, and M. Lewenstein, Phys. Rev. Lett. **95**, 010403 (2005).

[240] Y.-J. Lin, R. L. Compton, A. R. Perry,W. D. Phillips, J. V. Porto, and I. B. Spielman, Phys. Rev. Lett. **102**, 130401 (2009).

[241] X.-J. Liu, X. Liu, L. C. Kwek, and C. H. Oh, Phys. Rev. Lett. **98**, 026602 (2007).

[242] S.-L. Zhu, H. Fu, C.-J.Wu, S.-C. Zhang, and L.-M. Duan, Phys. Rev. Lett. **97**, 240401 (2006).

[243] J. Dalibard, F. Gerbier, G. Juzeliunas, and P. Ohberg, Rev. Mod. Phys. **83**, 1523 (2011).

[244] Z. Fu, P. Wang, S. Chai, L. Huang, and J. Zhang, Phys. Rev. A **84**, 043609 (2011).

[245] G. Juzeliunas, J. Ruseckas, P. Ohberg, and M. Fleischhauer, Phys. Rev. A **73**, 025602 (2006).

[246] Y.-J. Lin, R. L. Compton, K. Jimenez-Garcia, J. V. Porto, and I. B. Spielman, Nature (London) **462**, 628 (2009).

[247] J. Ruseckas, G. Juzeliunas, P. Ohberg, and M. Fleischhauer, Phys. Rev. Lett. **95**, 010404 (2005).

[248] G. Juzeliunas, P. Ohberg, J. Ruseckas, and A. Klein, Phys. Rev. A **71**, 053614 (2005).

[249] V. Galitski and I. B Spielman, Nature **494**, 49 (2013).

[250] J. Radic, T. A. Sedrakyan, I. B. Spielman, and V. Galitski, Phys. Rev. A **84**, 063604 (2011).

[251] Y. K. Kato, R. C. Myers, A. C. Gossard, and D. D. Awschalom, Science **306**, 1910 (2004).

[252] T. D. Stanescu and V. Galitski, Phys. Rev. B **75**, 125307 (2007).

[253] J. D. Koralek, C. P. Weber, J. Orenstein, B. A. Bernevig, S.-C. Zhang, S. Mack, and D. D. Awschalom , Nature **458**, 610 (2009).

[254] A. Manchon, H. C. Koo, J. Nitta, S. M. Frolov, and R. A. Duine, Nat. Mater. **14**, 871 (2015).

[255] W. Zheng, Z.-Q. Yu, X. Cui, and H. Zhai, J. Phys. B: At. Mol. Opt. Phys. **46**, 134007 (2013).

[256] S. Datta and B. Das, Appl. Phys. Lett. **56**, 665 (1990).

[257] B. Das, S. Datta, and R. Reifenberger, Phys. Rev. B **41**, 8278 (1990).

[258] S. D. Ganichev, V. V. Belkov, L. E. Golub, E. L. Ivchenko, P. Schneider, S. Giglberger, J. Eroms, J. De Boeck, G. Borghs, W. Wegscheider, D. Weiss, and W. Prettl, Phys. Rev. Lett. **92**, 256601 (2004).

[259] G. Juzeliunas, J. Ruseckas, and J. Dalibard, Phys. Rev. A **81**, 053403 (2010).

[260] C.Wang, C. Gao, C.-M. Jian, and H. Zhai, Phys. Rev. Lett. **105**, 160403 (2010).

[261] H. Hu, B. Ramachandhran, H. Pu, and X.-J. Liu, Phys. Rev. Lett. **108**, 010402 (2012).

[262] S. Sinha, R. Nath, and L. Santos, Phys. Rev. Lett. **107**, 270401 (2011).

[263] T. Ozawa and G. Baym, Phys. Rev. A **85**, 013612 (2012).

[264] Z. F. Xu, Y. Kawaguchi, L. You, and M. Ueda, Phys. Rev. A **86**, 033628 (2012).

[265] T. Kawakami, T. Mizushima, and K. Machida, Phys. Rev. A **84**, 011607 (2011).

[266] Z. F. Xu, R. Lu, and L. You, Phys. Rev. A **83**, 053602 (2011).

[267] S.-K. Yip, Phys. Rev. A **83**, 043616 (2011).

[268] P.-S. He, W.-L. You, and W.-M. Liu, Phys. Rev. A **87**, 063603 (2013).

[269] L. Salasnich, W. B. Cardoso, and B. A. Malomed, Phys. Rev. A **90**, 033629 (2014).

[270] J. Jin, S. Zhang, and W. Han, J. Phys. B: At. Mol. Opt. Phys. **47** 115302 (2014).

[271] H. Sakaguchi, E. Ya. Sherman, and B. A. Malomed, Phys. Rev. E **94**, 032202 (2016).

[272] S. Liu, B. Liao, J. Kong, P. Chen, J. Lu, Y. Li, C. Huang, and Y. Li, J. Phys. Soc. Jpn. **87**, 094005 (2018).

[273] R. Winkler, *Spin—Orbit Coupling Effects in Two-Dimensional Electron and Hole Systems* (Springer-Verlag Berlin Heidelberg, New York, 2003).

[274] J. Schliemann, J. C. Egues, and D. Loss, Phys. Rev. Lett. **90**, 146801 (2003).

[275] J. Nitta, T. Koga , J. Supercond. **16**, 689 (2003).

[276] I. Zutic, J. Fabian, S. Das Sarma, Rev. Mod. Phys. **76**, 323 (2004).

[277] G. Usaj, C. A. Balseiro, Europhys. Lett. **72**, 631 (2004).

[278] X. -X. Li, R.-J. Cheng, A.-X. Zhang, and J.-K. Xue, Phys. Rev. E **100**, 032220 (2019).

[279] I. A. Bhat, T. Mithun, B. A. Malomed, and K. Porsezian, Phys. Rev. A **92**, 063606 (2015).

[280] S. Bhuvaneswari, K. Nithyanandan, P. Muruganandam and K. Porsezian, J. Phys. B: At. Mol. Opt. Phys. **49**, 245301 (2016).

[281] D. Singh, M. K. Parit, T. S. Raju, and P. K. Panigrahi, J. Phys. B: At. Mol. Opt. Phys. **53**, 245001 (2020).

[282] T.-L. Ho and V. B. Shenoy, Phys. Rev. Lett. **77**, 3276 (1996).

[283] Y. V. Kartashov, E. Ya Sherman, B. A. Malomed, and V. V. Konotop, New J. Phys. **22**, 103014 (2020).

[284] S. V. Samsonov, A. D. R. Phelps, V. L. Bratman, G. Burt, G. G. Denisov, A. W. Cross, K. Ronald, W. He, and H. Yin, Phys. Rev. Lett. **92**, 118301 (2004).

[285] G. Burt, S. V. Samsonov, K. Ronald, G. G. Denisov, A. R Young, V. L. Bratman, A. D. R. Phelps, A. W. Cross, I. V. Konoplev, W. He, J. Thomson, and C. G. Whyte, Phys. Rev. E **70**, 046402 (2004).

[286] M. C. Rechtsman, J. M. Zeuner, Y. Plotnik, Y. Lumer, D.Podolsky, F. Dreisow, S. Nolte, M. Segev, and A. Szameit, Nature (London) **496**, 196 (2013).

[287] Y. V. Kartashov, V. V. Konotop, M. Modugno, and E. Y. Sherman, Phys. Rev. Lett. 122, 064101 (2019).

[288] L. D. Carr and J. Brand, Phys. Rev. Lett. **92**, 040401 (2004).

[289] W. Hai, C. Lee, and G. Chong, Phys. Rev. A **70**, 053621 (2004).

[290] K. E. Strecker, G. B. Partridge, A. G. Truscott, and R. G. Hulet, Nature **417**, 150 (2002).

[291] L. Salasnich, A. Parola, and L. Reatto, Phys. Rev. Lett. **91**, 080405 (2003).

[292] H. Sakaguchi, Ben Li, and B. A. Malomed, Phys. Rev. E **89**, 032920 (2014).

[293] Y. V. Kartashov, V. V. Konotop, and L. Torner, Phys. Rev. B **86**, 205313 (2012).

[294] K. Mæland, A. T. G. Janssønn, J. H. Rygh, and A. Sudbø, Phys. Rev. A **102**, 053318 (2020).

[295] H. Sakaguchi and B. A. Malomed, Phys. Rev. A **96**, 043620 (2017).

[296] S. Gautam and S. K. Adhikari, Phys. Rev. A **97**, 013629 (2018).

[297] Y. Xu, L. Mao, B. Wu, and C. Zhang, Phys. Rev. Lett. **113**, 130404 (2014).

[298] J. R. Li, J. Lee, W. Huang, S. Burchesky, B. Shteynas, F. C. Top, A. O. Jamison, and W. Ketterle, Nature **543**, 91 (2017).

[299] C. Wang, C. Gao, C. M. Jian, and H. Zhai, Phys. Rev. Lett. **105**, 160403 (2010).

[300] Y.-F. Jiang, A.-X. Zhang, X.-W. Hu, Z.-F. Yu, J.-K. Xue, Phys. Lett. A **392**, 127169 (2021) .

[301] S. Liu, B. Liao, J. Kong, P. Chen, J. Lü, Y. Li, C. Huang, and Y. Li, J. Phys. Soc. Jpn. **87**, 094005 (2018).

[302] N. Q. Burdick, Y. Tang, and B. L. Lev, Phys. Rev. X **6**, 031022 (2016).

[303] M. A. Khamehchi, K. Hossain, M. E. Mossman, Y. Zhang, T. Busch, M. M. Forbes and P. Engels, Phys. Rev. Lett. **118**, 155301 (2017).

List of Publications

1. **P. Otlaadisa**, C. B. Tabi and T. C. Kofané, *"Modulation instability in helicoidal spin-orbit coupled open Bose-Einstein condensates"*, Physical Review E **103** (2021) 052206.

2. C. B. Tabi, **P. Otlaadisa**, and T. C. Kofané, *"Modulation instability of two-dimensional Bose-Einstein condensates with helicoidal and a mixture of Rashba-Dresselhaus spin-orbit couplings"*, Physics Letters A (2022) 128334, doi://doi.org/10.1016/j.physleta.2022.128334.

Modulation instability in helicoidal spin-orbit coupled open Bose-Einstein condensates

Phelo Otlaadisa,[1,*] Conrad Bertrand Tabi,[1,†] and Timoléon Crépin Kofané[1,2,3,‡]
[1]*Department of Physics and Astronomy, Botswana International University of Science and Technology, Private Mail Bag 16, Palapye, Botswana*
[2]*Laboratory of Mechanics, Department of Physics, Faculty of Science, University of Yaoundé I, P.O. Box 812, Yaoundé, Cameroon*
[3]*Centre d'Excellence Africain en Technologies de l'Information et de la Communication, University of Yaoundé I, Yaoundé, Cameroon*

(Received 15 November 2020; revised 10 March 2021; accepted 8 April 2021; published 5 May 2021)

We introduce a vector form of the cubic complex Ginzburg-Landau equation describing the dynamics of dissipative solitons in the two-component helicoidal spin-orbit coupled open Bose-Einstein condensates (BECs), where the addition of dissipative interactions is done through coupled rate equations. Furthermore, the standard linear stability analysis is used to investigate theoretically the stability of continuous-wave (cw) solutions and to obtain an expression for the modulational instability gain spectrum. Using direct simulations of the Fourier space, we numerically investigate the dynamics of the modulational instability in the presence of helicoidal spin-orbit coupling. Our numerical simulations confirm the theoretical predictions of the linear theory as well as the threshold for amplitude perturbations.

DOI: 10.1103/PhysRevE.103.052206

I. INTRODUCTION

The experimental observation of Bose-Einstein condensates (BECs) of trapped atomic vapors has allowed investigations of some fundamental concepts of atomic physics and condensed matter [1,2]. It is well known that, at very low temperatures, the dynamical behavior of a BEC is well described by the Gross-Pitaevskii (GP) equation [3,4], which is a nonlinear Schrödinger (NLS) equation with an external potential. The GPE exhibits many types of nonlinear excitations such as dark solitons [5], representing holes in the otherwise homogeneous atomic distributions, bright solitons [5], characterized by atomic density distribution localized in space, compactons [6], and nonlinear periodic waves [7]. In addition, gray solitons [8], gap matter solitons [9], vortices [10], vortex lattices [11], Faraday waves [12], Bloch oscillations of BECs, Landau-Zener tunneling [13], superfluid to Mott-insulator phase transition [14], and compression of a condensate [15], have been studied theoretically as well as experimentally.

All the nonlinear phenomena observed in matter-wave condensates can be better explained with exact analytical solutions of the GP equation [16–19]. It is well known that the matter wave dynamics of a BEC loaded in optical lattices, which can be effectively manipulated by external field, leads to a number of BEC applications, like atomic interferometry [20], quantum phase transitions [21], matter wave amplification [22], atom lasers [23], and others. For instance, the two-component BECs whose dynamics are described by the NLS equations or GP equations, in which both the self-phase-modulation (SPM) and cross-phase-modulation (XPM) terms are represented by cubic terms, lead to novel nonlinear structures, such as dark-bright complexes [24,25], dark-dark solitons [26], bright-bright solitons [27], domain walls [28], vortex-antivortex dipoles [29], and skyrmions [30]. Dark-bright (DB) solitons are arguably one of the most intriguing coherent structures in two-component systems. The DB structures are made up of a dark soliton in the first component, which is responsible for an effective trapping potential that localizes a bright soliton in the second component, through nonlinear coupling. In binary BEC, dark-bright soliton complexes were predicted in theory [24] and observed in experiments [31] in a repulsive ^{87}Rb BEC binary mixture, using a phase imprinting method [31]. Most recently, multiple dark-bright solitons [25] as well as dark-dark solitons [32] were also created in a counterflow experiment [25].

Very recently, the interest in the physics of mixtures of spinor Bose-Einstein condensates and, in particular, in spin-orbit coupling (SOC) of neutral atoms in BECs [33,34] and fermionic gases [35,36], is motivated by currently available experimental techniques allowing the creation of versatile effective gauge potentials in ultracold atoms, Abelian or even non-Abelian, relevant not only to condensed-matter physics but also to the understanding of interactions between particles [37]. More precisely, different from electrons that are fermions, the ultracold atoms with SOC can be bosons. The so-called SOC-BEC [38] is a model where a synthetic spin degree of freedom coupled with the momentum allows one to simulate spin-orbit interactions in condensed matter physics and at the same time naturally introduces different types of gauge fields [34] which can be created and controlled by external laser beams, and has profoundly advanced our understanding of many interesting phenomena, such as the quantum spin Hall effect, superconductivity, and topological insulators [37]. Moreover, coupling between atomic spin and its

*phelo.otlaadisa@studentmail.biust.ac.bw
†Corresponding author: tabic@biust.ac.bw
‡tckofane@yahoo.com

 ©2021 American Physical Society

momentum were experimentally achieved in a spin $-\frac{1}{2}$ of ^{87}Rb BEC [33], in a spin -1 of ^{87}Rb BEC [39], and in other laboratories [36,40], respectively, stimulating extensive theoretical investigations of the properties of SOC-BECs, which includes vortices [41], Skyrmions [30], Dirac monopoles [42], and dark solitons [43], as well as self-trapped states [44], bright solitons [45], and also gap solitons [46]. In addition, multipeak bright solitons [47] and bright single- and multipeak vector solitons [48] have been found in SOC-BECs.

BECs behave quite differently when in contact with an external environment (reservoir). When in contact with a reservoir, a BEC is subject to particle and heat exchange. Then, the statistical physics predicts large statistical number fluctuations of the order of the total particle number occurring deep in the condensed phase of the BEC [49]. The reservoir can be a thermal bath or noncondensate atoms. Thus, in such open BEC systems, atom losses and dissipation are unavoidable phenomena when interactions between the condensed and uncondensed atoms are taken into account, which significantly affect the dynamics of the system. The linear coupling between the reservoir and condensate atoms inside the traps corresponds to the energy exchange between the system and reservoir through the creation and absorption of bath quanta or condensate atoms in the traps. In the system, dissipation is induced by the reservoir fluctuation in agreement with the fluctuation-dissipation theorem [50]. The dissipation is compensated for by a transfer from the uncondensed fraction of trapped atoms into the condensate atoms. Those in turn are refilled by continuous pumping processes [51].

Dissipative phenomena are nowadays attracting a great deal of attention in nonlinear media studies. They are among the main forces acting against the formation of nonlinear coherent structures in extended systems. When dissipation is present in systems without additional gain mechanisms, typically all excitations decay into the regime of linear waves. Very recently, controlled dissipation proved to be a useful tool for probing a quantum system in an ultracold setup. Moreover, dissipation was engineered and exploited as a measurement tool to study quantum effects in ultracold atoms and various other systems [52]. In the meantime, dissipation in a double well BEC coupled to a thermal bath was found to cause a macroscopic quantum self-trapping state to decay away [53]. In addition to that localized particle, dissipation was also found to restore BEC coherence [54]. Furthermore, the real-time dynamics of open quantum spin-1/2 or hardcore boson systems on a spatial lattice, governed by a Markovian quantum master equation, has also been investigated [55]. On the other hand, experimentally, grand canonical conditions in the condensed phase have been realized in a photon BEC coupled to a dye medium [56], where thermalization of the photon gas is achieved by absorption and reemission processes on dye molecules [57].

One of the key issues of soliton wave theory is the universal modulation instability (MI) phenomena which is one of the most fundamental processes in nonlinear wave systems in nature. MI, which is an indispensable mechanism for understanding pattern formation in a uniform medium, is a process in which the amplitude and phase modulations of a wave grow under the combined effects of nonlinearity and diffraction or dispersion in a spatially nonlinear field. Generally, MI occurs in the same regions of parameters where bright solitons are observed, and can be considered as a precursor to formation of localized nonlinear excitations, or soliton trains, and is deeply studied in nonlinear optics [58], plasma physics [59], hydrodynamics [60], electrical transmission lines [61], and biophysics [62,63].

In the context of BEC, investigations show that the MI has been responsible for the dephasing and the localization of the condensate, which are vital in understanding the dynamic processes in the BEC systems, which include domain formation [28], generation and propagation of solitonic waves [64], quantum phase transitions [65], and so on. Moreover, there has been extensive research on the MI in BECs both experimentally and theoretically for single- as well as two-component systems [66–75].

As in other physical systems [76], it was concluded that the single-component MI is feasible only for attractive interactions, and, in such case, the phase fluctuations caused by the MI leads to the formation of soliton trains. However, the breakthrough work by Goldstein and Meystre [77] opens up the possibility of MI even for repulsive interactions in two-component BECs [28], similar to the result known in nonlinear optics [78], in the case when the XPM is stronger than the SPM of each component. In such a case, the MI does not create trains of bright solitons, but rather creates domain walls which realize the phase separation in the immiscible binary BEC [79]. In addition, due to the production of the SOC in BEC, the dynamical instability of supercurrents, as a consequence of the violation of Galilean invariance, was investigated [80,81]. In particular, one may expect that the MI will lead to the generation of striped structures which realize the ground state in the SOC-BEC with repulsive or attractive intrinsic nonlinearity. The MI of two-component BECs with SOC in one and two dimensions was recently explored [82,83].

The main scope of the present paper is to focus on such MI phenomena and solitary structures, emerging from spin-orbit coupling to dissipative Bose-Einstein condensates. It is known that the self-modulation of waves in the BEC dynamics in an atomic trap is governed by the GP equation, which in fact is the NLS equation describing a conservative motion [5]. Moreover, in the case of SOC dissipative BECs, an atomic BEC is coupled to a source of uncondensed atoms, at the same temperature, and to a sink. It has been shown that the idealized description in terms of a GP equation breaks down for this dissipative dynamics of open BECs [84]. In our contribution, we start with coupled GP equations describing the evolution of the condensate wave functions of the two-component helicoidal SO-coupled BECs equally distributed between the two pseudospin states. Then, we add dissipative terms to the coupled GP equations and we couple the resulting equations with rate equation coupling between condensed and uncondensed atoms. Thus, we apply an adiabatic elimination procedure and show that two-component helicoidal SO-coupled dissipative BECs obey coupled cubic complex Ginzburg-Landau (CGL) equations. Furthermore, we discuss theoretically and numerically the MI process by using the framework of this coupled cubic CGL equation in the effectively one-dimensional (1D) geometry. We examine their stability by means of both the rigorous analysis of linearized equations for small perturbations,

and in direct numerical simulations to support our analytical results.

The rest of the paper is organized as follows. In Sec. II, we introduce the coupled GP equations for the two-component helicoidal SOC dissipative BECs from which the coupled cubic CGL equations are derived using the adiabatic elimination procedure. In Sec. III, we undertake the analytical study of the linear stability and MI of plane wave solutions of the coupled cubic CGL equations. The instability zones as well as the analytical expressions of the gain of MI are obtained. Then, in Sec. IV, the results of linear stability analysis are validated by the direct numerical simulations of the governing equation using the split-step Fourier transform method. Section V concludes the paper.

II. BASIC EQUATIONS

A. A system of two coupled 1D cubic GP equations

There exist three different approaches towards a theoretical description of a continuous-wave (cw) atom laser. The first one relies on rate equations [85], the second one derives a quantum mechanical master equation [86], and the third one, which we consider in this paper, uses a classical treatment of the electromagnetic field [87], which was sufficient to describe many features of the laser. In doing so, we consider the evolution of the condensate wave functions of two-component helicoidal SO-coupled BECs equally distributed between the two pseudospin states, in a 1D setting. Within the framework of mean-field theory, the macroscopic wave functions of such a system obey the following coupled 1D cubic GP equations without an eternal trapping potential term [88]:

$$i\frac{\partial\psi_1}{\partial t} = -\frac{1}{2}\frac{\partial^2\psi_1}{\partial x^2} + i\beta\frac{\partial\psi_1}{\partial x} - i\alpha\frac{\partial\psi_2}{\partial x} + \frac{\Delta}{2}\psi_1 + (g_{11}|\psi_1|^2 + g_{12}|\psi_2|^2)\psi_1, \tag{1}$$

$$i\frac{\partial\psi_2}{\partial t} = -\frac{1}{2}\frac{\partial^2\psi_2}{\partial x^2} - i\beta\frac{\partial\psi_2}{\partial x} - i\alpha\frac{\partial\psi_1}{\partial x} - \frac{\Delta}{2}\psi_2 + (g_{22}|\psi_2|^2 + g_{21}|\psi_1|^2)\psi_2, \tag{2}$$

where ψ_1 and ψ_2 are the two-component BEC pseudo-spin states, β is the helicoidal gauge potential, α represents the SOC strength, and Δ is the strength of the Zeeman splitting. Next, $g_{11} = 2a_{11}/a_\perp$ and $g_{22} = 2a_{22}/a_\perp$ are the strengths of the two-body intraspecies interactions, while $g_{12} = 2a_{12}/a_\perp$ and $g_{21} = 2a_{21}/a_\perp$ denote the strength of the two-body interspecies interactions. Here $a_\perp = \sqrt{\hbar/(mw_\perp)}$ is the transverse characteristic length, $w_\perp$ is the transverse trap frequency, m is the atomic mass, and $\hbar$ is the Planck constant. The a_{11}, a_{22}, and a_{12} are the s-wave scattering lengths that can be adjusted by optical [89] and magnetic [90] Feshbach resonance techniques in experiment. Finally, the spatial variable x, time t, density $(|\psi_1|^2 + |\psi_2|^2)$, and energy are expressed in normalized units $a_\perp$, $w_\perp^{-1}$, $a_\perp^{-1}$, and $\hbar w_\perp$, respectively. The wave functions are normalized as $N_j = \int |\psi_j|^2 dx$, with $j = 1, 2$, while the total number of atoms, i.e., the sum of numbers N_1 and N_2 of atoms of the jth component, is

$$N = N_1 + N_2 = \int (|\psi_1|^2 + |\psi_2|^2)dx, \tag{3}$$

which is the dynamical invariant of the lossless system. We should, however, stress that the set of coupled cubic GP equations (1) and (2) was derived by Li *et al.* [88] following a procedure proposed by Kartashov and Konotop [91], based on the point translational symmetry induced by the helicoidal structure of the vector potential and the rotating frame using a gauge transformation. As a consequence, the point translational symmetry of their generic equations, with periodically varying parameters, was changed into continuous translational symmetry, leading to a vector GP equation with constant coefficients with no magnetic trap. Nevertheless, in the original model proposed in Ref. [91], in the absence of the Zeeman splitting, the system obeys $\mathcal{PT}$ symmetry.

The definitions of $\mathcal{PT}$-symmetric potentials and their properties have been discussed in the past few years [92–95]. In particular, for a $\mathcal{PT}$-symmetric Hamiltonian, there exists a critical threshold above which its eigenvalues are not real but become complex, and the system undergoes a phase transition because of the spontaneous $\mathcal{PT}$-symmetry breaking [92]. Transition through this exceptional point is the most typical scenario of $\mathcal{PT}$-symmetry breaking, which arises in a more general context of non-Hermitian physics [95]. Indeed, it has been suggested that in nonlinear optics there is a possibility of realizing $\mathcal{PT}$-symmetric structures, which are achieved through a suitable distribution of the regions of gain or loss in the environment [96]. Furthermore, BECs confined in $\mathcal{PT}$-symmetric potentials, both in realistic setups as well as in theoretical models, have been studied recently. It is assumed that the BEC interacts with the local environment by adding an imaginary component on the potential profile, accounting phenomenologically for gain and loss in the system. To experimentally implement gain-loss mechanisms in a BEC trapped in a single-well potential, a pumping scheme similar to the one implemented in atom lasers can be exploited, as well as optical dipole traps, suitably adjusting the detuning to red or blue, whereas the loss mechanisms can be implemented by illuminating the BEC with electron beams [52]. It was proposed [97] that a system similar to $\mathcal{PT}$-symmetric waveguides could be realized using a BEC in a double-well potential, where in one well particles are injected, while from the other well particles are removed. It was demonstrated that a $\mathcal{PT}$-symmetric external potential for BECs can be realized with tilted optical lattices with a defect. The defect, consisting of two potential wells at the same height, i.e., a discontinuity in the tilt, acts as a $\mathcal{PT}$-symmetric subsystem. The influxes and outfluxes of the condensate's probability density can be modeled as imaginary $\mathcal{PT}$-symmetric contributions [98]. On the other hand, in cold atom physics, the use of optical lattices gives rise to additional possibilities, including the creation of gap solitons [46,99]. A diversity of symmetric and asymmetric lattice gap solitons in a SO-coupled BEC subject to a spatially periodic Zeeman field, and classified with respect to their parity, time, and pseudocharge symmetries, has been reported [46]. At the same time, it has been shown that a rich variety of two-dimensional stable solitons may exist in a SOC-BEC held in a Zeeman lattice and classified on the basis of symmetries imposed by the Zeeman lattice. In this respect, multipole and half-vortex solitons have been identified [99].

So far, however, no linear and nonlinear stages of MI have been reported in a 1D SO-coupled BEC in lattice potentials,

where the addition of dissipative interactions is done through coupled rate equations. The extension of the model to realistic external potentials is expected to provide on a qualitative and often on a quantitative level interesting outcomes concerning the generation of a broader class of dissipative solitons in 1D SO-coupled BECs. However, we will leave this interesting subject for future studies, and in the present paper and will only be concerned with the dynamics of MI in a 1D two-component helicoidal SO-coupled open BEC with dissipative interactions, without the support of any trapping potential. Of course, in a real experiment, any matter-wave state is created in a trapping potential. But it has been demonstrated that the two-component model of the BEC with the SO-Rashba coupling and cubic attractive interactions gives rise to semivortices and mixed modes which readily self-trap under the protection of the usual isotropic harmonic-oscillator trapping potential, and remain stable if the potential is gradually switched off [100], revealing that the SOC and the harmonic-oscillator trap may be manipulated in a completely independent fashion. Interestingly, even in the absence of trapping potentials, other studies indicate that, in dissipative exciton-polariton condensates supported by a narrow external pump beam, there could be formation of strongly localized stationary dissipative solutions, which are termed quasicompactons [101].

To gain physical insights into the mechanism at work in the condensate-reservoir interactions, we introduce two additional loss and gain terms in the coupled cubic GP equations as done by Kneer *et al.* [87]. The loss terms,

$$H_{\rm loss}\psi_1 = -\frac{i}{2}\gamma_c\psi_1 \quad \text{and} \quad H_{\rm loss}\psi_2 = -\frac{i}{2}\gamma_c\psi_2, \tag{4}$$

which are due to coupling the atom wave out of the resonator, lead to an exponential decay of the number of atoms in the condensates ψ_1 and ψ_2, respectively, with γ_c being the condensed atoms' escape rate from the BEC. In contrast, the gain terms

$$H_{\rm gain}\psi_1 = +\frac{i}{2}\Gamma n_u\psi_1 \quad \text{and} \quad H_{\rm gain}\psi_2 = +\frac{i}{2}\Gamma n_u\psi_2 \tag{5}$$

lead to an increase of atoms in the condensates, with Γ being the rate constant coupling the condensate fields ψ_1 and ψ_2, respectively with the number of atoms outside the condensates, n_u. We can then, finally, rewrite Eqs. (1) and (2) as

$$i\frac{\partial\psi_1}{\partial t} = -\frac{1}{2}\frac{\partial^2\psi_1}{\partial x^2} + i\beta\frac{\partial\psi_1}{\partial x} - i\alpha\frac{\partial\psi_2}{\partial x} + \frac{\Delta}{2}\psi_1 + (g_{11}|\psi_1|^2 + g_{12}|\psi_2|)\psi_1 - \frac{i}{2}\gamma_c\psi_1 + \frac{i}{2}\Gamma n_u\psi_1, \tag{6}$$

$$i\frac{\partial\psi_2}{\partial t} = -\frac{1}{2}\frac{\partial^2\psi_2}{\partial x^2} - i\beta\frac{\partial\psi_2}{\partial x} - i\alpha\frac{\partial\psi_1}{\partial x} - \frac{\Delta}{2}\psi_2 + (g_{22}|\psi_2|^2 + g_{21}|\psi_1|^2)\psi_2 - \frac{i}{2}\gamma_c\psi_2 + \frac{i}{2}\Gamma n_u\psi_2. \tag{7}$$

In addition, for the number of uncondensed atoms, n_u, we assume the rate equation [84]

$$\frac{dn_u}{dt} = R(x) - \gamma_u n_u - \Gamma n_u n_c. \tag{8}$$

Here, we have written the rate equation by referring to a local coupling [84] instead of the overall atomic population over the whole trap volume [87]. The physical interpretation of the rate equation (8) can be given as follows. The first term indicates that atoms in an uncondensed state have been pumped into the reservoir of atoms at a rate $R(x)$, and relax at a rate γ_u. On the other hand, the term $-\gamma_u n_u$ takes into account that atoms can escape from our system without being trapped in the condensed state. Finally, the last term in the rate Eq. (8), $-\Gamma n_u n_c$, which is proportional to the number of atoms $n_c = (|\psi_1|^2 + |\psi_2|^2)$, describes the transition of atoms into the condensate.

It is relevant to mention the first observations of BEC of excitons in solid state systems, which have been recently reported in a gas of exciton polaritons [102]. One crucial difference between polariton condensates and other realizations of the two-dimensional Bose gas such as liquid ^{4}He films and tightly confined ultracold atomic gases comes from the finite lifetime of the microcavity polaritons of the order of a few picoseconds. In order to compensate for the polariton losses, new particles can be continuously injected into the microcavity. In general, the dynamics of exciton-polariton condensates is governed by a set of classical field equations for the polariton dynamics coupled to the exciton reservoir. The roles of the two subsystems are very different: the polaritonic field is the quantity of experimental interest because it is easily accessible in photoluminescence experiments and can be driven into the quantum degenerate regime. The role of the reservoir is to replenish the polariton region through relaxation. Here, the model is based on a mean-field description of the condensate in terms of a generalized GP equation for the macroscopic wave function including loss and amplification terms. Also included are interactions between condensate and reservoir. The condensate evolution has to be coupled to an equation for the density of reservoir polaritons [103–105]. Recently, a significant amount of research has also been focusing on the exciton-polariton condensate with different kinds of coupling terms [101,106–108] in order to understand fascinating effects, such as BEC, superfluidity, vortex formation, Josephson oscillations, Bloch oscillations, and parametric instabilities or bistability.

B. A system of two coupled 1D cubic CGL equations

In the above subsection, we have generalized a system of coupled 1D cubic GP equations governing the dynamics of the two-component condensed atoms with helicoidal coupling by including gain and loss, which in turn has been coupled to the rate equation governing the number of uncondensed atoms [87]. In the case of a one-component BEC without helicoidal coupling, a generic model of an atom laser including pump and loss terms in the GP equation was presented. As a result, it was shown that there exists a threshold for the pump above which the mean matter field assumes a nonvanishing value in the steady state. Oscillations around the stationary solution even in the presence of a loss term have been found in the transient regime [87]. In addition, to improve the model, it should be pointed out that the physical grounds for an additional space dependent diffusive process have been provided [84]. Using the same approach as in [84], under same

conditions, we show that dissipative two-component BECs with helicoidal coupling obey a system of coupled 1D cubic CGL equations. Based on physical considerations [84], the relation between the physical variables n_u for the uncondensed phase, which undergoes diffusion processes, is obtained by including diffusion in Eq. (8) as follows:

$$\frac{\partial n_u}{\partial t} = R(x) - \gamma_u n_u - \Gamma n_u(|\psi_1|^2 + |\psi_2|^2) + D_x \frac{\partial^2 n_u}{\partial x^2}. \quad (9)$$

The corresponding diffusion constant in real space is [84]

$$D_x = \frac{1}{\gamma_u}\frac{k_B T}{m}, \quad (10)$$

where m is the mass of the atoms, T the temperature and k_B the Boltzmann constant. It is also noteworthy that a mean field theory of the dynamics of a nonequilibrium BEC of exciton polaritons in a semiconductor microactivity has been used, and the Goldstone mode of a spatially homogeneous system has been found to be diffusive based on a generalized GP equations including loss and amplification terms, and coupled to an equation for the density of reservoir polaritons, and where the spatial diffusion rate of reservoir polaritons has been also taken into account [109]

For further nonlinear analysis, a space Fourier transform is applied on the physical variables of Eq. (9) as follows:

$$\begin{aligned}\mathcal{F}(k) &= \int_{-\infty}^{+\infty} \frac{\partial n_u(x,t)}{\partial t} e^{-ikx} dx \\ &= \int_{-\infty}^{+\infty} \left(R(x) - \gamma_u n_u(x,t) + D_x \frac{\partial^2 n_u(x,t)}{\partial x^2}\right) e^{-ikx} dx \\ &\quad - \int_{-\infty}^{+\infty} [\Gamma n_u(x,t)(|\psi_1(x,t)|^2 + |\psi_2(x,t)|^2)] e^{-ikx} dx.\end{aligned} \quad (11)$$

Consequently, we obtain the needed space Fourier transform for Eq. (9), which reads

$$\frac{\partial \tilde{n}_u}{\partial t} = \tilde{R} - (\gamma_u + D_x k^2)\tilde{n}_u - \Gamma \tilde{n}_u\big(|\psi_1|_0^2 + |\psi_2|_0^2\big)\delta(k), \quad (12)$$

where $\tilde{n}_u(k) = \mathcal{F} n_u(x)$, $\tilde{R}(k) = \mathcal{F} R(x)$, and

$$-k^2 \tilde{n}_u = \mathcal{F}\frac{\partial^2 n_u(x)}{\partial x^2}.$$

In deriving Eq. (12), we have considered only the $k = 0$ component in the nonlinear terms, which is just a perturbation [83]. Then, $\mathcal{F}(|\psi_1|^2 + |\psi_2|^2) = (|\psi_1|_0^2 + |\psi_2|_0^2)\delta(k)$, where the distribution $\delta(x)$ denotes the Dirac delta function. Next, the stationary solution of the rate equation (12) is

$$\tilde{n}_u = \frac{\frac{\tilde{R}}{\gamma_u}}{1 + \frac{D_x}{\gamma_u}k^2 + \frac{\Gamma}{\gamma_u}\big(|\psi_1|_0^2 + |\psi_2|_0^2\big)\delta(k)}. \quad (13)$$

For long-wavelength perturbations and far from saturation, the two additional terms in the denominator are less than unity, so we can then expand Eq. (13) as

$$\tilde{n}_u = \frac{\tilde{R}}{\gamma_u}\left(1 - \frac{D_x}{\gamma_u}k^2 - \frac{\Gamma}{\gamma_u}\big(|\psi_1|_0^2 + |\psi_2|_0^2\big)\delta(k)\right). \quad (14)$$

Taking the inverse Fourier transform of the obtained Eq. (14), we have an operator relation

$$n_u = \frac{R}{\gamma_u}\left[1 + \frac{D_x}{\gamma_u}\frac{\partial^2}{\partial x^2} - \frac{\Gamma}{\gamma_u}(|\psi_1|^2 + |\psi_2|^2)\right]. \quad (15)$$

The adiabatic elimination procedure consists of taking the stationary solution (15) and substituting into Eqs. (6) and (7). By doing this, we derive a system of two coupled 1D cubic CGL equations which reads as

$$\begin{aligned} i\frac{\partial \psi_1}{\partial t} &= \left(i\frac{RD_x\Gamma}{2\gamma_u^2} - \frac{1}{2}\right)\frac{\partial^2 \psi_1}{\partial x^2} + i\beta\frac{\partial \psi_1}{\partial x} \\ &\quad - i\alpha\frac{\partial \psi_2}{\partial x} + \left(\frac{\Delta}{2} - \frac{i}{2}\gamma_c + i\frac{R\Gamma}{2\gamma_u}\right)\psi_1 \\ &\quad + \left\{\left(g_{11} - i\frac{R\Gamma^2}{2\gamma_u^2}\right)|\psi_1|^2 + \left(g_{12} - i\frac{R\Gamma^2}{2\gamma_u^2}\right)|\psi_2|^2\right\}\psi_1, \end{aligned} \quad (16)$$

$$\begin{aligned} i\frac{\partial \psi_2}{\partial t} &= \left(i\frac{RD_x\Gamma}{2\gamma_u^2} - \frac{1}{2}\right)\frac{\partial^2 \psi_2}{\partial x^2} - i\beta\frac{\partial \psi_2}{\partial x} \\ &\quad - i\alpha\frac{\partial \psi_1}{\partial x} + \left(-\frac{\Delta}{2} - \frac{i}{2}\gamma_c + i\frac{R\Gamma}{2\gamma_u}\right)\psi_2 \\ &\quad + \left\{\left(g_{22} - i\frac{R\Gamma^2}{2\gamma_u^2}\right)|\psi_2|^2 + \left(g_{21} - i\frac{R\Gamma^2}{2\gamma_u^2}\right)|\psi_1|^2\right\}\psi_2. \end{aligned} \quad (17)$$

It is convenient to introduce in Eqs. (16) and (17) appropriate units for the measurements of time and spatial coordinates. After such transformations, the considered system is reduced to the following system of two coupled 1D rescaled cubic CGL equations:

$$\begin{aligned} i\frac{\partial \psi_1}{\partial \tau} &= (i\epsilon + \Delta_0)\psi_1 + (1 + iC_4)\frac{\partial^2 \psi_1}{\partial X^2} \\ &\quad + i\beta_0\frac{\partial \psi_1}{\partial X} - i\alpha_0\frac{\partial \psi_2}{\partial X} - (1 + iC_1)|\psi_1|^2\psi_1 \\ &\quad - (1 + iC_3)|\psi_2|^2\psi_1, \end{aligned} \quad (18)$$

$$\begin{aligned} i\frac{\partial \psi_2}{\partial \tau} &= (i\epsilon - \Delta_0)\psi_2 + (1 + iC_4)\frac{\partial^2 \psi_2}{\partial x^2} \\ &\quad - i\beta_0\frac{\partial \psi_2}{\partial x} - i\alpha_0\frac{\partial \psi_1}{\partial x} - (1 + iC_2)|\psi_2|^2\psi_2 \\ &\quad - (1 + iC_3)|\psi_1|^2\psi_2. \end{aligned} \quad (19)$$

Note that we have used the dimensionless time $\tau = \gamma_c t$, and the dimensionless space coordinate $X = x/l_0$, where $l_0 = \sqrt{\frac{\bar{R}D_x\Gamma}{2\gamma_u^2\gamma_c}} = 3 \times 10^{-6} m$ is the characteristic length associated with the dissipative dynamics, and the dimensionless wave function $|\tilde{\psi}_j|^2 = \frac{\bar{R}\Gamma^2}{2\gamma_u^2\gamma_c}|\psi_j|^2$. As mentioned before [84], the threshold condition (gain = losses) is fulfilled for $R = \bar{R}$,

where $\frac{\bar{R}\Gamma}{\gamma_u} = \gamma_c$. Thus, in the above dimensionless system,

$$\epsilon = \frac{1}{2}\left(\frac{R\Gamma}{\gamma_u\gamma_c} - 1\right) = \frac{1}{2}\left(\frac{R}{\bar{R}} - 1\right),$$
$$C_1 = \frac{2g_{11}\gamma_u^2}{R\Gamma^2}, \quad C_2 = \frac{2g_{22}\gamma_u^2}{R\Gamma^2} \quad C_3 = \frac{2g_{12}\gamma_u^2}{R\Gamma^2}, \tag{20}$$
$$C_4 = \frac{\gamma_u^2}{RD_x\Gamma}, \quad \beta_0 = \frac{\beta}{l_0\gamma_c}, \quad \alpha_0 = \frac{\alpha}{l_0\gamma_c}, \quad \Delta_0 = \frac{\Delta}{2\gamma_c}$$

are the other significant parameters. This equation is the new vector form of the cubic CGL equation in the presence of helicoidal spin-orbit coupling in BECs. Several authors [105,109–115] have derived the vector cubic CGL equation in the absence of spin-orbit coupling in a large variety of subfields. In this case, the vector cubic CGL equation appeared in the context of laser physics giving very appealing opportunities for the study of spatiotemporal phenomena due to the vector nature of the complex amplitude of the electric field. The vector degrees of freedom are associated with the polarization of laser light. On the other hand, it is also well known that laser systems are made of several components; an accurate model then should involve consecutive sets of propagation equations. The possibility of vectorial topological defects which are not predictable by the scalar theory has been analyzed [109]. The vector cubic CGL equation has been derived as an amplitude description of an atomic transition between spin sublevels, where the interplay between the polarization state of light and transverse effects leads to novel states of laser light such as standing waves with a spatially periodic linear polarization or coexisting traveling waves with different wave numbers and circular polarizations [110]. The vector cubic CGL equation has been studied in detail as a general model for the superposition of two counterpropagating waves with the same frequency in nonlinear electrical transmission lines [112] and for an electrically coupled Hindmarsh-Rose neuronal model with power-law long-range dispersive interactions [113]. In optics, the vector cubic CGL equation serves for modeling dual-core erbium-doped optical fibers, the dopant being used to induce linear gain in one core [115,116]. Exact solitary pulse solutions, that include space- or time-dependent wave numbers, have been obtained analytically, for special choices of variable coefficients of the nonlinear gain/loss terms, by a modified Hirota bilinear method. Different kinds of pattern formation are present in the dynamic states of one spatial dimension (localized structures) [115] and of two spatial dimensions (topological defects) [117–120] for the vectorial cubic CGL equation. Examples are the synchronization properties of spatiotemporally chaotic states [117], the identification of a transition from a glass to a gas phase [118], and the formation and annihilation processes leading to the different types of defects [119]. In addition, creation and annihilation processes of different kinds of vector defects, as well as a transition between different regimes of spatiotemporal dynamics, have been described [120]. For a finite geometry, predictions of confined states, temporally modulated confined states, and other dynamic states have been discussed, with applications to a phenomenological description of oscillatory convection in binary fluid convection [121]. Exact solitary pulse solutions, including space- or time-dependent wave numbers have been obtained analytically, for special choices of variable coefficients of the nonlinear gain/loss terms, by a modified Hirota bilinear method [122]. The vector cubic-quintic CGL equation has also been studied. Various families of solitary waves describing the evolution of progressive bright-bright, front-front, dark-dark, and other families of solitary waves have been found [123]. The evolution and the stability of vector dissipative optical light bullets [124] and MI gain regions [125] have been investigated in (2+1)-dimensional vectorial cubic-quintic CQL equations.

III. DERIVATION OF THE EXPRESSION FOR MI GAIN IN A SYSTEM OF TWO COUPLED 1D CUBIC CGL EQUATIONS WITH HELICOIDAL COUPLING

In order to study the MI of Eqs. (18) and (19), we use the standard linear stability analysis. For this, we consider the propagation of the cw or quasi-cw state in the form of a miscible binary condensate with uniform densities n_{10}, n_{20} and the common chemical potential μ of both components. The steady-state solutions of a system of two coupled 1D cubic CGL equations with helicoidal coupling (18) and (19), corresponding to the cw state, can be written as

$$\psi_j = e^{-i\mu\tau}\sqrt{n_{j0}}, \quad j = 1, 2, \tag{21}$$

and Eq. (21) shows that the densities, Zeeman splitting, interactions, and chemical potential are determined by algebraic equations

$$\begin{aligned}\Delta_0 = {} & (-1)^{3-j}(\mu + n_{3-j,0} - n_{j0}) \\ & + i(-1)^{3-j}(C_j n_{j0} + C_3 n_{3-j,0} - \epsilon).\end{aligned} \tag{22}$$

To study the MI of cw solutions, in the helicoidal SO-coupled BECs, we introduce a perturbed field of the form

$$\psi_j = e^{-i\mu\tau}(\sqrt{n_{j0}} + \delta\psi_j), \tag{23}$$

where $\delta\psi_j$ are small perturbations, with $|\delta\psi_j| \ll \sqrt{n_{j0}}$ being complex fields. Substituting Eq. (23) into Eqs. (18) and (19) and linearizing around the unperturbed solutions lead to the following equations for the perturbed fields:

$$\begin{aligned}i\frac{\partial(\delta\psi_1)}{\partial\tau} = {} & (1 + iC_4)\frac{\partial^2(\delta\psi_1)}{\partial X^2} + i\beta_0\frac{\partial(\delta\psi_1)}{\partial X} - i\alpha_0\frac{\partial(\delta\psi_2)}{\partial X} \\ & - (1 + iC_1)n_{10}(\delta\psi_1^* + \delta\psi_1) \\ & - (1 + iC_3)\sqrt{n_{10}n_{20}}(\delta\psi_2^* + \delta\psi_2),\end{aligned} \tag{24}$$

$$\begin{aligned}i\frac{\partial(\delta\psi_2)}{\partial\tau} = {} & (1 + iC_4)\frac{\partial^2(\delta\psi_2)}{\partial X^2} - i\beta_0\frac{\partial(\delta\psi_2)}{\partial X} - i\alpha_0\frac{\partial(\delta\psi_)}{\partial X} \\ & - (1 + iC_2)n_{20}(\delta\psi_2^* + \delta\psi_2) \\ & - (1 + iC_3)\sqrt{n_{10}n_{20}}(\delta\psi_1^* + \delta\psi_1),\end{aligned} \tag{25}$$

where $\delta\psi_j^*$ are the complex conjugates of the perturbed fields $\delta\psi_j$. Now we assume the following ansatz for the perturbed fields:

$$\delta\psi_j(x,t) = \zeta_j e^{i(KX-\Omega\tau)} + i\eta_j^* e^{-i(KX-\Omega\tau)}, \tag{26}$$

where K is the wave number, Ω is a complex modulation frequency, and ζ_j and η_j are constant complex amplitudes, respectively. The substitution of Eq. (26) into Eqs. (24) and

(25) gives the linear homogeneous system of equations in terms of ζ_1, ζ_2, η_1, and η_2, i.e.,

$$M \times (\zeta_1, \eta_1, \zeta_2, \eta_2)^T = 0, \tag{27}$$

where M is a 4×4 matrix given by

$$M = \begin{pmatrix} n_{11}+\Omega & n_{12} & n_{13} & n_{14} \\ n_{21} & n_{22}+\Omega & n_{23} & n_{24} \\ n_{31} & n_{32} & n_{33}-\Omega & n_{34} \\ n_{41} & n_{42} & n_{43} & n_{44}-\Omega \end{pmatrix}, \tag{28}$$

whose elements are as follows:

$$\begin{aligned}
n_{11} &= K\beta_0 + K^2(1+iC_4) + (1+iC_1)n_{10}, \\
n_{12} &= (1+iC_3)\sqrt{n_{10}n_{20}} - K\alpha_0, \\
n_{13} &= (1+iC_1)n_{10}, \\
n_{14} &= (1+iC_3)\sqrt{n_{10}n_{20}}, \\
n_{22} &= K^2(1+iC_4) + (1+iC_2)n_{20} - K\beta_0, \\
n_{23} &= n_{14}, \quad n_{24} = (1+iC_2)n_{20}, \\
n_{31} &= (1-iC_1)n_{10}, \\
n_{32} &= (1-iC_3)\sqrt{n_{10}n_{20}}, \quad n_{21} = n_{12}, \\
n_{33} &= K^2(1-iC_4) + (1-iC_1)n_{10} - K\beta_0, \\
n_{34} &= (1-iC_3)\sqrt{n_{10}n_{20}} + K\alpha_0, \quad n_{41} = n_{32}, \\
n_{42} &= (1-iC_2)n_{20}, \quad n_{43} = n_{34}, \\
n_{44} &= K^2(1-iC_4) + (1-iC_2)n_{20} + K\beta_0.
\end{aligned} \tag{29}$$

A nontrivial solution of a system of four equations requires that $\mathrm{Det}(\mathbf{M}) = 0$. After some straightforward calculations, we obtain the following nonlinear dispersion relation:

$$\Omega^4 + P_3\Omega^3 + P_2\Omega^2 + P_1\Omega + P_0 = 0, \tag{30}$$

with $P_j (j = 0, 1, 2, 3)$ being given in the Appendix. The four solutions obtained from Eq. (30) are

$$\begin{aligned}
\Omega_{1,2} &= -\frac{P_3}{4} - \frac{1}{2}\sqrt{\frac{1}{4}P_3^2 - \frac{2}{3}P_2 + \Lambda} \\
&\pm \frac{1}{2}\sqrt{-\frac{4}{3}P_2 + \frac{1}{2}P_3^2 - \Lambda + \frac{P_3^3 - 4P_3P_2 + 8P_0}{4\sqrt{\frac{1}{4}P_3^2 - \frac{2}{3}P_2 + \Lambda}}}, \\
\Omega_{3,4} &= -\frac{P_3}{4} + \frac{1}{2}\sqrt{\frac{1}{4}P_3^2 - \frac{2}{3}P_2 + \Lambda} \\
&\pm \frac{1}{2}\sqrt{-\frac{4}{3}P_2 + \frac{1}{2}P_3^2 - \Lambda - \frac{P_3^3 - 4P_3P_2 + 8P_0}{4\sqrt{\frac{1}{4}P_3^2 - \frac{2}{3}P_2 + \Lambda}}},
\end{aligned} \tag{31}$$

where

$$\Lambda = \frac{1}{3}\left(\sqrt[3]{\frac{\Delta_2 + \sqrt{\Delta_2^2 - 4\Delta_1^3}}{2}} + \frac{\Delta_1}{\sqrt[3]{\frac{\Delta_2 + \sqrt{\Delta_2^2 - 4\Delta_1^3}}{2}}}\right)$$

and $\Delta_1 = P_2^2 - 3P_3P_1 + 12P_0$, $\Delta_2 = 2P_2^3 - 9P_3P_2P_1 + 27P_3^2P_0 + 27P_1^2 - 72P_2P_0$. The set of solutions (31) implies that Ω may be positive, negative, or even complex, depending on the system parameters. However, real, negative or positive, values of Ω predict the stability of the cw. General complex solutions of Eq. (30) are such that $\Omega = \Omega_r + i\Omega_i$, so that $e^{-i\Omega t} = e^{-i\Omega_r t} \times e^{\Omega_i t}$. This means that the occurrence of instability fully depends on the imaginary part of the perturbation frequency and necessary information can be extracted through the maximum MI growth rate given by

$$G(\Omega) = \{|\mathrm{Im}(\Omega)|\}_{\max}. \tag{32}$$

From the elements of matrix (28), it is obvious that the growth rate is strongly dependent on system parameters, but does not depend on the coefficients $(\Delta_0 + i\epsilon)$ and $(-\Delta_0 + i\epsilon)$, which do not influence the MI spectrum. Also, for the rest of calculations, we consider two BEC components with equal densities $n_{01} = n_{02} = n_0$.

In Fig. 1, panels $(\mathrm{a}j)_{j=1,2,3,4}$ and $(\mathrm{b}j)_{j=1,2,3,4}$ depict the effect of the intra- (C_1) and intercomponent (C_3) interactions, respectively, in the presence and absence of the helicoidal gauge potential β_0. Figs. 1(a1) and 1(a2), where the intra- (C_2) and intercomponent (C_3) interactions are repulsive, i.e., $C_2 = C_3 > 0$, the maximum growth rate of MI is expected for $C_1 > 0$, for $\beta_0 = 0$. However, for $\beta_0 = 4$, there is an emergence of MI side bands, while most of the instability zones appear under intracomponent attraction, i.e., $C_1 < 0$. A reverse situation is ostensible in Figs. 1(a3) and 1(a4) for which the intra- (C_2) and intercomponent (C_3) interactions are attractive ($C_2 = C_3 < 0$). For $\beta_0 = 0$, the MI may likely take place in the zone $C_1 < 0$, while there is MI explosion in the instability domain, with $C_1 > 0$ being likely available for the cw to disintegrate into solitonic objects. Figures $1(\mathrm{b}j)_{j=1,2,3,4}$ show the MI growth rate in the (K, C_3) plane. We should stress once more that $C_3 > 0$ and $C_3 < 0$ imply repulsive and attractive intercomponent interactions, respectively. Figures 1(b1) and 1(b2) correspond to $C_1 = C_2 > 0$ and Figs. 1(b3) and 1(b4) give results for $C_1 = C_2 < 0$. In general, the MI development is highly affected by the atomic interactions and the presence of the helicoidal gauge potential brings about MI growth rate explosion, which implies that different zones of instability are available and may lead to a broad range of dynamical behaviors. It is with noting that, for the above, we have fixed the value of the SOC strength as $\alpha_0 = 1$, which does not reflect its impact on the appearance of MI. This explains why in Fig. 2 the growth rate is represented in the (α_0, β_0) plane under both repulsive and attractive intercomponent coupling. Panels $(\mathrm{a}j)_{j=1,2,3,4}$ of Fig. 2 depict the case $C_3 > 0$, and we vary the signs of the intracomponent interaction parameters C_1 and C_2. As a whole, asymmetric patterns of the MI growth rate are obtained for $C_1 = C_2 > 0$ and $C_1 = C_2 < 0$, i.e., when both components are intrinsically repulsive or attractive. Nevertheless, symmetric lobes of MI appear when C_1 and C_2 are of different sign. The same behaviors are obvious in Figs. $2(\mathrm{b}j)_{j=1,2,3,4}$, where $C_3 < 0$, except that for $(C_1 > 0; C_2 < 0)$ and $(C_1 < 0; C_2 > 0)$ only high values of α_0 and β_0 are likely to cause instability. Also, for $C_1 = C_2 > 0$ and $C_1 = C_2 < 0$, regions of MI are switched between $\alpha_0 > 0$ and $\alpha_0 < 0$, while such a context tends to enhance only one region of instability. To be noted is also the fact that the intensity of the MI growth rate is greater when intercomponent interaction effects are attractive.

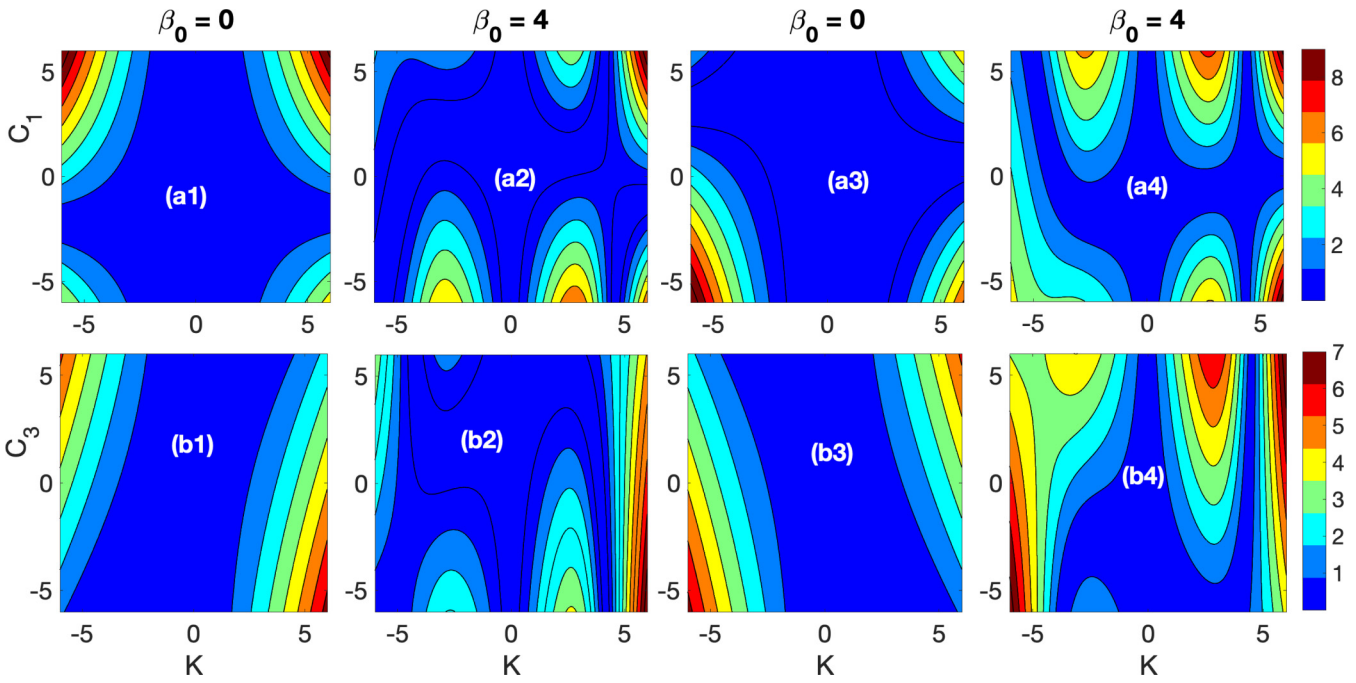


FIG. 1. Panels $(\mathrm{a}j)_{j=1,2,3,4}$ show the contour plots of the MI gain in the (K, C_1) plane for (a1)-(a2) $C_2 = C_3 = 2$, (a3)-(a4) $C_2 = C_3 = -2$. Panels $(\mathrm{b}j)_{j=1,2,3,4}$ display the contour plot of the MI gain in the (K, C_3) plane for (b1)-(b2) $C_1 = C_2 = 2$ and (b3)-(b4) $C_1 = C_2 = -2$, with $n_0 = 1$, $\alpha_0 = 1$ and $C_4 = 0.5$.

Figure 3 shows the behaviors of the MI growth rate in the plane (K, α_0) when $C_3 > 0$ [panels $(\mathrm{a}j)_{j=1,2,3,4}$] and when $C_3 < 0$ (panels $(\mathrm{b}j)_{j=1,2,3,4}$). In the first case, i.e., under repulsive intercomponent interactions, opposite signs of the intracomponent (C_1 and C_2) interactions give rise to symmetric lobes of instability with maximum growth rate appearing for $\alpha_0 < 0$ ($C_1 > 0$; $C_2 < 0$) and $\alpha_0 > 0$ ($C_1 < 0$; $C_2 > 0$), which are respectively depicted in Figs. 3(a1) and 3(a4). For the rest, asymmetric growth rate spectra appear both when the two components are simultaneously repulsive [see Fig. 3(a2)] and attractive [see Fig. 3(a3)], with additional windows of instability. Along the same line, when $C_3 < 0$, we have the features of Figs. $3(\mathrm{b}j)_{j=1,2,3,4}$, where changes in the signs of C_1 and C_2 modify the maximum MI growth rate zones.

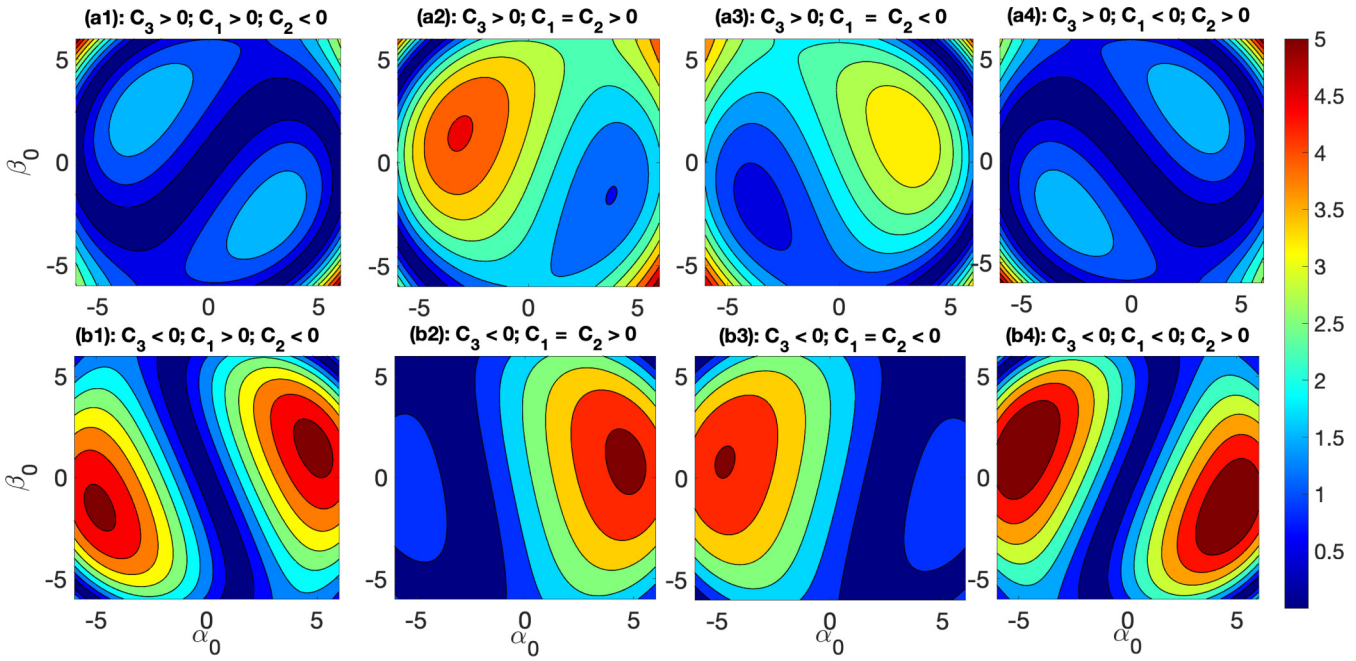


FIG. 2. MI gain in the (α_0, β_0) plane for $(\mathrm{a}j)_{j=1,2,3,4}$ $C_3 > 0$ and $(\mathrm{b}j)_{j=1,2,3,4}$ $C_3 < 0$. The coefficients C_1 and C_2 are taken such that in panels (a1)-(b1) $C_1 > 0, C_2 < 0$, (a2)-(b2) $C_1 = C_2 > 0$, (a3)-(b3) $C_1 = C_2 < 0$, and (a4)-(b4) $C_1 < 0, C_2 > 0$, with $n_0 = 1$ and $K = 1.5$.

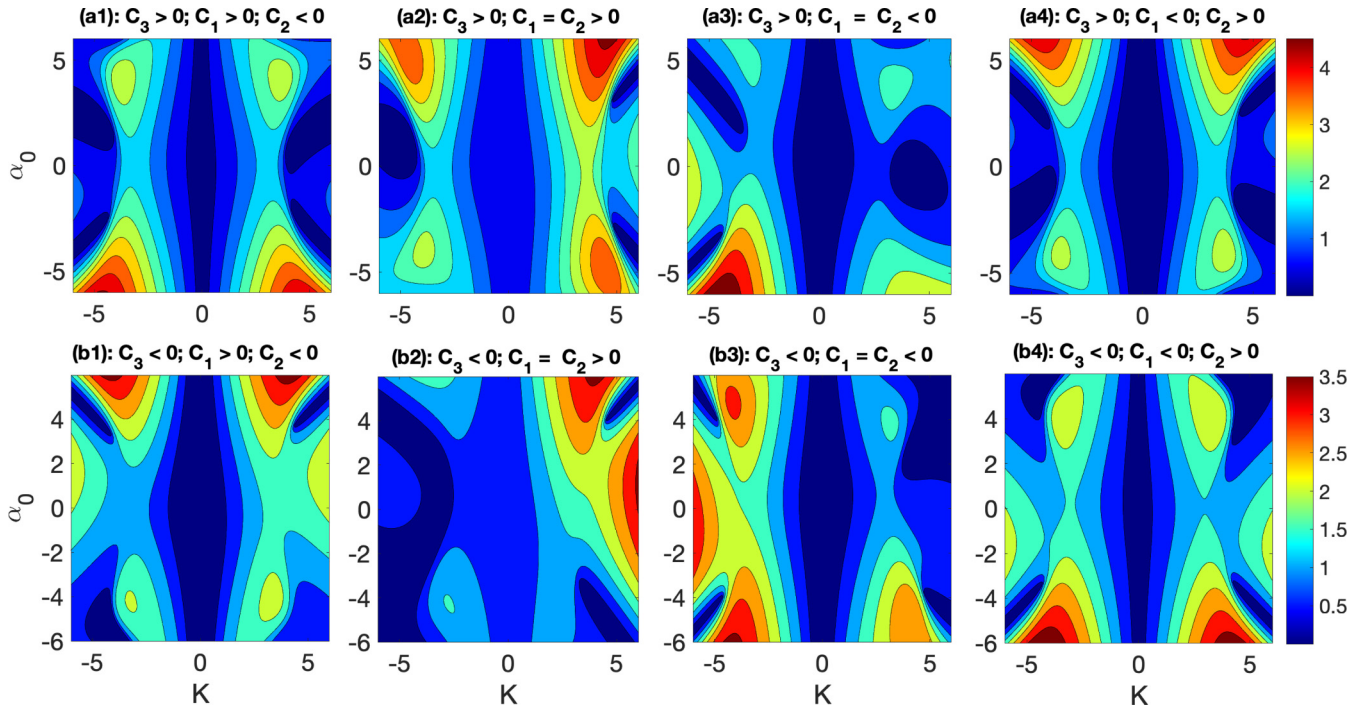


FIG. 3. The contour plots show the gain of MI in the (K, α_0) plane for $(\mathrm{a}j)_{j=1,2,3,4}$ $C_3 > 0$ and $(\mathrm{b}j)_{j=1,2,3,4}$ $C_3 < 0$. The coefficients C_1 and C_2 are taken such that in panels (a1)-(b1) $C_1 > 0$, $C_2 < 0$, (a2)-(b2) $C_1 = C_2 > 0$, (a3)-(b3) $C_1 = C_2 < 0$, and (a4)-(b4) $C_1 < 0$, $C_2 > 0$, with $n_0 = 1$, $\beta_0 = 1$, and $C_4 = 0.5$, with $n_0 = 1$.

When $(C_1 > 0; C_2 < 0)$ and $(C_1 < 0; C_2 > 0)$, there are two symmetric lobes of instability with the maximum growth rate being respectively situated in the areas $\alpha_0 > 0$ [see Fig. 3(b1)] and $\alpha_0 < 0$ [see Fig. 3(b4)]. This also includes additional windows of instability around $\alpha_0 = 0$ that change the interval of K where the cw is supposed to disintegrate. Interestingly, such coherent figures of MI growth rate become asymmetric when the intracomponent interactions are both repulsive [see Fig. 3(b2)] and attractive [see Fig. 3(b3)]. Particularly, the growth rate maximum shifts to the area $K > 0$ for $C_1 = C_2 > 0$, and to the zone $K < 0$ for $C_1 = C_2 < 0$, while the instability tends to disappear in the other regions for K and α_0, the SOC parameter. Remarkably, the sign of the multicomponent coupling parameter has some important consequences on the intensity of the MI growth rate and on its distribution. The proposed model includes two BEC components. In that regard, the above analysis shows that the two types of intercomponent interactions can contribute to the emergence of MI. Most of the models that have been proposed until now not only consider the NLS equations but also avoid the difficulty brought by the dissipative effects and the resultant coupled cubic CGL equations.

IV. NUMERICAL SIMULATIONS OF CW INSTABILITY

Our results of Sec. III are based on the theory of linear stability analysis which amounts to linearizing the perturbed plane wave solution around the unperturbed one. Moreover, they can only predict the onset of MI and do not actually give any information about the long-time dynamical features of the system when instability develops. Therefore, in order to confirm the validity of such analytical predictions about the initial stage of MI, Eqs.(18) and (19) are solved numerically via the split-step Fourier method with the initial conditions

$$\psi_1(X, 0) = \psi_2(X, 0) = n_0 + \varepsilon \cos(KX), \tag{33}$$

where the perturbation wave number K takes values from the instability regions of Figs. 1–3, $n_0 = 1$ and $\varepsilon = 0.001$, so that $\varepsilon \ll n_0$. The manifestation of MI is detected through the amplitude maxima, while one gives importance to the combined effects of the SOC, the intercomponent interaction parameter, and the helicoidal gauge potential. Different combinations of the intracomponent interaction values have been used in a single CGL equation by Arecchi *et al.* [84]. They, however, found that for ^{87}Rb, with $C_1 = 0.52$ and $C_2 = 2.05$, instability could not develop, since such parameters were in the stability region. Nevertheless, instability was found for ^{7}Li, for which $C_1 = 0.04$ and $C_2 = -0.51$. Beyond the above one-component cases, we believe that other set of parameters can be investigated to meet the necessary criteria for instability to develop in two-component BECs with different atomic species, such as ^{41}K - ^{87}Rb and ^{7}Li - ^{133}Cs. The choice of suitable parameter values, especially when SOC and helicoidal gauge potential are involved, will be guided by the predictions from the linear stability analysis.

In the context where the intercomponent interactions are repulsive $(C_3 > 0)$, we address in Fig. 4 the effect of the helicoidal gauge potential in absence of the SOC, i.e, $\alpha_0 = 0$. Interestingly, when both the SOC and the helicoidal gauge potential are switched off, wave patterns are initiated but vanish with increasing time for both components. However, with increasing value of the helicoidal gauge potential β_0, there appear localized oscillations in the two condensates with a slight temporal cw background [see Figs. $4(\mathrm{a}j)_{j=1,2}$].

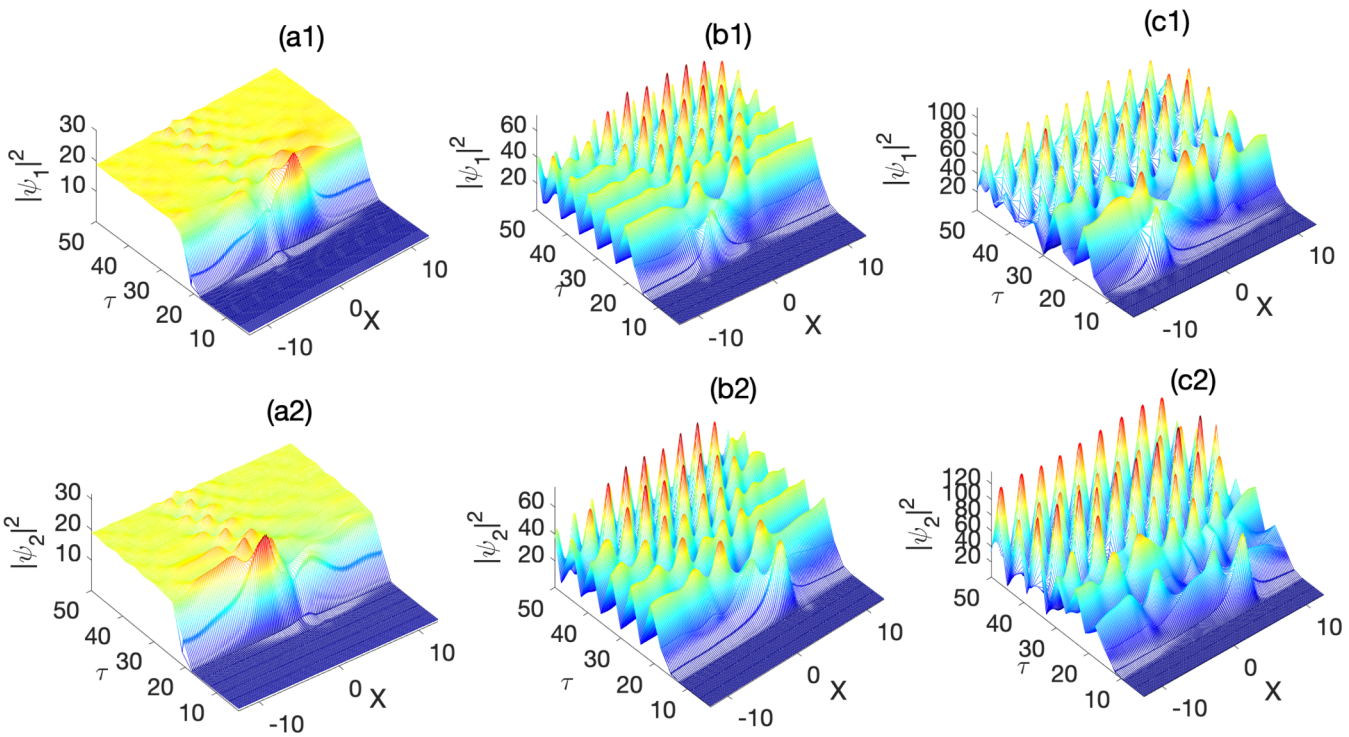


FIG. 4. Spatiotemporal development of MI for $\alpha_0 = 0$, and β_0 taking the values $(\mathrm{a}j)_{j=1,2}$ $\beta_0 = 0$, $(\mathrm{b}j)_{j=1,2}$ $\beta_0 = 1.5$, and $(\mathrm{c}j)_{j=1,2}$ $\beta_0 = 2.5$, with the other parameter values being $C_1 = C_2 = 5$, $C_3 = 2$, $C_4 = 0.5$, $K = 1.5$, $n_0 = 1$, $\Delta_0 = 0.01$.

This particular aspect is in agreement with our linear stability analysis of MI, since the obtained patterns have the shape of solitonic objects, which emerge as the consequence of the constructive interplay between dispersive and nonlinear effects. One fact to be noted here is that as β_0 increases, the delay in the occurrence of MI decreases. This is confirmed by Fig. $4(\mathrm{c}j)_{j=1,2}$, where the patterns are also more localized in amplitude, with $|\psi_2|^2 > |\psi_1|^2$.

The patterns of Fig. 5 show spatiotemporal evolution of MI in presence of the SOC, when the helicoidal gauge potential respectively takes the values $\beta_0 = 0$ [Figs. $5(\mathrm{a}j)_{j=1,2}$], $\beta_0 = 1.5$ [Figs. $5(\mathrm{b}j)_{j=1,2}$], and $\beta_0 = 2.5$ [Figs. $5(\mathrm{c}j)_{j=1,2}$]. It is illustrated that, even in the absence of the helicoidal gauge potential, the stability of the cw is strongly affected. In fact, from the structure of Eqs. (18) and (19), the helicoidal gauge potential is inherent to individual components and actually has been considered by a few authors. Recently, for example, Saha *et al.* [126] studied dilute superfluidity of spin-1 bosons and insisted on suitable balance between antiferromagnetic interactions and SOC as the condition for the superfluid spin-liquid phase to appear in coupled BECs. Along the same line, Chen *et al.* [127], who considered only Raman and SO couplings, showed that the SOC contributes efficiently to the occurrence of the instability, regardless of the nature of the intercomponent coupling. Moreover, in the context of the coupled NLS equations, it was further shown by Li *et al.* [88] that the helicoidal gauge potential can be used as an efficient tool to control MI in BECs. This is illustrated in Figs. $5(\mathrm{b}j)_{j=1,2}$ and $5(\mathrm{c}j)_{j=1,2}$, where β_0 takes the respective values 1.5 and 2.5. Additionally, as in Fig. 4, the time required for the effective onset of instability decreases with the increase in β_0, a fact that could not be predicted by the linear stability analysis. In the meantime, the reader should be aware that as the presence of the term in β_0 brings about helicity, the latter can be left handed ($\beta_0 > 0$) or right handed ($\beta_0 < 0$). It should also be emphasized that the results presented in Figs. 4 and 5 considered only the left-handed character of the helicoidal gauge potential. In Fig. 2 particularly, we have seen that a suitable choice of the values of α_0 and β_0 can lead to the instability of the cw, both under repulsive and attractive intercomponent interactions, with coefficient C_3. It is worth reminding that some theoretical and numerical investigations have revealed that patterns formation via the activation of MI was exclusively possible in attractive single-component BECs [128–130]. However, it was also found that when more than two wave fields are involved, the coupling between multicomponent waves can lead to MI development, even under exclusively repulsive BECs [77,83,131,132]. In order to explore the concomitant effect of C_3 and negative β_0, we represent in Fig. 6 the spatiotemporal manifestation of MI when $\beta_0 < 0$ and $C_3 > 0$, with α_0 taking different values. In Figs. $6(\mathrm{a}j)_{j=1,2}$, for which $\alpha_0 = 0$, slight localized patterns appear, but the MI phenomenon really develops when $\alpha_0 = 0.25$ and 0.5 as depicted in Figs. $6(\mathrm{b}j)_{j=1,2}$ and $6(\mathrm{c}j)_{j=1,2}$. Obviously, there is an increase in the density of the two components, but for $\alpha_0 = 0.5$ the amplitude of the component ψ_2 decreases progressively with time, likely due to the dissipative character of the proposed model, while the component ψ_1 tends to develop quasicoherent structures as time evolves. To further explore the impact of negative β_0, we consider in Fig. 7 the context where the two components undergo attractive interactions, i.e., $C_3 < 0$. As predicted by the MI growth rate, there is, in general, pattern formation, and the ostensible spectrum of behaviors reinforces the idea

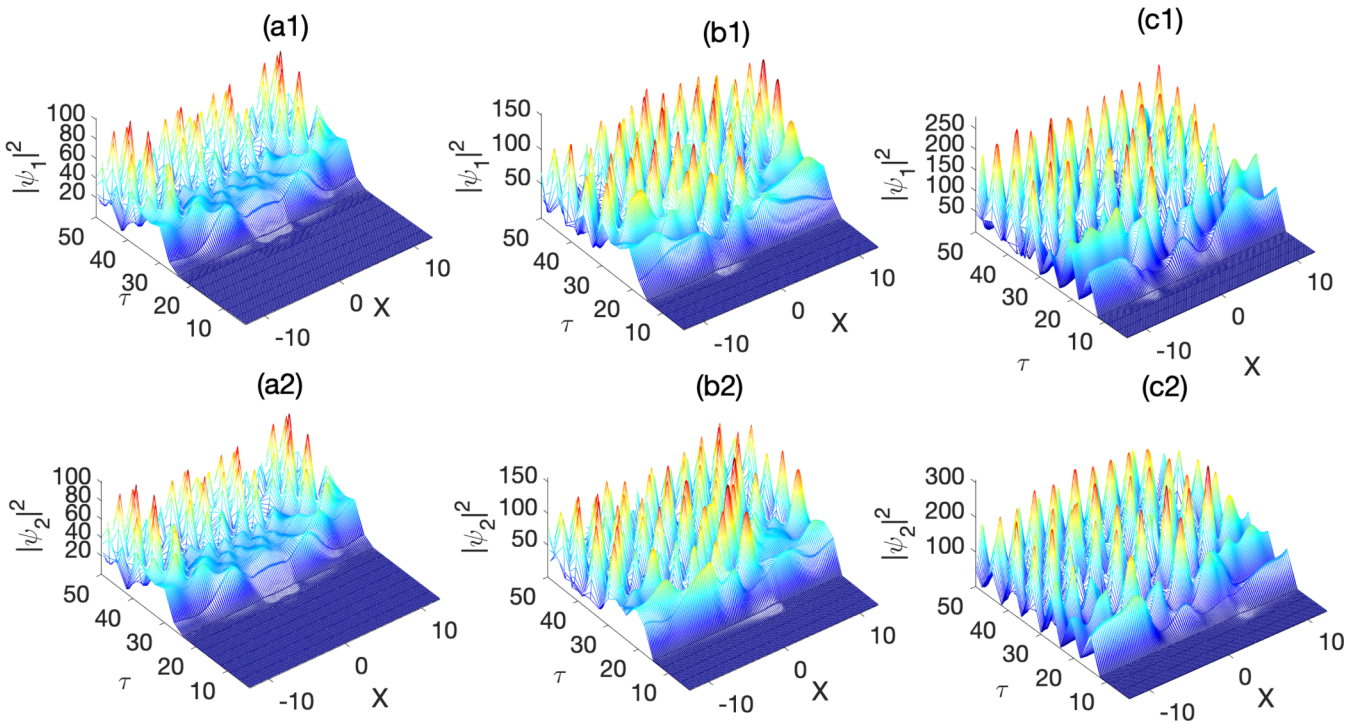


FIG. 5. Spatiotemporal development of MI for $\alpha_0 = 0.5$, and β_0 taking the values $(\mathrm{a}j)_{j=1,2}$ $\beta_0 = 0$, $(\mathrm{b}j)_{j=1,2}$ $\beta_0 = 1.5$, and $(\mathrm{c}j)_{j=1,2}$ $\beta_0 = 2.5$, with the other parameter values being $C_1 = C_2 = 5$, $C_3 = 2$, $C_4 = 0.5$, $K = 1.5$, $n_0 = 1$, $\Delta_0 = 0.01$.

that spatiotemporal patterns in our context may show features not present without spin-orbit coupling. This was already addressed by Xu *et al.* [133], who showed that SOC may dictate the shape of exact bright soliton solutions and lead to the formation of multihump solitons and their recombination to a single bright soliton. Albeit it is not exactly the case, we notice from Figs. 7$(\mathrm{c}j)_{j=1,2}$ that over long-time propagation the train of patterns tends to recombine to single structures when time

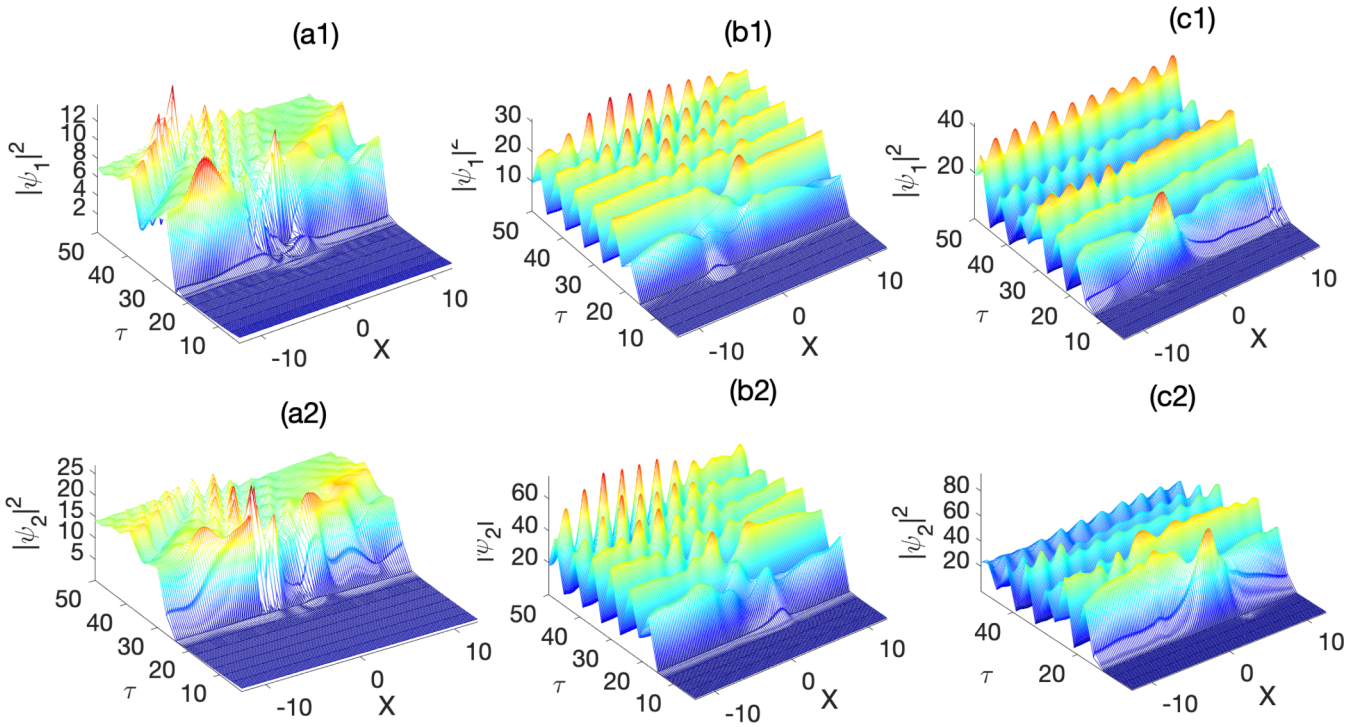


FIG. 6. Spatiotemporal development of MI for $\beta_0 = -1.5$, and $C_3 = 2$, with α_0 taking the values $(\mathrm{a}j)_{j=1,2}$ $\alpha_0 = 0$, $(\mathrm{b}j)_{j=1,2}$ $\alpha_0 = 0.25$, and $(\mathrm{c}j)_{j=1,2}$ $\alpha_0 = 0.5$, with the other parameter values being $C_1 = C_2 = 5$, $C_3 = 2$, $C_4 = 0.5$, $K = 1.5$, $n_0 = 1$, $\Delta_0 = 0.01$.

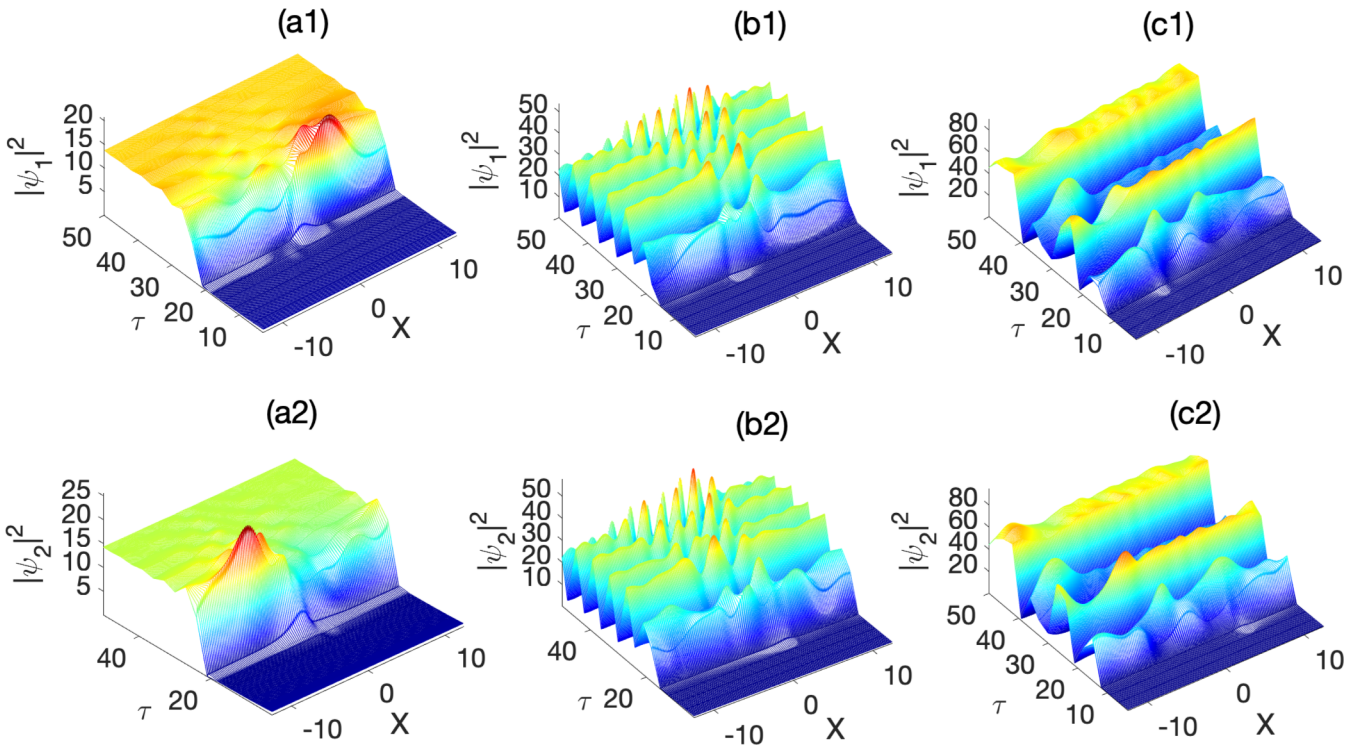


FIG. 7. Spatiotemporal development of MI for $\beta_0 = -1.5$, and $C_3 = -2$, with α_0 taking the values $(\mathrm{a}j)_{j=1,2}$ $\alpha_0 = 0$, $(\mathrm{b}j)_{j=1,2}$ $\alpha_0 = 0.25$, and $(\mathrm{c}j)_{j=1,2}$ $\alpha_0 = 0.5$, with the other parameter values being $C_1 = C_2 = 5$, $C_3 = 2$, $C_4 = 0.5$, $K = 1.5$, $n_0 = 1$, $\Delta_0 = 0.01$.

increases. This implies that switching between repulsive and attractive intercomponent couplings induces a radical modification of the solitonic patterns that emerge, which gives credit to our linear stability analysis and the proposed coupled cubic CGL equations. This also gives a direct explanation of why MI has been studied extensively in BECs for both single- and two-component systems, and realized experimentally as well. It is well known that the interplay of the spin-orbit coupling, which is a linear feature of the binary superfluid, and the mean-field BEC nonlinearity gives rise to a number of remarkable effects, such as vortices, monopoles and skyrmions, multidomain patterns, structures induced by nonlocal interactions, tricritical points, and solitons. Under suitable choices of system parameters, families of solitons can also be found, due to the strong relationship that exists between soliton formation and MI. As a good example, in the absence of Zeeman splitting, a recent investigation by Kartashov and Konotop [91] provided a theoretical derivation of four-parametric families of solitons that can be obtained in the exact form. Indeed, physical understanding of the interplay between the nonzero Zeeman splitting and the SOC has been discussed. Families of the quiescent solitons have been reported depending on the values of the SOC strength α. In particular, in the absence of the SOC, solutions exist and are described by the function $\mu(N)$, where μ are chemical potentials and N are numbers of atoms. For a small SOC strength, quiescent "+" solitons, described by the function $\mu(N) - \alpha\mu_1(N)$, and quiescent "−" solitons, corresponding to $\mu(N) + \alpha\mu_1(N)$, were found. For a moderate SOC strength, the domains of existence for quiescent "+" solitons and quiescent "−" solitons were presented, while, for sufficiently large SOC strength, multiple alternating narrow stability and instability domains were observed. We believe, in light of the above, in the importance of the Zeeman splitting, the SOC, and the chemical potential to bring about more exotic features as manifestations of MI, that are to be addressed in other contributions. Additionally, we expect the competition among the above three effects, combined in multidimensional geometry, to shed more light on the cooperative behaviors of coupled spinors, with clear ideas on experimental values to be used for eventual manipulations and characterization of one- and multidimensional dissipative solitons.

V. CONCLUSIONS

The main objective of this work was the study of MI phenomenon and solitary structures, emerging from dissipative BECs under the combined effect of helicoidal gauge potential and SOC. Starting from coupled GP equations describing the evolution of the condensate wave functions of the two-component helicoidal SO-coupled BECs, equally distributed between the two pseudospin states, we have considered dissipative effects together with a rate equation coupling condensed and uncondensed atoms to show that two-component helicoidal SO-coupled dissipative BECs obey coupled cubic CGL equations under the adiabatic approximation. The theory of MI has been addressed both analytically and numerically, along with its response to the simultaneous effects of the SOC, the helicoidal gauge potential, and the intercomponent interactions. Analytically, a nonlinear dispersion relation has been derived in the form of a fourth-order polynomial alongside the MI growth rate. Comprehensively, the possible combinations of signs of intra- and intercomponent interactions have been discussed, both in the repulsive and attractive contexts. Our analysis illustrates that SOC, and the intrinsic helicoidal

gauge potential, inevitably contribute to the cw disintegration, regardless of the nature of the interaction strength. This is manifested by the appearance of new instability sidebands, thereby enhancing the MI. Analytical predictions were corroborated by direct numerical simulations, which have shown that nonlinear and long-time spatiotemporal wave patterns of the underlying set of coupled cubic CGL equations exist and are, as a whole, robust for a broad range of the involved physical parameters. In the process, SOC and the helicoidal gauge potential may be used as tunable knobs to generate and control complicated nonlinear dynamical processes and the resulting localized long-lived excitations, both in left-handed and right-handed helicoidal dissipative two-component BECs. Evidently, the present contribution not only opens a route for the investigation of several interesting physical aspects of dissipative multicomponent condensates, but also reveals the richness in the complex dynamics exhibited by the SO-coupled BECs, as inspired by the recent theoretical and experimental results on dynamical instabilities [134,135]. Hence, an extended exploration in the parameter space is propitious to reveal large numbers of dissipative soliton varieties and bifurcations, including coherent structures such as pulses (solitary waves), fronts (shock waves), sinks, sources, periodic unbounded solutions, vacuum, periodic and quasiperiodic solutions, slowly varying fully nonlinear wave trains, creeping and chaotic solutions, new fascinating types of pulsating solitons (pulsations, explosions, soliton rain), and finally new families of spatiotemporal dissipative optical bullets, including self-trapped necklace rings, ring-vortex solitons, uniform-ring beams, spherical and rhombic distributions of light bullets, and fundamental and cluster solitons. So, the large and multiple regions of parameter domains of the coupled cubic CGL equations, in which stable dissipative solitons can be found, constitute a fertile ground for investigations. It is also a promising starting point for investigating the behaviors of the proposed system under the coupled effects the SOC and multibody interatomic interactions in higher dimensions. Finally, we believe that a powerful tool in probing novel dynamical behaviors will be provided by further studies on SO-coupled dissipative BECs, and will shed more light on the suitable system parameter values to be used both in experiment and theory.

ACKNOWLEDGMENTS

The work by C.B.T. is supported by the Botswana International University of Science and Technology under the grant DVC/RDI/2/1/16I (25). C.B.T. thanks the Kavli Institute for Theoretical Physics (KITP), University of California Santa Barbara (USA).

APPENDIX: COEFFICIENTS OF THE NONLINEAR DISPERSION RELATION (30)

$$
\begin{aligned}
P_3 &= n_{11} + n_{22} - n_{33} - n_{44},\\
P_2 &= n_{11}n_{22} - n_{11}n_{44} - n_{22}n_{33} - n_{22}n_{44} + n_{33}n_{44} - n_{34}^2 + n_{14}n_{32} + n_{42}n_{24} - n_{11}n_{33} + n_{14}n_{32} - n_{12}^2 + n_{13}n_{31},\\
P_1 &= n_{22}n_{33}n_{44} - n_{22}n_{34}^2 - n_{11}n_{34}^2 + n_{11}n_{33}n_{44} - n_{11}n_{22}n_{44} + n_{11}n_{14}n_{32} - n_{14}n_{32}n_{44} + n_{14}n_{34}n_{42} + n_{11}n_{42}n_{24}\\
&\quad + n_{24}n_{32}n_{34} - n_{24}n_{33}n_{42} - n_{11}n_{22}n_{33} + n_{33}n_{12}^2 + n_{12}^2n_{44} - n_{12}n_{14}n_{31} - n_{13}n_{12}n_{32} - n_{14}n_{12}n_{42} + n_{14}n_{31}n_{34}\\
&\quad - n_{14}n_{32}n_{33} + n_{13}n_{22}n_{31} - n_{13}n_{31}n_{44} + n_{13}n_{32}n_{34} - n_{12}n_{24}n_{32} + n_{13}n_{14}n_{31} + n_{14}n_{22}n_{32},\\
P_0 &= n_{11}n_{24}n_{34}n_{32} - n_{11}n_{24}n_{33}n_{42} - n_{11}n_{14}n_{32}n_{44} + n_{11}n_{14}n_{34}n_{42} + n_{11}n_{22}n_{44}n_{33} - n_{11}n_{22}n_{34}^2 - n_{12}n_{31}n_{24}n_{34}\\
&\quad + n_{12}n_{24}n_{32}n_{33} - n_{44}n_{33}n_{12}^2 + n_{12}^2n_{34}^2 + n_{14}n_{31}n_{12}n_{44} - n_{12}n_{14}n_{32}n_{34} + n_{13}n_{24}n_{31}n_{42} - n_{13}n_{24}n_{32}^2\\
&\quad + n_{13}n_{44}n_{12}n_{32} - n_{13}n_{12}n_{42}n_{34} - n_{13}n_{22}n_{31}n_{44} + n_{13}n_{22}n_{32}n_{34} - n_{14}n_{12}n_{34}n_{32} + n_{14}n_{12}n_{42}n_{33} + n_{14}n_{31}n_{34}n_{22}\\
&\quad - n_{14}n_{32}n_{33}n_{22} - n_{14}^2n_{31}n_{42} + n_{14}^2n_{32}^2.
\end{aligned}
$$

[1] M. H. Anderson, J. R. Ensher, M. R. Mathews, C. E. Wieman, and E. A. Cornell, Science **269**, 198 (1995).
[2] C. C. Bradley, C. A. Sackett, J. J. Tollett, and R. G. Hulet, Phys. Rev. Lett. **75**, 1687 (1995).
[3] E. P. Gross, Nuovo Cimento **20**, 454 (1961).
[4] L. P. Pitaevskii, Zh. Eksp. Teor. Fiz. **40**, 646 (1961) [Sov. Phys. JETP **13**, 451 (1961)].
[5] I. Bloch, J. Dalibard, and W. Zwerger, Rev. Mod. Phys. **80**, 885 (2008).
[6] F. K. Abdullaev, P. G. Kevrekidis, and M. Salerno, Phys. Rev. Lett. **105**, 113901 (2010).
[7] F. K. Abdullaev, V. V. Konotop, M. Salerno, and A. V. Yulin, Phys. Rev. E **82**, 056606 (2010).
[8] I. Shomroni, E. Lahoud, S. Levy, and J. Steinhauer, Nat. Phys. **5**, 193 (2009).
[9] F. K. Abdullaev, A. A. Abdumalikov, and R. M. Galimzyanov, Phys. Lett. A **367**, 149 (2007).
[10] M. R. Matthews, B. P. Anderson, P. C. Haljan, D. S. Hall, C. E. Wieman, and E. A. Cornell, Phys. Rev. Lett. **83**, 2498 (1999).
[11] P. Engels, I. Coddington, P. C. Haljan, and E. A. Cornell, Phys. Rev. Lett. **89**, 100403 (2002).

[12] K. Staliunas, S. Longhi, and G. J. de Valcarcel, Phys. Rev. Lett. **89**, 210406 (2002).
[13] F. K. Abdullaev and M. Salerno, Phys. Rev. A **72**, 033617 (2005).
[14] M. Greiner, O. Mandel, T. Esslinger, T. W. Hansch, and I. Bloch, Nature (London) **415**, 39 (2002).
[15] L. Fallani, F. S. Cataliotti, J. Catani, C. Fort, M. Modugno, M. Zawada, and M. Inguscio, Phys. Rev. Lett. **91**, 240405 (2003).
[16] V. K. Kuetche, T. B. Bouetou, T. C. Kofané, A. B. Moubissi, and K. Porsezian, Phys. Rev. A **82**, 053619 (2010).
[17] A. Mohamadou, E. Wamba, D. Lissouck, and T. C. Kofané, Phys. Rev. E **85**, 046605 (2012).
[18] D. Belebo Belobo, G. H. Ben-Bolie, and T. C. Kofané, Phys. Rev. E **89**, 042913 (2014).
[19] D. Belebo Belobo, G. H. Ben-Bolie, and T. C. Kofané, Phys. Rev. E **91**, 042902 (2015).
[20] B. P. Anderson, K. Dholakia, and E. M. Wright, Phys. Rev. A **67**, 033601 (2003).
[21] R. Kanamoto, H. Saito, and M. Ueda, Phys. Rev. A **67**, 013608 (2003).
[22] S. Inouye, T. Pfau, S. Gupta, A. P. Chikkatur, A. Gorlitz, D. E. Pritchard, and W. Ketterle, Nature (London) **402**, 641 (1999).
[23] E. W. Hagley, L. Deng, M. Kozuma, J. Wen, K. Helmerson, S. L. Rolston, and W. D. Phillips, Science **283**, 1706 (1999).
[24] T. Busch and J. R. Anglin, Phys. Rev. Lett. **87**, 010401 (2001).
[25] C. Hamner, J. J. Chang, P. Engels, and M. A. Hoefer, Phys. Rev. Lett. **106**, 065302 (2011).
[26] P. Ohberg and L. Santos, Phys. Rev. Lett. **86**, 2918 (2001).
[27] L. Salasnich and B. A. Malomed, Phys. Rev. A **74**, 053610 (2006).
[28] K. Kasamatsu and M. Tsubota, Phys. Rev. Lett. **93**, 100402 (2004).
[29] D. V. Freilich, D. M. Bianchi, A. M. Kaufman, T. K. Langin, and D. S. Hall, Science **329**, 1182 (2010).
[30] T. Kawakami, T. Mizushima, M. Nitta, and K. Machida, Phys. Rev. Lett. **109**, 015301 (2012).
[31] C. Becker, S. Stellmer, P. Soltan-Panahi, S. Dorscher, M. Baumert, E. M. Richter, J. Kronjager, K. Bongs, and K. Senhstock, Nat. Phys. **4**, 496 (2008).
[32] M. A. Hoefer, J. J. Chang, C. Hamner, and P. Engels, Phys. Rev. A **84**, 041605(R) (2011).
[33] Y.-J. Lin, K. Jimenez-Garcia, and I. B. Spielman, Nature (London) **471**, 83 (2011).
[34] V. Galitski and I. B. Spielman, Nature (London) **494**, 49 (2013).
[35] P. Wang, Z. Q. Yu, Z. Fu, J. Miao, L. Huang, S. Chai, H. Zhai, and J. Zhang, Phys. Rev. Lett. **109**, 095301 (2012).
[36] L. W. Cheuk, A. T. Sommer, Z. Hadzibabic, T. Yefsah, W. S. Bakr, and M. W. Zwierlein, Phys. Rev. Lett. **109**, 095302 (2012).
[37] J. Dalibard, F. Gerbier, G. Juzeliunas, and P. Ohberg, Rev. Mod. Phys. **83**, 1523 (2011).
[38] T. D. Stanescu, B. Anderson, and V. Galitski, Phys. Rev. A **78**, 023616 (2008).
[39] D. L. Campbell, R. M. Price, A. Putra, A. Valdes-Curiel, D. Trypogeorgos, and I. B. Spielman, Nat. Commun. **7**, 10897 (2016).
[40] M. Aidelsburger, M. Atala, S. Nascimbene, S. Trotzky, Y.-A. Chen, and I. Bloch, Phys. Rev. Lett. **107**, 255301 (2011).
[41] X.-Q. Xu and J. H. Han, Phys. Rev. Lett. **107**, 200401 (2011).
[42] G. J. Conduit, Phys. Rev. A **86**, 021605(R) (2012).
[43] O. Fialko, J. Brand, and U. Zulicke, Phys. Rev. A **85**, 051605(R) (2012).
[44] M. Merkl, A. Jacob, F. E. Zimmer, P. Ohberg, and L. Santos, Phys. Rev. Lett. **104**, 073603 (2010).
[45] V. Achilleos, D. J. Frantzeskakis, P. G. Kevrekidis, and D. E. Pelinovsky, Phys. Rev. Lett. **110**, 264101 (2013).
[46] Y. V. Kartashov, V. V. Konotop, and F. K. Abdullaev, Phys. Rev. Lett. **111**, 060402 (2013).
[47] Y. K. Liu and S. J. Yang, Europhys. Lett. **108**, 30004 (2014).
[48] S. Gautam and S. K. Adhikari, Laser Phys. Lett. **12**, 045501 (2015).
[49] R. M. Ziff, G. E. Uhlenbeck, and M. Kac, Phys. Rep. **32**, 169 (1977).
[50] M. O. Scully and M. S. Zubairy, *Quantum Optics* (Cambridge University Press, Cambridge, UK, 1997).
[51] I. Bloch, T. W. Hansch, and T. Esslinger, Phys. Rev. Lett. **82**, 3008 (1999).
[52] G. Barontini, R. Labouvie, F. Stubenrauch, A. Vogler, V. Guarrera, and H. Ott, Phys. Rev. Lett. **110**, 035302 (2013).
[53] J. Ruostekoski and D. F. Walls, Phys. Rev. A **58**, R50 (1998).
[54] D. Witthaut, F. Trimborn, H. Hennig, G. Kordas, T. Geisel, and S. Wimberger, Phys. Rev. A **83**, 063608 (2011).
[55] S. Caspar, F. Hebenstreit, D. Mesterhazy, and U. J. Wiese, New J. Phys. **18**, 073015 (2016).
[56] J. Marelic and R. A. Nyman, Phys. Rev. A **91**, 033813 (2015).
[57] P. Kirton and J. Keeling, Phys. Rev. Lett. **111**, 100404 (2013).
[58] K. K. Ndebele, C. B. Tabi, and T. C. Kofané, J. Opt. Soc. Am. B **32**, A214 (2020).
[59] C. B. Tabi, C. S. Panguetna, T. G. Motsumi, and T. C. Kofané, Phys. Scr. **95**, 075211 (2020).
[60] T. B. Benjamin and J. E. Feir, J. Fluid Mech. **27**, 417 (1967).
[61] P. Marquie, J. M. Bilbault, and M. Remoissenet, Phys. Rev. E **49**, 828 (1994).
[62] C. B. Tabi, A. S. Etémé, and T. C. Kofané, Nonlinear Dyn. **100**, 3799 (2020).
[63] N. R. Zaoro, C. B. Tabi, A. S. Etémé, and T. C. Kofané, Phys. Lett. A **384**, 126133 (2020).
[64] P. G. Kevrekidis, R. Carretero-Gonzalez, G. Theocharis, D. J. Frantzeskakis, and B. A. Malomed, Phys. Rev. A **68**, 035602 (2003).
[65] A. Smerzi, A. Trombettoni, P. G. Kevrekidis, and A. R. Bishop, Phys. Rev. Lett. **89**, 170402 (2002).
[66] G. Theocharis, Z. Rapti, P. G. Kevrekidis, D. J. Frantzeskakis, and V. V. Konotop, Phys. Rev. A **67**, 063610 (2003).
[67] L. Li, Z. Li, B. A. Malomed, D. Mihalache, and W. M. Liu, Phys. Rev. A **72**, 033611 (2005).
[68] E. V. Doktorov, V. M. Rothos, and Y. S. Kivshar, Phys. Rev. A **76**, 013626 (2007).
[69] V. I. Bespalov and V. I. Talanov, Pis'ma Zh. Eksp. Teor. Fiz. **3**, 471 (1966).
[70] J. K. Xue, G. Q. Li, A. X. Zhang, and P. Peng, Phys. Rev. E **77**, 016606 (2008).
[71] B. B. Baizakov, A. Bouketir, A. Messikh, and B. A. Umarov, Phys. Rev. E **79**, 046605 (2009).
[72] A. Mohamadou, E. Wamba, S. Y. Doka, T. B. Ekogo, and T. C. Kofané, Phys. Rev. A **84**, 023602 (2011).
[73] E. Kengne, A. Lakhssassi, W. M. Liu, and R. Vaillancourt, Phys. Rev. E **87**, 022914 (2013).
[74] E. Kengne and W. M. Liu, Phys. Rev. E **98**, 012204 (2018).

[75] D. Zanga, S. I. Fewo, C. B. Tabi, and T. C. Kofané, Commun. Nonlinear Sci. Numer. Simul. **80**, 104993 (2020).

[76] Y. K. Liu and S. J. Yang, Phys. Lett. **108**, 30004 (2014).

[77] E. V. Goldstein and P. Meystre, Phys. Rev. A **55**, 2935 (1997).

[78] M. Yu, C. J. McKinstrie, and G. P. Agrawal, Phys. Rev. E **48**, 2178 (1993).

[79] N. P. Robins, W. Zhang, E. A. Ostrovskaya, and Y. S. Kivshar, Phys. Rev. A **64**, 021601(R) (2001).

[80] T. Ozawa, L. P. Pitaevskii, and S. Stringari, Phys. Rev. A **87**, 063610 (2013).

[81] S. Gautam and S. K. Adhikari, Phys. Rev. A **90**, 043619 (2014).

[82] I. A. Bhat, T. Mithun, B. A. Malomed, and K. Porsezian, Phys. Rev. A **92**, 063606 (2015).

[83] S. Bhuvaneswari, K. Nithyanandan, P. Muruganandam, and K. Porsezian, J. Phys. B: At. Mol. Opt. Phys. **49**, 245301 (2016).

[84] F. T. Arecchi, J. Bragard, and L. M. Castellano, Opt. Commun. **179**, 156 (1999).

[85] G. M. Moy, J. J. Hope, and C. M. Savage, Phys. Rev. A **55**, 3631 (1997).

[86] A. M. Guzman, M. Moore, and P. Meystre, Phys. Rev. A **53**, 977 (1996).

[87] B. Kneer, T. Wong, K. Vogel, W. P. Schleich, and D. F. Walls, Phys. Rev. A **58**, 4841 (1998).

[88] X.-X. Li, R.-J. Cheng, A.-X. Zhang, and J.-K. Xue, Phys. Rev. E **100**, 032220 (2019).

[89] S. Blatt, T. L. Nicholson, B. J. Bloom, J. R. Williams, J. W. Thomsen, P. S. Julienne, and J. Ye, Phys. Rev. Lett. **107**, 073202 (2011).

[90] S. Inouye, M. R. Andrews, J. Stenger, H.-J. Miesner, D. M. Stamper-Kurn, and W. Ketterle, Nature (London) **392**, 151 (1998).

[91] Y. V. Kartashov and V. V. Konotop, Phys. Rev. Lett. **118**, 190401 (2017).

[92] C. M. Bender and S. Boettcher, Phys. Rev. Lett. **80**, 5243 (1998).

[93] C. M. Bender, D. C. Brody, and H. F. Jones, Phys. Rev. Lett. **89**, 270401 (2002).

[94] C. M. Bender, D. C. Brody, H. F. Jones, and B. K. Meister, Phys. Rev. Lett. **98**, 040403 (2007).

[95] I. Rotter, Phys. Rev. E **65**, 026217 (2002).

[96] E. A. Ultanir, G. I. Stegeman, and D. N. Christodoulides, Opt. Lett. **29**, 845 (2004).

[97] S. Klaiman, U. Günther, and N. Moiseyev, Phys. Rev. Lett. **101**, 080402 (2008).

[98] M. Kreibich, J. Main, H. Cartarius, and G. Wunner, Phys. Rev. A **93**, 023624 (2016).

[99] V. E. Lobanov, Y. V. Kartashov, and V. V. Konotop, Phys. Rev. Lett. **112**, 180403 (2014).

[100] H. Sakaguchi, Ben Li, and B. A. Malomed, Phys. Rev. E **89**, 032920 (2014).

[101] Y. V. Kartashov, V. V. Konotop, and L. Torner, Phys. Rev. B **86**, 205313 (2012); R. J. C. Spreeuw, T. Pfau, U. Janicke, and M. Wilkens, Europhys. Lett. **32**, 469 (1995).

[102] J. Kasprzak *et al.*, Nature (London) **443**, 409 (2006).

[103] E. A. Ostrovskaya, J. Abdullaev, A. S. Desyatnikov, M. D. Fraser, and Y. S. Kivshar, Phys. Rev. A **86**, 013636 (2012).

[104] L. A. Smirnov, D. A. Smirnova, E. A. Ostrovskaya, and Y. S. Kivshar, Phys. Rev. B **89**, 235310 (2014).

[105] M. Wouters and I. Carusotto, Phys. Rev. Lett. **99**, 140402 (2007).

[106] C. Ciuti and I. Carusotto, Phys. Status Solidi B **242**, 2224 (2005).

[107] E. Cancellieri, F. M. Marchetti, M. H. Szymanska, and C. Tejedor, Phys. Rev. B **82**, 224512 (2010).

[108] H. Flayac, D. D. Solnyshkov, and G. Malpuech, Phys. Rev. B **83**, 045412 (2011).

[109] L. Gil, Phys. Rev. Lett. **70**, 162 (1993).

[110] L. M. Pismen, Phys. Rev. Lett. **72**, 2557 (1994).

[111] M. San Miguel, Phys. Rev. Lett. **75**, 425 (1995).

[112] F. II Ndzana, A. Mohamadou, and T. C. Kofané, Chaos **18**, 043121 (2008).

[113] A. S. Etémé, C. B. Tabi, and A. Mohamadou, Chaos Solitons Fractals **104**, 813 (2017).

[114] J. Atai and B. A. Malomed, Phys. Rev. E **54**, 4371 (1996).

[115] H. Sakaguchi and B. A. Malomed, Physica D **147**, 273 (2000).

[116] K. W. Madison, F. Chevy, W. Wohlleben, and J. Dalibard, Phys. Rev. Lett. **84**, 806 (2000).

[117] E. Hernandez-Garcia, M. Hoyuelos, P. Colet, M. S. Miguel, and R. Montagne, Int. J. Bif. Chaos **9**, 2257 (1999).

[118] M. Hoyuelos, E. Hernandez-Garcia, P. Colet, and M. S. Miguel, Comput. Phys. Commun. **121**, 414 (1999).

[119] E. Hernandez-Garcia, M. Hoyuelos, P. Colet, and M. San Miguel, Phys. Rev. Lett. **85**, 744 (2000).

[120] M. Hoyuelos, E. Hernandez-Garcia, P. Colet, and M. S. Miguel, Physica D **174**, 176 (2003).

[121] M. C. Cross, Phys. Rev. A **38**, 3593 (1988).

[122] O. S. Pak, C. K. Lam, K. Nakkeeran, B. Malomed, K. W. Chow, and K. Senthilnathan, J. Phys. Soc. Jpn **78**, 084001 (2009).

[123] G. A. Zakeri and E. Yomba, J. Phys. Soc. Jpn **82**, 084002 (2013).

[124] A. Djazet, C. B. Tabi, S. I. Fewo, and T. C. Kofané, Appl. Phys. B **126**, 74 (2020).

[125] G. A. Zakeri and E. Yomba, Phys. Rev. E **91**, 062904 (2015).

[126] S. Saha, E. J. König, J. Lee, and J. H. Pixley, Phys. Rev. Research **2**, 013252 (2020).

[127] L. Chen, Y. Zhang, and H. Pu, Phys. Rev. A **102**, 023317 (2020).

[128] H. Saito and M. Ueda, Phys. Rev. Lett. **86**, 1406 (2001).

[129] A. M. Kamchatnov, A. Gammal, F. K. Abdullaev, and R. A. Kraenkel, Phys. Lett. A **319**, 406 (2003).

[130] L. D. Carr and J. Brand, Phys. Rev. Lett. **92**, 040401 (2004).

[131] D. B. Belobo, G. H. Ben-Bolie, T. B. Ekogo, and T. C. Kofané, Int. Mod. Phys. B **52**, 1415 (2013).

[132] T. Mithun and K. Kasamatsu, J. Phys. B: At. Mol. Opt. Phys. **52**, 045301 (2019).

[133] Y. Xu, Y. Zhang, and C. Zhang, Phys. Rev. A **92**, 013633 (2015).

[134] N. Q. Burdick, Y. Tang, and B. L. Lev, Phys. Rev. X **6**, 031022 (2016).

[135] M. A. Khamehchi, K. Hossain, M. E. Mossman, Y. Zhang, T. Busch, M. M. Forbes, and P. Engels, Phys. Rev. Lett. **118**, 155301 (2017).

Physics Letters A 449 (2022) 128334

Contents lists available at ScienceDirect

Physics Letters A

www.elsevier.com/locate/pla

Modulation instability of two-dimensional Bose-Einstein condensates with helicoidal and a mixture of Rashba-Dresselhaus spin-orbit couplings

Conrad Bertrand Tabi [a,*], Phelo Otlaadisa [a], Timoléon Crépin Kofané [a,b,c]

[a] Department of Physics and Astronomy, Botswana International University of Science and Technology, Private Mail Bag 16 Palapye, Botswana
[b] Laboratory of Mechanics, Department of Physics, Faculty of Science, University of Yaoundé I, P.O. Box 812, Yaoundé, Cameroon
[c] Centre d'Excellence Africain en Technologies de l'Information et de la Communication, University of Yaoundé I, Cameroon

ARTICLE INFO

Article history:
Received 12 September 2021
Received in revised form 22 July 2022
Accepted 24 July 2022
Available online 29 July 2022
Communicated by B. Malomed

Keywords:
Vector BECs
Rashba-Dresselhaus spin-orbit coupling
Helicoidal spin-orbit coupling
Modulational instability
Helicoidal gauge potential

ABSTRACT

The modulational instability (MI) process is exclusively studied in a two-component Bose-Einstein condensate (BEC) which includes Rashba-Dresselhaus (RD) spin-orbit (SO) and helicoidal SO couplings. A generalized set of two-dimensional (2D) Gross-Pitaevskii (GP) equations is derived. The tunability of the helicoidal gauge potential is exploited to address BECs dynamics in a square lattice. The MI growth rate is derived, and parametric analyses of MI show the dependence of the instability on interatomic interaction strengths, the RD SO coupling, and helicoidal SO coupling, which combines the gauge amplitude and the helicoidal gauge potential. Direct numerical simulations are carried out to confirm the analytical predictions. Trains of solitons are obtained, and their behaviors are debated when the RD SO parameters are varied under different combinations between the gauge amplitude and the helicoidal gauge potential. The latter gives a potential way to manipulate the trapping capacities of the proposed BEC model.
© 2022 Elsevier B.V. All rights reserved.

1. Introduction

Unique opportunities for quantum phenomena to be explored at a macroscopic scale were provided by the seminal experimental evidence of the Bose-Einstein condensation (BEC) of a weakly interacting Bose gas for lithium [1,2], rubidium [3] and sodium [4]. As it is well known, the macroscopic wave function of an atomic BEC is the solution to the time-dependent, nonlinear, mean-field Gross-Pitaevskii (GP) equation [5,6] at absolute zero temperature. Precision should be made that the GP equation, which is, in fact, a nonlinear Schrödinger equation that contains an external potential, exhibits many types of nonlinear matter waves [7–25].

Recently, the development of trapping techniques has allowed the creation of multicomponent condensates, which are formed by trapping atoms in different internal states [26,27]. Multicomponent condensates can consist of the same atoms with different hyperfine states [26,28] or different F-spin orientations [29], or atomic-molecular BECs [30]. In multicomponent systems, additional types of interaction such as interspecies interactions can occur between different components of the condensates leading to rich dynamical phenomena not observable in a single condensate [31–40]. Interestingly, the study of Bose-Einstein solitons was extended to multispecies condensates in a higher-dimensional manifold. On that note, a wide variety of localized and periodic excitations were constructed via the generalized Lax representation of the coupled GP equations, with a particular interest in elastic and nonelastic interactions among such structures alongside the splitting and resonance phenomena occurring during their motion [41].

SO coupling, which describes the interaction between a quantum particle's spin and orbital momentum, is ubiquitous in physical systems. In crystals lacking an inversion center, electronic energy bands are split by SO coupling. The Rashba SO coupling was initially proposed for noncentrosymmetric wurtzite semiconductors [42]. After establishing modulation-doped semiconductor heterostructures, Bychkov and Rashba applied it to the SO coupling in a two-dimensional electron gas with structural inversion asymmetry [43]. Considering SO coupling in different contexts has remarkably improved our perception of many fundamental phenomena related, for example, to GaAs quantum wells [44], Majorana [45], the fractional quantum spin-Hall effect [46], and topological insulators [47], to cite a few. In the

* Corresponding author.
E-mail addresses: tabic@biust.ac.bw (C.B. Tabi), phelo.otlaadisa@studentmail.biust.ac.bw (P. Otlaadisa), tckofane@yahoo.com (T.C. Kofané).

https://doi.org/10.1016/j.physleta.2022.128334
0375-9601/© 2022 Elsevier B.V. All rights reserved.

structure of an ultracold gas of alkali-metal atoms, the role of spin is characterized by the hyperfine spin degrees of freedom of the atoms. SO coupling acts between the motion of the entire neutral atom to its hyperfine spin and not the coupling between the orbital momentum of the atom's valence electron to its spin. Because the atoms are neutral, this SO coupling arises differently from electrons and has to be engineered. It is therefore referred to as synthetic SO coupling [48]. Recently, a synthetic SO coupling has been successfully engineered in experiments in gases of fermions [49], or bosons [50] in one and two dimensions [51]. Stimulating extensive theoretical investigations of the properties of SO-coupled BECs have been carried out, which include Skyrmions [37], vortices [52], Dirac [53], dark [54], gap [55], bright [56]. In addition, multi-peak bright [57] and bright single- and multi-peak vector solitons [58] have been found in SO coupling BECs.

Of the many issues related to soliton wave theory, the modulation instability (MI) phenomenon is a universal process closely related to nonlinear wave occurrence in nature [59]. It is a process whereby an instability is subjected to a spontaneous growth from small amplitude modulated waves as the consequence of the competition between the intrinsic nonlinearity and dispersion, which takes place in the same parameter regions where bright solitons are expected, leading to the emergence of soliton trains. Many theoretical, numerical, and experimental works clearly support the use of the MI as a practical tool to generate solitonic trains in one and two-component BECs [35, 60–80]. This letter addresses the nonlinear dynamics of solitary wave formation induced by MI in a mixture of two-component atomic-gas BECs in 2D space. We introduce a system of two-dimensional coupled GP equations with the inclusion of Rashba and Dresselhaus couplings. Only a few studies were devoted to 2D SO coupled BECs of mixed RD type and Rabi couplings [81–83]. In fact, it has been reported that 2D solitons are completely unstable in the case of a balanced Rashba and Dresselhaus mixture [84]. Moreover, for any mixing degree of RD SO couplings, stable solitons can be created in the dipolar BECs [85]. Here, we examine plane wave stability using linear stability analysis and propose linearized coupled 2D cubic GP equations under the combined effects of a mixture of RD and helicoidal SO couplings. The analytic expression of the growth rate of MI is discussed for different combinations of intra- and inter-component interaction strengths. Furthermore, we perform direct numerical integration of the initial coupled 2D cubic GP equations with helicoidal and RD SO couplings.

The rest of the letter is organized as follows. In Sec. 2, we introduce the energy functional and derive a 2D coupled GPE system which includes RD SO and helicoidal SO couplings. We also show that the tunability of the helicoidal gauge potential allows the derivation of a set of GPEs describing BECs in a square lattice. In Sec. 3, the linear stability analysis of CWs is addressed, where an analytical expression of the growth rates of MI is derived and used to discuss the stability and instability domains parametrically. Some numerical simulations are presented in Sec. 4, where predictions from the linear stability analysis are verified. One particularly insists on solitary wave formation in the condensates under the activation of MI, emphasizing the combined effects of a mixture of RD SO couplings and different combinations of the helicoidal gauge potential and the gauge amplitude. Some concluding remarks are given in Sec. 5.

2. 2D vector GP equation model derivation

A two-component BEC model is proposed and includes the helicoidal and a mixture of RD SO couplings. Within the mean-field formulation, the two pseudospin states are described by an energy functional given by

$$\mathcal{E} = \int_{-\infty}^{+\infty}\int_{-\infty}^{+\infty} (\mathcal{E}_0 + \mathcal{E}_{int})\, dxdy \tag{1}$$

where

$$\mathcal{E}_0 = \frac{1}{2}\left(\Psi^* H_0 \Psi\right), \tag{2}$$

where $\Psi = (\Psi_1, \Psi_2)^T$ (T stands for the transpose) is the condensate wavefunction, Ψ_1 and Ψ_2 are associated with the pseudo-spin components. The interaction Hamiltonian $\mathcal{E}_{int}$ takes the common contact form of the scattering interaction of the s-wave [86]. The model Hamiltonian H_0 assumes the form:

$$H_0 = H_{HSO} + H_Z + H_{RSO} + H_{DSO}, \tag{3}$$

where H_{HSO}, H_Z, H_{RSO}, and H_{DSO} are the helicoidal SO coupling Hamiltonian, Zeeman Hamiltonian, Rashba Hamiltonian, and Dresselhaus Hamiltonian, respectively. The single-particle Hamiltonian of the system can be written as [87]:

$$H_{HSO} = \frac{1}{2}\left[\left(\sigma_0 p_x + \alpha(\vec{\sigma}\cdot\vec{u})\right)^2 + \left(\sigma_0 p_y + \alpha(\vec{\sigma}\cdot\vec{v})\right)^2\right], \tag{4}$$

where $p_x = -i\partial/\partial x$ and $p_y = -i\partial/\partial y$ are the momentum operators, $\sigma = (\sigma_x, \sigma_y, \sigma_z)$ is the vector Pauli matrices, σ_0 is the identity matrix, α is the strength of helicoidal SO coupling, and the position-dependent unit vectors $\vec{u}$ and $\vec{v}$ determine the SO coupling direction. Let us recall that SO coupling in the 2D geometry, subject to spatially periodic modulation, has been considered [87]. In fact, it has been shown that the complexes are bound states of several out-of-phase fundamental solitons whose centers are placed at the local maxima of the SO coupling-modulation phase. Moreover, the helicoidal SO coupling depends mainly on the choice of vectors that yield the component of a non-Abelian spin-dependent gauge field. Interestingly, the SO coupling has been realized with a lattice symmetry where, in particular, the coordinate-dependent phase $\theta(x, y)$ is a cosine function for which two-component fundamental solitons were obtained for $\theta(x, y) = \pi$ [87]. Considering the cosine and sine components will determine the direction of local vectors of the helicoidal SO coupling, leading to a wide variety of lattice structures capable of supporting other patterns related to binary ultracold bosonic gas. Remarkably, it was proposed that the impact of the helicoidal SO coupling landscape on the solitons is identical to that of a periodic 2D potential, which opens new routes for other parametrizations. Based on that, and for the sake of simplicity, we consider a helicoidal SO coupling with the periods π/β_x and π/β_y given, respectively, by:

$$\vec{u} = \left(\cos(2\beta_x x + 2\beta_y y), 0, \sin(2\beta_x x + 2\beta_y y)\right),$$
$$\vec{v} = \left(-\sin(2\beta_x x + 2\beta_y y), 0, \cos(2\beta_x x + 2\beta_y y)\right), \tag{5}$$

where β_x and β_y are the frequencies of rotation in the x- and y-directions. The positive and negative values of β_x and β_y are referred to the right- and left-handed modes, respectively [88–90]. We should note that the components of a non-Abelian spin-dependent gauge field could also be done, for instance, by relating the position-dependent unit vectors to a more generalized coordinate-dependent phase parametrization [87]. Next, the Zeeman Hamiltonian is given by:

$$H_Z = \frac{\Delta\sigma_z}{2}, \tag{6}$$

where Δ is the strength of Zeeman splitting. The Hamiltonian H_{RSO} is responsible for the Rashba SO coupling. It is adopted here under its common form given by [84]

$$H_{RSO} = \lambda_R(\sigma_x p_y - \sigma_y p_x), \tag{7}$$

where λ_R is the strength of Rashba SO coupling. Additionally, the 2D Dresselhaus SO coupling Hamiltonian is given by [84]:

$$H_{DSO} = \lambda_D(\sigma_x p_x - \sigma_y p_y), \tag{8}$$

where λ_D is the 2D strength of Dresselhaus SO coupling. Recently SO couplings with equal Rashba and Dresselhaus strengths have been demonstrated in a neutral atomic BEC by dressing two atomic spin states with a pair of Raman lasers, which create a momentum-sensitive coupling between two internal atomic states. The interaction Hamiltonian is given by:

$$\mathcal{E}_{int} = \frac{1}{2}\left(g_{11}|\Psi_1|^4 + g_{22}|\Psi_2|^4 + 2g_{12}|\Psi_1|^2|\Psi_2|^2\right), \tag{9}$$

where $g_{11} = 2a_{11}/a_\perp$ and $g_{22} = 2a_{22}/a_\perp$ are the two-body intraspecies interactions coefficients, while $g_{12} = 2a_{12}/a_\perp$ and $g_{21} = 2a_{21}/a_\perp$ are the two-body inter-species interaction coefficients. Here, $a_\perp = \sqrt{\hbar/(m w_\perp)}$ denotes the transverse characteristic length, with $w_\perp$ being the transverse trap frequency. m is the atomic mass, and $\hbar$ is the Planck constant. a_{11}, a_{22}, and a_{12} are the scattering lengths of the s-wave, experimentally adjustable via optical [45] and magnetic [48] Feshbach resonance techniques. The BEC dynamics in the mean-field approximation is governed by $i\hbar\partial\Psi_j/\partial t = \delta\mathcal{E}/\delta\Psi_j^*$, $(j = 1, 2)$, from which the following equations are obtained:

$$\begin{aligned} i\frac{\partial\Psi_1}{\partial t} =& -\frac{1}{2}\left(\frac{\partial^2}{\partial x^2} + \frac{\partial^2}{\partial y^2}\right)\Psi_1 + i(\beta_x - \alpha\nu)\frac{\partial\Psi_1}{\partial x} - i\alpha\mu\frac{\partial\Psi_1}{\partial y} + (\lambda_R - i\lambda_D - i\alpha\mu)\frac{\partial\Psi_2}{\partial x} \\ &+ i(\beta_y + \alpha\nu - \lambda_R - i\lambda_D)\frac{\partial\Psi_2}{\partial y} + \left[\frac{\Delta}{2} - \alpha\nu(\beta_x - \beta_y) - \beta_y(\lambda_R + i\lambda_D)\right]\Psi_1 \\ &+ \left[\alpha\mu(\beta_x - \beta_y) + i\beta_x(\lambda_R - i\lambda_D)\right]\Psi_2 + (g_{11}|\Psi_1|^2 + g_{12}|\Psi_2|^2)\Psi_1, \end{aligned} \tag{10a}$$

$$\begin{aligned} i\frac{\partial\Psi_2}{\partial t} =& -\frac{1}{2}\left(\frac{\partial^2}{\partial x^2} + \frac{\partial^2}{\partial y^2}\right)\Psi_2 - i(\beta_x - \alpha\nu)\frac{\partial\Psi_2}{\partial x} - i\alpha\mu\frac{\partial\Psi_2}{\partial y} - (\lambda_R - i\lambda_D + i\alpha\mu)\frac{\partial\Psi_1}{\partial x} \\ &+ i(\beta_y + \alpha\nu - \lambda_R - i\lambda_D)\frac{\partial\Psi_1}{\partial y} - \left[\frac{\Delta}{2} + \alpha\nu(\beta_x - \beta_y) + \beta_y(\lambda_R - i\lambda_D)\right]\Psi_2 \\ &+ \left[-\alpha\mu(\beta_x - \beta_y) + i\beta_x(\lambda_R - i\lambda_D)\right]\Psi_1 + (g_{22}|\Psi_2|^2 + g_{21}|\Psi_1|^2)\Psi_2, \end{aligned} \tag{10b}$$

where $\mu = \cos(2\beta_x x + 2\beta_y y)$ and $\nu = \sin(2\beta_x x + 2\beta_y y)$. As it is obvious, some coefficients of the above set of GP equations are dependent on space, which takes us away from the main objective of this work. To obtain the free space equation, specific values must be taken by β_x and β_y. There are, in fact, two different cases related to the values of β_x and β_y that are such that $\beta_x = \beta_y = 0$ and $\beta_x = \beta_y = \beta$, with $(\beta x + \beta y) = \pi/2$. In the first case, the helicoidal gauge potential is switched off, leaving the system with, among other terms, the gauge amplitude α and the RD SO coupling terms supported by λ_R and λ_D, respectively. The second case, however, is a complete one that includes both the helicoidal gauge potential and the gauge amplitude and includes the effects of the RD SO coupling. In fact, a special family of soliton solutions known as line Solitons was investigated for the Kadomtsev-Petviashvili equation, which is a prototypical $(2+1)D$ integrable system and is a universal model for weakly two-dimensional small-amplitude waves in the long wavelength regime [91]. Moreover, soliton amplitudes and directions have been used to study two elastic 3-soliton solutions about different combinations of pairwise interactions. Additionally, the nonlinear excitations of a vortex line in a BEC trapped in a 1D optical lattice were studied [92]. For example, a vortex line in an ordinary magnetically trapped BEC without an optical lattice has been revealed, with competing processes involving the inhomogeneous condensate-density distribution in the radial direction and an interaction-like energy term, leading to energetic cost for bending the vortex line with specific kinetic energy. This reduces the vortex's stiffness in expense to the lattice depth, which is specific to the line-amplitude solitons. In the rest of this letter, attention will be paid to such consideration both analytically and numerically by imposing $(\beta x + \beta y) = \pi/2$, where $\beta_x = \beta_y = \beta$, which is the equation of a single straight line. In doing so, the proposed parametrization has the merit of generating a periodic structure and, consequently, phase-line solitons. That reduces Eqs. (10) to the following set of GPEs:

$$
\begin{aligned}
i\frac{\partial\psi_1}{\partial t} &= -\frac{1}{2}\left(\frac{\partial^2}{\partial x^2}+\frac{\partial^2}{\partial y^2}\right)\psi_1 + i\beta\left(\frac{\partial\psi_1}{\partial x}+\frac{\partial\psi_2}{\partial y}\right) + i\alpha\left(\frac{\partial\psi_1}{\partial y}+\frac{\partial\psi_2}{\partial x}\right)\\
&+\lambda_R\left(\frac{\partial\psi_2}{\partial x}-i\frac{\partial\psi_2}{\partial y}\right) - i\lambda_D\left(\frac{\partial\psi_2}{\partial x}-i\frac{\partial\psi_2}{\partial y}\right) + \left(g_{11}|\psi_1|^2+g_{12}|\psi_2|^2\right)\psi_1 \qquad (11a)\\
&+\left[\frac{\Delta}{2}-\beta(\lambda_R+i\lambda_D)\right]\psi_1+\beta(\lambda_D+i\lambda_R)\psi_2,\\
i\frac{\partial\psi_2}{\partial t} &= -\frac{1}{2}\left(\frac{\partial^2}{\partial x^2}+\frac{\partial^2}{\partial y^2}\right)\psi_2 - i\beta\left(\frac{\partial\psi_2}{\partial x}-\frac{\partial\psi_1}{\partial y}\right) - i\alpha\left(\frac{\partial\psi_1}{\partial x}-\frac{\partial\psi_2}{\partial y}\right)\\
&-\lambda_R\left(\frac{\partial\psi_1}{\partial x}+i\frac{\partial\psi_1}{\partial y}\right) + i\lambda_D\left(\frac{\partial\psi_1}{\partial x}-i\frac{\partial\psi_1}{\partial y}\right) + \left(g_{22}|\psi_2|^2+g_{21}|\psi_1|^2\right)\psi_2 \qquad (11b)\\
&-\left[\frac{\Delta}{2}+\beta(\lambda_R-i\lambda_D)\right]\psi_2+\beta(\lambda_D+i\lambda_R)\psi_1.
\end{aligned}
$$

We should also stress that in order to get the system of Eqs. (10), we have introduced the gauge transformations

$$\Psi_j = e^{-i\alpha^2 t}e^{-i(\beta_x^2+\beta_y^2)t/2}e^{-i(\sigma_z\beta_x x+\sigma_x\beta_y y)}\psi_j,\ \ j=1,2, \qquad (12)$$

that switches to the rotating frame for the chosen gauge field. In doing so, the point translation symmetry transforms into a continuous translational symmetry of the derived equation. Finally, the spatial variables x and y, time t, density $(|\psi_1|^2+|\psi_2|^2)$, and energy are given in the normalized units $a_\perp$, $w_\perp^{-1}$, $a_\perp^{-1}$, and $\hbar w_\perp$, respectively. The wave functions are normalized as $N_j=\int(|\psi_j|^2 dxdy)$, $(j=1,2)$, while the total number of atoms of the jth component is $N=N_1+N_2=\int\int\left(|\psi_1|^2+|\psi_2|^2\right)dxdy$, which is a dynamical invariant of non-dissipative BEC systems. In what follows, we comprehensively address the instability of CW solutions, taking advantage of the above two cases.

3. Linear stability analysis and instability criteria

According to the general theory of MI, the above systems admit CW solutions $\psi_j = e^{-i\mu t}\sqrt{n_{j0}},\quad j=1,2$, where μ is the common chemical potential of both components, related to the Zeeman splitting energy via the linear dispersion relation

$$\frac{\Delta}{2} = (-1)^j\left(g_j n_{j0}+g_{12}n_{3-j,0}-\mu\right)-(-1)^j\beta\lambda_R+i\beta\lambda_D-(-1)^{3-j}\beta\lambda_D+(-1)^j i\beta\lambda_R,\ \ j=1,2, \qquad (13)$$

with uniform densities $n_{10}=n_{20}=n_0$. By replacing such solutions into the generic GPEs, a linear dispersion relation is found between the chemical potential, the Zeeman splitting energy, the density n_0 and the interatomic interaction parameters g_{11}, g_{22} and g_{12}. In general, the stability of the CW solutions is checked by introducing small perturbations so that $\psi_j = e^{-i\mu t}(\sqrt{n_{j0}}+\delta\psi_j)$, $j=1,2$, where the perturbed fields $\delta\psi_j$ are taken in the form

$$\delta\psi_j = \zeta_j\cos(K_1x+K_2y-\Omega t)+i\eta_j\sin(K_1x+K_2y-\Omega t), \qquad (14)$$

where K_1 and K_2 are the perturbation wavenumbers in the x- and y-direction, respectively; Ω is a complex modulation frequency, ζ_j, and η_j are constant complex amplitudes. Linearizing the above-perturbed solutions around the unperturbed ones leads to a linear homogeneous system of equations in terms of ζ_1, ζ_2, η_1 and η_2 of the form

$$\begin{pmatrix} \Omega+n_{11} & n_{12} & n_{13} & n_{14}\\ n_{21} & \Omega+n_{22} & n_{23} & n_{24}\\ n_{31} & n_{32} & -\Omega+n_{33} & n_{34}\\ n_{41} & n_{42} & n_{43} & -\Omega+n_{44}\end{pmatrix}\begin{pmatrix}\zeta_1\\ \zeta_2\\ \eta_1\\ \eta_2\end{pmatrix}=\begin{pmatrix}0\\0\\0\\0\end{pmatrix}, \qquad (15)$$

where the elements n_{ij} of the matrix (given in Appendix A) depend not only on the perturbation frequency Ω and the wavenumbers K_1 and K_2, but also on the other parameters including the SO coupling strengths and the interatomic interaction parameters. Interestingly, for system (15) to admit a non-trial solution, the determinant of its matrix should be null, which leads to a general nonlinear dispersion relation of the form

$$\Omega^4+P_3\Omega^3+P_2\Omega^2+P_1\Omega+P_0=0, \qquad (16)$$

where general expressions for the coefficients P_j $(j=1,2,3)$ are given in Appendix B. Eq. (16) can be solved analytically to obtain the solutions

$$
\begin{aligned}
\Omega_{1,2} &= -\frac{P_3}{4}-\frac{1}{2}\sqrt{\frac{1}{4}P_3^2-\frac{2}{3}P_2+\Lambda}\pm\frac{1}{2}\sqrt{-\frac{4}{3}P_2+\frac{1}{2}P_3^2-\Lambda+\frac{P_3^3-4P_3P_2+8P_0}{4\sqrt{\frac{1}{4}P_3^2-\frac{2}{3}P_2+\Lambda}}},\\
\Omega_{3,4} &= -\frac{P_3}{4}+\frac{1}{2}\sqrt{\frac{1}{4}P_3^2-\frac{2}{3}P_2+\Lambda}\pm\frac{1}{2}\sqrt{-\frac{4}{3}P_2+\frac{1}{2}P_3^2-\Lambda-\frac{P_3^3-4P_3P_2+8P_0}{4\sqrt{\frac{1}{4}P_3^2-\frac{2}{3}P_2+\Lambda}}},
\end{aligned} \qquad (17)
$$

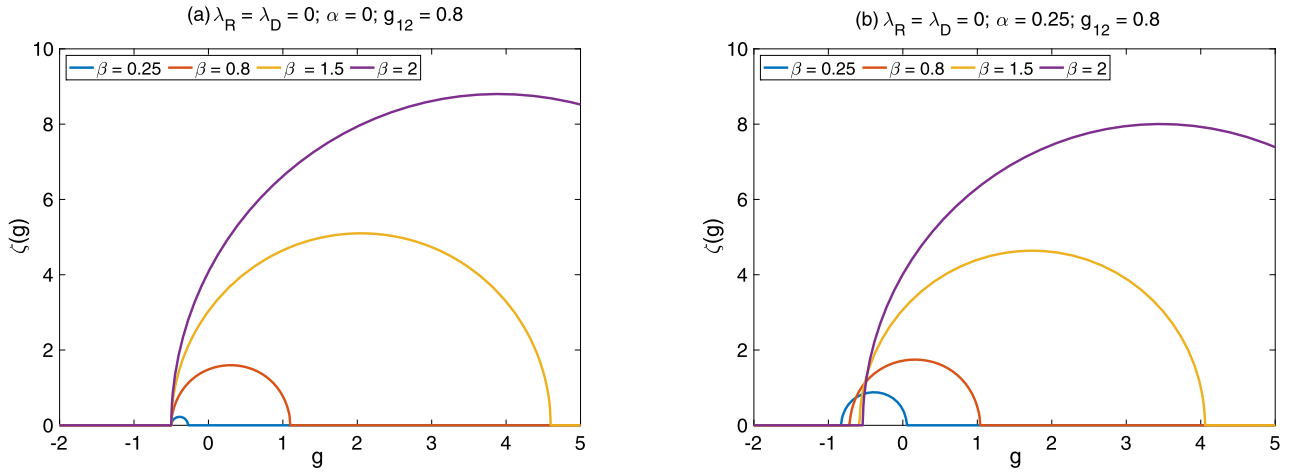


Fig. 1. Distribution of the MI growth rate versus the interatomic coupling $g = g_{11} = g_{22}$ for different values of the SO coupling strength when: (a) the RD SO coupling is absent, i.e., $\lambda_D = \lambda_R = 0$ and (b) in presence of the RD SO coupling, i.e., $\lambda_D = \lambda_R = 0.01$, with $g_{12} = 0.8$, $K_1 = K_2 = 1$ and $n_0 = 1$.

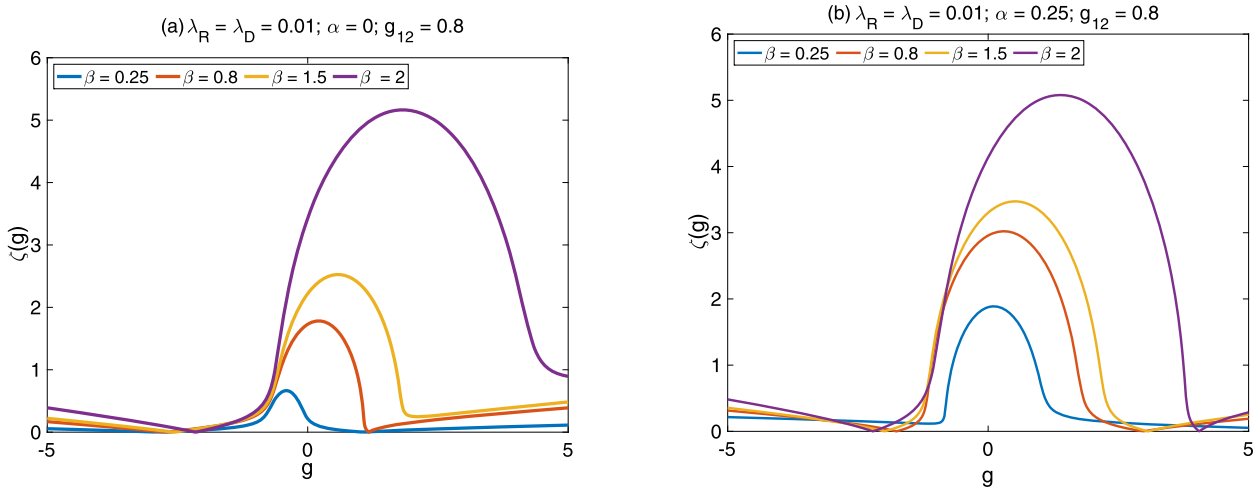


Fig. 2. Distribution of the MI growth rate versus the interatomic coupling $g = g_{11} = g_{22}$ for different values of the SO coupling strength when: (a) the RD SO coupling is absent, i.e., $\lambda_D = \lambda_R = 0$ and (b) in presence of the RD SO coupling, i.e., $\lambda_D = \lambda_R = 0.01$, with $g_{12} = 0.8$, $K_1 = K_2 = 1$ and $n_0 = 1$.

where

$$\Lambda = \frac{1}{3}\left(\sqrt[3]{\frac{\Delta_2 + \sqrt{\Delta_2^2 - 4\Delta_1^3}}{2}} + \frac{\Delta_1}{\sqrt[3]{\frac{\Delta_2 + \sqrt{\Delta_2^2 - 4\Delta_1^3}}{2}}}\right),$$

with $\Delta_1 = P_2^2 - 3P_3P_1 + 12P_0$, and $\Delta_2 = 2P_2^3 - 9P_3P_2P_1 + 27P_3^2P_0 + 27P_1^2 - 72P_2P_0$. Depending on system parameters, solutions (17) can be positive, negative, or even complex. Nevertheless, the stability of the CW is due to real, negative, or positive values of Ω. In general, complex solutions of Eq. (15) are written as $\Omega = \Omega_r + i\Omega_i$, so that $e^{-i\Omega t} = e^{-i\Omega_r t} \times e^{\Omega_i t}$. The latter implies that MI will take for a non-zero imaginary part of the perturbation frequency, which allows extracting necessary information on the occurrence of the instability using the maximum MI growth rate

$$\zeta(\Omega) = \{|\mathrm{Im}(\Omega)|\}_{\max}. \tag{18}$$

When $\lambda_D = \lambda_R = 0$, the RD SO coupling is absent, and one recovers the two-dimensional system proposed by Kartashov [93] and studied recently by Li et al. [73]. Such a system takes advantage of the presence of the helicoidal SO coupling and includes a strong impact from the interatomic interactions. In order to find suitable values for $g = g_{11} = g_{22}$ and g_{12} capable of giving rise to instability in this context, we have plotted the MI growth rate versus g in Fig. 1. There, panel (a) corresponds to $\alpha = 0$ and panel (b) to $\alpha = 0.25$. When the gauge amplitude is switched off, i.e., $\alpha = 0$, $\beta = 0.25$ instability is announced in areas where $g < 0$, around, and including, the point $g = -0.5$. That repulsive effect of the intracomponent interaction is broken when β increases, therefore extending the MI growth rate spectrum towards positive values of g. The phenomenon becomes more pronounced as the helicoidal gauge potential increases, leading to a marginal instability zone appearing in the whole area $g > g_{cr}$, with $g_{cr} < -0.5$ being the lower values taken by g. The same spectrum of behaviors is ostensible in Fig. 1(b), where the gauge amplitude $\alpha \neq 0$, with β taking the same values as in Fig. 1(a). We should, however, stress that the MI growth rate corresponding to $\beta = 0.25$ is more localized than the one in Fig. 1(a) and covers a large interval of g that

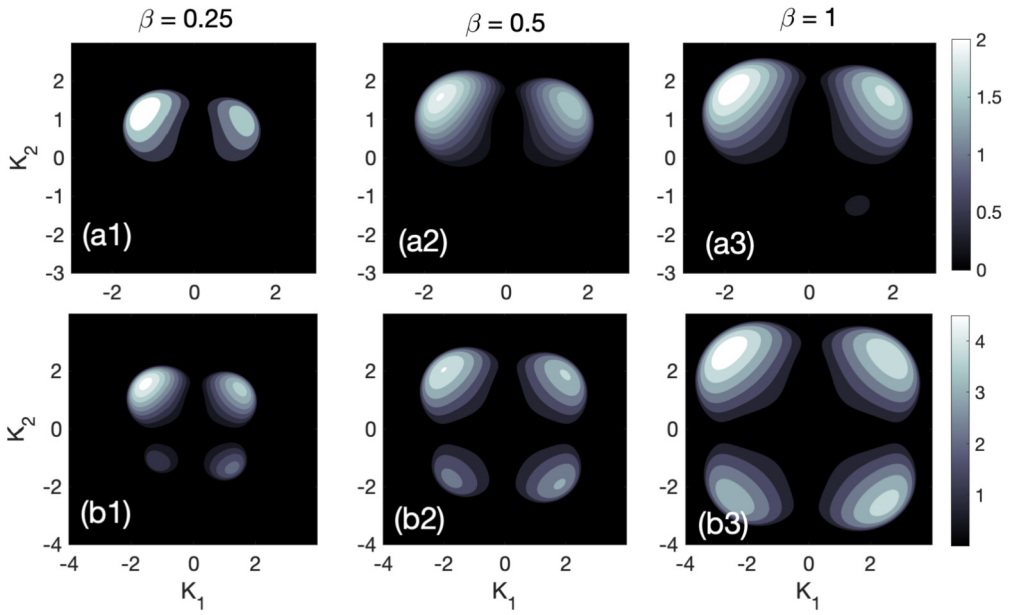


Fig. 3. The panels show the distribution of the growth rate of MI in the (K_1, K_2)-plane for $\lambda_R = \lambda_D = 0$ (panels $(\text{aj})_{j=1,2,3}$) and $\lambda_R = \lambda_D \neq 0$ (panel$(\text{bj})_{j=1,2,3}$). From left to right, the columns correspond to the different cases $\beta = 0.25$, $\beta = 0.5$ and $\beta = 1$, respectively, with $g_{12} = 0.8$, $\alpha = 0.25$ and $n_0 = 1$. White regions correspond to zones of instability, while dark areas are where the CW solutions are likely to remain stable under modulation.

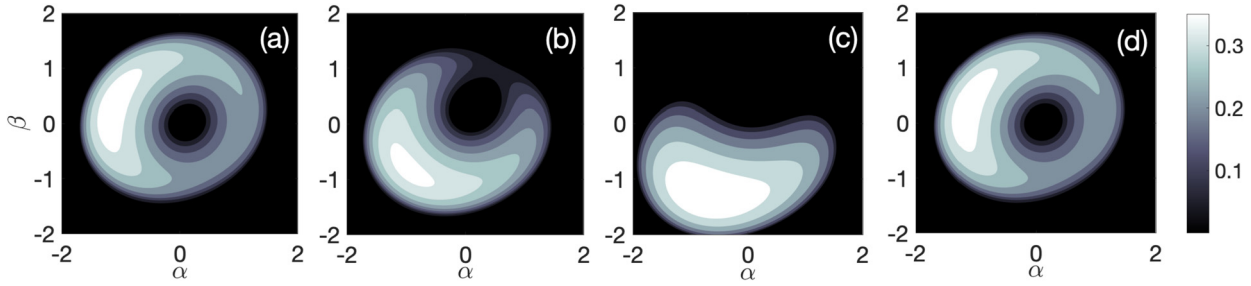


Fig. 4. The panels show the growth rate of MI (α, β)-plane for (a) $\lambda_R = \lambda_D = 0.01$, (b) $\lambda_R = 0.01$ and $\lambda_D = 0.02$ (c) $\lambda_R = 0.01$ and $\lambda_D = 0.04$, and (d) $\lambda_R = 0.04$ and $\lambda_D = 0.04$.

supports instability. Increasing the helicoidal gauge potential, the zone of instability gets slightly delocalized and expands more and more with increasing β.

The most interesting case, which deserves to be regarded with emphasis, is realized when $\lambda_D = \lambda_R \neq 0$, in the presence of the gauge amplitude α and the helicoidal gauge potential β. When α and β take non-zero values, they constitute the helicoidal SO coupling [93]. The competition between the two types of SO coupling on the values of g supporting instability is summarized in Fig. 2, where the instability growth rate is displayed for different values of the helicoidal gauge potential β. Fig. 2(a) shows the MI growth rate distribution when the gauge amplitude α is zero. There are intervals of g where ζ is non-zero, which get expanded by increasing the helicoidal gauge potential β from 0.25 to 2. Interestingly, minor zones of instability appear from where some possible values of g can be extracted to obtain instability. Fully considering the helicoidal SO coupling, ζ is shown in Fig. 2(b), where $\alpha = 0.25$. The main behavior that appears here is the enlargement of the instability zone with increasing β. Also, the interval of g where instability is expected is well delimited and includes positive and negative values of the intracomponent interaction parameter.

The spectrum of Figs. 1 and 2 gave us information on values of some key parameters, like the interatomic coupling parameters, to be used for instability to manifest itself. Taking advantage of that, the growth rate of MI is plotted in Fig. 3, in the plane of the perturbation wavenumbers K_1 and K_2. Fixing $\alpha = 0.25$, $g = -0.4$ and $g_{12} = 0.8$, the panels $(\text{aj})_{j=1,2,3}$ of Fig. 3 show the growth rate spectrum for $\lambda_R = \lambda_D = 0$, while panels, from left to right correspond respectively to $\beta = 0.25$, $\beta = 0.5$ and $\beta = 1$. Initially, instability is supported by a set of asymmetric breasts, with maximum mainly situated in the area $K_2 > 0$, while minor and major objects belong, respectively, to areas $K_1 > 0$ and $K_1 < 0$. Increasing the helicoidal gauge potential β to 0.5, the instability zones expand, covering wider areas where unstable patterns could be expected. This fact is confirmed by the last figure of instability in this series, where the breasts are amplified, with hallows of points visible in the negative part of the wavenumber K_2, which might give rise to instability. We should stress that by switching off the RD SO coupling, the system at hand just feels the effect of the helicoidal SO coupling. Otherwise, the model comprises two submodels that can constitute individual studies, especially when generalized to three-dimensional formulations. For instance, bringing back the RD SO coupling by imposing $\lambda_R = \lambda_D \neq 0$, one gets the instability figures of Figs. $3(\text{bj})_{j=1,2,3}$, where β, the helicoidal gauge potential, changes in the same manner. The competition between the helicoidal SO coupling and the RD SO coupling modifies the instability figure. For example, instead of the two breasts of instability obtained in Figs. $3(\text{aj})_{j=1,2,3}$, the instability develops under four lobes, distributed in positive and negative zones of K_1 and K_2. In this context, the intensity of the MI growth rate gets amplified as β increases, leading to four expanded instability regions.

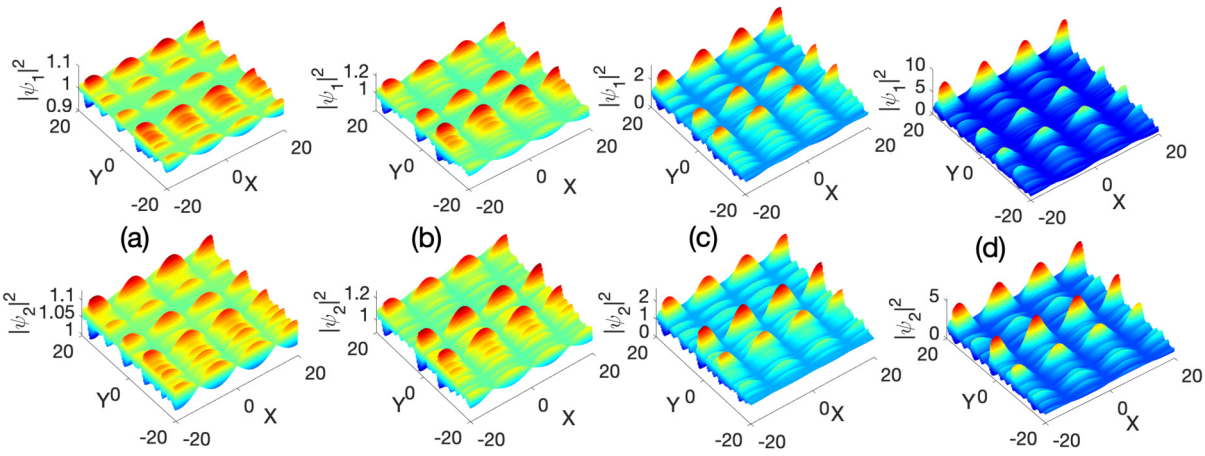


Fig. 5. MI evolution in both condensates with increasing time in the presence of both the SO coupling and the RD SO coupling. Fixing $\alpha = 0.1$, $\beta = 0.25$, and $\lambda_R = \lambda_D = 0.01$, panels from (a) to (d) correspond to the respective instants $t = 25$, $t = 60$, $t = 100$ and $t = 170$. The other parameters are $K_1 = K_2 = 1.5$, $n_0 = 1$, $g = g_{11} = g_{22} = 0.5$ and $g_{12} = 0.6$.

To conclude our linear stability analysis, we represent in Fig. 4 the MI growth rate distribution versus α and β. Fixing $g_{12} = 0.8$ and $g = 1.2$, different combinations of λ_D and λ_R are used to assess the competitive impact between the helicoidal and the RD SO coupling on the MI growth rate behavior. For $\lambda_R = \lambda_D = 0.01$, instability is supported by an asymmetric cylinder with a hole of stability around, and including, the point $(\alpha, \beta) = (0, 0)$. Interestingly, the maximum instability growth rate is shared between some areas $\beta > 0$ and $\beta < 0$. Precision should be made that when $\beta > 0$, the coupling is said to be left-handed, and right-handed when $\beta < 0$. With increasing the Dresselhaus SO-coupling parameter λ_D to 0.02, one obtains the features of Fig. 4(b), where the zone of maximum instability tends to shift to the $\beta < 0$, and $\alpha < 0$, zones into a broken cylindrical MI growth rate. This is more visible in Fig. 4(c), where the cylindrical structure of the MI growth rate is completely broken, with the maximum growth rate taking place exclusively for right-handed SO coupling, with $\lambda_D = 0.02$ and $\lambda_R = 0.01$. Interestingly, the initial MI spectrum of Fig. 4(a) is recovered when increasing λ_R to 0.04, as shown in Fig. 4(d). This implies that the Rashba SO coupling, in this particular context, has the reverse effect of the Dresselhaus SO coupling. To remind, MI in BEC has been given considerable importance over a long period, owing to its fundamental and applied interest in various aspects [94]. In particular, MI has been found to be relevant in understanding the formation and propagation of solitonic waves and also apparent in explaining the domain formation and quantum phase transition. Overall, the above linear stability analysis shows that the MI growth rate ζ is very sensitive to the variation of the competing SO parameters, which offers different figures of instability, to be confirmed numerically in the next section.

4. Numerical results on wave train formation

The linear stability analysis performed in Sec. 3 relies on linearizing the perturbed CWs around the unperturbed solutions. Therefore, only the onset of MI can be predicted, while no information about the longtime spatiotemporal evolution of the instability growth can be obtained, which requires their confrontation with direct numerical simulations on Eqs. (11). This is achieved using the split-step Fourier method using the initial conditions:

$$\psi_1(x, y, 0) = \psi_2(x, y, 0) = \sqrt{n_0} + \varepsilon \cos(K_1 x + K_2 y), \tag{19}$$

where the perturbation wavenumbers $K = K_1 = K_2$ have been chosen based on the growth rate spectra of Figs. 1-4, with $n_0 = 1$ and $\varepsilon = 0.001$, so that $\varepsilon \ll n_0$. The features of MI are discussed in terms of the amplitude maxima, while one pays particular attention to the simultaneous effects brought by the helicoidal and the RD SO couplings. Different combinations of such parameter values are used according to the predictions of the linear stability analysis.

To start, we should remind the reader that the gauge amplitude and the helicoidal gauge potential are the combined quantities that bring about the helicoidal SO coupling. In 2D, considering $(\beta x + \beta y) = \pi/2$ constitutes a square lattice that will be used for numerical simulations in the presence of the RD SO coupling. The results showing the MI evolution in such a model are presented in Figs. 5-11. In fact, Fig. 5 shows results for $\alpha \neq 0$ and $\beta \neq 0$, with $\lambda_R = \lambda_D = 0.1$, which indeed show the emergence of train of wave, periodic along the x-axis, but erratic along the y-axis. This is contrary to what was observed in the previous case and pictures the impact of the helicoidal gauge potential on the MI process. However, erratic patterns are more distributed for $|\psi_2|^2$ than for $|\psi_1|^2$, which support a certain energy concentration, knowing that the initial state was the same. At this point, the presence of β gives the possibility to characterize patterns for right- and left-handed helicoidal SO couplings, respectively obtained for $\beta < 0$ and $\beta > 0$. The features of Fig. 5 correspond to the left-handed coupling context. Further calculations, especially for the right-handed SO coupling, are recorded in Fig. 6, where trains of solitons are generated for $\beta < 0$. In Fig. 7, wave patterns due to right-handed and left-handed helicoidal SO couplings are compared. It is clear that not only β affects the occurrence of MI, but it also sustains the robustness of the soliton-like objects in the proposed model. The formation of solitary peaks in BEC systems has been debated in several contributions. That phenomenon was described by Hai et al. [71], where they showed that breathing wave packets can display some deformation while propagating. Although this was shown on a single BEC, and based on Strecker's et al. experiment [69], the width and frequency of the wave train oscillation may be affected, therefore delocalizing the center of the soliton, with the direct result being what is displayed in Fig. 7. Although the calculations made in the present work are a result of the activation of the MI, it remains that such structures are inherent to BEC systems, especially when a suitable balance between nonlinear and dispersive effects is found, as interestingly demonstrated by Salasnich et al. [95] in a one-component BEC of ^{7}Li.

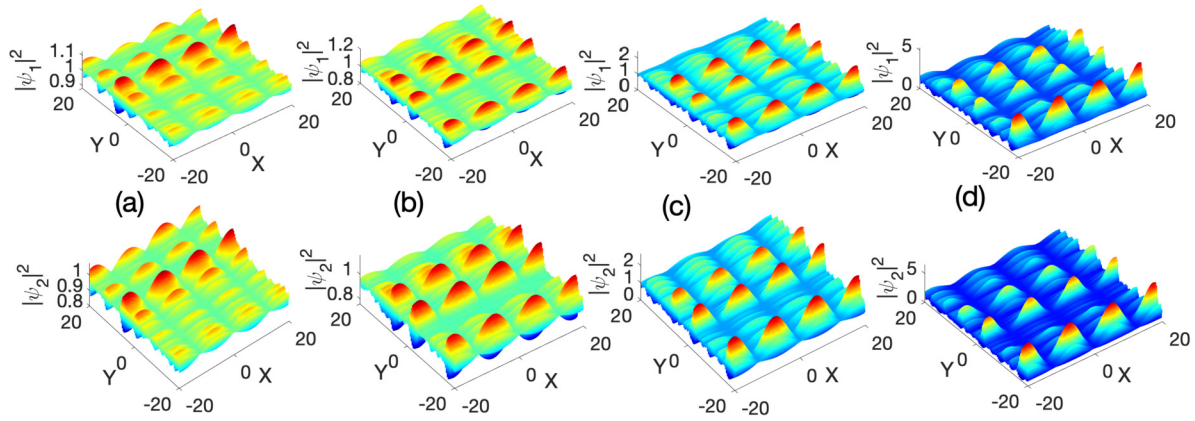


Fig. 6. MI evolution in both condensates with increasing time in the presence of both the SO coupling and the RD SO coupling. Fixing $\alpha = 0.1$, $\beta = -0.25$, and $\lambda_R = \lambda_D = 0.01$, panels from (a) to (d) correspond to the respective instants $t = 25$, $t = 60$, $t = 100$ and $t = 170$. The other parameters are $K_1 = K_2 = 1.5$, $n_0 = 1$, $g = g_{11} = g_{22} = 0.5$ and $g_{12} = 0.6$.

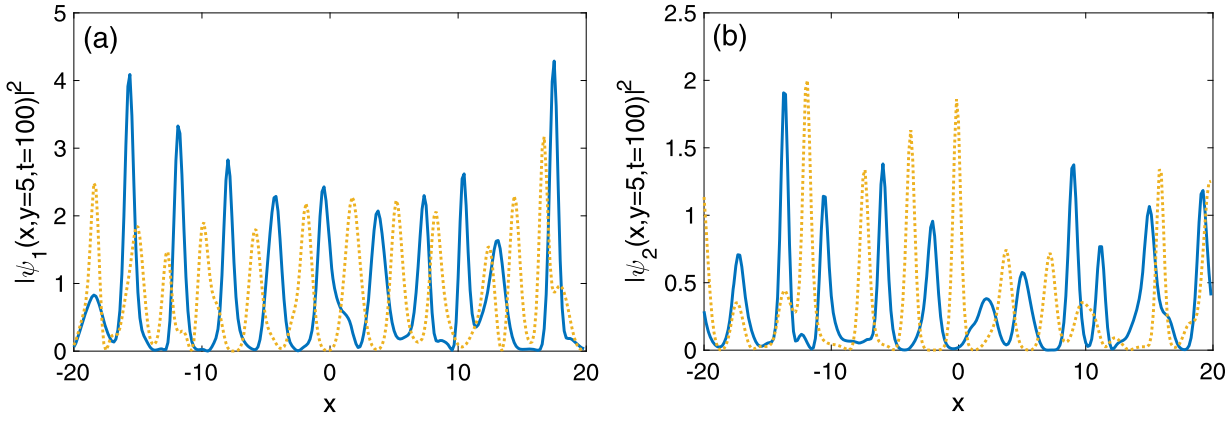


Fig. 7. The panels show cross sections of the density profiles at time $t = 100$, when $y = 10$, $\beta = 0.25$ (solid blue line), $\beta = -0.25$ (dotted yellow line) and $\lambda_R = \lambda_D = 0.1$. The other parameters are $K_1 = K_2 = 1.5$, $n_0 = 1$, $g = g_{11} = g_{22} = 0.5$, $g_{12} = 0.6$, and $\alpha = 0.1$. (For interpretation of the colors in the figure(s), the reader is referred to the web version of this article.)

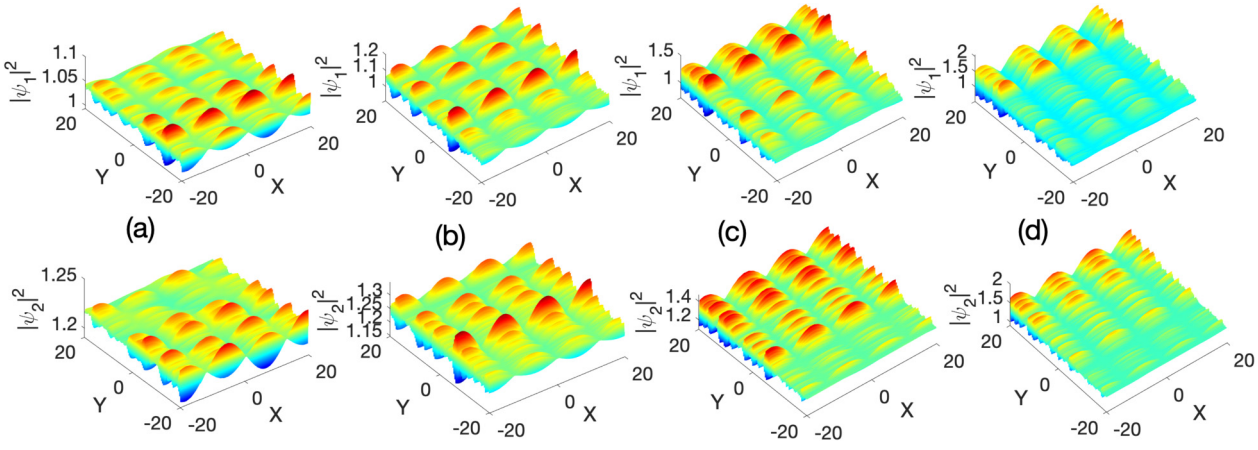


Fig. 8. MI evolution in both condensates with increasing time in the presence of both the SO coupling and the RD SO coupling. Fixing $\alpha = 0.1$, $\beta = 0.25$, and $\lambda_R > \lambda_D$, panels from (a) to (d) correspond to the respective instants $t = 25$, $t = 60$, $t = 100$ and $t = 170$. The other parameters are $K_1 = K_2 = 1.5$, $n_0 = 1$, $g = g_{11} = g_{22} = 0.5$ and $g_{12} = 0.6$.

The effect of λ_R and λ_D cannot be neglected in this context, as the cross terms between the two condensates modulate the balance between nonlinearity and dispersion, which brings about new behaviors. This can be more effective when $\lambda_R > \lambda_D$ as shown in Fig. 8, where $\alpha = 0.1$ and $\beta = 0.25$. Initially, the distribution of wave patterns is high for $|\psi_1|^2$, but during propagation, there is energy transfer through the coupling, which increases pattern distribution in favor of $|\psi_2|^2$. With time, the MI persists, which justifies a strong disturbance of the CW stability by the Rashba SO coupling term. Still, propagation takes place in the y-direction. The numerical results recorded in Fig. 9 further show how the balance between λ_R and λ_D influences the MI progression both under left- and right-handed SO coupling. At the time $t = 20$, strong density disturbance generates envelope solitons in both components. With time increasing, the breather soliton expands, and the number of oscillations increases, probably due to multiple collisions among the emerging solitons. However, the effect of the sign

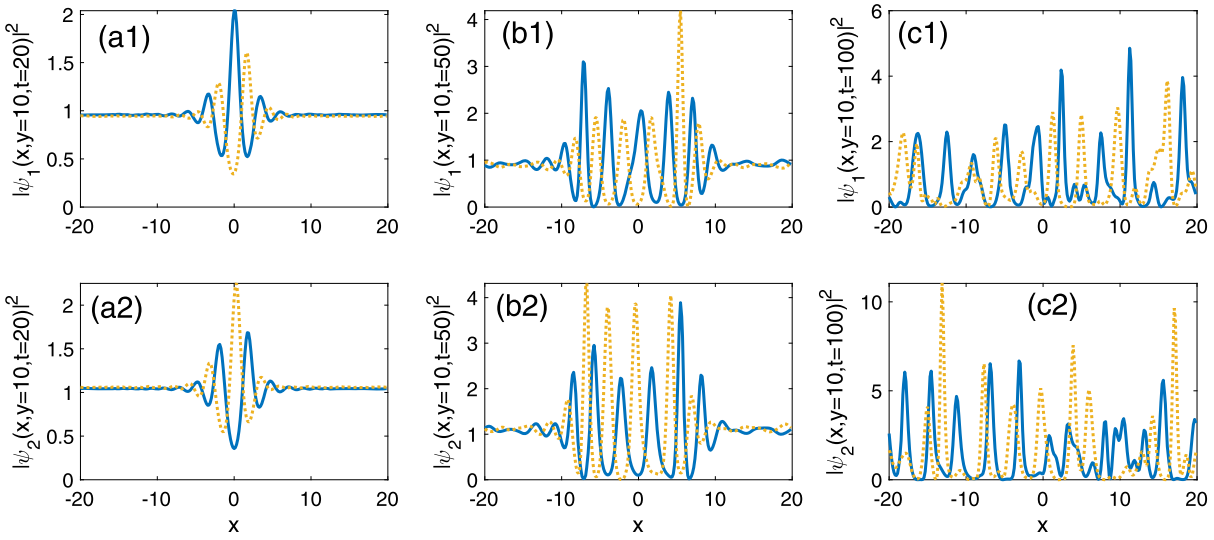


Fig. 9. The panels show cross sections of the density profiles when $y = 10$, $\beta = 0.25$ (solid blue line), $\beta = -0.25$ (dotted yellow line) and $\lambda_R > \lambda_D$. Panels $(\text{aj})_{j=1,2}$, $(\text{bj})_{j=1,2}$ and $(\text{cj})_{j=1,2}$ respectively correspond to instants $t = 20$, $t = 50$ and $t = 100$, with $K_1 = K_2 = 1.5$, $n_0 = 1$, $g = g_{11} = g_{22} = 0.5$, $g_{12} = 0.6$ and $\alpha = 0.1$.

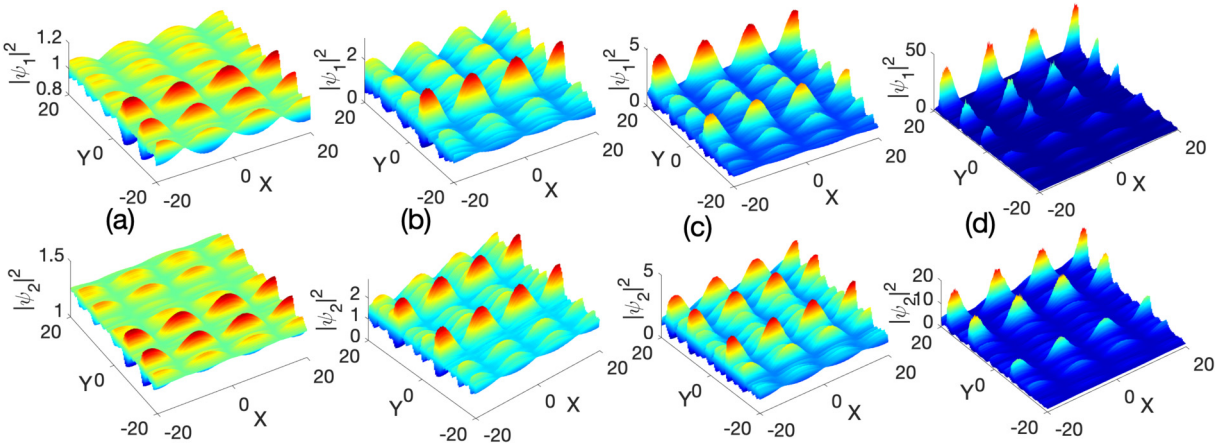


Fig. 10. MI evolution in both condensates with increasing time in the presence of both the SO coupling and the RD SO coupling. Fixing $\alpha = 0.1$, $\beta = 0.25$, and $\lambda_R < \lambda_D$, panels from (a) to (d) correspond to the respective instants $t = 25$, $t = 60$, $t = 100$ and $t = 170$. The other parameters are $K_1 = K_2 = 1.5$, $n_0 = 1$, $g = g_{11} = g_{22} = 0.5$ and $g_{12} = 0.6$.

β manifests itself by intermittent alternations between in- and out-of-phase oscillations. Being in the presence of a mixture of open BECs, the oscillations, after a certain time, extend to the boundaries, as supported by Fig. 9$(\text{bj})_{1=1,2}$, where the train is made of ordinary and composite solitons. Moreover, it is evident that the structures of Figs. 9$(\text{aj})_{j=1,2}$ are more confined and, therefore, support the presence of a virtual potential. Of course, a real experiment predicts any matter-wave state to be created in a trapping potential. The two-component model of the BEC that combines the SO-Rashba coupling and attractive cubic interactions supports semi-vortices and mixed modes, which get readily self-trapped in the common isotropic harmonic-oscillator trapping potential and remain robust even when the potential gets quenched [96]. This otherwise reveals the independent tunability of the Rashba SO coupling and the harmonic-oscillator trap. Even in the absence of trapping potentials, other seminal contributions have indicated that in exciton-polariton condensates with dissipation due to a narrow external pump beam, the formation of strongly localized stationary solutions, also known as quasicompactons [97], may take place. Indeed, the models are modified by the presence of the RD terms, which may explain the observed behaviors in a certain way. This means that the helicoidal SO coupling should be complete through the presence of α and β for the trapping effect to be strong. Otherwise, the gauge amplitude alone, mixed with the RD SO coupling, cannot trap the soliton trains that expand from the onset, even though nonlinear structures emerge over a long time. This is also true for the case $\lambda_R > \lambda_D$ depicted in Fig. 10, where the final instant $t = 170$ displays patterns whose amplitude increases with y. More interestingly, the cross-section of both component oscillations, depicted in Fig. 11, shows an increase in the number of peaks. This shows the real effect of a dominating Dresselhaus SO coupling parameter λ_D. Also, when the system is switched from left- to right-handed helicoidal SO coupling, the last stage shows dominating peaks belonging to the condensate ψ_1.

When the helicoidal gauge potential is well-tuned, combining the two effects of RD SO-coupling may bring about new classes of patterns as already debated in several contributions dealing with vortices and more exotic topological excitations in rotating two- and three-dimensional SO-coupled BECs. In such contexts, it was shown that RD SO coupling may lead to a broad range of quantum phases among which plane wave phase [98], bright soliton phase [99,100], dark soliton phase [101], stripe phase [98,102,103], topological superfluid phase [51], polarized and unpolarized phases [104], just to name a few. Most of such excitation phases may be observed via the activation of MI, but the difficulty remains in manipulating the large number of parameters involved. This explains why we restricted

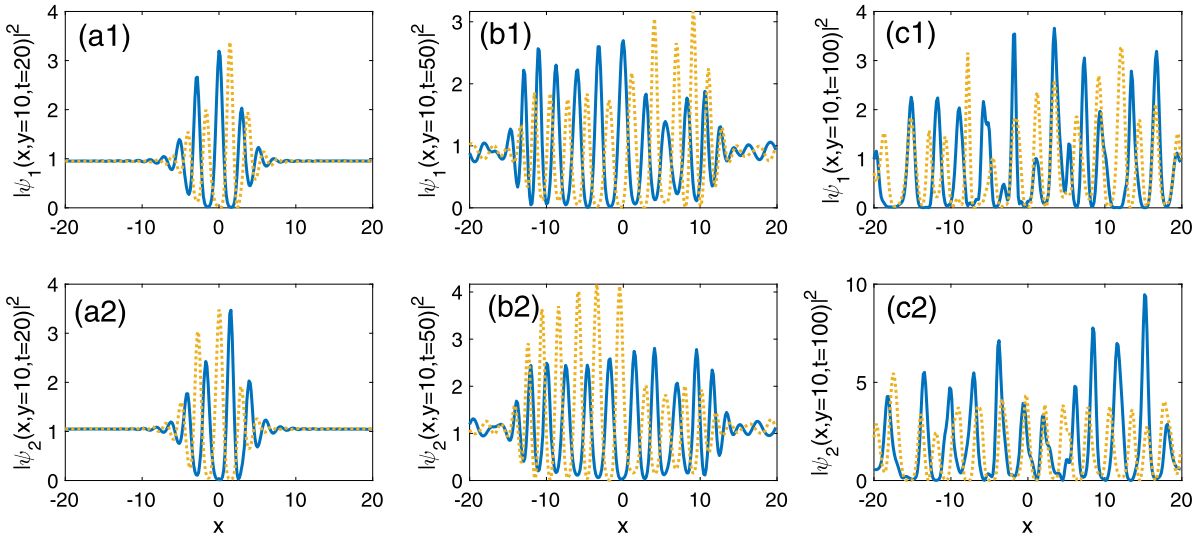


Fig. 11. The panels show cross sections of the density profiles when $y = 10$, $\beta = 0.25$ (solid blue line), $\beta = -0.25$ (dotted yellow line) and $\lambda_R < \lambda_D$. Panels $(aj)_{j=1,2}$, $(bj)_{j=1,2}$ and $(cj)_{j=1,2}$ respectively correspond to instants $t = 20$, $t = 50$ and $t = 100$, with $K_1 = K_2 = 1.5$, $n_0 = 1$, $g = g_{11} = g_{22} = 0.5$, $g_{12} = 0.6$ and $\alpha = 0.1$.

ourselves to repulsive intra- and intercomponent interactions and, more importantly, how they compete with other parameters like the helicoidal gauge potential and the subsequent Rashba and Dresselhaus SO-coupling parameters.

5. Concluding remarks

In this letter, we have introduced a 2D BEC system that combines the helicoidal SO coupling and a mixture of RD SO coupling. Taking advantage of the helicoidal gauge potential tunability, the dynamical model of BEC has been reduced to a set GPEs in the square lattice approximation. The analysis of MI has been carried out, and new distribution behaviors of the growth rate spectra under the combined effects of the two types of SO couplings have been found. In a context where the full helicoidal SO coupling and the RD coupling are involved, confined and coherent structures have been found to characterize MI, which further revealed the trapping capacity of the helicoidal SO coupling via the emergence of breathing-like solitons extending progressively to the domain edges as time increases. Such dynamics have been explored for $\lambda_R = \lambda_D$, $\lambda_R > \lambda_D$ and $\lambda_R < \lambda_D$. In free space, however, the change in the gauge amplitude α, together with the above combinations between λ_R and λ_D, does not allow the confinement of the emerging solitons, which corroborates the fact that RD SO coupling does not provide any trapping mechanism [84], the latter being recovered by applying the helicoidal SO coupling, and the helicoidal gauge potential particularly. It was, for example, shown by Liu et al. [105] that another mechanism to stabilize 2D and 3D solitons under simultaneous Rashba and Dresselhaus SO couplings was through the application of long-range anisotropic attractive dipole-dipole interactions. Anisotropic vector solitons were generated, and their collision confirmed the trapping effect of the dipole-dipole interactions. A new direction to the present study may be soliton generation via wave collision and their stabilization through the helicoidal SO coupling.

CRediT authorship contribution statement

Conrad Bertrand Tabi: Writing – review & editing, Writing – original draft, Supervision, Project administration, Funding acquisition, Data curation, Conceptualization. **Phelo Otlaadisa:** Writing – original draft, Visualization, Software, Methodology, Formal analysis, Data curation, Conceptualization. **Timoléon Crépin Kofané:** Writing – review & editing, Validation, Supervision, Project administration, Methodology, Investigation, Formal analysis.

Declaration of competing interest

The authors declare that they have no known competing financial interests or personal relationships that could have appeared to influence the work reported in this paper.

Data availability

Data will be made available on request.

Acknowledgements

The work by CBT is financially supported by the Botswana International University of Science and Technology under the grant **DVC/RDI/2/1/16I (25)**. CBT is also grateful to the Kavli Institute for Theoretical Physics (KITP).

Appendix A. Matrix (15) elements for $\beta_x = \beta_y = \beta$, with $(\beta x + \beta y) = \pi/2$

$$
\begin{aligned}
&n_{11} = \beta K_1 + \alpha K_2,\ \ n_{12} = K_1\alpha + K_2\beta - (iK_1 + K_2)\lambda_R - \lambda_D(K_1 + iK_2),\\
&n_{13} = -\frac{1}{2}(K_1^2 + K_2^2) + \beta(\lambda_D + i\lambda_R),\ \ n_{14} = -\beta(\lambda_D + i\lambda_R),\\
&n_{21} = (\beta K_2 + \alpha K_1) + \lambda_R(iK_1 - K_2) + \lambda_D(K_1 - iK_2),\ \ n_{22} = \alpha K_2 + \beta K_1,\ \ n_{23} = -\beta(\lambda_D + i\lambda_R),\\
&n_{24} = -\frac{1}{2}(K_1^2 + K_2^2) + \beta(\lambda_D + i\lambda_R),\ \ n_{31} = \frac{1}{2}(K_1^2 + K_1^2) + 2g_{11}n_0 - \beta(\lambda_D + i\lambda_R),\\
&n_{32} = 2g_{12}n_0 + \beta(\lambda_D + i\lambda_R),\ \ n_{33} = -(\beta K_1 + \alpha K_2),\ \ n_{34} = \lambda_R(K_2 + iK_1) + \lambda_D(K_1 + iK_2) - (K_1\alpha + K_2\beta),\\
&n_{41} = 2g_{12}n_0 + \beta(\lambda_D + i\lambda_R),\ \ n_{42} = \frac{1}{2}(K_1^2 + K_2^2) + 2g_{22}n_0 - \beta(\lambda_D + i\lambda_R),\\
&n_{43} = \lambda_R(K_2 - iK_1) + \lambda_D(iK_2 - K_1) - (\beta K_2 + k_1\alpha),\ \ n_{44} = \beta K_1 - \alpha K_2.
\end{aligned}
\tag{A.1}
$$

Appendix B. Coefficients P_j ($j = 0, 1, 2, 3$) of the dispersion relation (16)

$$
\begin{aligned}
P_3 &= n_{11} + n_{22} - n_{33} - n_{44},\\
P_2 &= -n_{12}n_{21} + n_{13}n_{31} + n_{23}n_{32} + n_{14}n_{41} + n_{24}n_{42} - n_{34}n_{43}\\
&\quad + n_{22}(-n_{33} - n_{44}) + n_{11}(n_{22} - n_{33} - n_{44}) + n_{33}n_{44},\\
P_1 &= n_{14}(n_{22}n_{41} - n_{33}n_{41} - n_{21}n_{42} + n_{31}n_{43}) + n_{24}(n_{32}n_{43} - n_{33}n_{42})\\
&\quad + n_{22}(n_{33}n_{44} - n_{34}n_{43}) + n_{11}(n_{23}n_{32} + n_{24}n_{42} - n_{34}n_{43} + n_{22}(-n_{33} - n_{44}) + n_{33}n_{44})\\
&\quad + n_{13}(n_{22}n_{31} - n_{44}n_{31} - n_{21}n_{32} + n_{34}n_{41}) + n_{23}(n_{34}n_{42} - n_{32}n_{44})\\
&\quad + n_{12}(-n_{23}n_{31} - n_{24}n_{41} + n_{21}(n_{33} + n_{44})),\\
P_0 &= n_{14}(n_{23}(n_{32}n_{41} - n_{31}n_{42}) + n_{22}(n_{31}n_{43} - n_{33}n_{41}) + n_{21}(n_{33}n_{42} - n_{32}n_{43}))\\
&\quad + n_{13}(n_{24}(n_{31}n_{42} - n_{32}n_{41}) + n_{21}(n_{32}n_{44} - n_{34}n_{42}) + n_{22}(n_{34}n_{41} - n_{31}n_{44}))\\
&\quad + n_{11}(n_{24}(n_{32}n_{43} - n_{33}n_{42}) + n_{22}(n_{33}n_{44} - n_{34}n_{43}) + n_{23}(n_{34}n_{42} - n_{32}n_{44}))\\
&\quad + n_{12}(n_{24}(n_{33}n_{41} - n_{31}n_{43}) + n_{23}(n_{31}n_{44} - n_{34}n_{41}) + n_{21}(n_{34}n_{43} - n_{33}n_{44})).
\end{aligned}
\tag{B.1}
$$

References

[1] C.C. Bradley, C.A. Sackett, J.J. Tollett, R.G. Hulet, Phys. Rev. Lett. 75 (1995) 1687.
[2] C.C. Bradley, C.A. Sackett, R.G. Hulet, Phys. Rev. Lett. 78 (1997) 985.
[3] M.H. Anderson, J.R. Ensher, M.R. Mathews, C.E. Wieman, E.A. Cornell, Science 269 (1995) 198.
[4] K.B. Davis, M.-O. Mewes, M.R. Andrews, N.J. van Druten, D.S. Durfee, D.M. Kurn, W. Ketterle, Phys. Rev. Lett. 75 (1995) 3969.
[5] F. Dalfovo, S. Giorgini, L.P. Pitaevskii, S. Stringari, Rev. Mod. Phys. 71 (1999) 463.
[6] I. Bloch, J. Dalibard, W. Zwerger, Rev. Mod. Phys. 80 (2008) 885.
[7] K.E. Strecker, G.B. Partridge, A.G. Truscott, R.G. Hulet, Nature 417 (2002) 150.
[8] L. Khaykovich, F. Schreck, G. Ferrari, T. Bourdel, J. Cubizolles, L.D. Carr, Y. Castin, C. Salomon, Science 296 (2002) 1290.
[9] D.B. Belobo, G.H. Ben-Bolie, T.C. Kofané, Phys. Rev. E 89 (2014) 042913.
[10] D.B. Belobo, G.H. Ben-Bolie, T.C. Kofané, Phys. Rev. E 91 (2015) 042902.
[11] S. Burger, K. Bongs, S. Dettmer, W. Ertmer, K. Sengstock, A. Sanpera, G.V. Shlyapnikov, M. Lewenstein, Phys. Rev. Lett. 83 (1999) 5198.
[12] A. Mohamadou, E. Wamba, D. Lissouck, T.C. Kofané, Phys. Rev. E 85 (2012) 046605.
[13] F.K. Abdullaev, A.A. Abdumalikov, R.M. Galimzyanov, Phys. Lett. A 367 (2007) 149.
[14] F.K. Abdullaev, P.G. Kevrekidis, M. Salerno, Phys. Rev. Lett. 105 (2010) 113901.
[15] F.K. Abdullaev, V.V. Konotop, M. Salerno, A.V. Yulin, Phys. Rev. E 82 (2010) 056606.
[16] I. Shomroni, E. Lahoud, S. Levy, J. Steinhauer, Nat. Phys. 5 (2009) 193.
[17] M.R. Matthews, B.P. Anderson, P.C. Haljan, D.S. Hall, C.E. Wieman, E.A. Cornell, Phys. Rev. Lett. 83 (1999) 2498.
[18] P. Engels, I. Coddington, P.C. Haljan, E.A. Cornell, Phys. Rev. Lett. 89 (2002) 100403.
[19] Q. Gu, K. Bongs, K. Sengstock, Phys. Rev. A 70 (2004) 063609.
[20] H. Sakaguchi, B.A. Malomed, Europhys. Lett. 72 (2005) 698.
[21] N. Bar-Gill, G. Kurizki, M. Oberthaler, N. Davidson, Phys. Rev. A 80 (2009) 053613.
[22] K. Staliunas, S. Longhi, G.J. de Valcarcel, Phys. Rev. Lett. 89 (2002) 210406.
[23] F.K. Abdullaev, M. Salerno, Phys. Rev. A 72 (2005) 033617.
[24] M. Greiner, O. Mandel, T. Esslinger, T.W. Hansch, I. Bloch, Nature 415 (2002) 39.
[25] L. Fallani, F.S. Cataliotti, J. Catani, C. Fort, M. Modugno, M. Zawada, M. Inguscio, Phys. Rev. Lett. 91 (2003) 240405.
[26] C.J. Myatt, E.A. Burt, R.W. Ghrist, E.A. Cornell, C.E. Wieman, Phys. Rev. Lett. 78 (1977) 586.
[27] J. Stenger, S. Inouye, D.M. Stamper-Kurn, H.-J. Miesner, A.P. Chikkatur, W. Ketterle, Nature (London) 396 (1998) 345.
[28] D.S. Hall, M.R. Matthews, J.R. Ensher, C.E. Wieman, E.A. Cornell, Phys. Rev. Lett. 81 (1998) 1539.
[29] D.M. Stamper-Kurn, M.R. Andrews, A.P. Chikkatur, S. Inouye, H.-J. Miesner, J. Stenger, W. Ketterle, Phys. Rev. Lett. 80 (1998) 2072.
[30] R. Wynar, R.S. Freeland, D.J. Han, C. Ryu, D.J. Heinzen, Science 287 (2000) 1016.
[31] T. Busch, J.R. Anglin, Phys. Rev. Lett. 87 (2001) 010401.
[32] C. Hamner, J.J. Chang, P. Engels, M.A. Hoefer, Phys. Rev. Lett. 106 (2011) 065302.
[33] P. Ohberg, L. Santos, Phys. Rev. Lett. 86 (2001) 2918.
[34] L. Salasnich, B.A. Malomed, Phys. Rev. A 74 (2006) 053610.
[35] K. Kasamatsu, M. Tsubota, Phys. Rev. Lett. 93 (2004) 100402.
[36] D.V. Freilich, D.M. Bianchi, A.M. Kaufman, T.K. Langin, D.S. Hall, Science 329 (2010) 1182.

[37] T. Kawakami, T. Mizushima, M. Nitta, K. Machida, Phys. Rev. Lett. 109 (2012) 015301.
[38] H.G. Luo, W.M. Liu, Phys. Rev. A 84 (2011) 053631.
[39] S. Stellmer, C. Becker, P. Soltan-Panahi, E.M. Richter, S. Dörscher, M. Baumert, J. Kronjäger, K. Bongs, K. Sengstock, Phys. Rev. Lett. 101 (2008) 120406.
[40] C. Hamner, Y. Zhang, J.J. Chang, C. Zhang, P. Engels, Phys. Rev. Lett.111 (2013) 264101.
[41] V.K. Kuetche, T.B. Bouetou, T.C. Kofané, A.B. Moubissi, K. Porsezian, Phys. Rev. A 82 (2010) 053619.
[42] E. Rashba, Sov. Phys., Solid State 2 (1960) 1109.
[43] Y.A. Bychkov, E.I. Rasbha, Pis'ma Zh. Eksp. Teor. Fiz. 39 (1984) 66.
[44] T.D. Stanescu, V. Galitski, Phys. Rev. B 75 (2007) 125307.
[45] W. Zheng, Z.-Q. Yu, X. Cui, H. Zhai, J. Phys. B, At. Mol. Opt. Phys. 46 (2013) 134007.
[46] Y.K. Kato, R.C. Myers, A.C. Gossard, D.D. Awschalom, Science 306 (2004) 1910.
[47] C.L. Kane, E.J. Mele, Phys. Rev. Lett. 95 (2005) 146802.
[48] V.M. Galitski, I.B. Spielman, Nature (London) 494 (2013) 49.
[49] P. Wang, Z.-Q. Yu, Z. Fu, J. Miao, L. Huang, S. Chai, H. Zhai, J. Zhang, Phys. Rev. Lett. 109 (2012) 095301.
[50] B.K. Stuhl, H.-I. Lu, L.M. Aycock, D. Genkina, I.B. Spielman, Science 349 (2015) 1514.
[51] Z. Wu, L. Zhang, W. Sun, X.-T. Xu, B.-Z. Wang, S.-C. Ji, Y. Deng, S. Chen, X.-J. Liu, J.-W. Pan, Science 354 (2016) 83.
[52] X.-Q. Xu, J.H. Han, Phys. Rev. Lett. 107 (2011) 200401.
[53] G.J. Conduit, Phys. Rev. A 86 (2012) 021605.
[54] O. Fialko, J. Brand, U. Zülicke, Phys. Rev. A 85 (2012) 051605.
[55] V.E. Lobanov, Y.V. Kartashov, V.V. Konotop, Phys. Rev. Lett. 112 (2014) 180403.
[56] V. Achilleos, D.J. Frantzeskakis, P.G. Kevrekidis, D.E. Pelinovsky, Phys. Rev. Lett. 110 (2013) 264101.
[57] Y.K. Liu, S.J. Yang, Europhys. Lett. 108 (2014) 30004.
[58] S. Gautam, S.K. Adhikari, Phys. Rev. A 90 (2014) 043619.
[59] V. Zakharov, L. Ostrovsky, Physica D 238 (2009) 540.
[60] E.V. Goldstein, P. Meystre, Phys. Rev. A 55 (1997) 2935.
[61] V.V. Konotop, M. Salerno, Phys. Rev. A 65 (2002) 021602.
[62] A. Smerzi, A. Trombettoni, P.G. Kevrekidis, A.R. Bishop, Phys. Rev. Lett. 89 (2002) 170402.
[63] G. Theocharis, Z. Rapti, P.G. Kevrekidis, D.J. Frantzeskakis, V.V. Konotop, Phys. Rev. A 67 (2003) 063610.
[64] L.D. Carr, J. Brand, Phys. Rev. Lett. 92 (2004) 040401.
[65] E. Wamba, A. Mohamadou, T.C. Kofane, Phys. Rev. E 77 (2008) 046216.
[66] E. Wamba, A. Mohamadou, T.B. Ekogo, J. Atangana, T.C. Kofané, Phys. Lett. A 375 (2011) 4288.
[67] J.H.V. Nguyen, De Luo, R.G. Hulet, Science 356 (2017) 422.
[68] I. Ferrier-Barbut, M. Wenzel, M. Schmitt, F. Battcher, T. Pfau, Phys. Rev. A 97 (2018) 011604.
[69] K.E. Strecker, G.B. Partridge, A.G. Truscott, R.G. Hulet, Nature 417 (2002) 150.
[70] I. Vidanovi, N.J. van Druten, M. Haque, New J. Phys. 15 (2013) 035008.
[71] W. Hai, C. Lee, G. Chong, Phys. Rev. A 70 (2004) 053621.
[72] K. Kasamatsu, M. Tsubota, Phys. Rev. A 74 (2006) 013617.
[73] X.-X. Li, R.-J. Cheng, A.-X. Zhang, J.-K. Xue, Phys. Rev. E 100 (2019) 032220.
[74] T. Mithun, K. Kasamatsu, J. Phys. B, At. Mol. Opt. Phys. 52 (2019) 045301.
[75] I.A. Bhat, T. Mithun, B.A. Malomed, K. Porsezian, Phys. Rev. A 92 (2015) 063606.
[76] S. Bhuvaneswari, K. Nithyanandan, P. Muruganandam, K. Porsezian, J. Phys. B, At. Mol. Opt. Phys. 49 (2016) 245301.
[77] D. Singh, M.K. Parit, T.S. Raju, P.K. Panigrahi, J. Phys. B, At. Mol. Opt. Phys. 53 (2020) 245001.
[78] P. Otlaadisa, C.B. Tabi, T.C. Kofané, Phys. Rev. E 103 (2021) 052206.
[79] C.B. Tabi, S. Veni, T.C. Kofané, Phys. Rev. A 104 (2021) 033325.
[80] C.B. Tabi, S. Veni, T.C. Kofané, Phys. Lett. A 442 (2022) 128192.
[81] P.-S. He, W.-L. You, W.-M. Liu, Phys. Rev. A 87 (2013) 063603.
[82] L. Salasnich, W.B. Cardoso, B.A. Malomed, Phys. Rev. A 90 (2014) 033629.
[83] J. Jin, S. Zhang, W. Han, J. Phys. B, At. Mol. Opt. Phys. 47 (2014) 115302.
[84] H. Sakaguchi, E.Ya. Sherman, B.A. Malomed, Phys. Rev. E 94 (2016) 032202.
[85] S. Liu, B. Liao, J. Kong, P. Chen, J. Lu, Y. Li, C. Huang, Y. Li, J. Phys. Soc. Jpn. 87 (2018) 094005.
[86] T.-L. Ho, V.B. Shenoy, Phys. Rev. Lett. 77 (1996) 3276.
[87] Y.V. Kartashov, E.Y. Sherman, B.A. Malomed, V.V. Konotop, New J. Phys. 22 (2020) 103014.
[88] S.V. Samsonov, A.D.R. Phelps, V.L. Bratman, G. Burt, G.G. Denisov, A.W. Cross, K. Ronald, W. He, H. Yin, Phys. Rev. Lett. 92 (2004) 118301.
[89] G. Burt, S.V. Samsonov, K. Ronald, G.G. Denisov, A.R. Young, V.L. Bratman, A.D.R. Phelps, A.W. Cross, I.V. Konoplev, W. He, J. Thomson, C.G. Whyte, Phys. Rev. E 70 (2004) 046402.
[90] M.C. Rechtsman, J.M. Zeuner, Y. Plotnik, Y. Lumer, D. Podolsky, F. Dreisow, S. Nolte, M. Segev, A. Szameit, Nature (London) 496 (2013) 196.
[91] G. Biondini, Phys. Rev. Lett. 99 (2007) 064103.
[92] J.-P. Martikainen, H.T.C. Stoof, Phys. Rev. Lett. 93 (2004) 070402.
[93] Y.V. Kartashov, V.V. Konotop, M. Modugno, E.Y. Sherman, Phys. Rev. Lett. 122 (2019) 064101.
[94] L.D. Carr, J. Brand, Phys. Rev. Lett. 92 (2004) 040401.
[95] L. Salasnich, A. Parola, L. Reatto, Phys. Rev. Lett. 91 (2003) 080405.
[96] H. Sakaguchi, Ben Li, B.A. Malomed, Phys. Rev. E 89 (2014) 032920.
[97] Y.V. Kartashov, V.V. Konotop, L. Torner, Phys. Rev. B 86 (2012) 205313.
[98] K. Mæland, A.T.G. Janssønn, J.H. Rygh, A. Sudbø, Phys. Rev. A 102 (2020) 053318.
[99] H. Sakaguchi, B.A. Malomed, Phys. Rev. A 96 (2017) 043620.
[100] S. Gautam, S.K. Adhikari, Phys. Rev. A 97 (2018) 013629.
[101] Y. Xu, L. Mao, B. Wu, C. Zhang, Phys. Rev. Lett. 113 (2014) 130404.
[102] J.R. Li, J. Lee, W. Huang, S. Burchesky, B. Shteynas, F.C. Top, A.O. Jamison, W. Ketterle, Nature 543 (2017) 91.
[103] C. Wang, C. Gao, C.M. Jian, H. Zhai, Phys. Rev. Lett. 105 (2010) 160403.
[104] Y.-F. Jiang, A.-X. Zhang, X.-W. Hu, Z.-F. Yu, J.-K. Xue, Phys. Lett. A 392 (2021) 127169.
[105] S. Liu, B. Liao, J. Kong, P. Chen, J. Lü, Y. Li, C. Huang, Y. Li, J. Phys. Soc. Jpn. 87 (2018) 094005.